A Perspective of Photocatalytic Materials Applications for Sustainable Agriculture

Yanjie Wang,[1] Juliana A. Torres,[3] Meital Shviro,[2] Marcelo Carmo,[2] Tao He,[1] Caue Ribeiro[3]

1. **Chinese Academy of Sciences, Key Laboratory of Nanosystem and Hierarchical Fabrication, CAS Center for Excellence in Nanoscience, National Center for Nanoscience and Technology, Beijing 100190, China.**
   E-mail address: het@nanoctr.cn
2. **Forschungszentrum Julich, Institute of Energy & Climate Research, IEK 14, D-52425 Julich, Germany. E-mail address: m.carmo@fz-juelich.de**
3. **Embrapa Instrumentation, Rua XV de Novembro, 1452, C.P. 741, São Carlos, Sao Paulo 13560-970, Brazil. E-mail address: caue.ribeiro@embrapa.br**

Abstract

The pressure for more sustainable, environmentally friendly Agriculture is a trend that affects its value chain in several levels, including the production of fertilizers, the management of pesticides and other chemicals, and solutions for the related greenhouse gas emissions (N_2O, NO_x, CH_4, and CO_2). Moreover, the search for value motivates novel routes to utilize biomass in chemical production, including sustainable fuels. These topics are interconnected to developing photocatalytic materials, i.e., those promoting reactions by light activation, primarily through the solar light incidence. Thus, this review summarizes the many efforts done to develop adequate materials for photocatalysis in the context of Agriculture problems, discussing the recent advances and challenges for application in the real world.

1. Introduction

Agriculture is one of the major activities of human life. The perception that food production is affected by modern chemical techniques is undisputed, but the general public does not fully understand the consequences [1]. The continuous increase in agricultural production depends on the development of agrichemicals – a term that comprises the chemical nutrient sources (e.g., fertilizers) but also the defensives (e.g., pesticides, insecticides, herbicides, etc.), including a molecules' plethora [2]. The importance of developing catalytic materials for agricultural productivity is largely unrecognized. The so-called *green revolution* [3] was only possible by the increase in ammonium production resulting from the Haber-Bosch (HB) process, [4] which is the basis of nitrogen fertilization. This term was coined by Norman Borlaug (1970 Peace Nobel Prize), referring to the contributions of novel agriculture practices (e.g., seed technology, soil correction, fertilization, pest control, etc.) that have impacted food production worldwide, especially in developing countries. Indeed, nitrogenated synthetic fertilizers are responsible for half of the agricultural output, resulting in doubling the world's population (Fig. 1). The development of catalytic materials for the HB process has been one of the essential chemical issues in the last century, and it is still the most critical technology for converting N_2 into chemical products [5]. In this sense, we can understand that the link between catalytic materials and agricultural production is more robust than common sense says.

However, the pressure for production is still growing, influencing the increased utilization of models based on monocultures (i.e., the specialized production of one or two crops in an alternated process) and crop production for animal feeding. This production model also increases the demand for fertilizers and targeted pesticides since the large extensions of determined crops mean that some pests are growing faster. Also, specialized production means that certain nutrients are more required by plants, leading to

deficiencies managed by intensive application of specific fertilizers. Their applications have frequently been associated with ecological disbalances, as water eutrophication and greenhouse gas emissions [6,7]. On the other hand, the increase in pest incidences, also due to climate changes, has led to higher pesticide applications, which, besides the ecological risk, are associated with food contamination in some cases [8,9]. By these examples, the general public often has the perception that the agriculture chemistry is *"unclean"* and claims for a novel agriculture paradigm, based on reduced utilization of agrichemicals and better efficiency in input consumption [10]. Thus, developing innovative clean processes based on advanced management of inputs is necessary to aim for far more sustainable agriculture. Also, other production methods are required, replacing energy sources with renewable ones and avoiding environmental contaminations before happening.

In this context, the interest in coupling these processes with photocatalysis has increased due to the possibility of solar light utilization as an energy source, replacing non-renewable ones. The range of possible reactions driven by light virtually covers any agriculture input production. However, the catalytic materials to enable them are still largely underexplored, and the economic viability is still unclear. To date, most of the research done about photocatalytic applications in agriculture regards the role of semiconductors in oxidative reactions, which have mainly been studied for the abatement of pesticides in water [11,12]. On the other hand, the range of different possible reactions, from the treatment of greenhouse gases (NO_x) [13–15] to the coupling with energy production and conversion (CH_4 controlled oxidation [16] and CO_2 reduction [17] should be emphasized in this context (Fig. 2) [18]. Therefore, this review aims to address the scientific opportunities and challenges for photocatalytic materials in agriculture and the threats that can impede the transition of scientific achievements to applied technologies.

1.1 Review Outline

The structure of this review paper is divided to cover the most common applications of photocatalytic materials to prospective topics in agriculture. Initially, a general view of the fundamental basis of photocatalytic properties in materials introduces the reader to the topic (2). Topic 3 deals with the role of photocatalytic materials in pollutant degradation. The review summarizes the research about pesticide treatment through photocatalytic materials in the last five years (2017-2021, Topic 3.1) since this is the most addressed problem in this context. An overview of the photocatalytic materials studied for the treatment of animal medicines and hormones is also discussed (Topic 3.2). A general view of the direct application of photocatalysts in plants, aiming to use them as inorganic pesticides, and its effects are presented (Topic 3.3).

Topic 4 surveys the photocatalytic materials used in the abatement of greenhouse and pollutant gases produced in agriculture is addressed, discussing NO_x and N_2O decomposition (Topic 4.1), CH_4 reforming (Topic 4.2), and H_2S (Topic 4.3). A general view of photocatalytic materials prospective applications in biorefining follows in Topic 5, discussing cellulose bleaching treatment (Topic 5.1), lignin (Topic 5.2), and glycerol reforming (Topic 5.3).

In Topic 6, a discussion of CO_2 photoreforming from agricultural process to energy storage is introduced, addressing the challenges for high-volume CO_2 conversion. Finally, in Topic 7, we present a summary of prospective photocatalytic materials research to convert N_2 to NH_3, being that this is the essential reaction to produce fertilizers. Therefore, the review covers many possible applications of these materials in different levels for agriculture, showing the importance of this research.

2. Fundaments of Photocatalytic Properties in Materials

The history of the photocatalytic process becomes with the rising to the Advanced Oxidative Methods (AOPs) in the context of environmental pollution treatment, which comprises methods that produce aggressive radicals capable of recalcitrant oxidizing pollutants in water bodies. Among the methods, Fenton oxidation and its derivation Photo-Fenton are precursors of all AOPs, based on the ability of Fe^{2+} and Fe^{3+} ions to react against H_2O_2 forming respectively high-oxidative *OH and *OOH radicals, which oxidize molecules in solution [19]. The changes of valences keep a sustainable reaction, although consuming H_2O_2, whose concentration limits the reaction extension.

These radicals are non-selective, i.e., they will react with any molecule dispersed in solution, not only contaminants. This condition initially is an advantage since, in principle, Fenton reactants could oxidize all the byproducts, hypothetically converting them to CO_2 and water. However, in actual conditions (i.e., rivers, lakes, etc.), these radicals can oxidize other components that are not contaminants, such as humic acids and other dispersed organic matter [20]. The concentrations of these other compounds are typically much higher than the contaminants, indicating that the process is practically limited in many of the real conditions.

During the 1970s, the capacity of semiconductors, especially oxides, to react with water has been studied, showing that these materials could produce *OH radicals if dispersed in water and illuminated in suitable conditions [21,22]. The process is based on the surface interaction of these semiconductors with water since most of them are hydrophilic or form surface hydroxides. When these semiconductors are irradiated, the formation of electron-hole pairs – an *exciton*[23] – lead to an in-situ redox process: OH^- is oxidized by the valence band holes, while the conduction band electron reduces species, mainly water-dissolved O_2, forming O_2^-. It reacts with H^+ in solution, forming *OOH, a

strong oxidant, leading to a sustainable oxidative radical production-driven only by irradiation [24].

Fig. 3 shows a general scheme of the photoactivation of semiconductors, listing some relevant reactions that can be performed. These reactions depend on the relative potential of electrons and holes (band energy position). Thus, different semiconductors can favor different oxidative and reductive reactions.[25] The process efficiency is governed by the charge recombination that is determined by electron and hole mobilities, factors that increase the *exciton* lifetime.[26] The recombination can be reduced by promoting electron and hole migration by designing heterojunctions, i.e., combinations of two semiconductors or semiconductor/metal in contact at interface allowing charge conduction.[27]

Regarding single phases, semiconductors as TiO_2 [11] and ZnO [28] have significantly long exciton lifetimes and are the more representative examples in literature. However, both are wide-bandgap oxides, i.e., they are excited only in light wavelengths below the near-ultraviolet (UVC) range. It corresponds to less than 7% of the total solar spectrum, limiting energy harvesting and process efficiency. Thus, efforts to shift bandgaps to the visible range by doping to increase solar light harvesting are an essential matter of concern in the literature [29].

The similarity of the degradation mechanism with the Fenton mentioned above has suggested that some authors name it a *Fenton-like* process [30]. Indeed, both are indirect oxidation methods based on the previous formation of oxidative radicals, which are the proper oxidant reactants. Since the radical formation comes directly from water dissociation equilibrium (H^+:OH^- relation) with no further H_2O_2, the process is advantageous and possible to be sustained in more extended periods, especially in the alkaline medium due to the higher availability of OH^- groups. On the other hand, the original Fenton and

photo-Fenton processes tend to be more aggressive and faster, leading to complete degradation in shorter times [31].

As seen in Fig. 3, the electron transference from the conduction band can promote other reduction reactions, depending on the components in the medium. If O_2 is not available or limited, molecules such as CO_2 or N_2 can capture electrons leading to reduction processes in a sequence of steps [32,33]. Another important electron transference process is sensitization, i.e., the alignment between the LUMO level of molecules at the surface (e.g., organic molecules) and the semiconductor's conduction band. It may result in the direct transference of electrons from the molecule to the photocatalyst (Fig. 4) [46]. This phenomenon has been explored mainly in dye-sensitized solar cells, which utilize the absorption of many dyes in visible light to transfer electrons to the semiconductor, increasing the wavelength range where the light is harvested [36].

Therefore, Fig. 5 summarizes the several process of interest to Agriculture that are promoted by photocatalysts. The application is often proposed by dispersing fine, nanoparticulated oxide semiconductors in water with the contaminant to be oxidized or compound to be reduced and exposed to the solar light. Variations include preparing pellets, catalytic supports (*Raschig* rings, etc.), and others to facilitate the materials recovery [37]. Other propositions are the immobilization at reflective or transparent surfaces, and at conductive electrodes (i.e., photoelectrodes for photoelectrochemical devices), depending on the desired application [38]. These features will be highlighted in the following topics, showing the advantages of each application approach.

3. Materials for the Photodegradation of agriculture-related contaminants

3.1 Pesticide degradation: an overview of research in the last five years (2017-2021)

The concern about water utilization in agriculture is based on its extensive use. It is estimated that 70% of the total drinkable water on the planet is used in agriculture, whereas pesticides are considered the second most crucial contamination source. A general overview of pesticide utilization in the world indicates that consumption is increasing in all continents and has almost doubled in 30 years – which justifies the increase in environmental problems (Fig. 6). Decontamination is frequently not possible, given that the contaminants tend to migrate to groundwaters and water bodies (rivers, lakes, etc.), making economically impossible to treat in these scales [39].

Therefore, procedures to avoid contamination before it happens are more effective, limiting the environmental damage in the long term. Usually, these approaches should identify where the contamination comes from and apply some method to eliminate or, at least, reduce the pesticide concentration before disposal [40]. Noteworthy to mention, international regulations define the maximum concentration of active principles in disposed water, considering the natural capacity of biota for treating them. It means that a total degradation of these contaminants is not a necessary target, although desirable [41].

A revision of the published papers about photocatalytic materials applied on pesticide degradation in the last 5 years indicates that TiO_2 and ZnO materials are still the most studied materials (Table 1). Bi-based (Bi_2O_3, BiOBr) and C-based materials (g-C_3N_4 and graphene) are also frequently seen (Table 2). Generally, authors are still investing in applying freestanding nanoparticles (i.e., unsupported) with sizes smaller than 50 nm and in simulated effluents, e.g., deionized water contaminated with low pesticides concentration.

Efforts to increase the solar light absorption have been developed, but even with some advances, the efficiency of TiO_2, particularly P25 TiO_2, is still remarkable [42]. This material (as illustrated in Fig. 7) [43] is a heterostructure, comprising around 20% TiO_2 rutile and 80% TiO_2 anatase phase, with better performance than isolated phases. The heterostructure promotes better electron-hole separation, increasing the electron-hole pair lifetime and reducing recombination. Both are critical for photocatalytic efficiency since the pairs should migrate to the surface to react with adsorbed OH^- groups. Also, TiO_2 has high chemical stability, with negligible dissolution – compared to TiO_2, ZnO suffers from photocorrosion, dissolving during the process [44]. Several authors [45–49] have proposed synthesizing similar heterostructures with TiO_2 and other semiconductors, looking forward to the P25 performance or higher. It is essential to notice that several examples regard Z-schemes instead of heterojunctions, although the charge separation effect is similar, as exemplified in Fig. 8. These results indicate that, for photodegradation, heterojunctions are in general superior to isolated phases. The investigation of doped materials is still an issue. However, the increase in TiO_2 light absorption range by anion-doping (C, N, and S) has lost its initial interest [50,51], with few authors dedicating to these syntheses in the last years at least for pesticide degradation [52–55].

Some distinctive aspects of pesticide chemistry affect photochemical degradation performance. Their surface interaction with irradiated semiconductors can promote sensitization leading to their direct oxidation [45]. However, it is less representative in pesticides since most of them do not absorb visible light. Therefore, their excitation wavelengths are in the same range as semiconductors' bandgap. Thus the most important mechanism for their degradation is the attack of oxidative radicals in water (Equation 23 in Fig. 4) [56]. Another critical point is that most of the pesticides' effluents are acidic (increasing the molecule's solubility), limiting the availability of OH radicals.

Considering that most of the oxide semiconductors are better dispersed in an alkaline environment, the acidic medium can induce nanoparticle agglomeration, reducing the process' effectiveness [57].

In any case, the photodegradation of pesticides is still challenging since degradation byproducts can be more toxic than the starting molecules. An example is atrazine degradation, a common herbicide initially oxidized to hydroxyatrazine, considered a more toxic molecule [58]. It is an essential concern since many byproducts are more recalcitrant, i.e., they have increased oxidation potentials. Tables 1 and 2 also include a list of targeted pesticides, where triazines (atrazine, simazine, and ametrine) are still more frequent than other molecules. Furthermore, several common pesticides are more soluble in organic media instead of water. The degradation tends in some cases (as in this example above) to increase hydrophilicity, making the molecule more dispersed in water than in its original state. Thus, a more toxic byproduct with higher solubility can increase the exposition of aqueous biota to the hazard instead of reducing the risk (as exemplified for atrazine, in Fig. 9) [59]. On the other hand, higher solubility can increase its interaction with oxidant species, leading to sustained degradation, despite it usually tends to stop until some stable molecule is formed [60,61]. For instance, in atrazine degradation, the process tends to stabilize in cyanuric acid instead of CO_2 and water, as desired [62].

Other practical concerns about process applicability relate to the low pesticide concentration of real effluents and the fact that pesticide application in the field is made in formulations with several components (as solvents, oils, surfactants, and other adjuvants). This mixture typically exceeds pesticide concentration significantly, implying that these oxidative processes are only efficient with the previous separation. Fig. 10 exemplifies the difference between actual and simulated effluents. Although some separation processes can help as a 1st treatment process (filtration, decantation, etc.), soluble

adjuvants tend to be kept in the system, interfering with pesticide degradation. These components generally are less influent in drainage water, which the physical process acts as a pre-filtering process (Fig. 11) [63]. The mixture of two or more pesticides in the same formulations is still a current practice, making the system more and more complex [64].

Most of the literature reports experiments using simulated effluents, i.e., water solutions with low concentrations of pesticides (as seen in Tables 1 and 2). More efforts are necessary to address how mixtures interact with the photooxidative system, including the effect of soluble fractions as surfactants. The recent research done with real effluents is summarized in Table 3. As one can see, the number of investigations found is minimal compared to the experiments with simulated contaminations, with more examples using drainage or rainwater (which is expected to be cleaner than raw effluents).

3.2 Animal hormones and pharmaceutics degradation

Despite the strong interest in pesticides, hormones and veterinary pharmaceutics can be more hazardous due to their specific effects on biota [65]. Pharmaceuticals are an essential part of animal production (especially in large-scale poultry and swine productions), and residues can be found in excrements and disposed water. Commercial pharmaceutics also includes molecules that act as endocrine disruptors, antibiotics, and anti-inflammatories. All of them can affect non-target organisms triggered by tiny amounts of these compounds [66]. These effects are exceptionally high in fish and amphibians, which can develop teratogenic problems that affect a large part of the population in the ecosystem [67]. Therefore, the dispersion of these compounds is somewhat uncontrollable, and treatments should – as proposed for pesticides – previse the retention of contaminated water and its treatment before disposal. Contrary to the case of pesticides, the typic water

solubility of these compounds is a disadvantage for dispersion but favorable to increase its photodegradability [68].

An illustrative example is the application of antibiotics for mastitis control. This disease caused by *Staphylococcus aureus*, the most common pathology for dairy cattle, is treated by intramammary injection of the drug formulation (generally as a paste or gel containing antibiotics like penicillins, aminoglycosides, oxytetracycline, chloramphenicol, trimethoprim, and several other sulphonamides). It leads the animal (cow, sheep, or any other milk producer) to eliminate significant antibiotic amounts in the milk during the treatment [69]. This milk, being not adequate for consumption, is therefore discarded in water causing contaminations.

Compared to pesticides, the number of research papers about these contaminants is still low, as summarized in Table 4. However, the oxidation mechanisms are similar, based on the capacity of *OH radicals to oxidize them – as well, the proposed catalysts are the same. It is noteworthy that several authors have studied the direct photodegradation of these antibiotics, getting efficiencies of 60 to 80% of degradation, which emphasizes the gain with the photocatalysts (Table 5). On the other hand, these performances indirectly reveal that these pharmaceuticals are, in general, less recalcitrant than pesticides, which can explain the lower interest for the development of photocatalytic materials specifically for these contaminants.

3.3 Direct application of Photocatalysts in plants

The strong oxidant capacity of semiconductor photocatalysts has suggested their direct utilization as “inorganic” antibiotics. The photo-bactericidal effect of TiO_2 has been demonstrated for different microorganisms, such as *Escherichia coli* [70], *S. Aureus* [71], and fungi, as *Fusarium* species [72,73]. The mechanism involves the photooxidation

of cellular walls and possible permeation in the cell membrane, allowing DNA oxidation and leading to inactivation. The application of TiO_2 suspensions, pristine or modified with Ag or Cu, has been tested in leaves based on the principle that the solar irradiation could locally excite the nanoparticles and oxidize the microorganism or inhibit its fixation reducing the contamination. This effect has been shown in controlled contamination in seed and leaves of *Arabidopsis thaliana*, a typical control plant test (Fig. 12). However, there is still a lack of large-scale experiments, which could prove the efficiency of this strategy in actual cultivation [74]. Compared to the conventional pesticide treatment, the advantage is that some of these candidate materials are not toxic for plant growth in small amounts. Some others, as ZnO [75], can also be absorbed as a micronutrient, beneficial for plant growth and reducing further contamination [76].

However, other effects in the field can be more visible, as the UV-light protective factor provided by ZnO, which affects the plant physiology (e.g., increasing photosynthetic rate) and can interfere in microorganisms (plagues) development (Fig. 13) [77]. Unfortunately, then, the reported effects are still underexplored and not fully explained, being necessary more studies to understand the advantages of that strategy. Furthermore, to the moment, no research about the utilization of photocatalysis to disinfection or treatment in the animal chain (as in the as-mentioned mastitis treatment) has been identified, given that this is a field open for investigation.

4. Photocatalytic materials in agri-gases treatment: greenhouse and non-greenhouse emissions

Agriculture processes are extensive, and the absorption of atmospheric CO_2 through photosynthesis is by far the essential process of CO_2 conversion. However, except in forest and fiber production, the CO_2 fixation in food and bioenergy products is

negligible due to the utilization cycle. I.e., the biomass after consumption and digestion returns the same amount of carbon to the atmosphere [78]. This balance is the same in wildfire and wildland fire. This last is often used as an ancient technique for land preparation for planting, but it is considered one of the most relevant contributions of agriculture for global warming [79].

However, none of these impacts compares to cattle production, which is the most relevant agriculture-related greenhouse gas emitter: ruminants produce methane during their digestion cycle, which is continuously eliminated by breathing, corresponding to 44% of their emission. Methane has Global Warming Power (*GWP*) in 100 years of 25 CO_2e (CO_2 equivalence, i.e., the *GWP* of 1 mol of CH_4 equals the effect of 25 mol CO_2) [80], which means that even its burning would reduce the associated greenhouse effect. A single cow produces an average of 70 to 120 kg CH_4/year, which mainly depends on the used feeding material. Considering that there are more than 1.5 billion cattle globally, their contribution is around 150 MTon CH_4/year. Other components of animal emissions include N_2O (29%) and CO_2 (27%). These are all non-centralized emissions except in particular cases (e.g., confined production), i.e., the emission directly goes to the atmosphere, meaning that few can be done to recover and treat them [81].

It has been proposed that planting new trees could compensate these emissions since, during their growth, they convert carbon into biomass in a decentralized form as well [82]. However, recent estimations of how many trees should be planted to neutralize these emissions are controversial, given that it will demand extremely high re-forestation areas – which ultimately would include biomes that do not support extensive forestation. (e.g. savannas, cerrado, etc) [83]. Therefore, developing decentralized alternatives to treat these gases is necessary, especially for those with high *GWP*.

4.1 Nitrogenated compounds

The emissions related to agrichemicals, mainly fertilizers, are less discussed but critical to comprehend the specific effects of agriculture on global warming. Nitrogenated fertilization is primarily done with urea, $CO(NH_2)_2$, due to its low price and easy application [84]. Its uptake in plants (as a nutrient) initially passes through its hydrolysis (driven by urease, a common soil enzyme) to NH_4^+ and further oxidation to NO_3^-, both species absorbed by plants in different mechanisms [85]. However, each soil has a buffering property defined by its cation exchange capacity (CEC), represented mainly by the equilibrium of Ca^{2+} and Mg^{2+} ions with OH^- and CO_3^- in soil moisture. NH_4^+ will compete with these cations, and it should be fast absorbed or converted to NO_3^-, unless it will tend to volatilize, losing the fertilizer. Urea volatilization may indeed represent losses of around 30 to 50% of the total N application, one of the most important economic problems for large-scale agriculture [86].

More concerning, the accumulation of NO_3^- and intermediary NO_x species can lead to their conversion to nitrous oxide, N_2O, which has an impressive *GWP* of 298 CO_2e [80]. Generally speaking, since N_2O composes around 4 – 6% of the total emissions in crop cultures, its global warming effect can exceed the total of all the other emissions [87]. The photocatalytic abatement of NO_x and, ultimately, N_2O has two possible pathways: reducing N_2 [88] or oxidation to NO_3^- [89–92]. Table 6 summarizes the materials studied for NO_x and N_2O photodecomposition, mainly leading to N_2 and O_2 (reductive route). Again, TiO_2-derived materials are still the most common for these purposes, and a lack of studies in high scales is seen – although some authors have addressed the application in *in-flux* reactors, a scenario more feasible for pretended large scale application. Prospective materials (Bi-based and C_3N_4) are also found. Moreover, Table 7 summarizes the research done focusing on photooxidation to NO_3^-. The high overpotential for N_2O

reduction (+1,3 V NHE, pH 7) leads that generally oxidation is preferred – the potential for N_2O oxidation to NO_3^- is 0.33 V NHE (pH 7), i.e., easily covered by most conventional photocatalysts' valence bands [93,94]. Moreover, NO_3^- is very soluble and tends to readily adsorb in soil due to the cation availability, which means it can return as fertilizer [95].

Since these compounds are gases, their oxidation process is direct, i.e., it depends on the proper adsorption over the photocatalyst [96]. The selective NO_x photooxidation is probably related to its adsorption process. Indeed, some researchers have shown materials that could preferentially oxidize N_2O, making the process more efficient in terms of final environmental impact, as surveyed by Table 8. Unfortunately, the research about reactor projects for these reactions is scarce [97]. Despite some reports about filtering systems [98], it is necessary to consider that these are free emissions, i.e., contrary to concentrated processes (e.g., flue gases from a chimney), dispersed in the environment and of complex treatment. Some efforts were made to project concrete (mortar) formulation with TiO_2 (generally P25, spread in the surface coating or layer of pavement and walls), intending that the surfaces of surrounding buildings in the emission point can oxidize these nitrous oxides (Fig. 14) [99–101]. Surprisingly, this strategy produces a reduction of up to 80% of the nitrous oxide atmospheric concentration in the surrounding area, suggesting that the method is potentially feasible [102]. Table 9 lists examples of photocatalytic materials applied in large-scale and pilot plants studies, confirming that the proposition can be applied. However, there are no case studies in agriculture, possibly due to the larger extensions of agricultural fields, limiting the possibility of using existing buildings.

Although some authors suggested directly adding photocatalysts in soil for local photodegradation of contaminants [103,104], this strategy has not been reported for NO_x

emission reduction. Until this moment, a single research report about the photocatalytic properties of naturally-containing TiO_2 soils has been found [105]. Since these emissions are originated in soil microbiota, the intimate contact with the photocatalyst could locally oxidize NO_x to NO_3^- before the proper emission, keeping them as a nutrient (Fig. 15) [105,106]. However, a critical remark is that NO_3^- and NH_3 can react again, producing N_2O and N_2 – this effect was shown in TiO_2 surfaces under UV light [107] – which is highly undesirable. Moreover, the extensive addition of a metal oxide can unbalance the soil micronutrient composition or act as another contaminant: materials as ZnO, as previously mentioned, can be absorbed as a nutrient, but in high amounts, they can be phytotoxic (Fig. 16) [108]. Other photoactive materials studied for N_2O and NO_x oxidation, as graphene-decorated nanoparticles [109], still have unknown effects in soil microbiota. At the same time, some, as $BiVO_4$, can release toxic compounds for some microorganisms as V [110]. These limitations, although natural for large-scale cultures (e.g., grains), can be adequately addressed in small-farm production and specialized models, as plasticulture (i.e., protection of soil with plastic films, used for roots such as potato and creeping plants, as strawberry) [111].

4.2 Methane

Other emissions with significant importance are those related to biomass composting, a naturally occurring process used to produce organic fertilizers [112]. In composting, the bacterial action over the biomass converts the materials in humic substances, which are nutrient carriers with high amounts of N and P. In this process, it mainly emits CO_2 and CH_4, depending on the oxygenation degree that regulates the higher proliferation of aerobic or anaerobic bacteria strands (Fig. 17) [113,114]. The perception that biomass composting can be beneficial for fertilizer production as well as for energy is growing

worldwide. [115] For instance, in 2019, Europe has cataloged 18,943 biogas and 725 biomethane (separated) installations, with an increased number of plants running on agricultural substrates. Agricultural plants are followed by biogas plants running on sewage sludge, landfill waste, and various other types of waste, currently producing approximately 167 TWh of biogas and 26 TWh of purified biomethane (CH_4) [116].

These numbers hide that most CH_4 emissions are uncontrolled, from very dispersed sources, and of natural occurrence. Besides the cattle emission [81], other examples include rice pad fields, which show natural composting of dispersed organic matter dissolved in lower water layers closer to the roots [117]. However, this process, while beneficial for nutrient cycling, produces significant methane amounts. Other processes, such as biomass decomposition in landfills and animal manure maturation, also play essential roles, despite increasing efforts to replace the disposal of these residues for confined biodigesters [118].

The photooxidation of CH_4 to CO_2 is reported with the same approach of pollutant abatement [119], but since this molecule is a fuel considered as a bio, renewable energy, its simple oxidation does not make sense in a broad perspective. On the other hand, the controlled oxidation of CH_4 to other hydrocarbons might be an intelligent alternative to convert gaseous emissions in liquid fuels, as CH_3OH, or to other specialized chemicals (CO or HCOOH) [120,121]. However, studies about these reactions are still incipient since CH_4 is highly inert, with few examples reported in the literature. Among them, TiO_2 [122] and doped variants have been shown as capable of oxidizing CH_4, and some as Fe-doped TiO_2 have better performances for CH_4 controlled oxidation to methanol [123]. This process seems to be kinetically governed since authors generally reported better results when using H_2O_2 as a source of radicals instead of OH^-. The mechanism is still unclear, but similarly to electrochemical experiments about methane oxidation [124],

this reaction provides a less reactive radical but more specific to activate the C-H bond due to the interaction with the peroxide group (in *OOH radical) [125]. Identifying suitable catalysts is still an issue since the best-reported conversions are low (around 15%) [123]. Other photocatalysts include La-doped WO_3 [126] and Beta-Zeolites modified with V_2O_5 [127]. Theoretical calculations of the electrochemical oxidation potential of some materials indicated that V_2O_5 and other photoactive candidates fit the energetic criteria for CH_4-controlled oxidation.

Table 10 summarizes the materials studied as photocatalysts for methane-controlled oxidation and the main byproducts obtained in each case. More materials have been explored compared to other oxidative photoreactions, including more examples of supported materials (i.e., photocatalysts over SiO_2 and Al_2O_3). Byproducts include CH_3OH, C_2H_6, C_2H_6O, HCHO, CO, and H_2 and CO_2, frequently as a mixture. For instance, a photoelectrochemical approach using TiO_2 irradiated electrodes efficiently produced CO with a selectivity of around 60% [128]. CO is an essential component of syngas and, considering that currently, the industrial production of CO is based on natural gas, the replacement for a renewable source and using solar light is promising [129]. Noteworthy, several papers do not report the byproducts but only the CH_4 conversion efficiency. These aspects indicate that an essential open issue is the byproduct selectivity. Another point of care is that few papers have used solar light simulators or direct sunlight. Several still explore UV lamps – a condition far from the actual solar light application.

It is essential to point out that CH_4 controlled oxidation application is expected to be more feasible only in confined biomethane productions, where the gas capture and upgrading (to a high concentration CH_4 stream) is possible, with reaction byproducts separation [130,131]. However, the current state-of-the-art indicates that the efforts are still in their infancy, and more research is needed to provide concrete scenarios.

4.3 Hydrogen Sulfide

Hydrogen sulfide (H_2S), although less relevant on composting gases' composition (<1% of the emission) [131,132], is undoubtedly the most noticed due to its strong smell, similar to rotten eggs. This emission is more pronounced in animal manure decomposition and carcass decomposition (bodies, blood, etc.). Therefore higher amounts of H_2S in principle can be produced in the meat production cycle composting [133,134]. Although not considered a global warming gas, there is an environmental concern due to its conversion cycle to SO_2 in the atmosphere, related to acid rain [135]. However, its agricultural emissions are still low to be a significant concern (primary emissions are from natural gas purification) compared to the other agri-gases. Table 11 summarizes the research done for H_2S destruction using freestanding photocatalysts. Although TiO_2 nanoparticles are still the most frequently used catalysts, some examples of supported materials (Table 12) – including TiO_2-containing paints [136] or in tiles [137] – are seen. Generally, most of the papers have used UV lamps instead of solar light, limiting the extension of these data to real conditions.

The by-product of this reaction is SO_4^{2-} or elemental S, which can be re-oxidized to SO_4^{2-} by soil microorganisms forming an essential nutrient for plants [138]. S deficiency is currently one of the most critical bottlenecks for increasing crop production (mainly soybean and corn), meaning subsequent S disposal is still attractive as a nutrient [139]. Thus, photooxidation could be used to oxidize S, given that S/SO_4^{2-} is low compared to OER (E^o = 0.357 V SHE) [93,140]. But this process is naturally driven by soil microorganisms such as *thiobacillus* (e.g., *Acidithiobacillus thiooxidans* and *Acidithiobacillus ferrooxidans*), which oxidizes S instead of carbohydrates as an energy source [141].

One point of concern is that H_2S can be directly decomposed by UV light. Examples from the literature (Table 13) confirm that the light application is efficient for oxidation with no need of catalysts. However, the typical efficiencies are below the observed in the photocatalytic experiments, and the experiment times are usually longer.

Alternatively, H_2S photooxidation has been proposed as a choice of sacrificial reactant for H_2 production in water photosplitting [140]. The oxidation potential for the pair $H_2S_{(aq)}/S$ is 0.144 V (SHE), significantly below the oxygen evolution potential from water (OER), H_2O/O_2, 1.23 V (SHE).[93,140] This difference is remarkable since both reactions produce 2 electrons, i.e., the H_2 evolution reaction is not limited by the coupled oxidation with H_2S but favored [142]. Table 14 summarizes the efforts for using H_2S as a sacrificial agent. The catalysts are generally heterojunctions or nanocomposites (i.e., two or more catalysts in the same particle) – the highest catalytic performance observed was for MnCdS/CdMnS, in the range of 100 mmol $h^{-1}.g_{catalyst}^{-1}$ (Fig. 18) [143]. However, the few examples indicate that this topic should be more studied to support a technological approach.

5. Perspectives for photocatalytic materials in bio-refining

5.1 Cellulose and Cellulose-bleach

The concept of biorefining is becoming popular, claimed as the next revolution for agriculture. The idea comprises producing chemicals from biomass as a renewable source by sequential unitary operations similar to oil refining [144]. In this sense, bioethanol production is the easier-to-look example since based on sugar extraction (e.g., from sugarcane) followed by fermentation, which effectively produces ethanol. Moreover, several others can be made from this molecule by sequential reactions, including complex molecules as polymers [145].

However, the biorefining concept is often associated with the re-utilization of byproducts, mainly lignocelluloses – the fundamental constituents of biomass (wood, grasses, etc.) – to produce other molecules by breaking their long chains in smaller parts [146]. Lignocelluloses are formed by plant photosynthesis, basically comprising cellulose, hemicellulose, and lignin. Their specific contents vary with the plant, with some examples with more than 90% cellulose (e.g., cotton), to 40-45% cellulose with 20-25% lignin (e.g., pinus wood). Cellulose is of greater commercial interest because of paper and textile production, while lignin is often discarded or burned for heat [147].

Since cellulose has a glycol structure, oxidation can convert it to elemental sugars (sucrose or glucose) for fermentation. There is significant research in acid hydrolysis and enzymatic processes for cellulose conversion to sugars, being used in pilot scale for the so-called *2nd Generation Ethanol* [148]. However, photooxidation has been rarely proposed for these specific means since it is hardly efficient due to cellulose's high chemical stability despite being investigated for H_2 evolution [149]. Coupling photocatalytic oxidation with cellulose acid hydrolysis (e.g., sulfuric acid solutions) tends to be more efficient due to the *in-situ* production of hemicelluloses and reducing sugars, which are the compounds oxidized leading to H_2 production [150]. The limitation of the process is the photocatalytic activity of semiconductors in an acidic medium, which tends to be lower than in an alkaline environment [11]. In this case, the oxidation process happens by sensitization, i.e., the as-produced (by acid hydrolysis) reducing sugars are likely to be adsorbed over catalyst surfaces being directly oxidized [151]. Therefore, they generally have low oxidation potentials and can provide several electrons per molecule (e.g., glucose oxidation leads to 24 e^-), but for complete oxidation to CO_2, the potential can be as high as 1V [140], despite still possible for wide-gap semiconductors such as TiO_2.

Thus, TiO_2 and surface-modified (Pt [152], NiO [153], Pd and Au [154]) TiO_2 are common examples in literature. In practical situations, oxidation tends to some stable intermediaries, e.g., gluconic acid. At the same time, the undegraded part of the cellulose comprises nanocellulose of cellulose whiskers, high-crystalline cellulose that is a novel material for other applications (plastic nanocomposites, suspensions, etc.) [155]. Moreover, the literature has several examples of the photocatalytic process for treating cellulose bleach. It is an example of practical application, although not directly related to cellulose valorization. Table 15 shows selected examples, but notably, the investigation of novel catalysts is incipient (authors are investing in TiO_2 and ZnO catalysts).

5.2 Lignin

The case of lignin is more challenging. Lignin has a very complex, aromatic structure, with an approximate formula of $(C_{31}H_{34}O_{11})_n$, also described as a polymer of para-coumaryl (4-[(E)-3-Hydroxyprop-1-enyl]phenol), coniferyl (4-hydroxy-3-methoxycinnamyl alcohol), and sinapyl (4-hydroxy-3,5-dimethoxycinnamyl alcohol) alcohols. This structure means that several different molecules can be obtained by breaking its structure – from phenols to higher alcohols (Fig. 19) [156]. However, its complexity means that lignin is very chemically stable, making any oxidation process hard to be done. Moreover, lignin strongly absorbs around 350-300 nm, reducing the efficiency of UV-light active photocatalysts [157]. Even with these limitations, the oxidation of lignocellulosic matrices using photocatalysts is possible, producing a plethora of products that include complete degradation to CO_2 and water (TiO_2) [158], H_2 generation (CdS/CdO_x photocatalyst) [149], C-C cleavage for producing aldehydes (Vanadium oxides, VO(acac) and $VO(OPr_3)$) [159] among other examples, as summarized in Table 16. The final product is often a mixture of organic and fatty acids with carbohydrates, separable by

conventional physical methods. Therefore, product selectivity is still an issue that should be better investigated to increase process efficiency.

The mechanism of lignin photodegradation is still under debate, but probably the oxidation by *OH radical is the first step. However, since many alkoxide groups are in its structure, direct oxidation is possible by coupling at the catalyst surface, forming M-O-R bonds (e.g., Ti-O-R bonds in TiO_2), which can be eventually interact with alcohols with two neighboring M-O-R groups. This process facilitates the oxidation of C-C bonds by radicals, crucial for reducing the chain size. Moreover, some authors propose a two-step process to interpret breaking C-O bonds, starting from the initial oxidation of the alcohol groups to ketones (O=C-O groups) to reduce C-O bond energy [159]. Therefore, surfaces with specific affinities may have better photocatalytic performances by directing the action of radicals and possibly, leading to better selectivity.

5.3 Glycerol

The third byproduct of biorefining that attracts attention is glycerol, produced mainly by transesterification reactions for biodiesel production [160]. Although with well-known technological applications (cosmetic and pharmaceuticals), this molecule is often contaminated with methanol, increasing the utilization cost and motivating other utilization [161]. Glycerol is an attractive sacrificial agent for H_2 evolution in water photolysis [162,163]. Different catalysts have been studied for this reaction, producing molecules with commercial interest like CH_4, CO, CH_3OH, H_2O_2, 1,3 dihydroxyacetone, and glyceraldehyde [164–168], as summarized in Table 17 and exemplified in Fig. 20 [166]. Interestingly, for this application, there are more examples of TiO_2 – decorated materials, i.e., heterojunctions including noble-metals (as seen in Fig. 21 [169]). It reflects that the role of glycerol is to suppress the *OH radical formation due to its lower oxidation

potential and higher electron availability per molecule (14 e^- to complete oxidation to CO_2), enabling lower recombination and, consequently, higher H_2 evolution from water. The same concept is proposed for CO_2 reforming hydrocarbons, reducing the total cell potential for the full reaction [170].

6. Photocatalytic materials in renewable agri-energy

Renewable energies are intrinsically linked to agriculture. The biomass utilization for energy purposes is diverse, from the old conventional burning for heat and vapor production [166] to the fermentation for bioethanol and biomethane [171]. In a broad view, any biomass is a solar energy product: natural photosynthesis is still the most significant way to convert solar energy to the chemical on an enormous scale. [172] However, its energy conversion efficiency is low, generally below 1% to 5% in the best case in some microalgae [173]. It means that, even in ideal conditions, the production of agri-energy sources is limited to this range of efficiency – however, the aspect of sustainability is maintained by the return of atmospheric CO_2 for biomass growth, making a closed cycle.

Co-generation is frequently used in the biofuel sector to optimize the use of biomass energy. For instance, in bioethanol production, the residual bagasse is burned to produce thermoelectricity, which is counted in the energy balance of the biofuel [174]. Photocatalysis can also be a choice for co-generation by reforming CO_2 in a localized process and returning to some associated energetic process. In the bioethanol case, the sugar fermentation process produces on average 0.95 kg CO_2 per L ethanol by the yeast activity. This effluent has typically high CO_2 concentration (> 98%) with water vapor as the residual part, meaning that it is adequate for CO_2 reusing with no further purification [175].

However, CO_2 photoreduction is very challenging. In principle, compared to the O_2 reduction to hydroperoxide radical (HO_2), which is the most common process in photooxidative applications, the CO_2 reduction can be more favorable (– 0.13 V in O_2/HO_2 *vs.* – 0.11 V SHE to CO_2/CO) [93]. Nevertheless, the high overpotential necessary to produce the CO_2^- radical (– 1.5 V SHE) limits the reaction, which needs to find other ways to transfer electrons to CO_2 by increasing the surface interaction with catalysts [140]. In spite that the photooxidative capacity of semiconductors means that a coupled reduction should take place, this process depends on the semiconductor's surface affinity to CO_2 and the ability of transfer electrons. These factors mean that normally *p*-type semiconductors as Cu_2O and CuO are more active for that reaction [176]. Moreover, the charge separation here plays a crucial role, especially in processes carried on liquid medium. Since the reduction product (CO, CH4, HCOOH, or other C1, C2 molecules) can be re-oxidized by the *OH radicals, it is crucial that the reactions can occur in different parts of the catalytic system, preferably two compartments [38]. Several papers deal with the development of heterostructures with two semiconductors, normally a *p*-*n* junction. In this design, it is expected that the reduction reaction will take place in the *p* semiconductor, while *n* semiconductor plays the oxidation reaction [27]. Table 18 summarizes a list of recently studied photocatalysts, where many promising materials are seen under investigation. Several examples have been proposed, such as $CuO:TiO_2$, $Cu_2O:TiO_2$, and Cu_2O:ZnO. Alternatively, authors propose to decorate *n* semiconductors with metallic nanoparticles, as $Ag:TiO_2$ and $Pd:TiO_2$, aiming to an *in situ* electrochemical system, i.e., the photogenerated electrons would migrate to the metal islands where the reduction reaction would take place. Electrocatalysts have been more studied, with some consensus in the literature about Ag higher selectivity for CO and Cu for CH_4 production [177]. Finally, other materials such as TiO_2, Nb_2O_5, and ZnO, even being *n* semiconductors,

have some performance for this reaction, generally attributed to the surface hydroxylation that can increase the interaction with dissolved CO_2.

Even in ideal conditions, CO_2 reduction competes against H_2 evolution from water [178,179]. This situation is more common in CO_2 dissolved in water since its solubility is very low (around 1.5 $g.L^{-1}$) [140]. Among the alternatives, some papers propose to perform the reactions in gas-solid systems, feeding the catalysts with CO_2 + H_2O gaseous mixtures [180]. The coupled oxidative reaction can be OER, released to the environment, or other sacrificial electron donors – as the above-mentioned H_2S [181].

Despite other industrial processes generating concentrated amounts of CO_2 (e.g., cement production, fossil fuel burning, etc.), it is notable that the fermentative process can produce a very pure source that reduces the purification costs involved in these others [175]. Furthermore, incorporating existing agri-energy cycles can reduce the implementation costs, facilitating the adoption of these technologies. However, it is worthy of mentioning that most of the papers are focusing on lab scale, simulated CO_2/H_2O mixtures instead of relevant conditions for the high CO_2 production expected in these effluents – at the moment, there is no application of photocatalytic CO_2 reduction in pilot scale, except one outdoor experiment on reducing pure CO_2 [182]. Furthermore, it is remarkable that the research is still concentrated in batch experiments and few catalytic cycles, limiting the application in real conditions. Indeed, the investigation of photoreduction of low CO_2 mixtures, aiming to simulate the conditions of CO_2 environmentally dispersed or even converting fresh air, is still more frequent, as summarized in Table 19. Thus, efforts towards implementing long-term catalyst utilization, in-flux experimentation, and high-volume treatment are still essential for the realization of CO_2 photoreduction in the agricultural context.

7. Perspectives for photocatalytic materials in fertilizer production

As discussed before, chemical fertilizers, especially nitrogenated compounds, are the basis of high production agriculture. However, the reduction of atmospheric N_2 to produce NH_3 or NH_4^+ demands high energy, which now is mainly by thermal activation, using metals or complexes as catalysts [183]. The carbon footprint of ammonium production is very high since the Haber-Bosch process is based on natural gas (from H_2 production to the reaction temperature conditions) [4]. Therefore, it would be expected that there is an interest in developing other methods, using renewable energies, to produce these inputs [184]. The problem here lies in the low water solubility and high chemical stability of N_2. It requires 0.06 V SHE for NH_3 but an extremely high potential for activation ($3/2\ N_2 + H^+ + e^- \rightarrow HN_3$, –3.33 SHE).[93,185] Thus, it means that other reduction reactions can be favored before properly N_2 reduction [186].

Associated with its low solubility and chemical inertness, N_2 photoreduction is a topic that only in recent years has been intensively investigated, despite the potential technologic interest – worth to mention that the first report of N_2 photoreduction using TiO_2 dates back to 1977 [187]. However, the state-of-art has not developed too much since these first reports, at least compared to the CO_2 reduction, although several advances in the comprehension of N_2 reduction mechanism through electrochemical experiments (Fig. 22) [188]. Noteworthy, some papers demonstrated that rutile TiO_2 has a role in N_2 photoreduction [189], probably due to its *p*-type character compared to anatase, and Fe-doping is also promising.

A summary of related literature about N_2 reduction photocatalysts is given in Table 20. Compared to other topics herein discussed, it is interesting to notice that more catalysts are being explored, from C-based materials to Bi and V oxides. It can indicate that the effective catalysts are in discussion yet, leading to the scientific community still

seeking more promising candidates. Generally, structures in which the photocatalytic activity is affected by N vacancies or doping have been explored – indeed, the most common candidates are TiO_2 and g-C_3N_4 and heterojunctions with them.

Most of the literature examples are very recent (last 5 years), confirming the emerging interest in this topic. For instance, single-atom catalysts supported over lamellar structures have been shown as good choices for this reaction. Fe^{3+} dispersed over graphitic C_3N_4 (*g*-C_3N_4) produced more reasonable NH_3 amounts, around 50 $\mu mol.g_{cat}^{-1}.h^{-1}$, a range that compares to the reported for CO_2 photoreduction [190]. The decoration of TiO_2 nanosheets with Ru has been also suggested, with some promising results in N_2 dissolved in water [191]. Several researchers have also invested in sacrificial agents as CH_3OH or Na_2SO_3, which can increase the H^+ availability and reduce the electron-hole recombination. Using these agents, an increase to $mmol.g_{catalyst}^{-1}.h^{-1}$ yields has been shown. Recently some authors have suggested by theoretical calculations single-atom catalyst, B, supported over lamellar semiconductors, *g*-CN, as a promising candidate. Still, to the moment, its experimental realization has not yet been reported [192].

To summarizing, N_2 photoreduction is still very far from the necessary production levels required by the fertilizer industry, but it is a fair candidate for sustainable fertilizer production. The current state suggests that significant efforts are necessary to increase this reaction to a more acceptable level, even considering pilot testing. However, the interest in these reactions will grow according to the increasing demand of fertilizers *versus* awareness about the environmental impacts of their production.

8. Concluding remarks and future perspectives

This review has intended to demonstrate the interconnections among agriculture problems with the current state of photocatalytic materials research. The challenges are

still unaddressed, despite some topics –the photodegradation of agrichemicals – have been extensively studied in the past years. However, the replacement of more hazardous agrichemicals by newer ones with higher biodegradability tends to limit the application of these technologies, which still need to be contextualized in the agriculture scenario – i.e., liquid effluents with many components, massive water amounts, and widespread contamination in the environment.

On the other hand, there are possibilities related to the value chain of agriculture, i.e., considering converting byproducts (residues, fibers, products of fermentation) to more valuable ones using sunlight. These photocatalytic processes can support prospective applications, from biorefining of agri-products to valuable chemicals, until energy production and conversion. These processes can increase the energetic efficiency in agriculture as a whole and, consequently, reduce the carbon footprint. It is also seen in the application of these catalysts to abate greenhouse gases, which can return them as nutrients for the soil. Finally, it is necessary to see the future perspective of fertilizer demand, whose efforts in the development of photocatalytic materials can be worth – although still very nascent. The many opportunities need to be adequately addressed, discussing the application requirements and making the current agriculture supplying processes more sustainable.

Acknowledgments

The authors are grateful to the Ministry of Science, Technology, and Innovation (through SisNANO Program – National System of Laboratories in Nanotechnology), the National Council for Scientific and Technological Development (CNPq, Brazil China Virtual Center in Nanotechnology Project and grant #402.287/2013-4), Sao Paulo Research Foundation (FAPESP, grants #2016/21515-7 and 2018/01258-5), and Embrapa

Rede AgroNano for their financial support. Caue Ribeiro also acknowledges the Chinese Academy of Sciences (CAS) President's International Fellowship Initiative (PIFI) by financial aid and CAPES – Alexander von Humboldt Foundation for Experienced Researchers Fellowship and Return Grant (CAPES Finance Code 001 – CAPES Process 88881.145566/2017-1).

References

[1] FAO. The future of food and agriculture: trends and challenges. Rome, Italy: 2017.

[2] Ribeiro C, Carmo M. Why nonconventional materials are answers for sustainable agriculture. MRS Energy Sustain 2019;6. https://doi.org/10.1557/mre.2019.7.

[3] Evenson RE, Gollin D. Assessing the impact of the Green Revolution, 1960 to 2000. Science (80-) 2003;300:758–62. https://doi.org/10.1126/science.1078710.

[4] MacFarlane DR, Cherepanov P V., Choi J, Suryanto BHR, Hodgetts RY, Bakker JM, et al. A Roadmap to the Ammonia Economy. Joule 2020;4:1186–205. https://doi.org/10.1016/j.joule.2020.04.004.

[5] Foster SL, Bakovic SIP, Duda RD, Maheshwari S, Milton RD, Minteer SD, et al. Catalysts for nitrogen reduction to ammonia. Nat Catal 2018;1:490–500. https://doi.org/10.1038/s41929-018-0092-7.

[6] Snyder CS, Bruulsema TW, Jensen TL, Fixen PE. Review of greenhouse gas emissions from crop production systems and fertilizer management effects. Agric Ecosyst Environ 2009;133:247–66. https://doi.org/10.1016/j.agee.2009.04.021.

[7] Mäder P, Fließbach A, Dubois D, Gunst L, Fried P, Niggli U. Soil fertility and biodiversity in organic farming. Science (80-) 2002;296:1694–7. https://doi.org/10.1126/science.1071148.

[8] Damalas CA, Eleftherohorinos IG. Pesticide exposure, safety issues, and risk assessment indicators. Int J Environ Res Public Health 2011;8:1402–19. https://doi.org/10.3390/ijerph8051402.

[9] Ghini R, Bettiol W, Hamada E. Diseases in tropical and plantation crops as affected by climate changes: Current knowledge and perspectives. Plant Pathol 2011;60:122–32. https://doi.org/10.1111/j.1365-3059.2010.02403.x.

[10] Saleh R, Bearth A, Siegrist M. How chemophobia affects public acceptance of pesticide use and biotechnology in agriculture. Food Qual Prefer 2021;91. https://doi.org/10.1016/j.foodqual.2021.104197.

[11] Diebold U. The surface science of titanium dioxide. Surf Sci Rep 2003;48:53–229.

[12] Ahmed S, Rasul MG, Brown R, Hashib MA. Influence of parameters on the heterogeneous photocatalytic degradation of pesticides and phenolic contaminants in wastewater: A short review. J Environ Manage 2011;92:311–30. https://doi.org/10.1016/j.jenvman.2010.08.028.

[13] Khin MM, Nair AS, Babu VJ, Murugan R, Ramakrishna S. A review on nanomaterials for environmental remediation. Energy Environ Sci 2012;5:8075–109. https://doi.org/10.1039/c2ee21818f.

[14] Ângelo J, Andrade L, Madeira LM, Mendes A. An overview of photocatalysis phenomena applied to NOx abatement. J Environ Manage 2013;129:522–39. https://doi.org/10.1016/j.jenvman.2013.08.006.

[15] de_Richter R, Ming T, Davies P, Liu W, Caillol S. Removal of non-CO 2 greenhouse gases by large-scale atmospheric solar photocatalysis. Prog Energy Combust Sci 2017;60:68–96. https://doi.org/10.1016/j.pecs.2017.01.001.

[16] Yuliati L, Yoshida H. Photocatalytic conversion of methane 2008:1592–602. https://doi.org/10.1039/b710575b.

[17] Albero J, Peng Y, García H. Photocatalytic CO2Reduction to C2+ Products. ACS Catal 2020;10:5734–49. https://doi.org/10.1021/acscatal.0c00478.

[18] Intergovernmental Panel on Climate Change IPCC. 2019 Refinement to 2006 IPCC Guidel Natl Greenh Gas Invent 2019:1–91.

[19] Wang JL, Xu LJ. Advanced oxidation processes for wastewater treatment: Formation of hydroxyl radical and application. Crit Rev Environ Sci Technol 2012;42:251–325. https://doi.org/10.1080/10643389.2010.507698.

[20] Matilainen A, Sillanpää M. Removal of natural organic matter from drinking water by advanced oxidation processes. Chemosphere 2010;80:351–65. https://doi.org/10.1016/j.chemosphere.2010.04.067.

[21] Fujishima A, Honda K. Electrochemical photolysis of water at a semiconductor

electrode. Nature 1972;238:37–8. https://doi.org/10.1038/238037a0.
[22] Fujihira M, Satoh Y, Osa T. Heterogeneous photocatalytic oxidation of aromatic compounds on TiO 2. Nature 1981;293:206–8. https://doi.org/10.1038/293206a0.
[23] Talapin D V., Lee J-S, Kovalenko M V., Shevchenko E V. Prospects of Colloidal Nanocrystals for Electronic and Optoelectronic Applications. Chem Rev 2010;110:389–458. https://doi.org/10.1021/cr900137k.
[24] Hoffmann MR, Martin ST, Choi W, Bahnemann DW. Environmental Applications of Semiconductor Photocatalysis. Chem Rev 1995;95:69–96. https://doi.org/10.1021/cr00033a004.
[25] Hagfeldt A, Gratzel M. Light-induced redox reactions in nanocrystalline systems. Chem Rev 1995;95:49–68.
[26] Shockley W, Read WT. Statistics of the Recombinations of Holes and Electrons. Phys Rev 1952;87:835–42. https://doi.org/10.1103/PhysRev.87.835.
[27] Low J, Yu J, Jaroniec M, Wageh S, Al-ghamdi AA. Heterojunction Photocatalysts 2017. https://doi.org/10.1002/adma.201601694.
[28] Evgenidou E, Fytianos K, Poulios I. Semiconductor-sensitized photodegradation of dichlorvos in water using TiO2 and ZnO as catalysts. Appl Catal B Environ 2005;59:81–9. https://doi.org/10.1016/j.apcatb.2005.01.005.
[29] Bakar SA, Ribeiro C. Nitrogen-doped titanium dioxide: An overview of material design and dimensionality effect over modern applications. J Photochem Photobiol C Photochem Rev 2016;27:1–29. https://doi.org/10.1016/j.jphotochemrev.2016.05.001.
[30] Deng J, Jiang J, Zhang Y, Lin X, Du C, Xiong Y. FeVO4 as a highly active heterogeneous Fenton-like catalyst towards the degradation of Orange II. Appl Catal B Environ 2008;84:468–73. https://doi.org/10.1016/j.apcatb.2008.04.029.
[31] Chiron S, Fernandez-Alba A, Rodriguez A, Garcia-Calvo E. Pesticide chemical oxidation: State-of-the-art. Water Res 2000;34:366–77. https://doi.org/10.1016/S0043-1354(99)00173-6.
[32] Galan-Mascaros JR. Photoelectrochemical solar fuels from carbon dioxide, water and sunlight. Catal Sci Technol 2020;10:1967–74. https://doi.org/10.1039/c9cy02606a.
[33] Medford AJ, Hatzell MC. Photon-Driven Nitrogen Fixation: Current Progress, Thermodynamic Considerations, and Future Outlook. ACS Catal 2017;7:2624–43. https://doi.org/10.1021/acscatal.7b00439.
[34] Soares GB, Bravin B, Vaz CMP, Ribeiro C. Facile synthesis of N-doped TiO2 nanoparticles by a modified polymeric precursor method and its photocatalytic properties. Appl Catal B Environ 2011;106:287–94.
[35] Zhang D, Stojanovic M, Ren Y, Cao Y, Eickemeyer FT, Socie E, et al. A molecular photosensitizer achieves a V oc of 1.24 V enabling highly efficient and stable dye-sensitized solar cells with copper(II/I)-based electrolyte. Nat Commun 2021;12. https://doi.org/10.1038/s41467-021-21945-3.
[36] Grätzel M. The light and shade of perovskite solar cells. Nat Mater 2014;13:838–42. https://doi.org/10.1038/nmat4065.
[37] Spasiano D, Marotta R, Malato S, Fernandez-Ibañez P, Di Somma I. Solar photocatalysis: Materials, reactors, some commercial, and pre-industrialized applications. A comprehensive approach. Appl Catal B Environ 2015;170–171:90–123. https://doi.org/10.1016/j.apcatb.2014.12.050.
[38] Castro S, Albo J, Irabien A. Photoelectrochemical Reactors for CO2 Utilization. ACS Sustain Chem Eng 2018;6:15877–94. https://doi.org/10.1021/acssuschemeng.8b03706.
[39] Food and Agriculture Organization of the United Nations. Water for Sustainable Food and Agriculture. A Rep Prod G20 Pres Ger 2017:1–33.
[40] Fenner K, Canonica S, Wackett LP, Elsner M. Evaluating pesticide degradation in the environment: Blind spots and emerging opportunities. Science (80-) 2013;341:752–8. https://doi.org/10.1126/science.1236281.
[41] Hamilton DJ, Ambrus Á, Dieterle RM, Felsot AS, Harris CA, Holland PT, et al. Regulatory limits for pesticide residues in water (IUPAC technical report). Pure Appl Chem 2003;75:1123–55. https://doi.org/10.1351/pac200375081123.

[42] Hurum DC, Agrios AG, Gray KA, Rajh T, Thurnauer MC. Explaining the enhanced photocatalytic activity of Degussa P25 mixed-phase TiO2 using EPR. J Phys Chem B 2003;107:4545–9. https://doi.org/10.1021/jp0273934.
[43] Uddin MJ, Cesano F, Chowdhury AR, Trad T, Cravanzola S, Martra G, et al. Surface Structure and Phase Composition of TiO2 P25 Particles After Thermal Treatments and HF Etching. Front Mater 2020;7. https://doi.org/10.3389/fmats.2020.00192.
[44] Meulenkamp EA. Size dependence of the dissolution of ZnO nanoparticles. J Phys Chem B 1998;102:7764–9. https://doi.org/10.1021/jp982305u.
[45] Singh J, Sharma S, Aanchal, Basu S. Synthesis of Fe2O3/TiO2 monoliths for the enhanced degradation of industrial dye and pesticide via photo-Fenton catalysis. J Photochem Photobiol A Chem 2019;376:32–42. https://doi.org/10.1016/j.jphotochem.2019.03.004.
[46] Boruah PK, Das MR. Dual responsive magnetic Fe3O4-TiO2/graphene nanocomposite as an artificial nanozyme for the colorimetric detection and photodegradation of pesticide in an aqueous medium. J Hazard Mater 2020;385. https://doi.org/10.1016/j.jhazmat.2019.121516.
[47] Mohamed RM, Zaki ZI. Degradation of Imazapyr herbicide using visible light-active CdO-TiO2heterojunction photocatalyst. J Environ Chem Eng 2021;9. https://doi.org/10.1016/j.jece.2020.104732.
[48] Garcia-Muñoz P, Fresno F, Ivanez J, Robert D, Keller N. Activity enhancement pathways in LaFeO3@TiO2 heterojunction photocatalysts for visible and solar light driven degradation of myclobutanil pesticide in water. J Hazard Mater 2020;400. https://doi.org/10.1016/j.jhazmat.2020.123099.
[49] Chenchana A, Nemamcha A, Moumeni H, Doña Rodríguez JM, Araña J, Navío JA, et al. Photodegradation of 2,4-dichlorophenoxyacetic acid over TiO 2 (B)/anatase nanobelts and Au-TiO 2 (B)/anatase nanobelts. Appl Surf Sci 2019;467–468:1076–87. https://doi.org/10.1016/j.apsusc.2018.10.175.
[50] Fujishima A, Zhang X, Tryk DA. TiO2 photocatalysis and related surface phenomena. Surf Sci Rep 2008;63:515–82. https://doi.org/10.1016/j.surfrep.2008.10.001.
[51] Serpone N. Is the band gap of pristine TiO2 narrowed by anion- and cation-doping of titanium dioxide in second-generation photocatalysts? J Phys Chem B 2006;110:24287–93. https://doi.org/10.1021/jp065659r.
[52] Berberidou C, Kyzas GZ, Paspaltsis I, Sklaviadis T, Poulios I. Photocatalytic disinfection and purification of water employing reduced graphene oxide/TiO2 composites. J Chem Technol Biotechnol 2019;94:3905–14. https://doi.org/10.1002/jctb.6188.
[53] Ortega-Liebana MC, Hueso JL, Ferdousi S, Arenal R, Irusta S, Yeung KL, et al. Extraordinary sensitizing effect of co-doped carbon nanodots derived from mate herb: Application to enhanced photocatalytic degradation of chlorinated wastewater compounds under visible light. Appl Catal B Environ 2017;218:68–79. https://doi.org/10.1016/j.apcatb.2017.06.021.
[54] Abdelhaleem A, Chu W. Photodegradation of 4-chlorophenoxyacetic acid under visible LED activated N-doped TiO2 and the mechanism of stepwise rate increment of the reused catalyst. J Hazard Mater 2017;338:491–501. https://doi.org/10.1016/j.jhazmat.2017.05.056.
[55] Abdelhaleem A, Chu W. Monuron photodegradation using peroxymonosulfate activated by non-metal-doped TiO2 under visible LED and the modeling via a parallel-serial kinetic approach. Chem Eng J 2018;338:411–21. https://doi.org/10.1016/j.cej.2018.01.036.
[56] Lopes OF, Carvalho KTG, Nogueira AE, Avansi W, Ribeiro C. Controlled synthesis of BiVO4 photocatalysts: Evidence of the role of heterojunctions in their catalytic performance driven by visible-light. Appl Catal B Environ 2016;188:87–97. https://doi.org/10.1016/j.apcatb.2016.01.065.
[57] de Mendonça VR, Mourão HAJL, Malagutti AR, Ribeiro C. The Role of the Relative Dye/Photocatalyst Concentration in TiO 2 Assisted Photodegradation Process.

Photochem Photobiol 2014;90:66–72. https://doi.org/10.1111/php.12175.
[58] Scialli AR, Desesso JM, Breckenridge CB. Developmental toxicity studies with atrazine and its major metabolites in rats and rabbits. Birth Defects Res Part B - Dev Reprod Toxicol 2014;101:199–214. https://doi.org/10.1002/bdrb.21099.
[59] Wirbisky SE, Weber GJ, Sepúlveda MS, Lin TL, Jannasch AS, Freeman JL. An embryonic atrazine exposure results in reproductive dysfunction in adult zebrafish and morphological alterations in their offspring. Sci Rep 2016;6. https://doi.org/10.1038/srep21337.
[60] Gao Y, Ji Y, Li G, An T. Mechanism, kinetics and toxicity assessment of OH-initiated transformation of triclosan in aquatic environments. Water Res 2014;49:360–70. https://doi.org/10.1016/j.watres.2013.10.027.
[61] Hayes TB, Khoury V, Narayan A, Nazir M, Parka A, Brown T, et al. Atrazine induces complete feminization and chemical castration in male African clawed frogs (Xenopus laevis). Proc Natl Acad Sci U S A 2010;107:4612–7. https://doi.org/10.1073/pnas.0909519107.
[62] Pérez MH, Peñuela G, Maldonado MI, Malato O, Fernández-Ibáñez P, Oller I, et al. Degradation of pesticides in water using solar advanced oxidation processes. Appl Catal B Environ 2006;64:272–81. https://doi.org/10.1016/j.apcatb.2005.11.013.
[63] Bessergenev VG, Mateus MC, Morgado IM, Hantusch M, Burkel E. Photocatalytic reactor, CVD technology of its preparation and water purification from pharmaceutical drugs and agricultural pesticides. Chem Eng J 2017;312:306–16. https://doi.org/10.1016/j.cej.2016.11.148.
[64] Foy CL, Pritchard DW. Pesticide Formulation and Adjuvant Technology. Pestic Formul Adjuv Technol 2018. https://doi.org/10.1201/9780203743751.
[65] Kemper N. Veterinary antibiotics in the aquatic and terrestrial environment. Ecol Indic 2008;8:1–13. https://doi.org/10.1016/j.ecolind.2007.06.002.
[66] Hanamoto S, Yamamoto-Ikemoto R, Tanaka H. Predicting mass loadings of sulfamonomethoxine, sulfamethoxazole, and lincomycin discharged into surface waters in Japanese river catchments. Sci Total Environ 2021;776. https://doi.org/10.1016/j.scitotenv.2021.146032.
[67] Daghrir R, Drogui P. Tetracycline antibiotics in the environment: A review. Environ Chem Lett 2013;11:209–27. https://doi.org/10.1007/s10311-013-0404-8.
[68] Kolpin DW, Furlong ET, Meyer MT, Thurman EM, Zaugg SD, Barber LB, et al. Pharmaceuticals, hormones, and other organic wastewater contaminants in U.S. streams, 1999-2000: A national reconnaissance. Environ Sci Technol 2002;36:1202–11. https://doi.org/10.1021/es011055j.
[69] Sawant AA, Sordillo LM, Jayarao BM. A survey on antibiotic usage in dairy herds in Pennsylvania. J Dairy Sci 2005;88:2991–9. https://doi.org/10.3168/jds.S0022-0302(05)72979-9.
[70] Sunada K, Watanabe T, Hashimoto K. Studies on photokilling of bacteria on TiO 2 thin film. J Photochem Photobiol A Chem 2003;156:227–33. https://doi.org/10.1016/S1010-6030(02)00434-3.
[71] Kühn KP, Chaberny IF, Massholder K, Stickler M, Benz VW, Sonntag HG, et al. Disinfection of surfaces by photocatalytic oxidation with titanium dioxide and UVA light. Chemosphere 2003;53:71–7. https://doi.org/10.1016/S0045-6535(03)00362-X.
[72] Lonnen J, Kilvington S, Kehoe SC, Al-Touati F, McGuigan KG. Solar and photocatalytic disinfection of protozoan, fungal and bacterial microbes in drinking water. Water Res 2005;39:877–83. https://doi.org/10.1016/j.watres.2004.11.023.
[73] Sichel C, de Cara M, Tello J, Blanco J, Fernández-Ibáñez P. Solar photocatalytic disinfection of agricultural pathogenic fungi: Fusarium species. Appl Catal B Environ 2007;74:152–60. https://doi.org/10.1016/j.apcatb.2007.02.005.
[74] Garcidueñas-Piña C, Medina-Ramírez IE, Guzmán P, Rico-Martínez R, Morales-Domínguez JF, Rubio-Franchini I. Evaluation of the Antimicrobial Activity of Nanostructured Materials of Titanium Dioxide Doped with Silver and/or Copper and Their Effects on Arabidopsis thaliana. Int J Photoenergy 2016;2016.

https://doi.org/10.1155/2016/8060847.
[75] Luksiene Z, Rasiukeviciute N, Zudyte B, Uselis N. Innovative approach to sunlight activated biofungicides for strawberry crop protection: ZnO nanoparticles. J Photochem Photobiol B Biol 2020;203. https://doi.org/10.1016/j.jphotobiol.2019.111656.
[76] Liu R, Lal R. Potentials of engineered nanoparticles as fertilizers for increasing agronomic productions. Sci Total Environ 2015;514:131–9. https://doi.org/10.1016/j.scitotenv.2015.01.104.
[77] Rizwan M, Ali S, Zia ur Rehman M, Adrees M, Arshad M, Qayyum MF, et al. Alleviation of cadmium accumulation in maize (Zea mays L.) by foliar spray of zinc oxide nanoparticles and biochar to contaminated soil. Environ Pollut 2019;248:358–67. https://doi.org/10.1016/j.envpol.2019.02.031.
[78] Le Quéré C, Raupach MR, Canadell JG, Marland G, Bopp L, Ciais P, et al. Trends in the sources and sinks of carbon dioxide. Nat Geosci 2009;2:831–6. https://doi.org/10.1038/ngeo689.
[79] Smith P, Martino D, Cai Z, Gwary D, Janzen H, Kumar P, et al. Greenhouse gas mitigation in agriculture. Philos Trans R Soc B Biol Sci 2008;363:789–813. https://doi.org/10.1098/rstb.2007.2184.
[80] UNFCCC COP 19. Report on COP 19 (FCCC/CP/2013/10/Add.3). UNFCCC Conf Parties 2013:1–54.
[81] De Oliveira Silva R, Barioni LG, Hall JAJ, Folegatti Matsuura M, Zanett Albertini T, Fernandes FA, et al. Increasing beef production could lower greenhouse gas emissions in Brazil if decoupled from deforestation. Nat Clim Chang 2016;6:493–7. https://doi.org/10.1038/nclimate2916.
[82] Bastin JF, Finegold Y, Garcia C, Mollicone D, Rezende M, Routh D, et al. The global tree restoration potential. Science (80-) 2019;364:76–9. https://doi.org/10.1126/science.aax0848.
[83] Skidmore AK, Wang T, de Bie K, Pilesjö P. Comment on “The global tree restoration potential.” Science (80-) 2019;366. https://doi.org/10.1126/science.aaz0111.
[84] Glibert PM, Harrison J, Heil C, Seitzinger S. Escalating worldwide use of urea - A global change contributing to coastal eutrophication. Biogeochemistry 2006;77:441–63. https://doi.org/10.1007/s10533-005-3070-5.
[85] Kemmitt SJ, Wright D, Goulding KWT, Jones DL. pH regulation of carbon and nitrogen dynamics in two agricultural soils. Soil Biol Biochem 2006;38:898–911. https://doi.org/10.1016/j.soilbio.2005.08.006.
[86] Cameron KC, Di HJ, Moir JL. Nitrogen losses from the soil/plant system: A review. Ann Appl Biol 2013;162:145–73. https://doi.org/10.1111/aab.12014.
[87] Vitousek PM, Aber JD, Howarth RW, Likens GE, Matson PA, Schindler DW, et al. Technical Report: Human Alteration of the Global Nitrogen Cycle: Sources and Consequences. Ecol Appl 1997;7:737. https://doi.org/10.2307/2269431.
[88] Chen H, Kuranari S, Matsuoka M, Zhang J, Anpo M. Synthesis of the ag+-bipyridine complexes anchored within MCM-41 and their photocatalytic reactivity for N2O reduction with CO. Catal Letters 2008;126:218–23. https://doi.org/10.1007/s10562-008-9682-3.
[89] Kočí K, Krejčíková S, Šolcová O, Obalová L. Photocatalytic decomposition of N 2O on Ag-TiO 2. Catal Today 2012;191:134–7. https://doi.org/10.1016/j.cattod.2012.01.021.
[90] Reli M, Troppová I, Šihor M, Pavlovský J, Praus P, Kočí K. Photocatalytic decomposition of N 2 O over g-C 3 N 4 /BiVO 4 composite. Appl Surf Sci 2019;469:181–91. https://doi.org/10.1016/j.apsusc.2018.10.255.
[91] Lasek J, Yu YH, Wu JCS. Removal of NOx by photocatalytic processes. J Photochem Photobiol C Photochem Rev 2013;14:29–52. https://doi.org/10.1016/j.jphotochemrev.2012.08.002.
[92] deRichter R, Caillol S. Fighting global warming: The potential of photocatalysis against CO2, CH4, N2O, CFCs, tropospheric O3, BC and other major contributors to climate change. J Photochem Photobiol C Photochem Rev 2011;12:1–19. https://doi.org/10.1016/j.jphotochemrev.2011.05.002.

[93] Pourbaix M. Atlas of Electrochemical Equilibria in Aqueous Solution. 2nd ed. National Association of Corrosion Engineers; 1974.
[94] Dima G., de Vooys AC., Koper MT. Electrocatalytic reduction of nitrate at low concentration on coinage and transition-metal electrodes in acid solutions. J Electroanal Chem 2003;554–555:15–23. https://doi.org/10.1016/S0022-0728(02)01443-2.
[95] Di HJ, Cameron KC. Nitrate leaching in temperate agroecosystems: Sources, factors and mitigating strategies. Nutr Cycl Agroecosystems 2002;64:237–56. https://doi.org/10.1023/A:1021471531188.
[96] Bonsen EM, Schroeter S, Jacobs H, Broekaert JAC. Photocatalytic degradation of ammonia with TIO2 as photocatalyst in the laboratory and under the use of solar radiation. Chemosphere 1997;35:1431–45. https://doi.org/10.1016/S0045-6535(97)00216-6.
[97] Boyjoo Y, Sun H, Liu J, Pareek VK, Wang S. A review on photocatalysis for air treatment : From catalyst development to reactor design. Chem Eng J 2017;310:537–59. https://doi.org/10.1016/j.cej.2016.06.090.
[98] Mamaghani AH, Haghighat F, Lee CS. Photocatalytic oxidation technology for indoor environment air purification: The state-of-the-art. Appl Catal B Environ 2017;203:247–69. https://doi.org/10.1016/j.apcatb.2016.10.037.
[99] Maggos T, Plassais A, Bartzis JG, Vasilakos C, Moussiopoulos N, Bonafous L. Photocatalytic degradation of NOx in a pilot street canyon configuration using TiO2-mortar panels. Environ Monit Assess 2008;136:35–44. https://doi.org/10.1007/s10661-007-9722-2.
[100] Ballari MM, Hunger M, Hüsken G, Brouwers HJH. NOx photocatalytic degradation employing concrete pavement containing titanium dioxide. Appl Catal B Environ 2010;95:245–54. https://doi.org/10.1016/j.apcatb.2010.01.002.
[101] Chen M, Chu JW. NOx photocatalytic degradation on active concrete road surface - From experiment to real-scale application. J Clean Prod 2011;19:1266–72. https://doi.org/10.1016/j.jclepro.2011.03.001.
[102] Chen J, Kou S cong, Poon C sun. Photocatalytic cement-based materials: Comparison of nitrogen oxides and toluene removal potentials and evaluation of self-cleaning performance. Build Environ 2011;46:1827–33. https://doi.org/10.1016/j.buildenv.2011.03.004.
[103] Zhang L, Li P, Gong Z, Li X. Photocatalytic degradation of polycyclic aromatic hydrocarbons on soil surfaces using TiO2 under UV light. J Hazard Mater 2008;158:478–84. https://doi.org/10.1016/j.jhazmat.2008.01.119.
[104] Higarashi MM, Jardim WF. Remediation of pesticide contaminated soil using TiO2 mediated by solar light. Catal Today 2002;76:201–7. https://doi.org/10.1016/S0920-5861(02)00219-5.
[105] Barrón V, Méndez JM, Balbuena J, Cruz-Yusta M, Sánchez L, Giménez C, et al. Photochemical emission and fixation of NOX gases in soils. Sci Total Environ 2020;702. https://doi.org/10.1016/j.scitotenv.2019.134982.
[106] Skalska K, Miller JS, Ledakowicz S. Trends in NOx abatement: A review. Sci Total Environ 2010;408:3976–89. https://doi.org/10.1016/j.scitotenv.2010.06.001.
[107] Cant NW, Cole JR. Photocatalysis of the reaction between ammonia and nitric oxide on TiO2 surfaces. J Catal 1992;134:317–30. https://doi.org/10.1016/0021-9517(92)90231-6.
[108] Lin D, Xing B. Root uptake and phytotoxicity of ZnO nanoparticles. Environ Sci Technol 2008;42:5580–5. https://doi.org/10.1021/es800422x.
[109] Trapalis A, Todorova N, Giannakopoulou T, Boukos N, Speliotis T, Dimotikali D, et al. TiO2/graphene composite photocatalysts for NOx removal: A comparison of surfactant-stabilized graphene and reduced graphene oxide. Appl Catal B Environ 2016;180:637–47. https://doi.org/10.1016/j.apcatb.2015.07.009.
[110] Lopes OF, Carvalho KTG, Avansi W, Ribeiro C. Growth of BiVO4 Nanoparticles on a Bi2O3 Surface: Effect of Heterojunction Formation on Visible Irradiation-Driven Catalytic Performance. J Phys Chem C 2017;121:13747–56.

https://doi.org/10.1021/acs.jpcc.7b03340.
[111] Kasirajan S, Ngouajio M. Polyethylene and biodegradable mulches for agricultural applications: A review. Agron Sustain Dev 2012;32:501–29. https://doi.org/10.1007/s13593-011-0068-3.
[112] Diacono M, Montemurro F. Long-term effects of organic amendments on soil fertility. A review. Agron Sustain Dev 2010;30:401–22. https://doi.org/10.1051/agro/2009040.
[113] Hellmann B, Zelles L, Palojärvi A, Bai Q. Emission of climate-relevant trace gases and succession of microbial communities during open-windrow composting. Appl Environ Microbiol 1997;63:1011–8. https://doi.org/10.1128/aem.63.3.1011-1018.1997.
[114] Almomani F, Bhosale RR. Enhancing the production of biogas through anaerobic co-digestion of agricultural waste and chemical pre-treatments. Chemosphere 2020;255. https://doi.org/10.1016/j.chemosphere.2020.126805.
[115] Scarlat N, Dallemand JF, Fahl F. Biogas: Developments and perspectives in Europe. Renew Energy 2018;129:457–72. https://doi.org/10.1016/j.renene.2018.03.006.
[116] EBA Statistical Report 2020.
[117] Kögel-Knabner I, Amelung W, Cao Z, Fiedler S, Frenzel P, Jahn R, et al. Biogeochemistry of paddy soils. Geoderma 2010;157:1–14. https://doi.org/10.1016/j.geoderma.2010.03.009.
[118] Le Mer J, Roger P. Production, oxidation, emission and consumption of methane by soils: A review. Eur J Soil Biol 2001;37:25–50. https://doi.org/10.1016/S1164-5563(01)01067-6.
[119] Grčić I, Marčec J, Radetić L, Radovan AM, Melnjak I, Jajčinović I, et al. Ammonia and methane oxidation on TiO2 supported on glass fiber mesh under artificial solar irradiation. Environ Sci Pollut Res 2021;28:18354–67. https://doi.org/10.1007/s11356-020-09561-y.
[120] Baltrusaitis J, Jansen I, Schuttlefield Christus JD. Renewable energy based catalytic CH4 conversion to fuels. Catal Sci Technol 2014;4:2397–411. https://doi.org/10.1039/c4cy00294f.
[121] Meng X, Cui X, Rajan NP, Yu L, Deng D, Bao X. Direct Methane Conversion under Mild Condition by Thermo- , Electro- , or Photocatalysis. CHEMPR 2019;5:2296–325. https://doi.org/10.1016/j.chempr.2019.05.008.
[122] Noceti RP, Taylor CE, D'Este JR. Photocatalytic conversion of methane. Catal Today 1997;33:199–204. https://doi.org/10.1016/S0920-5861(96)00155-1.
[123] Xie J, Jin R, Li A, Bi Y, Ruan Q, Deng Y, et al. Highly selective oxidation of methane to methanol at ambient conditions by titanium dioxide-supported iron species. Nat Catal 2018;1:889–96. https://doi.org/10.1038/s41929-018-0170-x.
[124] Frese KW. Partial Electrochemical Oxidation of Methane under Mild Conditions. Langmuir 1991;7:13–5. https://doi.org/10.1021/la00049a004.
[125] López-Martín Á, Caballero A, Colón G. Photochemical methane partial oxidation to methanol assisted by H2O2. J Photochem Photobiol A Chem 2017;349:216–23. https://doi.org/10.1016/j.jphotochem.2017.09.039.
[126] Villa K, Murcia-López S, Morante JR, Andreu T. An insight on the role of La in mesoporous WO3 for the photocatalytic conversion of methane into methanol. Appl Catal B Environ 2016;187:30–6. https://doi.org/10.1016/j.apcatb.2016.01.032.
[127] Murcia-López S, Bacariza MC, Villa K, Lopes JM, Henriques C, Morante JR, et al. Controlled Photocatalytic Oxidation of Methane to Methanol through Surface Modification of Beta Zeolites. ACS Catal 2017;7:2878–85. https://doi.org/10.1021/acscatal.6b03535.
[128] Li W, He D, Hu G, Li X, Banerjee G, Li J, et al. Selective CO Production by Photoelectrochemical Methane Oxidation on TiO 2 2018. https://doi.org/10.1021/acscentsci.8b00130.
[129] Da Silva MJ. Synthesis of methanol from methane: Challenges and advances on the multi-step (syngas) and one-step routes (DMTM). Fuel Process Technol 2016;145:42–61. https://doi.org/10.1016/j.fuproc.2016.01.023.
[130] Rochelle GT. Amine Scrubbing for CO2 Capture. Science (80-) 2009;325:1652–4.

https://doi.org/10.1126/science.1176731.
[131] Angelidaki I, Treu L, Tsapekos P, Luo G, Campanaro S, Wenzel H, et al. Biogas upgrading and utilization: Current status and perspectives. Biotechnol Adv 2018;36:452–66. https://doi.org/10.1016/j.biotechadv.2018.01.011.
[132] Abatzoglou N, Boivin S. A review of biogas purification processes. Biofuels, Bioprod Biorefining 2009;3:42–71. https://doi.org/10.1002/bbb.117.
[133] Ki BM, Kim YM, Jeon JM, Ryu HW, Cho KS. Characterization of bacterial community dynamics during the decomposition of pig carcasses in simulated soil burial and composting systems. J Microbiol Biotechnol 2017;27:2199–210. https://doi.org/10.4014/jmb.1709.09032.
[134] Appels L, Baeyens J, Degrève J, Dewil R. Principles and potential of the anaerobic digestion of waste-activated sludge. Prog Energy Combust Sci 2008;34:755–81. https://doi.org/10.1016/j.pecs.2008.06.002.
[135] Selvaraj PT, Little MH, Kaufman EN. Biodesulfurization of flue gases and other sulfate/sulfite waste streams using immobilized mixed sulfate-reducing bacteria. Biotechnol Prog 1997;13:583–9. https://doi.org/10.1021/bp970073v.
[136] Lied EB, Morejon CFM, Basso RL de O, Trevisan AP, Bittencourt PRS, Fronza FL. Photocatalytic degradation of H2S in the gas-phase using a continuous flow reactor coated with TiO2-based acrylic paint. Environ Technol (United Kingdom) 2019;40:2276–89. https://doi.org/10.1080/09593330.2018.1440010.
[137] Lied EB, Morejon CFM, de Oliveira Basso RL, Trevisan AP, de Oliveira Tavares F, Boroski M, et al. Photocatalytic Properties of Commercially Available TiO2: Study of Fotosan® and InterBrasil® FA-101 for H2S Degradation Using UV and Solar Radiation. Water Air Soil Pollut 2020;231. https://doi.org/10.1007/s11270-020-04560-8.
[138] Canela MC, Alberici RM, Jardim WF. Gas-phase destruction of H2S using TiO2/UV-VIS. J Photochem Photobiol A Chem 1998;112:73–80. https://doi.org/10.1016/S1010-6030(97)00261-X.
[139] Guimarães GGF, Klaic R, Giroto AS, Majaron VF, Avansi W, Farinas CS, et al. Smart Fertilization Based on Sulfur-Phosphate Composites: Synergy among Materials in a Structure with Multiple Fertilization Roles. ACS Sustain Chem Eng 2018;6:12187–96. https://doi.org/10.1021/acssuschemeng.8b02511.
[140] Rumble JR, Bruno TJ, Doa M. CRC handbook of chemistry and physics. CRC Handb. Chem. Phys. a ready-reference B. Chem. Phys. data. 101th ed., Boca Raton; 2021.
[141] Stamford NP, Santos PR, Santos CES, Freitas ADS, Dias SHL, Lira MA. Agronomic effectiveness of biofertilizers with phosphate rock, sulphur and Acidithiobacillus for yam bean grown on a Brazilian tableland acidic soil. Bioresour Technol 2007;98:1311–8. https://doi.org/10.1016/j.biortech.2006.04.037.
[142] Kaloidas VE, Papayannakos NG. Hydrogen production from the decomposition of hydrogen sulphide. Equilibrium studies on the system H2S/ H2/Si, (i = 1,...,8) in the gas phase. Int J Hydrogen Energy 1987;12:403–9. https://doi.org/10.1016/0360-3199(87)90159-5.
[143] Dan M, Xiang J, Yang J, Wu F, Han C, Zhong Y, et al. Beyond hydrogen production: Solar−driven H2S−donating value−added chemical production over MnxCd1−xS/CdyMn1−yS catalyst. Appl Catal B Environ 2021;284. https://doi.org/10.1016/j.apcatb.2020.119706.
[144] Ragauskas AJ, Williams CK, Davison BH, Britovsek G, Cairney J, Eckert CA, et al. The path forward for biofuels and biomaterials. Science (80-) 2006;311:484–9. https://doi.org/10.1126/science.1114736.
[145] Cherubini F. The biorefinery concept: Using biomass instead of oil for producing energy and chemicals. Energy Convers Manag 2010;51:1412–21. https://doi.org/10.1016/j.enconman.2010.01.015.
[146] Ragauskas AJ, Beckham GT, Biddy MJ, Chandra R, Chen F, Davis MF, et al. Lignin valorization: Improving lignin processing in the biorefinery. Science (80-) 2014;344. https://doi.org/10.1126/science.1246843.
[147] Wei H, Yingting Y, Jingjing G, Wenshi Y, Junhong T. Lignocellulosic Biomass

Valorization: Production of Ethanol. Encycl Sustain Technol 2017:601–4. https://doi.org/10.1016/B978-0-12-409548-9.10239-8.
[148] Sun Y, Cheng J. Hydrolysis of lignocellulosic materials for ethanol production: A review. Bioresour Technol 2002;83:1–11. https://doi.org/10.1016/S0960-8524(01)00212-7.
[149] Wakerley DW, Kuehnel MF, Orchard KL, Ly KH, Rosser TE, Reisner E. Solar-driven reforming of lignocellulose to H2 with a CdS/CdOx photocatalyst. Nat Energy 2017;2. https://doi.org/10.1038/nenergy.2017.21.
[150] Zhang G, Ni C, Huang X, Welgamage A, Lawton LA, Robertson PKJ, et al. Simultaneous cellulose conversion and hydrogen production assisted by cellulose decomposition under UV-light photocatalysis. Chem Commun 2016;52:1673–6. https://doi.org/10.1039/c5cc09075j.
[151] Da Già L, Recchi C, Gonzalez-Yañez EO, Davies TE, Lopez-Sanchez JA. Visible light selective photocatalytic conversion of glucose by TiO2. Appl Catal B Environ 2017;202:281–8. https://doi.org/10.1016/j.apcatb.2016.08.035.
[152] Lan L, Shao Y, Jiao Y, Zhang R, Hardacre C, Fan X. Systematic study of H2 production from catalytic photoreforming of cellulose over Pt catalysts supported on TiO2. Chinese J Chem Eng 2020;28:2084–91. https://doi.org/10.1016/j.cjche.2020.03.030.
[153] Zhang L, Wang W, Zeng S, Su Y, Hao H. Enhanced H2 evolution from photocatalytic cellulose conversion based on graphitic carbon layers on TiO2/NiOx. Green Chem 2018;20:3008–13. https://doi.org/10.1039/c8gc01398e.
[154] Caravaca A, Jones W, Hardacre C, Bowker M. H2 production by the photocatalytic reforming of cellulose and raw biomass using Ni, Pd, Pt and Au on titania. Proc R Soc A Math Phys Eng Sci 2016;472. https://doi.org/10.1098/rspa.2016.0054.
[155] Habibi Y. Key advances in the chemical modification of nanocelluloses. Chem Soc Rev 2014;43:1519–42. https://doi.org/10.1039/c3cs60204d.
[156] Hasegawa I, Inoue Y, Muranaka Y, Yasukawa T, Mae K. Selective production of organic acids and depolymerization of lignin by hydrothermal oxidation with diluted hydrogen peroxide. Energy and Fuels 2011;25:791–6. https://doi.org/10.1021/ef101477d.
[157] Yu X, Wei Z, Lu Z, Pei H, Wang H. Activation of lignin by selective oxidation: An emerging strategy for boosting lignin depolymerization to aromatics. Bioresour Technol 2019;291:121885. https://doi.org/10.1016/j.biortech.2019.121885.
[158] Tanaka K, Calanag RCR, Hisanaga T. Photocatalyzed degradation of lignin on TiO2. J Mol Catal A Chem 1999;138:287–94. https://doi.org/10.1016/S1381-1169(98)00161-7.
[159] Liu H, Li H, Luo N, Wang F. Visible-light-induced oxidative lignin c-c bond cleavage to aldehydes using vanadium catalysts. ACS Catal 2020;10:632–43. https://doi.org/10.1021/acscatal.9b03768.
[160] Zhou CH, Beltramini JN, Lu GQ. Chemoselective catalytic conversion of glycerol as a biorenewable source to valuable commodity chemicals. Chem Soc Rev 2008;37:527–49. https://doi.org/10.1039/b707343g.
[161] Yang F, Hanna MA, Sun R. Value-added uses for crude glycerol--a byproduct of biodiesel production. Biotechnol Biofuels 2012;5:13. https://doi.org/10.1186/1754-6834-5-13.
[162] Tran NH, Kannangara GSK. Conversion of glycerol to hydrogen rich gas. Chem Soc Rev 2013;42:9454–79. https://doi.org/10.1039/c3cs60227c.
[163] Shimura K, Yoshida H. Heterogeneous photocatalytic hydrogen production from water and biomass derivatives. Energy Environ Sci 2011;4:2467. https://doi.org/10.1039/c1ee01120k.
[164] Montini T, Gombac V, Sordelli L, Delgado JJ, Chen X, Adami G, et al. Nanostructured Cu/TiO 2 photocatalysts for H 2 production from ethanol and glycerol aqueous solutions. ChemCatChem 2011;3:574–7. https://doi.org/10.1002/cctc.201000289.
[165] Fujita S ichiro, Kawamori H, Honda D, Yoshida H, Arai M. Photocatalytic hydrogen production from aqueous glycerol solution using NiO/TiO2 catalysts: Effects of preparation and reaction conditions. Appl Catal B Environ 2016;181:818–24.

https://doi.org/10.1016/j.apcatb.2015.08.048.
[166] Wang M, Liu M, Lu J, Wang F. Photo splitting of bio-polyols and sugars to methanol and syngas. Nat Commun 2020;11. https://doi.org/10.1038/s41467-020-14915-8.
[167] Zhao S, Dai Z, Guo W, Chen F, Liu Y, Chen R. Highly selective oxidation of glycerol over Bi/Bi3.64Mo0.36O6.55 heterostructure: Dual reaction pathways induced by photogenerated 1O2 and holes. Appl Catal B Environ 2019;244:206–14. https://doi.org/10.1016/j.apcatb.2018.11.047.
[168] Jedsukontorn T, Meeyoo V, Saito N, Hunsom M. Route of glycerol conversion and product generation via TiO2-induced photocatalytic oxidation in the presence of H2O2. Chem Eng J 2015;281:252–64. https://doi.org/10.1016/j.cej.2015.06.078.
[169] Fajrina N, Tahir M. Engineering approach in stimulating photocatalytic H2 production in a slurry and monolithic photoreactor systems using Ag-bridged Z-scheme pCN/TiO2 nanocomposite. Chem Eng J 2019;374:1076–95. https://doi.org/10.1016/j.cej.2019.06.011.
[170] Verma S, Lu S, Kenis PJA. Co-electrolysis of CO2 and glycerol as a pathway to carbon chemicals with improved technoeconomics due to low electricity consumption. Nat Energy 2019;4:466–74. https://doi.org/10.1038/s41560-019-0374-6.
[171] Antoni D, Zverlov V V., Schwarz WH. Biofuels from microbes. Appl Microbiol Biotechnol 2007;77:23–35. https://doi.org/10.1007/s00253-007-1163-x.
[172] Blankenship RE, Tiede DM, Barber J, Brudvig GW, Fleming G, Ghirardi M, et al. Comparing photosynthetic and photovoltaic efficiencies and recognizing the potential for improvement. Science (80-) 2011;332:805–9. https://doi.org/10.1126/science.1200165.
[173] Song C, Liu Q, Qi Y, Chen G, Song Y, Kansha Y, et al. Absorption-microalgae hybrid CO2 capture and biotransformation strategy—A review. Int J Greenh Gas Control 2019;88:109–17. https://doi.org/10.1016/j.ijggc.2019.06.002.
[174] Botha T, von Blottnitz H. A comparison of the environmental benefits of bagasse-derived electricity and fuel ethanol on a life-cycle basis. Energy Policy 2006;34:2654–61. https://doi.org/10.1016/j.enpol.2004.12.017.
[175] Filho RBDA, Danielski L, De Carvalho FR, Stragevitch L. Recovery of carbon dioxide from sugarcane fermentation broth in the ethanol industry. Food Bioprod Process 2013;91:287–91. https://doi.org/10.1016/j.fbp.2012.09.009.
[176] Habisreutinger SN, Schmidt-Mende L, Stolarczyk JK. Photocatalytic reduction of CO2 on TiO2 and other semiconductors. Angew Chemie - Int Ed 2013;52:7372–408. https://doi.org/10.1002/anie.201207199.
[177] Larrazábal GO, Martín AJ, Pérez-Ramírez J. Building Blocks for High Performance in Electrocatalytic CO2 Reduction: Materials, Optimization Strategies, and Device Engineering. J Phys Chem Lett 2017;8:3933–44. https://doi.org/10.1021/acs.jpclett.7b01380.
[178] Ooka H, Figueiredo MC, Koper MTM. Competition between Hydrogen Evolution and Carbon Dioxide Reduction on Copper Electrodes in Mildly Acidic Media. Langmuir 2017;33:9307–13. https://doi.org/10.1021/acs.langmuir.7b00696.
[179] Goyal A, Marcandalli G, Mints VA, Koper MTM. Competition between CO2Reduction and Hydrogen Evolution on a Gold Electrode under Well-Defined Mass Transport Conditions. J Am Chem Soc 2020;142:4154–61. https://doi.org/10.1021/jacs.9b10061.
[180] Varghese OK, Paulose M, LaTempa TJ, Grimes CA. High-Rate Solar Photocatalytic Conversion of CO 2 and Water Vapor to Hydrocarbon Fuels . Nano Lett 2009;9:731–7. https://doi.org/10.1021/nl803258p.
[181] Zong X, Han J, Seger B, Chen H, Lu G, Li C, et al. An integrated photoelectrochemical-chemical loop for solar-driven overall splitting of hydrogen sulfide. Angew Chemie - Int Ed 2014;53:4399–403. https://doi.org/10.1002/anie.201400571.
[182] Liang S, Liu X, Zhong Z, Han B, Zhong X, Chen W, et al. Lattice-strained nanotubes facilitate efficient natural sunlight-driven CO2 photoreduction. Nano Res 2021;14:2558–67. https://doi.org/10.1007/s12274-020-3252-4.
[183] Chatt J, Dilworth JR, Richards RL. Recent Advances in the Chemistry of Nitrogen

Fixation. Chem Rev 1978;78:589–625. https://doi.org/10.1021/cr60316a001.
[184] Forrest SJK, Schluschaß B, Yuzik-Klimova EY, Schneider S. Nitrogen Fixation via Splitting into Nitrido Complexes. Chem Rev 2021. https://doi.org/10.1021/acs.chemrev.0c00958.
[185] Harris DC. Standard Reduction Potentials. Quant. Chem. Anal. 7th ed., New York: W. H. Freeman and Company; 2007, p. 1008.
[186] Martín AJ, Shinagawa T, Pérez-Ramírez J. Electrocatalytic Reduction of Nitrogen: From Haber-Bosch to Ammonia Artificial Leaf. Chem 2019;5:263–83. https://doi.org/10.1016/j.chempr.2018.10.010.
[187] Schrauzer GN, Guth TD. Photolysis of Water and Photoreduction of Nitrogen on Titanium Dioxide1. J Am Chem Soc 1977;99:7189–93. https://doi.org/10.1021/ja00464a015.
[188] Deng J, Iñiguez JA, Liu C. Electrocatalytic Nitrogen Reduction at Low Temperature. Joule 2018;2:846–56. https://doi.org/10.1016/j.joule.2018.04.014.
[189] Comer BM, Medford AJ. Analysis of Photocatalytic Nitrogen Fixation on Rutile TiO2(110). ACS Sustain Chem Eng 2018;6:4648–60. https://doi.org/10.1021/acssuschemeng.7b03652.
[190] Yao C, Wang R, Wang Z, Lei H, Dong X, He C. Highly dispersive and stable Fe3+ active sites on 2D graphitic carbon nitride nanosheets for efficient visible-light photocatalytic nitrogen fixation. J Mater Chem A 2019;7:27547–59. https://doi.org/10.1039/c9ta09201c.
[191] Liu S, Wang Y, Wang S, You M, Hong S, Wu TS, et al. Photocatalytic Fixation of Nitrogen to Ammonia by Single Ru Atom Decorated TiO 2 Nanosheets. ACS Sustain Chem Eng 2019;7:6813–20. https://doi.org/10.1021/acssuschemeng.8b06134.
[192] Lv X, Wei W, Li F, Huang B, Dai Y. Metal-Free B@ g-CN: Visible/Infrared Light-Driven Single Atom Photocatalyst Enables Spontaneous Dinitrogen Reduction to Ammonia. Nano Lett 2019;19:6391–9. https://doi.org/10.1021/acs.nanolett.9b02572.
[193] Erisman JW, Sutton MA, Galloway J, Klimont Z, Winiwarter W. How a century of ammonia synthesis changed the world. Nat Geosci 2008;1:636–9. https://doi.org/10.1038/ngeo325.
[194] Smil V. Nitrogen and food production: Proteins for human diets. Ambio 2002;31:126–31. https://doi.org/10.1579/0044-7447-31.2.126.
[195] Stewart WM, Dibb DW, Johnston AE, Smyth TJ. The contribution of commercial fertilizer nutrients to food production. Agron J 2005;97:1–6. https://doi.org/10.2134/agronj2005.0001.
[196] Roser M, Ritchie H. Our World in Data: Fertilizers 2013.
[197] Scott M, May M, Manning J. Agricultural Pesticide Formulations 2007:1–6.
[198] Cavalcante RP, De Oliveira DM, Da Silva LDM, Giménez J, Esplugas S, De Oliveira SC, et al. Evaluation of the main active species involved in the TiO2photocatalytic degradation of ametryn herbicide and its by-products. J Environ Chem Eng 2021;9. https://doi.org/10.1016/j.jece.2021.105109.
[199] Finčur N, Sfîrloagă P, Putnik P, Despotović V, Lazarević M, Uzelac M, et al. Removal of emerging pollutants from water using environmentally friendly processes: Photocatalysts preparation, characterization, intermediates identification and toxicity assessment. Nanomaterials 2021;11:1–21. https://doi.org/10.3390/nano11010215.
[200] Nobre FX, Mariano FAF, Santos FEP, Rocco MLM, Manzato L, De Matos JME, et al. Heterogeneous photocatalysis of Tordon 2,4-D herbicide using the phase mixture of TiO2. J Environ Chem Eng 2019;7. https://doi.org/10.1016/j.jece.2019.103501.
[201] Farner Budarz J, Cooper EM, Gardner C, Hodzic E, Ferguson PL, Gunsch CK, et al. Chlorpyrifos degradation via photoreactive TiO2 nanoparticles: Assessing the impact of a multi-component degradation scenario. J Hazard Mater 2019:61–8. https://doi.org/10.1016/j.jhazmat.2017.12.028.
[202] Ye Y, Bruning H, Liu W, Rijnaarts H, Yntema D. Effect of dissolved natural organic matter on the photocatalytic micropollutant removal performance of TiO2 nanotube array. J Photochem Photobiol A Chem 2019;371:216–22.

https://doi.org/10.1016/j.jphotochem.2018.11.012.
[203] Zhang K, Zhou W, Zhang X, Sun B, Wang L, Pan K, et al. Self-floating amphiphilic black TiO2 foams with 3D macro-mesoporous architectures as efficient solar-driven photocatalysts. Appl Catal B Environ 2017;206:336–43. https://doi.org/10.1016/j.apcatb.2017.01.059.
[204] Garcia-Muñoz P, Dachtler W, Altmayer B, Schulz R, Robert D, Seitz F, et al. Reaction pathways, kinetics and toxicity assessment during the photocatalytic degradation of glyphosate and myclobutanil pesticides: Influence of the aqueous matrix. Chem Eng J 2020;384. https://doi.org/10.1016/j.cej.2019.123315.
[205] Hama Aziz KH, Miessner H, Mueller S, Mahyar A, Kalass D, Moeller D, et al. Comparative study on 2,4-dichlorophenoxyacetic acid and 2,4-dichlorophenol removal from aqueous solutions via ozonation, photocatalysis and non-thermal plasma using a planar falling film reactor. J Hazard Mater 2018;343:107–15. https://doi.org/10.1016/j.jhazmat.2017.09.025.
[206] Orge CA, Pereira MFR, Faria JL. Photocatalytic-assisted ozone degradation of metolachlor aqueous solution. Chem Eng J 2017;318:247–53. https://doi.org/10.1016/j.cej.2016.06.136.
[207] Fiorenza R, Di Mauro A, Cantarella M, Privitera V, Impellizzeri G. Selective photodegradation of 2,4-D pesticide from water by molecularly imprinted TiO 2. J Photochem Photobiol A Chem 2019;380. https://doi.org/10.1016/j.jphotochem.2019.111872.
[208] Fiorenza R, Di Mauro A, Cantarella M, Iaria C, Scalisi EM, Brundo MV, et al. Preferential removal of pesticides from water by molecular imprinting on TiO2 photocatalysts. Chem Eng J 2020;379. https://doi.org/10.1016/j.cej.2019.122309.
[209] Zhang YN, Dai W, Wen Y, Zhao G. Efficient enantioselective degradation of the inactive (S)-herbicide dichlorprop on chiral molecular-imprinted TiO2. Appl Catal B Environ 2017;212:185–92. https://doi.org/10.1016/j.apcatb.2017.04.062.
[210] Rózsa G, Náfrádi M, Alapi T, Schrantz K, Szabó L, Wojnárovits L, et al. Photocatalytic, photolytic and radiolytic elimination of imidacloprid from aqueous solution: Reaction mechanism, efficiency and economic considerations. Appl Catal B Environ 2019;250:429–39. https://doi.org/10.1016/j.apcatb.2019.01.065.
[211] Anirudhan TS, Madanan Anju S. Synthesis and evaluation of TiO2 nanotubes/silylated graphene oxide-based molecularly imprinted polymer for the selective adsorption and subsequent photocatalytic degradation of 2,4-Dichlorophenoxyacetic acid. J Environ Chem Eng 2019;7. https://doi.org/10.1016/j.jece.2019.103355.
[212] Nekooie R, Shamspur T, Mostafavi A. Novel CuO/TiO2/PANI nanocomposite: Preparation and photocatalytic investigation for chlorpyrifos degradation in water under visible light irradiation. J Photochem Photobiol A Chem 2021;407. https://doi.org/10.1016/j.jphotochem.2020.113038.
[213] Carvalho LM, Soares-Filho AF, Lima MS, Cruz-Filho JF, Dantas TCM, Luz GE. 2,4-Dichlorophenoxyacetic acid (2,4-D) photodegradation on WO3-TiO2-SBA-15 nanostructured composite. Environ Sci Pollut Res 2021;28:7774–85. https://doi.org/10.1007/s11356-020-11085-4.
[214] Shoneye A, Tang J. Highly dispersed FeOOH to enhance photocatalytic activity of TiO2 for complete mineralisation of herbicides. Appl Surf Sci 2020;511. https://doi.org/10.1016/j.apsusc.2020.145479.
[215] Lannoy A, Bleta R, Machut-Binkowski C, Addad A, Monflier E, Ponchel A. Cyclodextrin-Directed Synthesis of Gold-Modified TiO2 Materials and Evaluation of Their Photocatalytic Activity in the Removal of a Pesticide from Water: Effect of Porosity and Particle Size. ACS Sustain Chem Eng 2017;5:3623–30. https://doi.org/10.1021/acssuschemeng.6b03059.
[216] Liu Z, Zhang Y, Kong L, Liu L, Luo J, Liu B, et al. Preparation and preferential photocatalytic degradation of acephate by using the composite photocatalyst Sr/TiO2-PCFM. Chem Eng J 2019;374:852–62. https://doi.org/10.1016/j.cej.2019.06.013.
[217] Tabaja N, Brouri D, Casale S, Zein S, Jaafar M, Selmane M, et al. Use of SBA-15 silica

grains for engineering mixtures of oxides CoFe and NiFe for Advanced Oxidation Reactions under visible and NIR. Appl Catal B Environ 2019;253:369–78. https://doi.org/10.1016/j.apcatb.2019.04.073.
[218] Abdelhaleem A, Chu W. Prediction of carbofuran degradation based on the hydroxyl radical's generation using the FeIII impregnated N doped-TiO2/H2O2/visible LED photo-Fenton-like process. Chem Eng J 2020;382. https://doi.org/10.1016/j.cej.2019.122930.
[219] Sun B, Zhou W, Li H, Ren L, Qiao P, Xiao F, et al. Magnetic Fe2O3/mesoporous black TiO2 hollow sphere heterojunctions with wide-spectrum response and magnetic separation. Appl Catal B Environ 2018;221:235–42. https://doi.org/10.1016/j.apcatb.2017.09.023.
[220] Serrano-Lázaro A, Verdín-Betancourt FA, Jayaraman VK, López-González M de L, Hernández-Gordillo A, Sierra-Santoyo A, et al. Efficient photocatalytic elimination of Temephos pesticide using ZnO nanoflowers. J Photochem Photobiol A Chem 2020;393. https://doi.org/10.1016/j.jphotochem.2020.112414.
[221] Islam JB, Furukawa M, Tateishi I, Katsumata H, Kaneco S. Photocatalytic degradation of a typical neonicotinoid insecticide: nitenpyrum by ZnO nanoparticles under solar irradiation. Environ Sci Pollut Res 2020;27:20446–56. https://doi.org/10.1007/s11356-020-08424-w.
[222] Fenoll J, Garrido I, Pastor-Belda M, Campillo N, Viñas P, Yañez MJ, et al. Solar detoxification of water polluted with fungicide residues using ZnO-coated magnetic particles. Chem Eng J 2017;330:71–81. https://doi.org/10.1016/j.cej.2017.07.131.
[223] Berberidou C, Kitsiou V, Kazala E, Lambropoulou DA, Kouras A, Kosma CI, et al. Study of the decomposition and detoxification of the herbicide bentazon by heterogeneous photocatalysis: Kinetics, intermediates and transformation pathways. Appl Catal B Environ 2017;200:150–63. https://doi.org/10.1016/j.apcatb.2016.06.068.
[224] Flores K, Valdes C, Ramirez D, Eubanks TM, Lopez J, Hernandez C, et al. The effect of hybrid zinc oxide/graphene oxide (ZnO/GO) nano-catalysts on the photocatalytic degradation of simazine. Chemosphere 2020;259. https://doi.org/10.1016/j.chemosphere.2020.127414.
[225] Aghaei M, Sajjadi S, Keihan AH. Sono-coprecipitation synthesis of ZnO/CuO nanophotocatalyst for removal of parathion from wastewater. Environ Sci Pollut Res 2020;27:11541–53. https://doi.org/10.1007/s11356-020-07680-0.
[226] Premalatha N, Rose Miranda L. Surfactant modified ZnO–Bi2O3 nanocomposite for degradation of lambda- cyhalothrin pesticide in visible light: A study of reaction kinetics and intermediates. J Environ Manage 2019;246:259–66. https://doi.org/10.1016/j.jenvman.2019.05.155.
[227] Hanh NT, Le Minh Tri N, Van Thuan D, Thanh Tung MH, Pham TD, Minh TD, et al. Monocrotophos pesticide effectively removed by novel visible light driven Cu doped ZnO photocatalyst. J Photochem Photobiol A Chem 2019;382. https://doi.org/10.1016/j.jphotochem.2019.111923.
[228] Dehghan S, Jafari AJ, FarzadKia M, Esrafili A, Kalantary RR. Visible-light-driven photocatalytic degradation of Metalaxyl by reduced graphene oxide/Fe 3 O 4 /ZnO ternary nanohybrid: Influential factors, mechanism and toxicity bioassay. J Photochem Photobiol A Chem 2019;375:280–92. https://doi.org/10.1016/j.jphotochem.2019.01.024.
[229] Lakshmi K, Kadirvelu K, Mohan PS. Reclaimable La: ZnO/PAN nanofiber catalyst for photodegradation of methyl paraoxon and its toxicological evaluation utilizing early life stages of zebra fish (Danio rerio). Chem Eng J 2019;357:724–36. https://doi.org/10.1016/j.cej.2018.09.201.
[230] Veerakumar P, Sangili A, Saranya K, Pandikumar A, Lin KC. Palladium and silver nanoparticles embedded on zinc oxide nanostars for photocatalytic degradation of pesticides and herbicides. Chem Eng J 2021;410. https://doi.org/10.1016/j.cej.2021.128434.
[231] Rezaei SS, Dehghanifard E, Noorisepehr M, Ghadirinejad K, Kakavandi B, Esfahani AR. Efficient clean-up of waters contaminated with diazinon pesticide using photo-

decomposition of peroxymonosulfate by ZnO decorated on a magnetic core/shell structure. J Environ Manage 2019;250. https://doi.org/10.1016/j.jenvman.2019.109472.
[232] Alam U, Fleisch M, Kretschmer I, Bahnemann D, Muneer M. One-step hydrothermal synthesis of Bi-TiO2 nanotube/graphene composites: An efficient photocatalyst for spectacular degradation of organic pollutants under visible light irradiation. Appl Catal B Environ 2017;218:758–69. https://doi.org/10.1016/j.apcatb.2017.06.016.
[233] Odling G, Pong ZY, Gilfillan G, Pulham CR, Robertson N. Bismuth titanate modified and immobilized TiO2 photocatalysts for water purification: Broad pollutant scope, ease of re-use and mechanistic studies. Environ Sci Water Res Technol 2018;4:2170–8. https://doi.org/10.1039/c8ew00568k.
[234] Majhi D, Das K, Mishra A, Dhiman R, Mishra BG. One pot synthesis of CdS/BiOBr/Bi2O2CO3: A novel ternary double Z-scheme heterostructure photocatalyst for efficient degradation of atrazine. Appl Catal B Environ 2020;260. https://doi.org/10.1016/j.apcatb.2019.118222.
[235] Majhi D, Bhoi YP, Samal PK, Mishra BG. Morphology controlled synthesis and photocatalytic study of novel CuS-Bi 2 O 2 CO 3 heterojunction system for chlorpyrifos degradation under visible light illumination. Appl Surf Sci 2018;455:891–902. https://doi.org/10.1016/j.apsusc.2018.06.051.
[236] Bhoi YP, Mishra BG. Photocatalytic degradation of alachlor using type-II CuS/BiFeO3 heterojunctions as novel photocatalyst under visible light irradiation. Chem Eng J 2018;344:391–401. https://doi.org/10.1016/j.cej.2018.03.094.
[237] Das K, Majhi D, Bhoi YP, Mishra BG. Combustion synthesis, characterization and photocatalytic application of CuS/Bi4Ti3O12 p-n heterojunction materials towards efficient degradation of 2-methyl-4-chlorophenoxyacetic acid herbicide under visible light. Chem Eng J 2019;362:588–99. https://doi.org/10.1016/j.cej.2019.01.060.
[238] Cao L, Ma D, Zhou Z, Xu C, Cao C, Zhao P, et al. Efficient photocatalytic degradation of herbicide glyphosate in water by magnetically separable and recyclable BiOBr/Fe3O4 nanocomposites under visible light irradiation. Chem Eng J 2019;368:212–22. https://doi.org/10.1016/j.cej.2019.02.100.
[239] Xu J, Olvera-Vargas H, Teo FYH, Lefebvre O. A comparison of visible-light photocatalysts for solar photoelectrocatalysis coupled to solar photoelectro-Fenton: Application to the degradation of the pesticide simazine. Chemosphere 2021;276. https://doi.org/10.1016/j.chemosphere.2021.130138.
[240] Kumar A, Kumar A, Sharma G, Al-Muhtaseb AH, Naushad M, Ghfar AA, et al. Biochar-templated g-C3N4/Bi2O2CO3/CoFe2O4 nano-assembly for visible and solar assisted photo-degradation of paraquat, nitrophenol reduction and CO2 conversion. Chem Eng J 2018;339:393–410. https://doi.org/10.1016/j.cej.2018.01.105.
[241] Xie R, Zhang L, Xu H, Zhong Y, Sui X, Mao Z. Construction of up-converting fluorescent carbon quantum dots/Bi20TiO32 composites with enhanced photocatalytic properties under visible light. Chem Eng J 2017;310:79–90. https://doi.org/10.1016/j.cej.2016.10.089.
[242] Zhou P, Zhang L, Dai Y, Wu W, Sui X, Zhong Y, et al. Construction of a metallic silver nanoparticle-decorated bismuth oxybromide-based composite material as a readily recyclable photocatalyst. J Clean Prod 2020;246. https://doi.org/10.1016/j.jclepro.2019.119007.
[243] Padervand M, Ghasemi S, Hajiahmadi S, Wang C. K4Nb6O17/Fe3N/α-Fe2O3/C3N4 as an enhanced visible light-driven quaternary photocatalyst for acetamiprid photodegradation, CO2 reduction, and cancer cells treatment. Appl Surf Sci 2021;544. https://doi.org/10.1016/j.apsusc.2021.148939.
[244] Zhang B, Li C, Zhang Y, Yuan M, Wang J, Zhu J, et al. Improved photocatalyst: Elimination of triazine herbicides by novel phosphorus and boron co-doping graphite carbon nitride. Sci Total Environ 2021;757. https://doi.org/10.1016/j.scitotenv.2020.143810.
[245] Sudhaik A, Raizada P, Singh P, Hosseini-Bandegharaei A, Thakur VK, Nguyen VH. Highly effective degradation of imidacloprid by H2O2/fullerene decorated P-doped g-

C3N4photocatalyst. J Environ Chem Eng 2020;8. https://doi.org/10.1016/j.jece.2020.104483.
[246] Jo WK, Selvam NCS. Z-scheme CdS/g-C3N4 composites with RGO as an electron mediator for efficient photocatalytic H2 production and pollutant degradation. Chem Eng J 2017;317:913–24. https://doi.org/10.1016/j.cej.2017.02.129.
[247] Ghodsi S, Esrafili A, Kalantary RR, Gholami M, Sobhi HR. Synthesis and evaluation of the performance of g-C3N4/Fe3O4/Ag photocatalyst for the efficient removal of diazinon: Kinetic studies. J Photochem Photobiol A Chem 2020;389. https://doi.org/10.1016/j.jphotochem.2019.112279.
[248] Wu Z, He X, Xue Y, Yang X, Li Y, Li Q, et al. Cyclodextrins grafted MoS2/g-C3N4 as high-performance photocatalysts for the removal of glyphosate and Cr (VI) from simulated agricultural runoff. Chem Eng J 2020;399. https://doi.org/10.1016/j.cej.2020.125747.
[249] Zhao L, Deng C, Xue S, Liu H, Hao L, Zhu M. Multifunctional g-C3N4/Ag NPs intercalated GO composite membrane for SERS detection and photocatalytic degradation of paraoxon-ethyl. Chem Eng J 2020;402. https://doi.org/10.1016/j.cej.2020.126223.
[250] Samy M, Ibrahim MG, Gar Alalm M, Fujii M, Diab KE, ElKady M. Innovative photocatalytic reactor for the degradation of chlorpyrifos using a coated composite of ZrV2O7 and graphene nano-platelets. Chem Eng J 2020;395. https://doi.org/10.1016/j.cej.2020.124974.
[251] Liu Y, Yang D, Shi Y, Song L, Yu R, Qu J, et al. Silver Phosphate/Graphene Oxide Aerogel Microspheres with Radially Oriented Microchannels for Highly Efficient and Continuous Removal of Pollutants from Wastewaters. ACS Sustain Chem Eng 2019;7:11228–40. https://doi.org/10.1021/acssuschemeng.9b00561.
[252] Khavar AHC, Moussavi G, Mahjoub AR, Satari M, Abdolmaleki P. Synthesis and visible-light photocatalytic activity of In,S-TiO2@rGO nanocomposite for degradation and detoxification of pesticide atrazine in water. Chem Eng J 2018;345:300–11. https://doi.org/10.1016/j.cej.2018.03.095.
[253] Huang Y, Han C, Liu Y, Nadagouda MN, Machala L, O'Shea KE, et al. Degradation of atrazine by ZnxCu1−xFe2O4 nanomaterial-catalyzed sulfite under UV–vis light irradiation: Green strategy to generate SO4[rad]−. Appl Catal B Environ 2018;221:380–92. https://doi.org/10.1016/j.apcatb.2017.09.001.
[254] Tang M, Ao Y, Wang C, Wang P. Facile synthesis of dual Z-scheme g-C3N4/Ag3PO4/AgI composite photocatalysts with enhanced performance for the degradation of a typical neonicotinoid pesticide. Appl Catal B Environ 2020;268. https://doi.org/10.1016/j.apcatb.2019.118395.
[255] Qu R, Zhang W, Liu N, Zhang Q, Liu Y, Li X, et al. Antioil Ag3PO4 Nanoparticle/Polydopamine/Al2O3 Sandwich Structure for Complex Wastewater Treatment: Dynamic Catalysis under Natural Light. ACS Sustain Chem Eng 2018;6:8019–28. https://doi.org/10.1021/acssuschemeng.8b01469.
[256] Liu X, Zhou Y, Ma Y, Fang S, Kong F, Pang X. Photocatalytic degradation of dinotefuran by layered phosphorus-doped carbon nitride and its mechanism. J Photochem Photobiol A Chem 2021;414. https://doi.org/10.1016/j.jphotochem.2021.113287.
[257] Lee YJ, Kang JK, Park SJ, Lee CG, Moon JK, Alvarez PJJ. Photocatalytic degradation of neonicotinoid insecticides using sulfate-doped Ag3PO4 with enhanced visible light activity. Chem Eng J 2020;402. https://doi.org/10.1016/j.cej.2020.126183.
[258] Paris EC, Malafatti JOD, Sciena CR, Junior LFN, Zenatti A, Escote MT, et al. Nb2O5 nanoparticles decorated with magnetic ferrites for wastewater photocatalytic remediation. Environ Sci Pollut Res 2021;28:23731–41. https://doi.org/10.1007/s11356-020-11262-5.
[259] Lima MS, Cruz-Filho JF, Noleto LFG, Silva LJ, Costa TMS, Luz GE. Synthesis, characterization and catalytic activity of Fe3O4@WO3/SBA-15 on photodegradation of the acid dichlorophenoxyacetic (2,4-D) under UV irradiation. J Environ Chem Eng

2020;8. https://doi.org/10.1016/j.jece.2020.104145.
[260] Padervand M, Heidarpour H, Bargahi A. A mechanistic study and in-vivo toxicity bioassay on acetamiprid photodegradation over the zeolite supported cerium-based photocatalyst. J Photochem Photobiol A Chem 2020;395. https://doi.org/10.1016/j.jphotochem.2020.112526.
[261] Roselló-Márquez G, Fernández-Domene RM, Sánchez-Tovar R, García-Antón J. Photoelectrocatalyzed degradation of organophosphorus pesticide fenamiphos using WO3 nanorods as photoanode. Chemosphere 2020;246. https://doi.org/10.1016/j.chemosphere.2019.125677.
[262] Roselló-Márquez G, Fernández-Domene RM, Sánchez-Tovar R, García-Carrión S, Lucas-Granados B, García-Antón J. Photoelectrocatalyzed degradation of a pesticides mixture solution (chlorfenvinphos and bromacil) by WO 3 nanosheets. Sci Total Environ 2019;674:88–95. https://doi.org/10.1016/j.scitotenv.2019.04.150.
[263] Shi E, Xu Z, Wang W, Xu Y, Zhang Y, Yang X, et al. Ag2S-doped core-shell nanostructures of Fe3O4@Ag3PO4 ultrathin film: Major role of hole in rapid degradation of pollutants under visible light irradiation. Chem Eng J 2019;366:123–32. https://doi.org/10.1016/j.cej.2019.02.018.
[264] Fernández-Domene RM, Sánchez-Tovar R, Lucas-granados B, Muñoz-Portero MJ, García-Antón J. Elimination of pesticide atrazine by photoelectrocatalysis using a photoanode based on WO3 nanosheets. Chem Eng J 2018;350:1114–24. https://doi.org/10.1016/j.cej.2018.06.015.
[265] Liu X, Li C, Zhang Y, Yu J, Yuan M, Ma Y. Simultaneous photodegradation of multi-herbicides by oxidized carbon nitride: performance and practical application. Appl Catal B Environ 2017;219:194–9. https://doi.org/10.1016/j.apcatb.2017.07.007.
[266] Fan C, Dong H, Liang Y, Yang J, Tang G, Zhang W, et al. Sustainable synthesis of HKUST-1 and its composite by biocompatible ionic liquid for enhancing visible-light photocatalytic performance. J Clean Prod 2019;208:353–62. https://doi.org/10.1016/j.jclepro.2018.10.141.
[267] Liu J, Liu J, Xiong WH, Ye LY, Zhang WS, Yang H, et al. Developing a Novel Nanoscale Porphyrinic Metal-Organic Framework: A Bifunctional Platform with Sensitive Fluorescent Detection and Elimination of Nitenpyram in Agricultural Environment. J Agric Food Chem 2020;68:5572–8. https://doi.org/10.1021/acs.jafc.0c01313.
[268] Olejníček J, Brunclíková M, Kment Š, Hubička Z, Kmentová H, Kšírová P, et al. WO3 thin films prepared by sedimentation and plasma sputtering. Chem Eng J 2017;318:281–8. https://doi.org/10.1016/j.cej.2016.09.083.
[269] Zheng Z, Zhang K, Toe CY, Amal R, Zhang X, McCarthy DT, et al. Stormwater herbicides removal with a solar-driven advanced oxidation process: A feasibility investigation. Water Res 2021;190. https://doi.org/10.1016/j.watres.2020.116783.
[270] Xue Y, Wang P, Wang C, Ao Y. Efficient degradation of atrazine by BiOBr/UiO-66 composite photocatalyst under visible light irradiation: Environmental factors, mechanisms and degradation pathways. Chemosphere 2018;203:497–505. https://doi.org/10.1016/j.chemosphere.2018.04.017.
[271] Chen CC, Shaya J, Polychronopoulou K, Golovko VB, Tesana S, Wang SY, et al. Photocatalytic degradation of ethiofencarb by a visible light-driven snin4s8 photocatalyst. Nanomaterials 2021;11. https://doi.org/10.3390/nano11051325.
[272] Samy M, Ibrahim MG, Fujii M, Diab KE, ElKady M, Gar Alalm M. CNTs/MOF-808 painted plates for extended treatment of pharmaceutical and agrochemical wastewaters in a novel photocatalytic reactor. Chem Eng J 2021;406. https://doi.org/10.1016/j.cej.2020.127152.
[273] Farkas J, Náfrádi M, Hlogyik T, Cora Pravda B, Schrantz K, Hernádi K, et al. Comparison of advanced oxidation processes in the decomposition of diuron and monuron-efficiency, intermediates, electrical energy per order and the effect of various matrices. Environ Sci Water Res Technol 2018;4:1345–60. https://doi.org/10.1039/c8ew00202a.

[274] Abellán MN, Giménez J, Esplugas S. Photocatalytic degradation of antibiotics: The case of sulfamethoxazole and trimethoprim. Catal Today 2009;144:131–6. https://doi.org/10.1016/j.cattod.2009.01.051.
[275] Calza P, Marchisio S, Medana C, Baiocchi C. Fate of antibacterial spiramycin in river waters. Anal Bioanal Chem 2010;396:1539–50. https://doi.org/10.1007/s00216-009-3318-3.
[276] Baran W, Adamek E, Sobczak A, Makowski A. Photocatalytic degradation of sulfa drugs with TiO2, Fe salts and TiO2/FeCl3 in aquatic environment-Kinetics and degradation pathway. Appl Catal B Environ 2009;90:516–25. https://doi.org/10.1016/j.apcatb.2009.04.014.
[277] Peleyeju MG, Umukoro EH, Tshwenya L, Moutloali R, Babalola JO, Arotiba OA. Photoelectrocatalytic water treatment systems: Degradation, kinetics and intermediate products studies of sulfamethoxazole on a TiO2-exfoliated graphite electrode. RSC Adv 2017;7:40571–80. https://doi.org/10.1039/c7ra07399b.
[278] Adamek E, Baran W, Sobczak A. Photocatalytic degradation of veterinary antibiotics: Biodegradability and antimicrobial activity of intermediates. Process Saf Environ Prot 2016;103:1–9. https://doi.org/10.1016/j.psep.2016.06.015.
[279] Rath S, Pereira LA, Bosco SMD, Maniero MG, Fostier AH, Guimarães JR. Fate of ivermectin in the terrestrial and aquatic environment: mobility, degradation, and toxicity towards Daphnia similis. Environ Sci Pollut Res 2016;23:5654–66. https://doi.org/10.1007/s11356-015-5787-6.
[280] Adamek E, Baran W, Ziemiańska J, Sobczak A. Effect of FeCl 3 on sulfonamide removal and reduction of antimicrobial activity of wastewater in a photocatalytic process with TiO 2. Appl Catal B Environ 2012;126:29–38. https://doi.org/10.1016/j.apcatb.2012.06.027.
[281] Yepsen O, Contreras D, Santander P, Yáñez J, Mansilla HD, Amarasiriwardena D. Photocatalytic degradation of thimerosal in human vaccine's residues and mercury speciation of degradation by-products. Microchem J 2015;121:41–7. https://doi.org/10.1016/j.microc.2015.02.001.
[282] Gaeta M, Sanfilippo G, Fraix A, Sortino G, Barcellona M, Conti GO, et al. Photodegradation of antibiotics by noncovalent porphyrin-functionalized tio2 in water for the bacterial antibiotic resistance risk management. Int J Mol Sci 2020;21. https://doi.org/10.3390/ijms21113775.
[283] Rodrigues-Silva C, Maniero MG, Rath S, Guimarães JR. Degradation of flumequine by photocatalysis and evaluation of antimicrobial activity. Chem Eng J 2013;224:46–52. https://doi.org/10.1016/j.cej.2012.11.002.
[284] Nasseh N, Al-Musawi TJ, Miri MR, Rodriguez-Couto S, Hossein Panahi A. A comprehensive study on the application of FeNi3@SiO2@ZnO magnetic nanocomposites as a novel photo-catalyst for degradation of tamoxifen in the presence of simulated sunlight. Environ Pollut 2020;261. https://doi.org/10.1016/j.envpol.2020.114127.
[285] Gao Z, Yao B, Ji L, Xu T. Effect of Reducing Agent NaBH4 on Photocatalytic Properties of Bi/BiOBr/Bi2WO6 Composites. ChemistrySelect 2019;4:10065–71. https://doi.org/10.1002/slct.201902150.
[286] Zhang XX, Li R, Jia M, Wang S, Huang Y, Chen C. Degradation of ciprofloxacin in aqueous bismuth oxybromide (BiOBr) suspensions under visible light irradiation: A direct hole oxidation pathway. Chem Eng J 2015;274:290–7. https://doi.org/10.1016/j.cej.2015.03.077.
[287] Guo C, Xu J, Wang S, Zhang Y, He Y, Li X. Photodegradation of sulfamethazine in an aqueous solution by a bismuth molybdate photocatalyst. Catal Sci Technol 2013;3:1603–11. https://doi.org/10.1039/c3cy20811g.
[288] Mafa PJ, Kuvarega AT, Mamba BB, Ntsendwana B. Photoelectrocatalytic degradation of sulfamethoxazole on g-C 3 N 4 /BiOI/EG p-n heterojunction photoanode under visible light irradiation. Appl Surf Sci 2019;483:506–20. https://doi.org/10.1016/j.apsusc.2019.03.281.

[289] Vinoth Kumar J, Karthik R, Chen SM, Chen KH, Sakthinathan S, Muthuraj V, et al. Design of novel 3D flower-like neodymium molybdate: An efficient and challenging catalyst for sensing and destroying pulmonary toxicity antibiotic drug nitrofurantoin. Chem Eng J 2018;346:11–23. https://doi.org/10.1016/j.cej.2018.03.183.
[290] Anirudhan TS, Deepa JR, Nair AS. Fabrication of chemically modified graphene oxide/nano hydroxyapatite composite for adsorption and subsequent photocatalytic degradation of aureomycine hydrochloride. J Ind Eng Chem 2017;47:415–30. https://doi.org/10.1016/j.jiec.2016.12.014.
[291] Malefane ME, Feleni U, Kuvarega AT. Cobalt (II/III) oxide and tungsten (VI) oxide p-n heterojunction photocatalyst for photodegradation of diclofenac sodium under visible light. J Environ Chem Eng 2020;8. https://doi.org/10.1016/j.jece.2019.103560.
[292] Chen J, Yang X, Zhu C, Xie X, Lin C, Zhao Y, et al. A research on shape-controllable synthesis of Ag3PO4/AgBr and its degradation of ciprofloxacin. Water Sci Technol 2018;77:1230–7. https://doi.org/10.2166/wst.2017.643.
[293] Lv Y, Yu Z, Huang S, Deng F, Zheng K, Yang G, et al. Rapidly photocatalytic mineralization of typical veterinary drugs with the SnO2/SnIn4S8 composite. Chemosphere 2021;271. https://doi.org/10.1016/j.chemosphere.2020.129452.
[294] de Godos I, Muñoz R, Guieysse B. Tetracycline removal during wastewater treatment in high-rate algal ponds. J Hazard Mater 2012;229–230:446–9. https://doi.org/10.1016/j.jhazmat.2012.05.106.
[295] García-Galán MJ, Díaz-Cruz MS, Barceló D. Kinetic studies and characterization of photolytic products of sulfamethazine, sulfapyridine and their acetylated metabolites in water under simulated solar irradiation. Water Res 2012;46:711–22. https://doi.org/10.1016/j.watres.2011.11.035.
[296] Prabhakaran D, Sukul P, Lamshöft M, Maheswari MA, Zühlke S, Spiteller M. Photolysis of difloxacin and sarafloxacin in aqueous systems. Chemosphere 2009;77:739–46. https://doi.org/10.1016/j.chemosphere.2009.08.031.
[297] Haddad T, Kümmerer K. Characterization of photo-transformation products of the antibiotic drug Ciprofloxacin with liquid chromatography-tandem mass spectrometry in combination with accurate mass determination using an LTQ-Orbitrap. Chemosphere 2014;115:40–6. https://doi.org/10.1016/j.chemosphere.2014.02.013.
[298] Sturini M, Speltini A, Maraschi F, Profumo A, Pretali L, Fasani E, et al. Sunlight-induced degradation of soil-adsorbed veterinary antimicrobials Marbofloxacin and Enrofloxacin. Chemosphere 2012;86:130–7. https://doi.org/10.1016/j.chemosphere.2011.09.053.
[299] Kitsiou V, Antoniadis A, Mantzavinos D, Poulios I. Homogeneous photo-Fenton mineralization of the antibiotic sulfamethazine in water under UV-A, visible and solar irradiation. J Chem Technol Biotechnol 2014;89:1668–74. https://doi.org/10.1002/jctb.4237.
[300] Wammer KH, Slattery MT, Stemig AM, Ditty JL. Tetracycline photolysis in natural waters: Loss of antibacterial activity. Chemosphere 2011;85:1505–10. https://doi.org/10.1016/j.chemosphere.2011.08.051.
[301] Qu S, Kolodziej EP, Cwiertny DM. Phototransformation rates and mechanisms for synthetic hormone growth promoters used in animal agriculture. Environ Sci Technol 2012;46:13202–11. https://doi.org/10.1021/es303091c.
[302] Niu XZ, Glady-Croué J, Croué JP. Photodegradation of sulfathiazole under simulated sunlight: Kinetics, photo-induced structural rearrangement, and antimicrobial activities of photoproducts. Water Res 2017;124:576–83. https://doi.org/10.1016/j.watres.2017.08.019.
[303] Oliveira C, Lima DLD, Silva CP, Calisto V, Otero M, Esteves VI. Photodegradation of sulfamethoxazole in environmental samples: The role of pH, organic matter and salinity. Sci Total Environ 2019;648:1403–10. https://doi.org/10.1016/j.scitotenv.2018.08.235.
[304] Sturini M, Speltini A, Maraschi F, Pretali L, Profumo A, Fasani E, et al. Environmental photochemistry of fluoroquinolones in soil and in aqueous soil suspensions under solar light. Environ Sci Pollut Res 2014;21:13215–21. https://doi.org/10.1007/s11356-013-

2124-9.
[305] Bian X, Zhang J. Photodegradation of sulfadiazine in aqueous solution and the affecting factors. J Chem 2016;2016. https://doi.org/10.1155/2016/8358960.
[306] Spina-Cruz M, Maniero MG, Guimarães JR. Advanced oxidation processes on doxycycline degradation: monitoring of antimicrobial activity and toxicity. Environ Sci Pollut Res 2019;26:27604–19. https://doi.org/10.1007/s11356-018-2149-1.
[307] Babić S, Pavlović DM, Biošić M, Ašperger D, Škorić I, Runje M. Fate of febantel in the aquatic environment—the role of abiotic elimination processes. Environ Sci Pollut Res 2018;25:28917–27. https://doi.org/10.1007/s11356-018-2935-9.
[308] Becerril ME, Ramírez-García JJ, Cavazos N, Serrano AR. Determination of the Kinetic Behavior of Diclofenac in Aqueous Solution by UV Light Radiation. Water Air Soil Pollut 2019;230. https://doi.org/10.1007/s11270-019-4274-y.
[309] Cordeiro SG, Ziem R, Schweizer YA, Costa B, Kuhn D, Haas P, et al. Degradation of micropollutant cephalexin by ultraviolet (UV) and assessment of residual antimicrobial activity of transformation products. Water Sci Technol 2021. https://doi.org/10.2166/wst.2021.170.
[310] Venancio WAL, Rodrigues-Silva C, Spina M, Diniz V, Guimarães JR. Degradation of benzimidazoles by photoperoxidation: metabolites detection and ecotoxicity assessment using Raphidocelis subcapitata microalgae and Vibrio fischeri. Environ Sci Pollut Res 2021;28:23742–52. https://doi.org/10.1007/s11356-020-11294-x.
[311] Saad AS, Ismail NS, Soliman M, Zaazaa HE. Study of oxyclozanide's innate stability coupled with the assessment of its aquatic photo-transformation using a validated isocratic HPLC method. J AOAC Int 2019;102:480–9. https://doi.org/10.5740/jaoacint.17-0364.
[312] Drobniewska A, Wójcik D, Kapłan M, Adomas B, Piotrowicz-Cieślak A, Nałęcz-Jawecki G. Recovery of Lemna minor after exposure to sulfadimethoxine irradiated and non-irradiated in a solar simulator. Environ Sci Pollut Res 2017;24:27642–52. https://doi.org/10.1007/s11356-016-7174-3.
[313] Liu Y, He X, Fu Y, Dionysiou DD. Kinetics and mechanism investigation on the destruction of oxytetracycline by UV-254 nm activation of persulfate. J Hazard Mater 2016;305:229–39. https://doi.org/10.1016/j.jhazmat.2015.11.043.
[314] Díaz-Quiroz C, Ulloa-Mercado G, Hernández-Chávez JF, Rentería-Mexía A, Serrano-Palacios D, Meza-Escalante E. Microalgae as biocatalyst in simultaneous photodegradation of antibiotics and hormones. J Chem Technol Biotechnol 2020;95:1453–9. https://doi.org/10.1002/jctb.6330.
[315] Takeuchi M, Yamashita H, Matsuoka M, Anpo M, Hirao T, Itoh N, et al. Photocatalytic decomposition of NO on titanium oxide thin film photocatalysts prepared by an ionized cluster beam technique. Catal Letters 2000;66:185–7. https://doi.org/10.1023/A:1019095406121.
[316] Sano T, Negishi N, Mas D, Takeuchi K. Photocatalytic Decomposition of N2O on Highly Dispersed Ag+ Ions on TiO2 Prepared by Photodeposition. J Catal 2000;194:71–9. https://doi.org/10.1006/jcat.2000.2915.
[317] Obalová L, Reli M, Lang J, Matějka V, Kukutschová J, Lacný Z, et al. Photocatalytic decomposition of nitrous oxide using TiO2 and Ag-TiO2 nanocomposite thin films. Catal Today 2013;209:170–5. https://doi.org/10.1016/j.cattod.2012.11.012.
[318] Xu M, Wang Y, Geng J, Jing D. Photodecomposition of NOx on Ag/TiO2 composite catalysts in a gas phase reactor. Chem Eng J 2017;307:181–8. https://doi.org/10.1016/j.cej.2016.08.080.
[319] Takeuchi M, Yamashita H, Matsuoka M, Anpo M, Hirao T, Itoh N, et al. Photocatalytic decomposition of NO under visible light irradiation on the Cr-ion-implanted TiO2 thin film photocatalyst. Catal Letters 2000;67:135–7. https://doi.org/10.1023/a:1019065521567.
[320] Wu Q, Yang CC, Van De Krol R. A dopant-mediated recombination mechanism in Fe-doped TiO2 nanoparticles for the photocatalytic decomposition of nitric oxide. Catal Today 2014;225:96–101. https://doi.org/10.1016/j.cattod.2013.09.026.

[321] Liu J, Wang L, Song W, Zhao M, Liu J, Wang H, et al. BiMO x Semiconductors as Catalysts for Photocatalytic Decomposition of N 2 O: A Combination of Experimental and DFT+U Study. ACS Sustain Chem Eng 2019;7:2811–20. https://doi.org/10.1021/acssuschemeng.8b06126.
[322] Wang L, Liu J, Song W, Wang H, Li Y, Liu J, et al. Experimental and DFT insights of BiVO4 as an effective photocatalytic catalyst for N2O decomposition. Chem Eng J 2019;366:504–13. https://doi.org/10.1016/j.cej.2019.02.038.
[323] Obalová L, Šihor M, Praus P, Reli M, Kočí K. Photocatalytic and photochemical decomposition of N2O on ZnS-MMT catalyst. Catal Today 2014;230:61–6. https://doi.org/10.1016/j.cattod.2013.09.047.
[324] Reli M, Svoboda L, Šihor M, Troppová I, Pavlovský J, Praus P, et al. Photocatalytic decomposition of N2O over g-C3N4/WO3 photocatalysts. Environ Sci Pollut Res 2018;25:34839–50. https://doi.org/10.1007/s11356-017-0723-6.
[325] Kočí K, Reli M, Troppová I, Šihor M, Kupková J, Kustrowski P, et al. Photocatalytic decomposition of N 2 O over TiO 2 /g-C 3 N 4 photocatalysts heterojunction. Appl Surf Sci 2017;396:1685–95. https://doi.org/10.1016/j.apsusc.2016.11.242.
[326] Wang J, Asakura Y, Yin S. Preparation of (Zn1+: XGe)(N2Ox) nanoparticles with enhanced NOx decomposition activity under visible light irradiation by nitridation of Zn2GeO4 nanoparticles designed precisely. Nanoscale 2019;11:20151–60. https://doi.org/10.1039/c9nr05244e.
[327] Asakura Y, Inaguma Y, Ueda K, Masubuchi Y, Yin S. Synthesis of gallium oxynitride nanoparticles through hydrothermal reaction in the presence of acetylene black and their photocatalytic NO: X decomposition. Nanoscale 2018;10:1837–44. https://doi.org/10.1039/c7nr07502b.
[328] Troppová I, Šihor M, Reli M, Ritz M, Praus P, Kočí K. Unconventionally prepared TiO 2 /g-C 3 N 4 photocatalysts for photocatalytic decomposition of nitrous oxide. Appl Surf Sci 2018;430:335–47. https://doi.org/10.1016/j.apsusc.2017.06.299.
[329] Saito K, Orikasa S, Asakura Y, Ide Y, Sugahara Y, Ogasawara M, et al. Ni-Doped Protonated Layered Titanate/TiO2Composite with Efficient Photocatalytic Activity for NO x Decomposition Reactions. Int J Photoenergy 2021;2021. https://doi.org/10.1155/2021/8847956.
[330] Higashimoto S, Matsuoka M, Yamashita H, Anpo M, Kitao O, Hidaka H, et al. Effect of the Si/Al ratio on the local structure of V Oxide/ZSM-5 catalysts prepared by solid-state reaction and their photocatalytic reactivity for the decomposition of NO in the absence and presence of propane. J Phys Chem B 2000;104:10288–92. https://doi.org/10.1021/jp000983m.
[331] Anpo M, Zhang SG, Mishima H, Matsuoka M, Yamashita H. Design of photocatalysts encapsulated within the zeolite framework and cavities for the decomposition of NO into N2 and O2 at normal temperature. Catal Today 1997;39:159–68. https://doi.org/10.1016/S0920-5861(97)00097-7.
[332] Wang J, Asakura Y, Yin S. Synthesis of zinc germanium oxynitride nanotube as a visible-light driven photocatalyst for NOx decomposition through ordered morphological transformation from Zn2GeO4 nanorod obtained by hydrothermal reaction. J Hazard Mater 2020;396. https://doi.org/10.1016/j.jhazmat.2020.122709.
[333] Komatsuda S, Asakura Y, Vequizo JJM, Yamakata A, Yin S. Enhanced photocatalytic NOx decomposition of visible-light responsive F-TiO2/(N,C)-TiO2 by charge transfer between F-TiO2 and (N,C)-TiO2 through their doping levels. Appl Catal B Environ 2018;238:358–64. https://doi.org/10.1016/j.apcatb.2018.07.038.
[334] Zhao Z, Fan J, Liu W, Xue Y, Yin S. In-situ hydrothermal synthesis of Ag3PO4/g-C3N4 composite and their photocatalytic decomposition of NOx. J Alloys Compd 2017;695:2812–9. https://doi.org/10.1016/j.jallcom.2016.12.001.
[335] Wu Q, Van De Krol R. Selective photoreduction of nitric oxide to nitrogen by nanostructured TiO 2 photocatalysts: Role of oxygen vacancies and iron dopant. J Am Chem Soc 2012;134:9369–75. https://doi.org/10.1021/ja302246b.
[336] Balci Leinen M, Dede D, Khan MU, Çağlayan M, Koçak Y, Demir HV, et al. CdTe

Quantum Dot-Functionalized P25 Titania Composite with Enhanced Photocatalytic NO 2 Storage Selectivity under UV and Vis Irradiation. ACS Appl Mater Interfaces 2019;11:865–79. https://doi.org/10.1021/acsami.8b18036.
[337] Cerrato G, Galli F, Boffito DC, Operti L, Bianchi CL. Correlation preparation parameters/activity for microTiO2 decorated with SilverNPs for NOx photodegradation under LED light. Appl Catal B Environ 2019;253:218–25. https://doi.org/10.1016/j.apcatb.2019.04.056.
[338] Huang Y, Wang P, Wang Z, Rao Y, Cao J ji, Pu S, et al. Protonated g-C3N4/Ti3+ self-doped TiO2 nanocomposite films: Room-temperature preparation, hydrophilicity, and application for photocatalytic NOx removal. Appl Catal B Environ 2019;240:122–31. https://doi.org/10.1016/j.apcatb.2018.08.078.
[339] Hu Y, Song X, Jiang S, Wei C. Enhanced photocatalytic activity of Pt-doped TiO2 for NOx oxidation both under UV and visible light irradiation: A synergistic effect of lattice Pt4+ and surface PtO. Chem Eng J 2015;274:102–12. https://doi.org/10.1016/j.cej.2015.03.135.
[340] Martinez-Oviedo A, Ray SK, Nguyen HP, Lee SW. Efficient photo-oxidation of NOx by Sn doped blue TiO2 nanoparticles. J Photochem Photobiol A Chem 2019;370:18–25. https://doi.org/10.1016/j.jphotochem.2018.10.032.
[341] Nguyen NH, Bai H. Effect of washing pH on the properties of titanate nanotubes and its activity for photocatalytic oxidation of NO and NO 2. Appl Surf Sci 2015;355:672–80. https://doi.org/10.1016/j.apsusc.2015.07.118.
[342] Martinez-Oviedo A, Ray SK, Joshi B, Lee SW. Enhancement of NOx photo-oxidation by Fe- and Cu-doped blue TiO2. Environ Sci Pollut Res 2020;27:26702–13. https://doi.org/10.1007/s11356-020-09078-4.
[343] Zhu W, Xiao S, Zhang D, Liu P, Zhou H, Dai W, et al. Highly Efficient and Stable Au/CeO2-TiO2 Photocatalyst for Nitric Oxide Abatement: Potential Application in Flue Gas Treatment. Langmuir 2015;31:10822–30. https://doi.org/10.1021/acs.langmuir.5b02232.
[344] Todorova N, Vaimakis T, Petrakis D, Hishita S, Boukos N, Giannakopoulou T, et al. N and N,S-doped TiO2 photocatalysts and their activity in NOx oxidation. Catal Today 2013;209:41–6. https://doi.org/10.1016/j.cattod.2012.11.019.
[345] Duan Y, Wang Y, Gan L, Meng J, Feng Y, Wang K, et al. Amorphous Carbon Nitride with Three Coordinate Nitrogen (N3C) Vacancies for Exceptional NOx Abatement in Visible Light. Adv Energy Mater 2021. https://doi.org/10.1002/aenm.202004001.
[346] Wang Z, Huang Y, Chen M, Shi X, Zhang Y, Cao J, et al. Roles of N-Vacancies over Porous g-C 3 N 4 Microtubes during Photocatalytic NO x Removal. ACS Appl Mater Interfaces 2019;11:10651–62. https://doi.org/10.1021/acsami.8b21987.
[347] Ai Z, Ho W, Lee S. A stable single-crystal Bi 3 NbO 7 nanoplates superstructure for effective visible-light-driven photocatalytic removal of nitric oxide. Appl Surf Sci 2012;263:266–72. https://doi.org/10.1016/j.apsusc.2012.09.041.
[348] Zhang P, Huang Y, Rao Y, Chen M, Li X, Ho W, et al. Chemical etching fabrication of uniform mesoporous Bi@Bi2O3 nanospheres with enhanced visible light-induced photocatalytic oxidation performance for NOx. Chem Eng J 2021;406. https://doi.org/10.1016/j.cej.2020.126910.
[349] Zhu G, Li S, Gao J, Zhang F, Liu C, Wang Q, et al. Constructing a 2D/2D Bi2O2CO3/Bi4O5Br2 heterostructure as a direct Z-scheme photocatalyst with enhanced photocatalytic activity for NOx removal. Appl Surf Sci 2019;493:913–25. https://doi.org/10.1016/j.apsusc.2019.07.119.
[350] Wu S, Yu X, Zhang J, Zhang Y, Zhu Y, Zhu M. Construction of BiOCl/CuBi2O4 S-scheme heterojunction with oxygen vacancy for enhanced photocatalytic diclofenac degradation and nitric oxide removal. Chem Eng J 2021;411. https://doi.org/10.1016/j.cej.2021.128555.
[351] Lu Y, Huang Y, Zhang Y, Huang T, Li H, Cao J ji, et al. Effects of H2O2 generation over visible light-responsive Bi/Bi2O2−xCO3 nanosheets on their photocatalytic NOx removal performance. Chem Eng J 2019;363:374–82.

https://doi.org/10.1016/j.cej.2019.01.172.
[352] Ou M, Wan S, Zhong Q, Zhang S, Song Y, Guo L, et al. Hierarchical Z-scheme photocatalyst of g-C3N4@Ag/BiVO4 (040) with enhanced visible-light-induced photocatalytic oxidation performance. Appl Catal B Environ 2018;221:97–107. https://doi.org/10.1016/j.apcatb.2017.09.005.
[353] Zhang Q, Huang Y, Peng S, Zhang Y, Shen Z, Cao J ji, et al. Perovskite LaFeO3-SrTiO3 composite for synergistically enhanced NO removal under visible light excitation. Appl Catal B Environ 2017;204:346–57. https://doi.org/10.1016/j.apcatb.2016.11.052.
[354] Chen M, Huang Y, Yao J, Cao J ji, Liu Y. Visible-light-driven N-(BiO) 2 CO 3 /Graphene oxide composites with improved photocatalytic activity and selectivity for NO x removal. Appl Surf Sci 2018;430:137–44. https://doi.org/10.1016/j.apsusc.2017.06.056.
[355] Rodriguez-Rivas F, Pastor A, Barriga C, Cruz-Yusta M, Sánchez L, Pavlovic I. Zn-Al layered double hydroxides as efficient photocatalysts for NOx abatement. Chem Eng J 2018;346:151–8. https://doi.org/10.1016/j.cej.2018.04.022.
[356] Geng Y, Chen D, Li N, Xu Q, Li H, He J, et al. Z-Scheme 2D/2D α-Fe2O3/g-C3N4 heterojunction for photocatalytic oxidation of nitric oxide. Appl Catal B Environ 2021;280. https://doi.org/10.1016/j.apcatb.2020.119409.
[357] Xie Y, Yu S, Zhong Y, Zhang Q, Zhou Y. SnO 2 /graphene quantum dots composited photocatalyst for efficient nitric oxide oxidation under visible light. Appl Surf Sci 2018;448:655–61. https://doi.org/10.1016/j.apsusc.2018.04.145.
[358] Zhang W, Zhang Q, Dong F. Visible-light photocatalytic removal of NO in air over BiOX (X = Cl, Br, I) single-crystal nanoplates prepared at room temperature. Ind Eng Chem Res 2013;52:6740–6. https://doi.org/10.1021/ie400615f.
[359] Luna M, Gatica JM, Vidal H, Mosquera MJ. Au-TiO2/SiO2 photocatalysts with NOx depolluting activity: Influence of gold particle size and loading. Chem Eng J 2019;368:417–27. https://doi.org/10.1016/j.cej.2019.02.167.
[360] Huang Y, Gao Y, Zhang Q, Zhang Y, Cao J ji, Ho W, et al. Biocompatible FeOOH-Carbon quantum dots nanocomposites for gaseous NOx removal under visible light: Improved charge separation and High selectivity. J Hazard Mater 2018;354:54–62. https://doi.org/10.1016/j.jhazmat.2018.04.071.
[361] Cui W, Li J, Sun Y, Wang H, Jiang G, Lee SC, et al. Enhancing ROS generation and suppressing toxic intermediate production in photocatalytic NO oxidation on O/Ba co-functionalized amorphous carbon nitride. Appl Catal B Environ 2018;237:938–46. https://doi.org/10.1016/j.apcatb.2018.06.071.
[362] Irfan M, Sevim M, Koçak Y, Balci M, Metin Ö, Ozensoy E. Enhanced photocatalytic NOx oxidation and storage under visible-light irradiation by anchoring Fe3O4 nanoparticles on mesoporous graphitic carbon nitride (mpg-C3N4). Appl Catal B Environ 2019;249:126–37. https://doi.org/10.1016/j.apcatb.2019.02.067.
[363] Wang B, Chen D, Li N, Xu Q, Li H, He J, et al. Enhanced Photocatalytic Oxidation of Nitric Oxide to MOF-derived Hollow Bimetallic Oxide Microcubes Supported on g-C3N4Nanosheets via p-n Heterojunction. Ind Eng Chem Res 2021;60:2921–30. https://doi.org/10.1021/acs.iecr.0c05834.
[364] Zhang G, Zhu X, Chen D, Li N, Xu Q, Li H, et al. Hierarchical: Z-scheme g-C3N4/Au/ZnIn2S4 photocatalyst for highly enhanced visible-light photocatalytic nitric oxide removal and carbon dioxide conversion. Environ Sci Nano 2020;7:676–87. https://doi.org/10.1039/c9en01325c.
[365] Li Y, Sun Y, Ho W, Zhang Y, Huang H, Cai Q, et al. Highly enhanced visible-light photocatalytic NOx purification and conversion pathway on self-structurally modified g-C3N4 nanosheets. Sci Bull 2018;63:609–20. https://doi.org/10.1016/j.scib.2018.04.009.
[366] Liu D, Chen D, Li N, Xu Q, Li H, He J, et al. Integration of 3D macroscopic graphene aerogel with 0D-2D AgVO3-g-C3N4 heterojunction for highly efficient photocatalytic oxidation of nitric oxide. Appl Catal B Environ 2019;243:576–84. https://doi.org/10.1016/j.apcatb.2018.11.012.
[367] Zhang R, Ran T, Cao Y, Ye L, Dong F, Zhang Q, et al. Oxygen activation of noble-

metal-free g-C3N4/α-Ni(OH)2 to control the toxic byproduct of photocatalytic nitric oxide removal. Chem Eng J 2020;382. https://doi.org/10.1016/j.cej.2019.123029.
[368] Dong G, Yang L, Wang F, Zang L, Wang C. Removal of Nitric Oxide through Visible Light Photocatalysis by g-C3N4 Modified with Perylene Imides. ACS Catal 2016;6:6511–9. https://doi.org/10.1021/acscatal.6b01657.
[369] Duan L, Li G, Zhang S, Wang H, Zhao Y, Zhang Y. Preparation of S-doped g-C3N4 with C vacancies using the desulfurized waste liquid extracting salt and its application for NOx removal. Chem Eng J 2021;411. https://doi.org/10.1016/j.cej.2021.128551.
[370] Dong G, Ho W, Zhang L. Photocatalytic NO removal on BiOI surface: The change from nonselective oxidation to selective oxidation. Appl Catal B Environ 2015;168–169:490–6. https://doi.org/10.1016/j.apcatb.2015.01.014.
[371] Li H, Shang H, Li Y, Cao X, Yang Z, Ai Z, et al. Interfacial Charging-Decharging Strategy for Efficient and Selective Aerobic NO Oxidation on Oxygen Vacancy. Environ Sci Technol 2019;53:6964–71. https://doi.org/10.1021/acs.est.9b01287.
[372] Liu D, Chen D, Li N, Xu Q, Li H, He J, et al. Surface Engineering of g-C3N4 by Stacked BiOBr Sheets Rich in Oxygen Vacancies for Boosting Photocatalytic Performance. Angew Chemie - Int Ed 2020;59:4519–24. https://doi.org/10.1002/anie.201914949.
[373] Li K, Cui W, Li J, Sun Y, Chu Y, Jiang G, et al. Tuning the reaction pathway of photocatalytic NO oxidation process to control the secondary pollution on monodisperse Au nanoparticles@g-C3N4. Chem Eng J 2019;378. https://doi.org/10.1016/j.cej.2019.122184.
[374] Ohko Y, Noguchi H, Nakamura Y, Negishi N, Takeuchi K. Highly selective photocatalytic reduction of NO2 in air to NO using Cu2+-loaded TiO2 thin films. J Photochem Photobiol A Chem 2009;206:27–31. https://doi.org/10.1016/j.jphotochem.2009.05.008.
[375] Liao L, Heylen S, Sree SP, Vallaey B, Keulemans M, Lenaerts S, et al. Photocatalysis assisted simultaneous carbon oxidation and NOx reduction. Appl Catal B Environ 2017;202:381–7. https://doi.org/10.1016/j.apcatb.2016.09.042.
[376] Bowering N, Walker GS, Harrison PG. Photocatalytic decomposition and reduction reactions of nitric oxide over Degussa P25. Appl Catal B Environ 2006;62:208–16. https://doi.org/10.1016/j.apcatb.2005.07.014.
[377] Nguyen NH, Wu HY, Bai H. Photocatalytic reduction of NO2 and CO2 using molybdenum-doped titania nanotubes. Chem Eng J 2015;269:60–6. https://doi.org/10.1016/j.cej.2015.01.099.
[378] Subbotina IR, Shelimov BN, Kazansky VB, Lisachenko AA, Che M, Coluccia S. Selective photocatalytic reduction of nitric oxide by carbon monoxide over silica-supported molybdenum oxide catalysts. J Catal 1999;184:390–5. https://doi.org/10.1006/jcat.1999.2436.
[379] Yu JCC, Nguyen VH, Lasek J, Wu JCS. Titania nanosheet photocatalysts with dominantly exposed (001) reactive facets for photocatalytic NOx abatement. Appl Catal B Environ 2017;219:391–400. https://doi.org/10.1016/j.apcatb.2017.07.077.
[380] Yamamoto A, Teramura K, Hosokawa S, Shishido T, Tanaka T. Visible-Light-Assisted Selective Catalytic Reduction of Nitric Oxide with Ammonia over Dye-Modified Titania Photocatalysts. ChemCatChem 2015;7:1818–25. https://doi.org/10.1002/cctc.201500207.
[381] Li X, Wang Z, Shi H, Dai D, Zuo S, Yao C, et al. Full spectrum driven SCR removal of NO over hierarchical CeVO4/attapulgite nanocomposite with high resistance to SO2 and H2O. J Hazard Mater 2020;386. https://doi.org/10.1016/j.jhazmat.2019.121977.
[382] Jin R, Wu Z, Liu Y, Jiang B, Wang H. Photocatalytic reduction of NO with NH3 using Si-doped TiO2 prepared by hydrothermal method. J Hazard Mater 2009;161:42–8. https://doi.org/10.1016/j.jhazmat.2008.03.041.
[383] Li X, Wang Z, Chu X, Gao B, Zuo S, Liu W, et al. Broad spectrum photo-driven selective catalytic reduction of NO over CeO2-CeVO4/palygorskite nanocomposite with enhanced SO2 tolerance. Appl Clay Sci 2020;199.

https://doi.org/10.1016/j.clay.2020.105871.
[384] Li X, Shi H, Zhu W, Zuo S, Lu X, Luo S, et al. Nanocomposite LaFe1-xNixO3 /Palygorskite catalyst for photo-assisted reduction of NOx: Effect of Ni doping. Appl Catal B Environ 2018;231:92–100. https://doi.org/10.1016/j.apcatb.2018.03.008.
[385] Li X, Shi H, Yan X, Zuo S, Zhang Y, Wang T, et al. Palygorskite Immobilized Direct Z-Scheme Nitrogen-Doped Carbon Quantum dots/PrFeO3 for Photo-SCR Removal of NOx. ACS Sustain Chem Eng 2018;6:10616–27. https://doi.org/10.1021/acssuschemeng.8b01956.
[386] Li X, Zhang H, Lü H, Zuo S, Zhang Y, Yao C. Photo-assisted SCR removal of NO by upconversion ceo2/pr3+/attapulgite nanocatalyst. Environ Sci Pollut Res 2019;26:12842–50. https://doi.org/10.1007/s11356-019-04802-1.
[387] Li X, Yan X, Lu X, Zuo S, Li Z, Yao C, et al. Photo-assisted selective catalytic reduction of NO by Z-scheme natural clay based photocatalyst: Insight into the effect of graphene coupling. J Catal 2018;357:59–68. https://doi.org/10.1016/j.jcat.2017.10.024.
[388] Li X, Shi H, Yan X, Zuo S, Zhang Y, Chen Q, et al. Rational construction of direct Z-scheme doped perovskite/palygorskite nanocatalyst for photo-SCR removal of NO: Insight into the effect of Ce incorporation. J Catal 2019;369:190–200. https://doi.org/10.1016/j.jcat.2018.11.009.
[389] Li X, Shi H, Wang T, Zhang Y, Lu X, Zuo S, et al. Visible light driven Z-scheme Fe2O3/SmFeO3/palygorskite nanostructure for photo-SCR of NOx. J Taiwan Inst Chem Eng 2018;89:119–28. https://doi.org/10.1016/j.jtice.2018.04.027.
[390] Yamamoto A, Mizuno Y, Teramura K, Hosokawa S, Shishido T, Tanaka T. Visible-light-assisted selective catalytic reduction of NO with NH3 on porphyrin derivative-modified TiO2 photocatalysts. Catal Sci Technol 2015;5:556–61. https://doi.org/10.1039/c4cy00598h.
[391] Yamazoe S, Masutani Y, Teramura K, Hitomi Y, Shishido T, Tanaka T. Promotion effect of tungsten oxide on photo-assisted selective catalytic reduction of NO with NH3 over TiO2. Appl Catal B Environ 2008;83:123–30. https://doi.org/10.1016/j.apcatb.2008.01.032.
[392] Yamamoto A, Mizuno Y, Teramura K, Shishido T, Tanaka T. Effects of reaction temperature on the photocatalytic activity of photo-SCR of NO with NH3 over a TiO2 photocatalyst. Catal Sci Technol 2013;3:1771–5. https://doi.org/10.1039/c3cy00022b.
[393] Teramura K, Tanaka T, Yamazoe S, Arakaki K, Funabiki T. Kinetic study of photo-SCR with NH3 over TiO2. Appl Catal B Environ 2004;53:29–36. https://doi.org/10.1016/j.apcatb.2004.05.005.
[394] Li X, Yan X, Zuo S, Lu X, Luo S, Li Z, et al. Construction of LaFe1−xMnxO3/attapulgite nanocomposite for photo-SCR of NOx at low temperature. Chem Eng J 2017;320:211–21. https://doi.org/10.1016/j.cej.2017.03.035.
[395] Su IH, Wu JCS. Photo selective catalytic reduction of nitric oxide with propane at room temperature. Catal Commun 2009;10:1534–7. https://doi.org/10.1016/j.catcom.2009.04.010.
[396] Maggos T, Bartzis JG, Leva P, Kotzias D. Application of photocatalytic technology for NOx removal. Appl Phys A Mater Sci Process 2007;89:81–4. https://doi.org/10.1007/s00339-007-4033-6.
[397] Yu JCC, Nguyen VH, Lasek J, Chiang SW, Li DX, Wu JCS. NOx abatement from stationary emission sources by photo-assisted SCR: Lab-scale to pilot-scale studies. Appl Catal A Gen 2016;523:294–303. https://doi.org/10.1016/j.apcata.2016.06.020.
[398] Kim YK, Hong SJ, Kim HB, Lee SW. Evaluation of in-situ NOx removal efficiency of photocatalytic concrete in expressways. KSCE J Civ Eng 2018;22:2274–80. https://doi.org/10.1007/s12205-017-0028-9.
[399] Rijkswaterstaat Centre for Transport and Navigation Air Quality Innovation Programme. Dutch Air Quality Innovation Programme. Innov Progr Air Qual 2011.
[400] Folli A, Strøm M, Madsen TP, Henriksen T, Lang J, Emenius J, et al. Field study of air purifying paving elements containing TiO2. Atmos Environ 2015;107:44–51. https://doi.org/10.1016/j.atmosenv.2015.02.025.

[401] Ballari MM, Brouwers HJH. Full scale demonstration of air-purifying pavement. J Hazard Mater 2013;254–255:406–14. https://doi.org/10.1016/j.jhazmat.2013.02.012.
[402] Gallus M, Akylas V, Barmpas F, Beeldens A, Boonen E, Boréave A, et al. Photocatalytic de-pollution in the Leopold II tunnel in Brussels: NOx abatement results. Build Environ 2015;84:125–33. https://doi.org/10.1016/j.buildenv.2014.10.032.
[403] Maggos T, Bartzis JG, Liakou M, Gobin C. Photocatalytic degradation of NOx gases using TiO2-containing paint: A real scale study. J Hazard Mater 2007;146:668–73. https://doi.org/10.1016/j.jhazmat.2007.04.079.
[404] Guerrini GL. Photocatalytic performances in a city tunnel in Rome: NOx monitoring results. Constr Build Mater 2012;27:165–75. https://doi.org/10.1016/j.conbuildmat.2011.07.065.
[405] Gallus M, Ciuraru R, Mothes F, Akylas V, Barmpas F, Beeldens A, et al. Photocatalytic abatement results from a model street canyon. Environ Sci Pollut Res 2015;22:18185–96. https://doi.org/10.1007/s11356-015-4926-4.
[406] Jiménez-Relinque E, Hingorani R, Rubiano F, Grande M, Castillo Á, Castellote M. In situ evaluation of the NOx removal efficiency of photocatalytic pavements: statistical analysis of the relevance of exposure time and environmental variables. Environ Sci Pollut Res 2019;26:36088–95. https://doi.org/10.1007/s11356-019-04322-y.
[407] Cordero JM, Hingorani R, Jimenez-Relinque E, Grande M, Borge R, Narros A, et al. NOx removal efficiency of urban photocatalytic pavements at pilot scale. Sci Total Environ 2020;719. https://doi.org/10.1016/j.scitotenv.2020.137459.
[408] Fan W, Chan KY, Zhang C, Zhang K, Ning Z, Leung MKH. Solar photocatalytic asphalt for removal of vehicular NOx: A feasibility study. Appl Energy 2018;225:535–41. https://doi.org/10.1016/j.apenergy.2018.04.134.
[409] Lee M, Koziel JA, Murphy W, Jenks WS, Chen B, Li P, et al. Evaluation of TiO2 based photocatalytic treatment of odor and gaseous emissions from swine manure with UV-A and UV-C. Animals 2021;11. https://doi.org/10.3390/ani11051289.
[410] Fernández-Pampillón J, Palacios M, Núñez L, Pujadas M, Sanchez B, Santiago JL, et al. NOx depolluting performance of photocatalytic materials in an urban area – Part I: Monitoring ambient impact. Atmos Environ 2021;251. https://doi.org/10.1016/j.atmosenv.2021.118190.
[411] Si H, Zhou M, Fang Y, He J, Yang L, Wang F. Photocatalytic concrete for NOx degradation: Influence factors and durability. Constr Build Mater 2021;298. https://doi.org/10.1016/j.conbuildmat.2021.123835.
[412] Jensen H, Pedersen PD. Real-life Field Studies of the NOx Removing Properties of Photocatalytic Surfaces in Roskilde and Copenhagen Airport, Denmark. J Photocatal 2020;2:71–81. https://doi.org/10.2174/2665976x01999200811155905.
[413] Gondal MA, Hameed A, Yamani ZH, Arfaj A. Photocatalytic transformation of methane into methanol under UV laser irradiation over WO3, TiO2 and NiO catalysts. Chem Phys Lett 2004;392:372–7. https://doi.org/10.1016/j.cplett.2004.05.092.
[414] Wu S, Tan X, Lei J, Chen H, Wang L, Zhang J. Ga-Doped and Pt-Loaded Porous TiO2-SiO2 for Photocatalytic Nonoxidative Coupling of Methane. J Am Chem Soc 2019;141:6592–600. https://doi.org/10.1021/jacs.8b13858.
[415] Yu L, Shao Y, Li D. Direct combination of hydrogen evolution from water and methane conversion in a photocatalytic system over Pt/TiO2. Appl Catal B Environ 2017;204:216–23. https://doi.org/10.1016/j.apcatb.2016.11.039.
[416] Yoshida H, Hirao K, Nishimoto JI, Shimura K, Kato S, Itoh H, et al. Hydrogen production from methane and water on platinum loaded titanium oxide photocatalysts. J Phys Chem C 2008;112:5542–51. https://doi.org/10.1021/jp077314u.
[417] Song H, Meng X, Wang ZJ, Wang Z, Chen H, Weng Y, et al. Visible-Light-Mediated Methane Activation for Steam Methane Reforming under Mild Conditions: A Case Study of Rh/TiO2 Catalysts. ACS Catal 2018;8:7556–65. https://doi.org/10.1021/acscatal.8b01787.
[418] Yoshida H, Matsushita N, Kato Y, Hattori T. Synergistic active sites on SiO2-Al2O3-TiO2 photocatalysts for direct methane coupling. J Phys Chem B 2003;107:8355–62.

https://doi.org/10.1021/jp034458+.
[419] Yoshida H, Kato S, Hirao K, Nishimoto JI, Hattori T. Photocatalytic steam reforming of methane over platinum-loaded semiconductors for hydrogen production. Chem Lett 2007;36:430–1. https://doi.org/10.1246/cl.2007.430.
[420] Yu L, Li D. Photocatalytic methane conversion coupled with hydrogen evolution from water over Pd/TiO2. Catal Sci Technol 2017;7:635–40. https://doi.org/10.1039/c6cy02435a.
[421] Yu X, Zholobenko VL, Moldovan S, Hu D, Wu D, Ordomsky V V., et al. Stoichiometric methane conversion to ethane using photochemical looping at ambient temperature. Nat Energy 2020;5:511–9. https://doi.org/10.1038/s41560-020-0616-7.
[422] Kato Y, Matsushita N, Yoshida H, Hattori T. Highly active silica-alumina-titania catalyst for photoinduced non-oxidative methane coupling. Catal Commun 2002;3:99–103. https://doi.org/10.1016/S1566-7367(02)00056-0.
[423] Han B, Wei W, Li M, Sun K, Hu YH. A thermo-photo hybrid process for steam reforming of methane: Highly efficient visible light photocatalysis. Chem Commun 2019;55:7816–9. https://doi.org/10.1039/c9cc04193a.
[424] Khan AA, Tahir M, Bafaqeer A. Constructing a Stable 2D Layered Ti3C2MXene Cocatalyst-Assisted TiO2/g-C3N4/Ti3C2Heterojunction for Tailoring Photocatalytic Bireforming of Methane under Visible Light. Energy and Fuels 2020;34:9810–28. https://doi.org/10.1021/acs.energyfuels.0c01354.
[425] Ayodele BV, Ghazali AA, Mohd Yassin MY, Abdullah S. Optimization of hydrogen production by photocatalytic steam methane reforming over lanthanum modified Titanium (IV) oxide using response surface methodology. Int J Hydrogen Energy 2019:20700–10. https://doi.org/10.1016/j.ijhydene.2018.06.185.
[426] Zeng Y, Liu HC, Wang JS, Wu XY, Wang SL. Synergistic photocatalysis-Fenton reaction for selective conversion of methane to methanol at room temperature. Catal Sci Technol 2020;10:2329–32. https://doi.org/10.1039/d0cy00028k.
[427] Lang J, Ma Y, Wu X, Jiang Y, Hu YH. Highly efficient light-driven methane coupling under ambient conditions based on an integrated design of a photocatalytic system. Green Chem 2020;22:4669–75. https://doi.org/10.1039/d0gc01608j.
[428] Tian X, Huang S, Wang L, Li L, Lou Z, Huang S, et al. Mitigation of low methane content landfill gas through visible-near-infrared photocatalysis over Y 2 O 3 :Er 3+ /Graphene/TiO 2. Appl Surf Sci 2018;456:854–60. https://doi.org/10.1016/j.apsusc.2018.06.138.
[429] Li X, Xie J, Rao H, Wang C, Tang J. Platinum- and CuOx-Decorated TiO2 Photocatalyst for Oxidative Coupling of Methane to C2 Hydrocarbons in a Flow Reactor. Angew Chemie - Int Ed 2020;59:19702–7. https://doi.org/10.1002/anie.202007557.
[430] Tahir B, Tahir M, Amin NAS. Photoinduced Dry and Bireforming of Methane to Fuels over La-Modified TiO2 in Fixed-Bed and Monolith Reactors. Energy Technol 2020;8. https://doi.org/10.1002/ente.202000106.
[431] Song H, Meng X, Wang S, Zhou W, Song S, Kako T, et al. Selective Photo-oxidation of Methane to Methanol with Oxygen over Dual-Cocatalyst-Modified Titanium Dioxide. ACS Catal 2020;10:14318–26. https://doi.org/10.1021/acscatal.0c04329.
[432] Chen X, Li Y, Pan X, Cortie D, Huang X, Yi Z. Photocatalytic oxidation of methane over silver decorated zinc oxide nanocatalysts. Nat Commun 2016;7. https://doi.org/10.1038/ncomms12273.
[433] Zhu X, Liang X, Wang P, Dai Y, Huang B. Porous Ag-ZnO microspheres as efficient photocatalyst for methane and ethylene oxidation: Insight into the role of Ag particles. Appl Surf Sci 2018;456:493–500. https://doi.org/10.1016/j.apsusc.2018.06.127.
[434] Wada K, Yoshida K, Watanabe Y, Suzuki T. The selective photooxidation of methane and ethane with oxygen over zinc oxide and molybdena-loaded zinc oxide catalysts. J Chem Soc Chem Commun 1991:726–7. https://doi.org/10.1039/C39910000726.
[435] Li Z, Pan X, Yi Z. Photocatalytic oxidation of methane over CuO-decorated ZnO nanocatalysts. J Mater Chem A 2019;7:469–75. https://doi.org/10.1039/c8ta09592b.

[436] Meng L, Chen Z, Ma Z, He S, Hou Y, Li HH, et al. Gold plasmon-induced photocatalytic dehydrogenative coupling of methane to ethane on polar oxide surfaces. Energy Environ Sci 2018;11:294–8. https://doi.org/10.1039/c7ee02951a.
[437] Zhou W, Qiu X, Jiang Y, Fan Y, Wei S, Han D, et al. Highly selective aerobic oxidation of methane to methanol over gold decorated zinc oxide: Via photocatalysis. J Mater Chem A 2020;8:13277–84. https://doi.org/10.1039/d0ta02793f.
[438] Yang J, Xiao W, Chi X, Lu X, Hu S, Wu Z, et al. Solar-driven efficient methane catalytic oxidation over epitaxial ZnO/La0.8Sr0.2CoO3 heterojunctions. Appl Catal B Environ 2020;265:118469. https://doi.org/10.1016/j.apcatb.2019.118469.
[439] Souza JD, Souza VS, Scholten JD. Synthesis of Hybrid Zinc-Based Materials from Ionic Liquids: A Novel Route to Prepare Active Zn Catalysts for the Photoactivation of Water and Methane. ACS Sustain Chem Eng 2019;7:8090–8. https://doi.org/10.1021/acssuschemeng.8b04809.
[440] Li Z, Boda MA, Pan X, Yi Z. Photocatalytic Oxidation of Small Molecular Hydrocarbons over ZnO Nanostructures: The Difference between Methane and Ethylene and the Impact of Polar and Nonpolar Facets. ACS Sustain Chem Eng 2019;7:19042–9. https://doi.org/10.1021/acssuschemeng.9b04661.
[441] Murcia-López S, Villa K, Andreu T, Morante JR. Partial oxidation of methane to methanol using bismuth-based photocatalysts. ACS Catal 2014;4:3013–9. https://doi.org/10.1021/cs500821r.
[442] Murcia-López S, Villa K, Andreu T, Morante JR. Improved selectivity for partial oxidation of methane to methanol in the presence of nitrite ions and BiVO4 photocatalyst. Chem Commun 2015;51:7249–52. https://doi.org/10.1039/c5cc00978b.
[443] Zhu W, Shen M, Fan G, Yang A, Meyer JR, Ou Y, et al. Facet-Dependent Enhancement in the Activity of Bismuth Vanadate Microcrystals for the Photocatalytic Conversion of Methane to Methanol. ACS Appl Nano Mater 2018;1:6683–91. https://doi.org/10.1021/acsanm.8b01490.
[444] Zhou Y, Zhang L, Wang W. Direct functionalization of methane into ethanol over copper modified polymeric carbon nitride via photocatalysis. Nat Commun n.d. https://doi.org/10.1038/s41467-019-08454-0.
[445] Tahir B, Tahir M, Amin NAS. Ag-La loaded protonated carbon nitrides nanotubes (pCNNT) with improved charge separation in a monolithic honeycomb photoreactor for enhanced bireforming of methane (BRM) to fuels. Appl Catal B Environ 2019;248:167–83. https://doi.org/10.1016/j.apcatb.2019.01.076.
[446] Shi S, Sun Z, Bao C, Gao T, Hu YH. The special route toward conversion of methane to methanol on a fluffy metal-free carbon nitride photocatalyst in the presence of H2O2. Int J Energy Res 2020;44:2740–53. https://doi.org/10.1002/er.5088.
[447] Li Y, Li J, Zhang G, Wang K, Wu X. Selective Photocatalytic Oxidation of Low Concentration Methane over Graphitic Carbon Nitride-Decorated Tungsten Bronze Cesium. ACS Sustain Chem Eng 2019;7:4382–9. https://doi.org/10.1021/acssuschemeng.8b06270.
[448] Khan AA, Tahir M. Well-designed 2D/2D Ti3C2TA/R MXene coupled g-C3N4 heterojunction with in-situ growth of anatase/rutile TiO2 nucleates to boost photocatalytic dry-reforming of methane (DRM) for syngas production under visible light. Appl Catal B Environ 2021;285. https://doi.org/10.1016/j.apcatb.2020.119777.
[449] Yang Z, Zhang Q, Ren L, Chen X, Wang D, Liu L, et al. Efficient photocatalytic conversion of CH4into ethanol with O2over nitrogen vacancy-rich carbon nitride at room temperature. Chem Commun 2021;57:871–4. https://doi.org/10.1039/d0cc07397k.
[450] Taylor CE, Noceti RP. New developments in the photocatalytic conversion of methane to methanol 2000;55:259–67.
[451] Taylor CE. Methane conversion via photocatalytic reactions 2003;84:9–15. https://doi.org/10.1016/S0920-5861(03)00295-5.
[452] Villa K, Murcia-López S, Andreu T, Morante JR. Mesoporous WO3 photocatalyst for the partial oxidation of methane to methanol using electron scavengers. Appl Catal B Environ 2015;163:150–5. https://doi.org/10.1016/j.apcatb.2014.07.055.

[453] Shimura K, Kato S, Yoshida T, Itoh H, Hattori T, Yoshida H. Photocatalytic steam reforming of methane over sodium tantalate. J Phys Chem C 2010;114:3493–503. https://doi.org/10.1021/jp902761x.
[454] Gondal MA, Hameed A, Suwaiyan A. Photo-catalytic conversion of methane into methanol using visible laser. Appl Catal A Gen 2003;243:165–74. https://doi.org/10.1016/S0926-860X(02)00562-8.
[455] Hameed A, Ismail IMI, Aslam M, Gondal MA. Applied Catalysis A : General Photocatalytic conversion of methane into methanol : Performance of silver impregnated WO 3. "Applied Catal A, Gen 2014;470:327–35. https://doi.org/10.1016/j.apcata.2013.10.045.
[456] Shimura K, Yoshida T, Yoshida H. Photocatalytic activation of water and methane over modified gallium oxide for hydrogen production. J Phys Chem C 2010;114:11466–74. https://doi.org/10.1021/jp1012126.
[457] Li L, Cai YY, Li GD, Mu XY, Wang KX, Chen JS. Synergistic effect on the photoactivation of the methane C-H bond over Ga 3+-modified ETS-10. Angew Chemie - Int Ed 2012;51:4702–6. https://doi.org/10.1002/anie.201200045.
[458] Sastre F, Fornés V, Corma A, García H. Selective, room-temperature transformation of methane to C1 oxygenates by deep UV photolysis over zeolites. J Am Chem Soc 2011;133:17257–61. https://doi.org/10.1021/ja204559z.
[459] Shimura K, Kawai H, Yoshida T, Yoshida H. Bifunctional rhodium cocatalysts for photocatalytic steam reforming of methane over alkaline titanate. ACS Catal 2012;2:2126–34. https://doi.org/10.1021/cs2006229.
[460] Kato Y, Yoshida H, Satsuma A, Hattori T. Photoinduced non-oxidative coupling of methane over H-zeolites around room temperature. Microporous Mesoporous Mater 2002;51:223–31. https://doi.org/10.1016/S1387-1811(02)00268-8.
[461] Yuliati L, Tsubota M, Satsuma A, Itoh H, Yoshida H. Photoactive sites on pure silica materials for nonoxidative direct methane coupling. J Catal 2006;238:214–20. https://doi.org/10.1016/j.jcat.2005.12.002.
[462] Yoshida H, Chaskar MG, Kato Y, Hattori T. Active sites on silica-supported zirconium oxide for photoinduced direct methane conversion and photoluminescence. J Photochem Photobiol A Chem 2003;160:47–53. https://doi.org/10.1016/S1010-6030(03)00220-X.
[463] Villa K, Murcia-López S, Andreu T, Morante JR. On the role of WO3 surface hydroxyl groups for the photocatalytic partial oxidation of methane to methanol. Catal Commun 2015;58:200–3. https://doi.org/10.1016/j.catcom.2014.09.025.
[464] Hu Y, Nagai Y, Rahmawaty D, Wei C, Anpo M. Characteristics of the photocatalytic oxidation of methane into methanol on V-containing MCM-41 catalysts. Catal Letters 2008;124:80–4. https://doi.org/10.1007/s10562-008-9491-8.
[465] Yuliati L, Hamajima T, Hattori T, Yoshida H. Highly dispersed Ce(III) species on silica and alumina as new photocatalysts for non-oxidative direct methane coupling. Chem Commun 2005:4824–6. https://doi.org/10.1039/b507698f.
[466] López HH, Martínez A. Selective photo-assisted oxidation of methane into formaldehyde on mesoporous VOx/SBA-15 catalysts. Catal Letters 2002;83:37–41. https://doi.org/10.1023/A:1020649313699.
[467] Hu Y, Anpo M, Wei C. Effect of the local structures of v-oxides in MCM-41 on the photocatalytic properties for the partial oxidation of methane to methanol. J Photochem Photobiol A Chem 2013;264:48–55. https://doi.org/10.1016/j.jphotochem.2013.05.005.
[468] Yamamoto A, Mizuba S, Saeki Y, Yoshida H. Platinum loaded sodium tantalate photocatalysts prepared by a flux method for photocatalytic steam reforming of methane. Appl Catal A Gen 2016;521:125–32. https://doi.org/10.1016/j.apcata.2015.10.031.
[469] Pan X, Chen X, Yi Z. Photocatalytic oxidation of methane over SrCO3 decorated SrTiO3 nanocatalysts via a synergistic effect. Phys Chem Chem Phys 2016;18:31400–9. https://doi.org/10.1039/c6cp04604e.
[470] Li L, Li GD, Yan C, Mu XY, Pan XL, Zou XX, et al. Efficient sunlight-driven dehydrogenative coupling of methane to ethane over a Zn+-modified zeolite. Angew Chemie - Int Ed 2011;50:8299–303. https://doi.org/10.1002/anie.201102320.

[471] Zhou L, Martirez JMP, Finzel J, Zhang C, Swearer DF, Tian S, et al. Light-driven methane dry reforming with single atomic site antenna-reactor plasmonic photocatalysts. Nat Energy 2020;5:61–70. https://doi.org/10.1038/s41560-019-0517-9.
[472] Shimura K, Yoshida H. Hydrogen production from water and methane over Pt-loaded calcium titanate photocatalyst. Energy Environ Sci 2010;3:615–7. https://doi.org/10.1039/b922793h.
[473] Wada K, Yamada H, Watanabe Y, Mitsudo TA. Selective photo-assisted catalytic oxidation of methane and ethane to oxygenates using supported vanadium oxide catalysts. J Chem Soc - Faraday Trans 1998;94:1771–8. https://doi.org/10.1039/a800938d.
[474] Yuliati L, Hattori T, Itoh H, Yoshida H. Photocatalytic nonoxidative coupling of methane on gallium oxide and silica-supported gallium oxide. J Catal 2008;257:396–402. https://doi.org/10.1016/j.jcat.2008.05.022.
[475] Yuliati L, Hattori T, Yoshida H. Highly dispersed magnesium oxide species on silica as photoactive sites for photoinduced direct methane coupling and photoluminescence. Phys Chem Chem Phys 2005;7:195–201. https://doi.org/10.1039/b410089a.
[476] Yoshida H, Matsushita N, Kato Y, Hattori T. Active sites in sol-gel prepared silica-alumina for photoinduced non-oxidative methane coupling. Phys Chem Chem Phys 2002;4:2459–65. https://doi.org/10.1039/b111101a.
[477] Chung WC, Tsao IY, Chang MB. Novel plasma photocatalysis process for syngas generation via dry reforming of methane. Energy Convers Manag 2018;164:417–28. https://doi.org/10.1016/j.enconman.2018.03.024.
[478] Yuliati L, Hamajima T, Hattori T, Yoshida H. Nonoxidative coupling of methane over supported ceria photocatalysts. J Phys Chem C 2008;112:7223–32. https://doi.org/10.1021/jp712029w.
[479] Yang J, Hao J, Wei J, Dai J, Li Y. Visible-light-driven selective oxidation of methane to methanol on amorphous FeOOH coupled m-WO 3. Fuel 2020;266:117104. https://doi.org/10.1016/j.fuel.2020.117104.
[480] Wibowo S, Yamaguchi A, Shoji S, Fujita T, Abe H, Miyauchi M. Photo-assisted dry reforming of methane over strontium titanate. Chem Lett 2018;47:935–7. https://doi.org/10.1246/cl.180347.
[481] Takami D, Ito Y, Kawaharasaki S, Yamamoto A, Yoshida H. Low temperature dry reforming of methane over plasmonic Ni photocatalysts under visible light irradiation. Sustain Energy Fuels 2019;3:2968–71. https://doi.org/10.1039/c9se00206e.
[482] Cho Y, Shoji S, Yamaguchi A, Hoshina T, Fujita T, Abe H, et al. Visible-light-driven dry reforming of methane using a semiconductor-supported catalyst. Chem Commun 2020;56:4611–4. https://doi.org/10.1039/d0cc00729c.
[483] Jiang H, Peng X, Yamaguchi A, Ueda S, Fujita T, Abe H, et al. Photocatalytic Partial Oxidation of Methane on Palladium-Loaded Strontium Tantalate. Sol RRL 2019;3. https://doi.org/10.1002/solr.201900076.
[484] Wei J, Yang J, Wen Z, Dai J, Li Y, Yao B. Efficient photocatalytic oxidation of methane over β-Ga2O3/activated carbon composites. RSC Adv 2017;7:37508–21. https://doi.org/10.1039/c7ra05692c.
[485] Amano F, Akamoto C, Ishimaru M, Inagaki S, Yoshida H. Pressure-induced dehydrogenative coupling of methane to ethane by platinum-loaded gallium oxide photocatalyst. Chem Commun 2020;56:6348–51. https://doi.org/10.1039/d0cc01730b.
[486] Wei S, Zhu X, Zhang P, Fan Y, Sun Z, Zhao X, et al. Aerobic oxidation of methane to formaldehyde mediated by crystal-O over gold modified tungsten trioxide via photocatalysis. Appl Catal B Environ 2021;283. https://doi.org/10.1016/j.apcatb.2020.119661.
[487] Yoshida H, Mizuba S, Yamamoto A. Preparation of sodium hexatitanate photocatalysts by a flux method for photocatalytic steam reforming of methane. Catal Today 2019;334:30–6. https://doi.org/10.1016/j.cattod.2019.02.055.
[488] Du J, Chen W, Wu G, Song Y, Dong X, Li G, et al. Evoked methane photocatalytic conversion to C2 oxygenates over ceria with oxygen vacancy. Catalysts 2020;10.

https://doi.org/10.3390/catal10020196.
[489] Jiang H, Peng X, Yamaguchi A, Fujita T, Abe H, Miyauchi M. Synergistic photothermal and photochemical partial oxidation of methane over noble metals incorporated in mesoporous silica. Chem Commun 2019;55:13765–8. https://doi.org/10.1039/c9cc06170c.
[490] Wu XY, Tang Z, Zhao X, Luo X, John Pennycook S, Wang SL. Visible-light driven room-temperature coupling of methane to ethane by atomically dispersed Au on WO3. J Energy Chem 2021;61:195–202. https://doi.org/10.1016/j.jechem.2021.03.029.
[491] Takami D, Yamamoto A, Yoshida H. Dry reforming of methane over alumina-supported rhodium catalysts at low temperatures under visible and near-infrared light. Catal Sci Technol 2020;10:5811–4. https://doi.org/10.1039/d0cy00858c.
[492] Tan B, Ye Y, Huang Z, Ye L, Ma M, Zhou Y. Promotion of photocatalytic steam reforming of methane over Ag0/Ag+-SrTiO3. Chinese Chem Lett 2020;31:1530–4. https://doi.org/10.1016/j.cclet.2019.11.007.
[493] Anzai A, Fujiwara K, Yamamoto A, Yoshida H. Platinum-loaded lanthanum-doped calcium titanate photocatalysts prepared by a flux method for photocatalytic steam reforming of methane. Catal Today 2020;352:1–9. https://doi.org/10.1016/j.cattod.2020.02.027.
[494] Kataoka S, Lee E, Tejedor-Tejedor MI, Anderson MA. Photocatalytic degradation of hydrogen sulfide and in situ FT-IR analysis of reaction products on surface of TiO2. Appl Catal B Environ 2005;61:159–63. https://doi.org/10.1016/j.apcatb.2005.04.018.
[495] Portela R, Canela MC, Sánchez B, Marques FC, Stumbo AM, Tessinari RF, et al. H2S photodegradation by TiO2/M-MCM-41 (M = Cr or Ce): Deactivation and by-product generation under UV-A and visible light. Appl Catal B Environ 2008;84:643–50. https://doi.org/10.1016/j.apcatb.2008.05.020.
[496] Sheng H, Chen D, Li N, Xu Q, Li H, He J, et al. Urchin-Inspired TiO2@MIL-101 Double-Shell Hollow Particles: Adsorption and Highly Efficient Photocatalytic Degradation of Hydrogen Sulfide. Chem Mater 2017;29:5612–6. https://doi.org/10.1021/acs.chemmater.7b01243.
[497] Alonso-Tellez A, Robert D, Keller N, Keller V. A parametric study of the UV-A photocatalytic oxidation of H 2S over TiO 2. Appl Catal B Environ 2012;115–116:209–18. https://doi.org/10.1016/j.apcatb.2011.12.014.
[498] Portela R, Suárez S, Rasmussen SB, Arconada N, Castro Y, Durán A, et al. Photocatalytic-based strategies for H2S elimination. Catal Today 2010;151:64–70. https://doi.org/10.1016/j.cattod.2010.03.056.
[499] Sopyan I. Kinetic analysis on photocatalytic degradation of gaseous acetaldehyde, ammonia and hydrogen sulfide on nanosized porous TiO2 films. Sci Technol Adv Mater 2007;8:33–9. https://doi.org/10.1016/j.stam.2006.10.004.
[500] Yu Y, Zhang T, Zheng L, Yu J. Photocatalytic degradation of hydrogen sulfide using TiO2 film under microwave electrodeless discharge lamp irradiation. Chem Eng J 2013;225:9–15. https://doi.org/10.1016/j.cej.2013.03.032.
[501] Hao X, Hou G, Zheng P, Liu R, Liu C. H2S in-situ removal from biogas using a tubular zeolite/TiO2 photocatalytic reactor and the improvement on methane production. Chem Eng J 2016;294:105–10. https://doi.org/10.1016/j.cej.2016.02.098.
[502] Brancher M, Franco D, de Melo Lisboa H. Photocatalytic oxidation of H2S in the gas phase over TiO2-coated glass fiber filter. Environ Technol (United Kingdom) 2016;37:2852–64. https://doi.org/10.1080/09593330.2016.1167250.
[503] Lee M, Wi J, Koziel JA, Ahn H, Li P, Chen B, et al. Effects of UV-A light treatment on ammonia, hydrogen sulfide, greenhouse gases, and ozone in simulated poultry barn conditions. Atmosphere (Basel) 2020;11. https://doi.org/10.3390/atmos11030283.
[504] Liu G, Ji J, Hu P, Lin S, Huang H. Efficient degradation of H 2 S over transition metal modified TiO 2 under VUV irradiation: Performance and mechanism. Appl Surf Sci 2018;433:329–35. https://doi.org/10.1016/j.apsusc.2017.09.257.
[505] Lee M, Li P, Koziel JA, Ahn H, Wi J, Chen B, et al. Pilot-Scale Testing of UV-A Light Treatment for Mitigation of NH3, H2S, GHGs, VOCs, Odor, and O3 Inside the Poultry

Barn. Front Chem 2020;8. https://doi.org/10.3389/fchem.2020.00613.
[506] Shahzad N, Azfar RW. Comparison of H2S gas destruction potential using TIO2 nanofibers and nanoparticles. Environ Sci Pollut Res 2017;24:1133–6. https://doi.org/10.1007/s11356-016-7644-7.
[507] Su JJ, Hong YY. Removal of hydrogen sulfide using a photocatalytic livestock biogas desulfurizer. Renew Energy 2020;149:181–8. https://doi.org/10.1016/j.renene.2019.12.068.
[508] Vu THT, Au HT, Nguyen TTT, Do MH, Pham MT, Bui DH, et al. Synthesis of carbon nanotube/titanate nanotube composites with photocatalytic activity for H2S oxidation. J Sulfur Chem 2017;38:264–78. https://doi.org/10.1080/17415993.2016.1276182.
[509] Wang Z, Ci X, Dai H, Yin L, Shi H. One-step synthesis of highly active Ti-containing Cr-modified MCM-48 mesoporous material and the photocatalytic performance for decomposition of H 2 S under visible light. Appl Surf Sci 2012;258:8258–63. https://doi.org/10.1016/j.apsusc.2012.05.033.
[510] Portela R, Sánchez B, Coronado JM, Candal R, Suárez S. Selection of TiO2-support: UV-transparent alternatives and long-term use limitations for H2S removal. Catal Today 2007;129:223–30. https://doi.org/10.1016/j.cattod.2007.08.005.
[511] Wang D, Noguchi H, Kako T, Ye J. Photocatalytic activity of silver-loaded or unloaded titanium dioxide coating in the removal of hydrogen sulfide. Res Chem Intermed 2005;31:441–8. https://doi.org/10.1163/1568567053956545.
[512] Zhang G, Sheng H, Chen D, Li N, Xu Q, Li H, et al. Hierarchical Titanium Dioxide Nanowire/Metal–Organic Framework/Carbon Nanofiber Membranes for Highly Efficient Photocatalytic Degradation of Hydrogen Sulfide. Chem - A Eur J 2018;24:15019–25. https://doi.org/10.1002/chem.201802747.
[513] Li X, Zhang G, Pan H. Experimental study on ozone photolytic and photocatalytic degradation of H 2S using continuous flow mode. J Hazard Mater 2012;199–200:255–61. https://doi.org/10.1016/j.jhazmat.2011.11.006.
[514] Rasmussen SB, Portela R, Suárez S, Coronado JM, Rojas-Cervantes ML, Avila P, et al. Hybrid TiO2-SiMgOx composite for combined chemisorption and photocatalytic elimination of gaseous H2S. Ind Eng Chem Res 2010;49:6685–90. https://doi.org/10.1021/ie901733p.
[515] Custódio P, Lied EB, da Silva AV, Frare LM, Bittencourt PRS, de Oliveira Basso RL, et al. TiO2 coated fiber cement composites: Effect of the load of TiO2 particles on photocatalytic degradation of H2S. Constr Build Mater 2020;262. https://doi.org/10.1016/j.conbuildmat.2020.120379.
[516] Zakarina NA, Volkova LD, Kim OK, Brodskii AR, Latypov IF, Yaskevich VI, et al. Natural iron-containing materials and catalysts on their basis on use for photocatalytic decomposition of hydrogen sulfide. Pet Chem 2013;53:181–6. https://doi.org/10.1134/S0965544113030146.
[517] Cox RA, Sandalls FJ. The photo-oxidation of hydrogen sulphide and dimethyl sulphide in air. Atmos Environ 1974;8:1269–81. https://doi.org/10.1016/0004-6981(74)90006-7.
[518] Xia LY, Gu DH, Tan J, Dong WB, Hou HQ. Photolysis of low concentration H2S under UV/VUV irradiation emitted from microwave discharge electrodeless lamps. Chemosphere 2008;71:1774–80. https://doi.org/10.1016/j.chemosphere.2008.01.050.
[519] Xu J, Li C, Liu P, He D, Wang J, Zhang Q. Photolysis of low concentration H2S under UV/VUV irradiation emitted from high frequency discharge electrodeless lamps. Chemosphere 2014;109:202–7. https://doi.org/10.1016/j.chemosphere.2014.01.065.
[520] Yu Y, Zhang T, Zheng L, Yu J. Detection of reactive oxygen species generated by microwave electrodeless discharge lamp and application in photodegradation of H2S. Korean J Chem Eng 2013;30:1423–8. https://doi.org/10.1007/s11814-013-0074-z.
[521] Baldovi HG, Albero J, Ferrer B, Mateo D, Alvaro M, García H. Gas-Phase Photochemical Overall H2S Splitting by UV Light Irradiation. ChemSusChem 2017;10:1996–2000. https://doi.org/10.1002/cssc.201700294.
[522] Xu J hui, Sun X, Lv X mei, Li C lin, Liu P. Rapid photolysis of H2S and the mechanism using high-frequency discharge electrodeless lamp. Environ Technol (United Kingdom)

2020. https://doi.org/10.1080/09593330.2020.1756421.
[523] Xu JH, Ding B Bin, Lv XM, Lan SH, Li CL, Peng L. Mathematical modeling and mechanism of VUV photodegradation of H2S in the Absence of O2. Int J Photoenergy 2018;2018. https://doi.org/10.1155/2018/2769213.
[524] Bryukov MG, Vasilyak LM, Vasiliev AI, Kostyuchenko S V., Kudryavtsev NN. Low-Temperature Oxidation of Hydrogen Sulfide and Formaldehyde Pollutants in Humid Air by UV Radiation at 184.95 and 253.65 nm. J Phys Chem A 2020;124:7935–42. https://doi.org/10.1021/acs.jpca.0c06552.
[525] Cai Q, Wang F, He J, Dan M, Cao Y, Yu S, et al. Oxygen defect boosted photocatalytic hydrogen evolution from hydrogen sulfide over active {0 0 1} facet in anatase TiO2. Appl Surf Sci 2020;517. https://doi.org/10.1016/j.apsusc.2020.146198.
[526] Oladipo H, Garlisi C, Sa J, Lewin E, Al-Ali K, Palmisano G. Unveiling the role of bisulfide in the photocatalytic splitting of H2S in aqueous solutions. Appl Catal B Environ 2020;270. https://doi.org/10.1016/j.apcatb.2020.118886.
[527] Navakoteswara Rao V, Lakshmana Reddy N, Mamatha Kumari M, Ravi P, Sathish M, Kuruvilla KM, et al. Photocatalytic recovery of H2 from H2S containing wastewater: Surface and interface control of photo-excitons in Cu2S@TiO2 core-shell nanostructures. Appl Catal B Environ 2019;254:174–85. https://doi.org/10.1016/j.apcatb.2019.04.090.
[528] Xie Z, Yu S, Fan XB, Wei S, Yu L, Zhong Y, et al. Wavelength-sensitive photocatalytic H2 evolution from H2S splitting over g-C3N4 with S,N-codoped carbon dots as the photosensitizer. J Energy Chem 2021;52:234–42. https://doi.org/10.1016/j.jechem.2020.04.051.
[529] Yu S, Xie Z, Ran M, Wu F, Zhong Y, Dan M, et al. Zinc ions modified InP quantum dots for enhanced photocatalytic hydrogen evolution from hydrogen sulfide. J Colloid Interface Sci 2020;573:71–7. https://doi.org/10.1016/j.jcis.2020.03.110.
[530] Lashgari M, Ghanimati M. Pollutant photo-conversion strategy to produce hydrogen green fuel and valuable sulfur element using H2S feed and nanostructured alloy photocatalysts: Ni-dopant effect, energy diagram and photo-electrochemical characterization. Chem Eng Res Des 2020;162:85–93. https://doi.org/10.1016/j.cherd.2020.07.024.
[531] Yu S, Wu F, Zou P, Fan XB, Duan C, Dan M, et al. Highly value-added utilization of H2S in Na2SO3solution over Ca-CdS nanocrystal photocatalysts. Chem Commun 2020;56:14227–30. https://doi.org/10.1039/d0cc05894g.
[532] Li Y, Yu S, Doronkin DE, Wei S, Dan M, Wu F, et al. Highly dispersed PdS preferably anchored on In2S3 of MnS/In2S3 composite for effective and stable hydrogen production from H2S. J Catal 2019;373:48–57. https://doi.org/10.1016/j.jcat.2019.03.021.
[533] Lashgari M, Ghanimati M. A new efficient eco-friendly quaternary solid-solution nanoenergy material for photocatalytic hydrogen fuel production from H2S aqueous feed. Chem Eng J 2019;358:153–9. https://doi.org/10.1016/j.cej.2018.10.011.
[534] Muñoz I, Rieradevall J, Torrades F, Peral J, Domènech X. Environmental assessment of different advanced oxidation processes applied to a bleaching Kraft mill effluent. Chemosphere 2006;62:9–16. https://doi.org/10.1016/j.chemosphere.2005.04.044.
[535] Merayo N, Hermosilla D, Blanco L, Cortijo L, Blanco Á. Assessing the application of advanced oxidation processes, and their combination with biological treatment, to effluents from pulp and paper industry. J Hazard Mater 2013;262:420–7. https://doi.org/10.1016/j.jhazmat.2013.09.005.
[536] Balcioglu IA, Arslan I. Application of photocatalytic oxidation treatment to pretreated and raw effluents from the Kraft bleaching process and textile industry. Environ Pollut 1998;103:261–8. https://doi.org/10.1016/S0269-7491(98)00112-2.
[537] Amat AM, Arques A, López F, Miranda MA. Solar photo-catalysis to remove paper mill wastewater pollutants. Sol Energy 2005;79:393–401. https://doi.org/10.1016/j.solener.2005.02.021.
[538] Rodrigues AC, Boroski M, Shimada NS, Garcia JC, Nozaki J, Hioka N. Treatment of

paper pulp and paper mill wastewater by coagulation-flocculation followed by heterogeneous photocatalysis. J Photochem Photobiol A Chem 2008;194:1–10. https://doi.org/10.1016/j.jphotochem.2007.07.007.
[539] Yeber MC, Rodríguez J, Freer J, Baeza J, Durán N, Mansilla HD. Advanced oxidation of a pulp mill bleaching wastewater. Chemosphere 1999;39:1679–88. https://doi.org/10.1016/S0045-6535(99)00068-5.
[540] Villaseñor J, Mansilla HD. Effect of temperature on kraft black liquor degradation by ZnO-photoassisted catalysis. J Photochem Photobiol A Chem 1996;93:205–9. https://doi.org/10.1016/1010-6030(95)04179-6.
[541] Ksibi M, Amor S Ben, Cherif S, Elaloui E, Houas A, Elaloui M. Photodegradation of lignin from black liquor using a UV/TiO2 system. J Photochem Photobiol A Chem 2003;154:211–8. https://doi.org/10.1016/S1010-6030(02)00316-7.
[542] MacHado AEH, Furuyama AM, Falone SZ, Ruggiero R, Perez DDS, Castellan A. Photocatalytic degradation of lignin and lignin models, using titanium dioxide: The role of the hydroxyl radical. Chemosphere 2000;40:115–24. https://doi.org/10.1016/S0045-6535(99)00269-6.
[543] Raja P, Bozzi A, Mansilla H, Kiwi J. Evidence for superoxide-radical anion, singlet oxygen and OH-radical intervention during the degradation of the lignin model compound (3-methoxy-4-hydroxyphenylmethylcarbinol). J Photochem Photobiol A Chem 2005;169:271–8. https://doi.org/10.1016/j.jphotochem.2004.07.009.
[544] Ohnishi H, Matsumura M, Tsubomura H, Iwasaki M. Bleaching of Lignin Solution by a Photocatalyzed Reaction on Semiconductor Photocatalysts. Ind Eng Chem Res 1989;28:719–24. https://doi.org/10.1021/ie00090a012.
[545] Wu X, Fan X, Xie S, Lin J, Cheng J, Zhang Q, et al. Solar energy-driven lignin-first approach to full utilization of lignocellulosic biomass under mild conditions. Nat Catal 2018;1:772–80. https://doi.org/10.1038/s41929-018-0148-8.
[546] Carraro G, MacCato C, Gasparotto A, Montini T, Turner S, Lebedev OI, et al. Enhanced hydrogen production by photoreforming of renewable oxygenates through nanostructured Fe2O3 polymorphs. Adv Funct Mater 2014;24:372–8. https://doi.org/10.1002/adfm.201302043.
[547] Chen WT, Chan A, Al-Azri ZHN, Dosado AG, Nadeem MA, Sun-Waterhouse D, et al. Effect of TiO2 polymorph and alcohol sacrificial agent on the activity of Au/TiO2 photocatalysts for H2 production in alcohol-water mixtures. J Catal 2015;329:499–513. https://doi.org/10.1016/j.jcat.2015.06.014.
[548] Daskalaki VM, Panagiotopoulou P, Kondarides DI. Production of peroxide species in Pt/TiO2 suspensions under conditions of photocatalytic water splitting and glycerol photoreforming. Chem Eng J 2011;170:433–9. https://doi.org/10.1016/j.cej.2010.11.093.
[549] Xu D, Hai Y, Zhang X, Zhang S, He R. Bi 2 O 3 cocatalyst improving photocatalytic hydrogen evolution performance of TiO 2. Appl Surf Sci 2017;400:530–6. https://doi.org/10.1016/j.apsusc.2016.12.171.
[550] Chen Z, Savateev A, Pronkin S, Papaefthimiou V, Wolff C, Willinger MG, et al. "The Easier the Better" Preparation of Efficient Photocatalysts—Metastable Poly(heptazine imide) Salts. Adv Mater 2017;29. https://doi.org/10.1002/adma.201700555.
[551] Liu R, Yoshida H, Fujita S ichiro, Arai M. Photocatalytic hydrogen production from glycerol and water with NiOx/TiO2 catalysts. Appl Catal B Environ 2014;144:47–45. https://doi.org/10.1016/j.apcatb.2013.06.024.
[552] Reddy NL, Kumar S, Krishnan V, Sathish M, Shankar M V. Multifunctional Cu/Ag quantum dots on TiO2 nanotubes as highly efficient photocatalysts for enhanced solar hydrogen evolution. J Catal 2017;350:226–39. https://doi.org/10.1016/j.jcat.2017.02.032.
[553] Dosado AG, Chen WT, Chan A, Sun-Waterhouse D, Waterhouse GIN. Novel Au/TiO2 photocatalysts for hydrogen production in alcohol-water mixtures based on hydrogen titanate nanotube precursors. J Catal 2015;330:238–54. https://doi.org/10.1016/j.jcat.2015.07.014.
[554] Chang CJ, Lin YG, Weng HT, Wei YH. Photocatalytic hydrogen production from

glycerol solution at room temperature by ZnO-ZnS/graphene photocatalysts. Appl Surf Sci 2018;451:198–206. https://doi.org/10.1016/j.apsusc.2018.05.004.
[555] Chen WT, Chan A, Sun-Waterhouse D, Llorca J, Idriss H, Waterhouse GIN. Performance comparison of Ni/TiO2 and Au/TiO2 photocatalysts for H2 production in different alcohol-water mixtures. J Catal 2018;367:27–42. https://doi.org/10.1016/j.jcat.2018.08.015.
[556] Petala A, Ioannidou E, Georgaka A, Bourikas K, Kondarides DI. Hysteresis phenomena and rate fluctuations under conditions of glycerol photo-reforming reaction over CuOx/TiO2 catalysts. Appl Catal B Environ 2015;178:201–9. https://doi.org/10.1016/j.apcatb.2014.09.021.
[557] Fajrina N, Tahir M. 2D-montmorillonite-dispersed g-C 3 N 4 /TiO 2 2D/0Dnanocomposite for enhanced photo-induced H 2 evolution from glycerol-water mixture. Appl Surf Sci 2019;471:1053–64. https://doi.org/10.1016/j.apsusc.2018.12.076.
[558] Schünemann S, Dodekatos G, Tüysüz H. Mesoporous Silica Supported Au and AuCu Nanoparticles for Surface Plasmon Driven Glycerol Oxidation. Chem Mater 2015;27:7743–50. https://doi.org/10.1021/acs.chemmater.5b03520.
[559] Lucchetti R, Onotri L, Clarizia L, Natale F Di, Somma I Di, Andreozzi R, et al. Removal of nitrate and simultaneous hydrogen generation through photocatalytic reforming of glycerol over “in situ” prepared zero-valent nano copper/P25. Appl Catal B Environ 2017;202:539–49. https://doi.org/10.1016/j.apcatb.2016.09.043.
[560] Seadira TWP, Sadanandam G, Ntho T, Masuku CM, Scurrell MS. Preparation and characterization of metals supported on nanostructured TiO2 hollow spheres for production of hydrogen via photocatalytic reforming of glycerol. Appl Catal B Environ 2018;222:133–45. https://doi.org/10.1016/j.apcatb.2017.09.072.
[561] Maldonado MI, López-Martín A, Colón G, Peral J, Martínez-Costa JI, Malato S. Solar pilot plant scale hydrogen generation by irradiation of Cu/TiO2 composites in presence of sacrificial electron donors. Appl Catal B Environ 2018;229:15–23. https://doi.org/10.1016/j.apcatb.2018.02.005.
[562] Fu X, Wang X, Leung DYC, Gu Q, Chen S, Huang H. Photocatalytic reforming of C3-polyols for H2 production. Part (I). Role of their OH groups. Appl Catal B Environ 2011;106:681–8. https://doi.org/10.1016/j.apcatb.2011.05.045.
[563] Umer M, Tahir M, Azam MU, Jaffar MM. Metals free MWCNTs@TiO 2 @MMT heterojunction composite with MMT as a mediator for fast charges separation towards visible light driven photocatalytic hydrogen evolution. Appl Surf Sci 2019;463:747–57. https://doi.org/10.1016/j.apsusc.2018.08.240.
[564] Wang C, Cai X, Chen Y, Cheng Z, Luo X, Mo S, et al. Improved hydrogen production from glycerol photoreforming over sol-gel derived TiO2 coupled with metal oxides. Chem Eng J 2017;317:522–32. https://doi.org/10.1016/j.cej.2017.02.033.
[565] Lakshmana Reddy N, Cheralathan KK, Durga Kumari V, Neppolian B, Muthukonda Venkatakrishnan S. Photocatalytic Reforming of Biomass Derived Crude Glycerol in Water: A Sustainable Approach for Improved Hydrogen Generation Using Ni(OH)2 Decorated TiO2 Nanotubes under Solar Light Irradiation. ACS Sustain Chem Eng 2018;6:3754–64. https://doi.org/10.1021/acssuschemeng.7b04118.
[566] Sanwald KE, Berto TF, Eisenreich W, Gutiérrez OY, Lercher JA. Catalytic routes and oxidation mechanisms in photoreforming of polyols. J Catal 2016;344:806–16. https://doi.org/10.1016/j.jcat.2016.08.009.
[567] Crișan M, Zaharescu M, Kumari VD, Subrahmanyam M, Crian D, Drăgan N, et al. Sol-gel based alumina powders with catalytic applications. Appl Surf Sci 2011;258:448–55. https://doi.org/10.1016/j.apsusc.2011.08.104.
[568] Tahir M, Siraj M, Tahir B, Umer M, Alias H, Othman N. Au-NPs embedded Z–scheme WO3/TiO2 nanocomposite for plasmon-assisted photocatalytic glycerol-water reforming towards enhanced H2 evolution. Appl Surf Sci 2020;503. https://doi.org/10.1016/j.apsusc.2019.144344.
[569] Beltram A, Melchionna M, Montini T, Nasi L, Fornasiero P, Prato M. Making H2 from light and biomass-derived alcohols: The outstanding activity of newly designed

hierarchical MWCNT/Pd@TiO2 hybrid catalysts. Green Chem 2017;19:2379–89. https://doi.org/10.1039/c6gc01979j.
[570] Majeed I, Nadeem MA, Hussain E, Waterhouse GIN, Badshah A, Iqbal A, et al. On the Synergism between Cu and Ni for Photocatalytic Hydrogen Production and their Potential as Substitutes of Noble Metals. ChemCatChem 2016;8:3146–55. https://doi.org/10.1002/cctc.201600697.
[571] Mandari KK, Do JY, Police AKR, Kang M. Natural solar light-driven preparation of plasmonic resonance-based alloy and core-shell catalyst for sustainable enhanced hydrogen production: Green approach and characterization. Appl Catal B Environ 2018;231:137–50. https://doi.org/10.1016/j.apcatb.2018.03.015.
[572] Kondamudi N, Misra M, Banerjee S, Mohapatra S, Mohapatra S. Simultaneous production of glyceric acid and hydrogen from the photooxidation of crude glycerol using TiSi 2. Appl Catal B Environ 2012;126:180–5. https://doi.org/10.1016/j.apcatb.2012.05.006.
[573] Honda Y, Watanabe M, Hagiwara H, Ida S, Ishihara T. Inorganic/whole-cell biohybrid photocatalyst for highly efficient hydrogen production from water. Appl Catal B Environ 2017;210:400–6. https://doi.org/10.1016/j.apcatb.2017.04.015.
[574] Krivtsov I, Mitoraj D, Adler C, Ilkaeva M, Sardo M, Mafra L, et al. Water-Soluble Polymeric Carbon Nitride Colloidal Nanoparticles for Highly Selective Quasi-Homogeneous Photocatalysis. Angew Chemie - Int Ed 2020;59:487–95. https://doi.org/10.1002/anie.201913331.
[575] Liu J, Li Y, Liu H, He D. Photo-thermal synergistically catalytic conversion of glycerol and carbon dioxide to glycerol carbonate over Au/ZnWO4-ZnO catalysts. Appl Catal B Environ 2019;244:836–43. https://doi.org/10.1016/j.apcatb.2018.12.018.
[576] Gombac V, Montini T, Falqui A, Loche D, Prato M, Genovese A, et al. From: Trash to resource: Recovered-Pd from spent three-way catalysts as a precursor of an effective photo-catalyst for H2 production. Green Chem 2016;18:2745–52. https://doi.org/10.1039/c5gc02908b.
[577] Guo L, Sun Q, Marcus K, Hao Y, Deng J, Bi K, et al. Photocatalytic glycerol oxidation on AuxCu-CuS@TiO2 plasmonic heterostructures. J Mater Chem A 2018;6:22005–12. https://doi.org/10.1039/c8ta02170h.
[578] Tahir B, Tahir M. Morphological effect of 1D/1D In2O3/TiO2 NRs/NWs heterojunction photo-embedded with Cu-NPs for enhanced photocatalytic H2 evolution under visible light. Appl Surf Sci 2020;506. https://doi.org/10.1016/j.apsusc.2019.145034.
[579] Sanwald KE, Berto TF, Jentys A, Camaioni DM, Gutiérrez OY, Lercher JA. Kinetic Coupling of Water Splitting and Photoreforming on SrTiO3-Based Photocatalysts. ACS Catal 2018;8:2902–13. https://doi.org/10.1021/acscatal.7b03192.
[580] Cai X, Wang C, Chen Y, Cheng Z, Shu R, Zhang J, et al. A novel approach for enhancing hydrogen production from bio-glycerol photoreforming by improving colloidal dispersion stability. Sci Total Environ 2018;627:1464–72. https://doi.org/10.1016/j.scitotenv.2018.02.009.
[581] Maldonado MI, Saggioro E, Peral J, Rodríguez-Castellón E, Jiménez-Jiménez J, Malato S. Hydrogen generation by irradiation of commercial CuO + TiO2 mixtures at solar pilot plant scale and in presence of organic electron donors. Appl Catal B Environ 2019;257. https://doi.org/10.1016/j.apcatb.2019.117890.
[582] Sakurai H, Kiuchi M, Jin T. Pt/TiO2 granular photocatalysts for hydrogen production from aqueous glycerol solution: Durability against seawater constituents and dissolved oxygen. Catal Commun 2018;114:124–8. https://doi.org/10.1016/j.catcom.2018.06.013.
[583] Estahbanati MRK, Feilizadeh M, Iliuta MC. Photocatalytic valorization of glycerol to hydrogen: Optimization of operating parameters by artificial neural network. Appl Catal B Environ 2017;209:483–92. https://doi.org/10.1016/j.apcatb.2017.03.016.
[584] Vo TG, Kao CC, Kuo JL, Chiu C chau, Chiang CY. Unveiling the crystallographic facet dependence of the photoelectrochemical glycerol oxidation on bismuth vanadate. Appl Catal B Environ 2020;278. https://doi.org/10.1016/j.apcatb.2020.119303.
[585] Lee SS, Bai H, Chua SC, Lee KW, Sun DD. Electrospun Bi3+/TiO2 nanofibers for

concurrent photocatalytic H2 and clean water production from glycerol under solar irradiation: A systematic study. J Clean Prod 2021;298. https://doi.org/10.1016/j.jclepro.2021.126671.
[586] Gu Z, An X, Liu R, Xiong L, Tang J, Hu C, et al. Interface-modulated nanojunction and microfluidic platform for photoelectrocatalytic chemicals upgrading. Appl Catal B Environ 2021;282. https://doi.org/10.1016/j.apcatb.2020.119541.
[587] Lalitha K, Sadanandam G, Kumari VD, Subrahmanyam M, Sreedhar B, Hebalkar NY. Highly stabilized and finely dispersed Cu2O/TiO2: A promising visible sensitive photocatalyst for continuous production of hydrogen from glycerol:water mixtures. J Phys Chem C 2010;114:22181–9. https://doi.org/10.1021/jp107405u.
[588] Zhang Y, Zhang N, Tang ZR, Xu YJ. Identification of Bi2WO6 as a highly selective visible-light photocatalyst toward oxidation of glycerol to dihydroxyacetone in water. Chem Sci 2013;4:1820–4. https://doi.org/10.1039/c3sc50285f.
[589] Kondarides DI, Daskalaki VM, Patsoura A, Verykios XE. Hydrogen production by photo-induced reforming of biomass components and derivatives at ambient conditions. Catal Letters 2008;122:26–32. https://doi.org/10.1007/s10562-007-9330-3.
[590] Yu J, Hai Y, Jaroniec M. Photocatalytic hydrogen production over CuO-modified titania. J Colloid Interface Sci 2011;357:223–8. https://doi.org/10.1016/j.jcis.2011.01.101.
[591] Gombac V, Sordelli L, Montini T, Delgado JJ, Adamski A, Adami G, et al. CuOx-TiO2 Photocatalysts for H2 production from ethanol and glycerol solutions. J Phys Chem A 2010;114:3916–25. https://doi.org/10.1021/jp907242q.
[592] Daskalaki VM, Kondarides DI. Efficient production of hydrogen by photo-induced reforming of glycerol at ambient conditions. Catal Today 2009;144:75–80. https://doi.org/10.1016/j.cattod.2008.11.009.
[593] Praveen Kumar D, Shankar M V., Mamatha Kumari M, Sadanandam G, Srinivas B, Durgakumari V. Nano-size effects on CuO/TiO2 catalysts for highly efficient H2 production under solar light irradiation. Chem Commun 2013;49:9443–5. https://doi.org/10.1039/c3cc44742a.
[594] Babu SG, Vinoth R, Praveen Kumar D, Shankar M V., Chou HL, Vinodgopal K, et al. Influence of electron storing, transferring and shuttling assets of reduced graphene oxide at the interfacial copper doped TiO2 p-n heterojunction for increased hydrogen production. Nanoscale 2015;7:7849–57. https://doi.org/10.1039/c5nr00504c.
[595] Sadanandam G, Lalitha K, Kumari VD, Shankar M V., Subrahmanyam M. Cobalt doped TiO2: A stable and efficient photocatalyst for continuous hydrogen production from glycerol: Water mixtures under solar light irradiation. Int J Hydrogen Energy 2013;38:9655–64. https://doi.org/10.1016/j.ijhydene.2013.05.116.
[596] Sang HX, Wang XT, Fan CC, Wang F. Enhanced photocatalytic H2 production from glycerol solution over ZnO/ZnS core/shell nanorods prepared by a low temperature route. Int J Hydrogen Energy 2012;37:1348–55. https://doi.org/10.1016/j.ijhydene.2011.09.129.
[597] Praveen Kumar D, Lakshmana Reddy N, Mamatha Kumari M, Srinivas B, Durga Kumari V, Sreedhar B, et al. Cu2O-sensitized TiO2 nanorods with nanocavities for highly efficient photocatalytic hydrogen production under solar irradiation. Sol Energy Mater Sol Cells 2015;136:157–66. https://doi.org/10.1016/j.solmat.2015.01.009.
[598] Bahruji H, Bowker M, Davies PR, Al-Mazroai LS, Dickinson A, Greaves J, et al. Sustainable H 2 gas production by photocatalysis. J Photochem Photobiol A Chem 2010;216:115–8. https://doi.org/10.1016/j.jphotochem.2010.06.022.
[599] Gallo A, Montini T, Marelli M, Minguzzi A, Gombac V, Psaro R, et al. H2 production by renewables photoreforming on Pt-Au/TiO 2 catalysts activated by reduction. ChemSusChem 2012;5:1800–11. https://doi.org/10.1002/cssc.201200085.
[600] Bowker M, Davies PR, Al-Mazroai LS. Photocatalytic reforming of glycerol over gold and palladium as an alternative fuel source. Catal Letters 2009;128:253–5. https://doi.org/10.1007/s10562-008-9781-1.
[601] Cargnello M, Montini T, Smolin SY, Priebe JB, Jaén JJD, Doan-Nguyen VVT, et al. Engineering titania nanostructure to tune and improve its photocatalytic activity. Proc

Natl Acad Sci U S A 2016;113:3966–71. https://doi.org/10.1073/pnas.1524806113.
[602] López CR, Melián EP, Ortega Méndez JA, Santiago DE, Doña Rodríguez JM, González Díaz O. Comparative study of alcohols as sacrificial agents in H2 production by heterogeneous photocatalysis using Pt/TiO2 catalysts. J Photochem Photobiol A Chem 2015;312:45–54. https://doi.org/10.1016/j.jphotochem.2015.07.005.
[603] Chong R, Li J, Zhou X, Ma Y, Yang J, Huang L, et al. Selective photocatalytic conversion of glycerol to hydroxyacetaldehyde in aqueous solution on facet tuned TiO2-based catalysts. Chem Commun 2014;50:165–7. https://doi.org/10.1039/c3cc46515b.
[604] Tan SS, Zou L, Hu E. Photocatalytic reduction of carbon dioxide into gaseous hydrocarbon using TiO2 pellets. Catal Today 2006;115:269–73. https://doi.org/10.1016/j.cattod.2006.02.057.
[605] Kočí K, Obalová L, Matějová L, Plachá D, Lacný Z, Jirkovský J, et al. Effect of TiO2 particle size on the photocatalytic reduction of CO2. Appl Catal B Environ 2009;89:494–502. https://doi.org/10.1016/j.apcatb.2009.01.010.
[606] Qamar S, Lei F, Liang L, Gao S, Liu K, Sun Y, et al. Ultrathin TiO2 flakes optimizing solar light driven CO2 reduction. Nano Energy 2016;26:692–8. https://doi.org/10.1016/j.nanoen.2016.06.029.
[607] Liu L, Zhao H, Andino JM, Li Y. Photocatalytic CO 2 reduction with H 2O on TiO 2 nanocrystals: Comparison of anatase, rutile, and brookite polymorphs and exploration of surface chemistry. ACS Catal 2012;2:1817–28. https://doi.org/10.1021/cs300273q.
[608] Sorcar S, Hwang Y, Grimes CA, In S Il. Highly enhanced and stable activity of defect-induced titania nanoparticles for solar light-driven CO2 reduction into CH4. Mater Today 2017;20:507–15. https://doi.org/10.1016/j.mattod.2017.09.005.
[609] Lin LY, Kavadiya S, He X, Wang WN, Karakocak BB, Lin YC, et al. Engineering stable Pt nanoparticles and oxygen vacancies on defective TiO2 via introducing strong electronic metal-support interaction for efficient CO2 photoreduction. Chem Eng J 2020;389. https://doi.org/10.1016/j.cej.2019.123450.
[610] Tahir M, Amin NAS. Indium-doped TiO2 nanoparticles for photocatalytic CO2 reduction with H2O vapors to CH4. Appl Catal B Environ 2015;162:98–109. https://doi.org/10.1016/j.apcatb.2014.06.037.
[611] Liu Y, Zhou S, Li J, Wang Y, Jiang G, Zhao Z, et al. Photocatalytic reduction of CO2 with water vapor on surface La-modified TiO2 nanoparticles with enhanced CH4 selectivity. Appl Catal B Environ 2015;168–169:125–31. https://doi.org/10.1016/j.apcatb.2014.12.011.
[612] Li Y, Wang WN, Zhan Z, Woo MH, Wu CY, Biswas P. Photocatalytic reduction of CO2 with H2O on mesoporous silica supported Cu/TiO2 catalysts. Appl Catal B Environ 2010;100:386–92. https://doi.org/10.1016/j.apcatb.2010.08.015.
[613] Albo J, Qadir MI, Samperi M, Fernandes JA, de Pedro I, Dupont J. Use of an optofluidic microreactor and Cu nanoparticles synthesized in ionic liquid and embedded in TiO2 for an efficient photoreduction of CO2 to methanol. Chem Eng J 2021;404. https://doi.org/10.1016/j.cej.2020.126643.
[614] Wang K, Lu J, Lu Y, Lau CH, Zheng Y, Fan X. Unravelling the C–C coupling in CO2 photocatalytic reduction with H2O on Au/TiO2-x: Combination of plasmonic excitation and oxygen vacancy. Appl Catal B Environ 2021;292. https://doi.org/10.1016/j.apcatb.2021.120147.
[615] Tahir B, Tahir M, Amin NS. Gold-indium modified TiO 2 nanocatalysts for photocatalytic CO 2 reduction with H 2 as reductant in a monolith photoreactor. Appl Surf Sci 2015;338:1–14. https://doi.org/10.1016/j.apsusc.2015.02.126.
[616] Billo T, Fu FY, Raghunath P, Shown I, Chen WF, Lien HT, et al. Ni-Nanocluster Modified Black TiO2 with Dual Active Sites for Selective Photocatalytic CO2 Reduction. Small 2018;14. https://doi.org/10.1002/smll.201702928.
[617] Akple MS, Low J, Qin Z, Wageh S, Al-Ghamdi AA, Yu J, et al. Nitrogen-doped TiO2 microsheets with enhanced visible light photocatalytic activity for CO2 reduction. Cuihua Xuebao/Chinese J Catal 2015;36:2127–34. https://doi.org/10.1016/S1872-2067(15)60989-5.

[618] Tan LL, Ong WJ, Chai SP, Mohamed AR. Photocatalytic reduction of CO2 with H2O over graphene oxide-supported oxygen-rich TiO2 hybrid photocatalyst under visible light irradiation: Process and kinetic studies. Chem Eng J 2017;308:248–55. https://doi.org/10.1016/j.cej.2016.09.050.
[619] Gao J, Shen Q, Guan R, Xue J, Liu X, Jia H, et al. Oxygen vacancy self-doped black TiO2 nanotube arrays by aluminothermic reduction for photocatalytic CO2 reduction under visible light illumination. J CO2 Util 2020;35:205–15. https://doi.org/10.1016/j.jcou.2019.09.016.
[620] Xu F, Zhang J, Zhu B, Yu J, Xu J. CuInS2 sensitized TiO2 hybrid nanofibers for improved photocatalytic CO2 reduction. Appl Catal B Environ 2018;230:194–202. https://doi.org/10.1016/j.apcatb.2018.02.042.
[621] Liu L, Zhao C, Pitts D, Zhao H, Li Y. CO2 photoreduction with H2O vapor by porous MgO-TiO2 microspheres: Effects of surface MgO dispersion and CO 2 adsorption-desorption dynamics. Catal Sci Technol 2014;4:1539–46. https://doi.org/10.1039/c3cy00807j.
[622] Zhao C, Liu L, Rao G, Zhao H, Wang L, Xu J, et al. Synthesis of novel MgAl layered double oxide grafted TiO2 cuboids and their photocatalytic activity on CO2 reduction with water vapor. Catal Sci Technol 2015;5:3288–95. https://doi.org/10.1039/c5cy00216h.
[623] Meng A, Zhang L, Cheng B, Yu J. TiO 2 -MnO x -Pt Hybrid Multiheterojunction Film Photocatalyst with Enhanced Photocatalytic CO 2 -Reduction Activity. ACS Appl Mater Interfaces 2019;11:5581–9. https://doi.org/10.1021/acsami.8b02552.
[624] Low J, Zhang L, Tong T, Shen B, Yu J. TiO2/MXene Ti3C2 composite with excellent photocatalytic CO2 reduction activity. J Catal 2018;361:255–66. https://doi.org/10.1016/j.jcat.2018.03.009.
[625] Asi MA, He C, Su M, Xia D, Lin L, Deng H, et al. Photocatalytic reduction of CO2 to hydrocarbons using AgBr/TiO2 nanocomposites under visible light. Catal Today 2011;175:256–63. https://doi.org/10.1016/j.cattod.2011.02.055.
[626] Tu W, Zhou Y, Liu Q, Tian Z, Gao J, Chen X, et al. Robust hollow spheres consisting of alternating titania nanosheets and graphene nanosheets with high photocatalytic activity for CO 2 conversion into renewable fuels. Adv Funct Mater 2012;22:1215–21. https://doi.org/10.1002/adfm.201102566.
[627] Tahir M, Amin NAS. Performance analysis of nanostructured NiO-In2O3/TiO2 catalyst for CO2 photoreduction with H2 in a monolith photoreactor. Chem Eng J 2016;285:635–49. https://doi.org/10.1016/j.cej.2015.10.033.
[628] Gui MM, Wong WMP, Chai SP, Mohamed AR. One-pot synthesis of Ag-MWCNT@TiO2 core-shell nanocomposites for photocatalytic reduction of CO2 with water under visible light irradiation. Chem Eng J 2015;278:272–8. https://doi.org/10.1016/j.cej.2014.09.022.
[629] Yu H, Li J, Zhang Y, Yang S, Han K, Dong F, et al. Three-in-One Oxygen Vacancies: Whole Visible-Spectrum Absorption, Efficient Charge Separation, and Surface Site Activation for Robust CO 2 Photoreduction. Angew Chemie - Int Ed 2019;58:3880–4. https://doi.org/10.1002/anie.201813967.
[630] Akatsuka M, Kawaguchi Y, Itoh R, Ozawa A, Yamamoto M, Tanabe T, et al. Preparation of Ga2O3 photocatalyst highly active for CO2 reduction with water without cocatalyst. Appl Catal B Environ 2020;262. https://doi.org/10.1016/j.apcatb.2019.118247.
[631] Wang L, Wan J, Zhao Y, Yang N, Wang D. Hollow Multi-Shelled Structures of Co3O4 Dodecahedron with Unique Crystal Orientation for Enhanced Photocatalytic CO2 Reduction. J Am Chem Soc 2019;141:2238–41. https://doi.org/10.1021/jacs.8b13528.
[632] Wang Y, Zhao J, Li Y, Wang C. Selective photocatalytic CO2 reduction to CH4 over Pt/In2O3: Significant role of hydrogen adatom. Appl Catal B Environ 2018;226:544–53. https://doi.org/10.1016/j.apcatb.2018.01.005.
[633] Pan YX, You Y, Xin S, Li Y, Fu G, Cui Z, et al. Photocatalytic CO2 Reduction by Carbon-Coated Indium-Oxide Nanobelts. J Am Chem Soc 2017;139:4123–9.

https://doi.org/10.1021/jacs.7b00266.
[634] Wan L, Zhou Q, Wang X, Wood TE, Wang L, Duchesne PN, et al. Cu2O nanocubes with mixed oxidation-state facets for (photo)catalytic hydrogenation of carbon dioxide. Nat Catal 2019;2:889–98. https://doi.org/10.1038/s41929-019-0338-z.
[635] Wu YA, McNulty I, Liu C, Lau KC, Liu Q, Paulikas AP, et al. Facet-dependent active sites of a single Cu2O particle photocatalyst for CO2 reduction to methanol. Nat Energy 2019;4:957–68. https://doi.org/10.1038/s41560-019-0490-3.
[636] Zhou J, Li Y, Yu L, Li Z, Xie D, Zhao Y, et al. Facile in situ fabrication of Cu2O@Cu metal-semiconductor heterostructured nanorods for efficient visible-light driven CO2 reduction. Chem Eng J 2020;385. https://doi.org/10.1016/j.cej.2019.123940.
[637] Wang J, Ji G, Liu Y, Gondal MA, Chang X. Cu2O/TiO2 heterostructure nanotube arrays prepared by an electrodeposition method exhibiting enhanced photocatalytic activity for CO2 reduction to methanol. Catal Commun 2014;46:17–21. https://doi.org/10.1016/j.catcom.2013.11.011.
[638] Hezam A, Namratha K, Drmosh QA, Ponnamma D, Wang J, Prasad S, et al. CeO2 Nanostructures Enriched with Oxygen Vacancies for Photocatalytic CO2 Reduction. ACS Appl Nano Mater 2020;3:138–48. https://doi.org/10.1021/acsanm.9b01833.
[639] Xiong X, Mao C, Yang Z, Zhang Q, Waterhouse GIN, Gu L, et al. Photocatalytic CO2 Reduction to CO over Ni Single Atoms Supported on Defect-Rich Zirconia. Adv Energy Mater 2020;10. https://doi.org/10.1002/aenm.202002928.
[640] Wu X, Lan D, Zhang R, Pang F, Ge J. Fabrication of Opaline ZnO Photonic Crystal Film and Its Slow-Photon Effect on Photoreduction of Carbon Dioxide. Langmuir 2019;35:194–202. https://doi.org/10.1021/acs.langmuir.8b03327.
[641] Sayed M, Xu F, Kuang P, Low J, Wang S, Zhang L, et al. Sustained CO2-photoreduction activity and high selectivity over Mn, C-codoped ZnO core-triple shell hollow spheres. Nat Commun 2021;12. https://doi.org/10.1038/s41467-021-25007-6.
[642] Nakada A, Kuriki R, Sekizawa K, Nishioka S, Vequizo JJM, Uchiyama T, et al. Effects of Interfacial Electron Transfer in Metal Complex-Semiconductor Hybrid Photocatalysts on Z-Scheme CO2 Reduction under Visible Light. ACS Catal 2018;8:9744–54. https://doi.org/10.1021/acscatal.8b03062.
[643] Paulino PN, Salim VMM, Resende NS. Zn-Cu promoted TiO2 photocatalyst for CO2 reduction with H2O under UV light. Appl Catal B Environ 2016;185:362–70. https://doi.org/10.1016/j.apcatb.2015.12.037.
[644] Tao X, Wang Y, Qu J, Zhao Y, Li R, Li C. Achieving selective photocatalytic CO 2 reduction to CO on bismuth tantalum oxyhalogen nanoplates . J Mater Chem A 2021. https://doi.org/10.1039/d1ta02504j.
[645] Di J, Zhu C, Ji M, Duan M, Long R, Yan C, et al. Defect-Rich Bi12O17Cl2 Nanotubes Self-Accelerating Charge Separation for Boosting Photocatalytic CO2 Reduction. Angew Chemie - Int Ed 2018;57:14847–51. https://doi.org/10.1002/anie.201809492.
[646] Jin J, Wang Y, He T. Preparation of thickness-tunable BiOCl nanosheets with high photocatalytic activity for photoreduction of CO2. RSC Adv 2015;5:100244–50. https://doi.org/10.1039/c5ra21888h.
[647] Shi Y, Zhan G, Li H, Wang X, Liu X, Shi L, et al. Simultaneous Manipulation of Bulk Excitons and Surface Defects for Ultrastable and Highly Selective CO 2 Photoreduction . Adv Mater 2021:2100143. https://doi.org/10.1002/adma.202100143.
[648] Wu J, Li X, Shi W, Ling P, Sun Y, Jiao X, et al. Efficient Visible-Light-Driven CO2 Reduction Mediated by Defect-Engineered BiOBr Atomic Layers. Angew Chemie - Int Ed 2018;57:8719–23. https://doi.org/10.1002/anie.201803514.
[649] Ye L, Jin X, Ji X, Liu C, Su Y, Xie H, et al. Facet-dependent photocatalytic reduction of CO2 on BiOI nanosheets. Chem Eng J 2016;291:39–46. https://doi.org/10.1016/j.cej.2016.01.032.
[650] Liu Y, Shen D, Zhang Q, Lin Y, Peng F. Enhanced photocatalytic CO2 reduction in H2O vapor by atomically thin Bi2WO6 nanosheets with hydrophobic and nonpolar surface. Appl Catal B Environ 2021;283. https://doi.org/10.1016/j.apcatb.2020.119630.
[651] Liu Y, Huang B, Dai Y, Zhang X, Qin X, Jiang M, et al. Selective ethanol formation

from photocatalytic reduction of carbon dioxide in water with BiVO4 photocatalyst. Catal Commun 2009;11:210–3. https://doi.org/10.1016/j.catcom.2009.10.010.
[652] Bian J, Zhang Z, Feng J, Thangamuthu M, Yang F, Sun L, et al. Energy Platform for Directed Charge Transfer in the Cascade Z-Scheme Heterojunction: CO 2 Photoreduction without a Cocatalyst . Angew Chemie Int Ed 2021. https://doi.org/10.1002/anie.202106929.
[653] Zu X, Zhao Y, Li X, Chen R, Shao W, Wang Z, et al. Ultrastable and Efficient Visible-light-driven CO2 Reduction Triggered by Regenerative Oxygen-Vacancies in Bi2O2CO3 Nanosheets. Angew Chemie - Int Ed 2021;60:13840–6. https://doi.org/10.1002/anie.202101894.
[654] Yu H, Chen F, Li X, Huang H, Zhang Q, Su S, et al. Synergy of ferroelectric polarization and oxygen vacancy to promote CO2 photoreduction. Nat Commun 2021;12. https://doi.org/10.1038/s41467-021-24882-3.
[655] Cao S, Shen B, Tong T, Fu J, Yu J. 2D/2D Heterojunction of Ultrathin MXene/Bi2WO6 Nanosheets for Improved Photocatalytic CO2 Reduction. Adv Funct Mater 2018;28. https://doi.org/10.1002/adfm.201800136.
[656] Han Q, Bai X, Man Z, He H, Li L, Hu J, et al. Convincing Synthesis of Atomically Thin, Single-Crystalline InVO4 Sheets toward Promoting Highly Selective and Efficient Solar Conversion of CO2 into CO. J Am Chem Soc 2019;141:4209–13. https://doi.org/10.1021/jacs.8b13673.
[657] Kumar A, Prajapati PK, Pal U, Jain SL. Ternary rGO/InVO4/Fe2O3 Z-Scheme Heterostructured Photocatalyst for CO2 Reduction under Visible Light Irradiation. ACS Sustain Chem Eng 2018;6:8201–11. https://doi.org/10.1021/acssuschemeng.7b04872.
[658] Nogueira AE, Silva GTST, Oliveira JA, Lopes OF, Torres JA, Carmo M, et al. CuO Decoration Controls Nb2O5Photocatalyst Selectivity in CO2Reduction. ACS Appl Energy Mater 2020;3:7629–36. https://doi.org/10.1021/acsaem.0c01047.
[659] Xie S, Wang Y, Zhang Q, Deng W, Wang Y. SrNb2O6 nanoplates as efficient photocatalysts for the preferential reduction of CO2 in the presence of H2O. Chem Commun 2015;51:3430–3. https://doi.org/10.1039/c4cc10241j.
[660] Pang R, Teramura K, Asakura H, Hosokawa S, Tanaka T. Highly selective photocatalytic conversion of CO2 by water over Ag-loaded SrNb2O6 nanorods. Appl Catal B Environ 2017;218:770–8. https://doi.org/10.1016/j.apcatb.2017.06.052.
[661] Iizuka K, Wato T, Miseki Y, Saito K, Kudo A. Photocatalytic reduction of carbon dioxide over Ag cocatalyst-loaded ALa 4Ti 4O 15 (A = Ca, Sr, and Ba) using water as a reducing reagent. J Am Chem Soc 2011;133:20863–8. https://doi.org/10.1021/ja207586e.
[662] Fresno F, Jana P, Reñones P, Coronado JM, Serrano DP, De La Peña O'Shea VA. CO2 reduction over NaNbO3 and NaTaO3 perovskite photocatalysts. Photochem Photobiol Sci 2017;16:17–23. https://doi.org/10.1039/c6pp00235h.
[663] Nakanishi H, Iizuka K, Takayama T, Iwase A, Kudo A. Highly Active NaTaO3-Based Photocatalysts for CO2 Reduction to Form CO Using Water as the Electron Donor. ChemSusChem 2017;10:112–8. https://doi.org/10.1002/cssc.201601360.
[664] Pei L, Yuan Y, Bai W, Li T, Zhu H, Ma Z, et al. In situ-grown island-shaped hollow graphene on Taon with spatially separated active sites achieving enhanced visible-light CO2 reduction. ACS Catal 2020;10:15083–91. https://doi.org/10.1021/acscatal.0c03918.
[665] Sekizawa K, Maeda K, Domen K, Koike K, Ishitani O. Artificial Z-scheme constructed with a supramolecular metal complex and semiconductor for the photocatalytic reduction of CO2. J Am Chem Soc 2013;135:4596–9. https://doi.org/10.1021/ja311541a.
[666] Feng S, Chen X, Zhou Y, Tu W, Li P, Li H, et al. Na2V6O16·xH2O nanoribbons: Large-scale synthesis and visible-light photocatalytic activity of CO2 into solar fuels. Nanoscale 2014;6:1896–900. https://doi.org/10.1039/c3nr05219b.
[667] Yin G, Nishikawa M, Nosaka Y, Srinivasan N, Atarashi D, Sakai E, et al. Photocatalytic carbon dioxide reduction by copper oxide nanocluster-grafted niobate nanosheets. ACS Nano 2015;9:2111–9. https://doi.org/10.1021/nn507429e.
[668] Shao K, Wang Y, Iqbal M, Lin L, Wang K, Zhang X, et al. Modification of Ag

nanoparticles on the surface of SrTiO 3 particles and resultant influence on photoreduction of CO 2. Appl Surf Sci 2018;434:717–24. https://doi.org/10.1016/j.apsusc.2017.11.004.
[669] Pan B, Luo S, Su W, Wang X. Photocatalytic CO2 reduction with H2O over LaPO4 nanorods deposited with Pt cocatalyst. Appl Catal B Environ 2015;168–169:458–64. https://doi.org/10.1016/j.apcatb.2014.12.046.
[670] Liu Q, Wu D, Zhou Y, Su H, Wang R, Zhang C, et al. Single-crystalline, ultrathin ZnGa2O4 nanosheet scaffolds to promote photocatalytic activity in CO2 reduction into methane. ACS Appl Mater Interfaces 2014;6:2356–61. https://doi.org/10.1021/am404572g.
[671] Huang Y, Wang Y, Bi Y, Jin J, Ehsan MF, Fu M, et al. Preparation of 2D hydroxyl-rich carbon nitride nanosheets for photocatalytic reduction of CO2. RSC Adv 2015;5:33254–61. https://doi.org/10.1039/c5ra04227e.
[672] Mo Z, Zhu X, Jiang Z, Song Y, Liu D, Li H, et al. Porous nitrogen-rich g-C3N4 nanotubes for efficient photocatalytic CO2 reduction. Appl Catal B Environ 2019;256. https://doi.org/10.1016/j.apcatb.2019.117854.
[673] Wang K, Li Q, Liu B, Cheng B, Ho W, Yu J. Sulfur-doped g-C3N4 with enhanced photocatalytic CO2-reduction performance. Appl Catal B Environ 2015;176–177:44–52. https://doi.org/10.1016/j.apcatb.2015.03.045.
[674] Ye L, Wu D, Chu KH, Wang B, Xie H, Yip HY, et al. Phosphorylation of g-C3N4 for enhanced photocatalytic CO2 reduction. Chem Eng J 2016;304:376–83. https://doi.org/10.1016/j.cej.2016.06.059.
[675] Fu J, Zhu B, Jiang C, Cheng B, You W, Yu J. Hierarchical Porous O-Doped g-C3N4 with Enhanced Photocatalytic CO2 Reduction Activity. Small 2017;13. https://doi.org/10.1002/smll.201603938.
[676] Barrio J, Mateo D, Albero J, García H, Shalom M. A Heterogeneous Carbon Nitride–Nickel Photocatalyst for Efficient Low-Temperature CO2 Methanation. Adv Energy Mater 2019;9. https://doi.org/10.1002/aenm.201902738.
[677] Cao S, Li Y, Zhu B, Jaroniec M, Yu J. Facet effect of Pd cocatalyst on photocatalytic CO2 reduction over g-C3N4. J Catal 2017;349:208–17. https://doi.org/10.1016/j.jcat.2017.02.005.
[678] Zhang JH, Yang W, Zhang M, Wang HJ, Si R, Zhong DC, et al. Metal-organic layers as a platform for developing single-atom catalysts for photochemical CO2 reduction. Nano Energy 2021;80. https://doi.org/10.1016/j.nanoen.2020.105542.
[679] Sharma P, Kumar S, Tomanec O, Petr M, Zhu Chen J, Miller JT, et al. Carbon Nitride-Based Ruthenium Single Atom Photocatalyst for CO2 Reduction to Methanol. Small 2021;17. https://doi.org/10.1002/smll.202006478.
[680] Ma B, Chen G, Fave C, Chen L, Kuriki R, Maeda K, et al. Efficient Visible-Light-Driven CO2 Reduction by a Cobalt Molecular Catalyst Covalently Linked to Mesoporous Carbon Nitride. J Am Chem Soc 2020;142:6188–95. https://doi.org/10.1021/jacs.9b13930.
[681] Shi H, Zhang C, Zhou C, Chen G. Conversion of CO2 into renewable fuel over Pt-g-C3N4/KNbO3 composite photocatalyst. RSC Adv 2015;5:93615–22. https://doi.org/10.1039/c5ra16870h.
[682] Wang M, Shen M, Zhang L, Tian J, Jin X, Zhou Y, et al. 2D-2D MnO2/g-C3N4 heterojunction photocatalyst: In-situ synthesis and enhanced CO2 reduction activity. Carbon N Y 2017;120:23–31. https://doi.org/10.1016/j.carbon.2017.05.024.
[683] Yu W, Xu D, Peng T. Enhanced photocatalytic activity of g-C3N4 for selective CO2 reduction to CH3OH via facile coupling of ZnO: A direct Z-scheme mechanism. J Mater Chem A 2015;3:19936–47. https://doi.org/10.1039/c5ta05503b.
[684] Liang M, Borjigin T, Zhang Y, Liu B, Liu H, Guo H. Controlled assemble of hollow heterostructured g-C3N4@CeO2 with rich oxygen vacancies for enhanced photocatalytic CO2 reduction. Appl Catal B Environ 2019;243:566–75. https://doi.org/10.1016/j.apcatb.2018.11.010.
[685] Tahir B, Tahir M, Ghazali M, Nawawi M. Highly stable 3D/2D WO3/g-C3N4 Z-scheme

heterojunction for stimulating photocatalytic CO2 reduction by H2O/H2 to CO and CH4 under visible light. J CO2 Util 2020;41. https://doi.org/10.1016/j.jcou.2020.101270.
[686] Jiang Z, Wan W, Li H, Yuan S, Zhao H, Wong PK. A Hierarchical Z-Scheme α-Fe2O3/g-C3N4 Hybrid for Enhanced Photocatalytic CO2 Reduction. Adv Mater 2018;30. https://doi.org/10.1002/adma.201706108.
[687] Ou M, Tu W, Yin S, Xing W, Wu S, Wang H, et al. Amino-Assisted Anchoring of CsPbBr3 Perovskite Quantum Dots on Porous g-C3N4 for Enhanced Photocatalytic CO2 Reduction. Angew Chemie - Int Ed 2018;57:13570–4. https://doi.org/10.1002/anie.201808930.
[688] Di T, Zhu B, Cheng B, Yu J, Xu J. A direct Z-scheme g-C3N4/SnS2 photocatalyst with superior visible-light CO2 reduction performance. J Catal 2017;352:532–41. https://doi.org/10.1016/j.jcat.2017.06.006.
[689] Liang M, Borjigin T, Zhang Y, Liu H, Liu B, Guo H. Z-Scheme Au@Void@g-C3N4/SnS Yolk-Shell Heterostructures for Superior Photocatalytic CO2 Reduction under Visible Light. ACS Appl Mater Interfaces 2018;10:34123–31. https://doi.org/10.1021/acsami.8b09455.
[690] Xu D, Cheng B, Wang W, Jiang C, Yu J. Ag2CrO4/g-C3N4/graphene oxide ternary nanocomposite Z-scheme photocatalyst with enhanced CO2 reduction activity. Appl Catal B Environ 2018;231:368–80. https://doi.org/10.1016/j.apcatb.2018.03.036.
[691] Shi H, Long S, Hu S, Hou J, Ni W, Song C, et al. Interfacial charge transfer in 0D/2D defect-rich heterostructures for efficient solar-driven CO2 reduction. Appl Catal B Environ 2019;245:760–9. https://doi.org/10.1016/j.apcatb.2019.01.036.
[692] He F, Zhu B, Cheng B, Yu J, Ho W, Macyk W. 2D/2D/0D TiO2/C3N4/Ti3C2 MXene composite S-scheme photocatalyst with enhanced CO2 reduction activity. Appl Catal B Environ 2020;272. https://doi.org/10.1016/j.apcatb.2020.119006.
[693] Li H, Gan S, Wang H, Han D, Niu L. Intercorrelated Superhybrid of AgBr Supported on Graphitic-C3N4-Decorated Nitrogen-Doped Graphene: High Engineering Photocatalytic Activities for Water Purification and CO2 Reduction. Adv Mater 2015;27:6906–13. https://doi.org/10.1002/adma.201502755.
[694] Yan Y, Chen J, Li N, Tian J, Li K, Jiang J, et al. Systematic Bandgap Engineering of Graphene Quantum Dots and Applications for Photocatalytic Water Splitting and CO2 Reduction. ACS Nano 2018;12:3523–32. https://doi.org/10.1021/acsnano.8b00498.
[695] Xu YF, Yang MZ, Chen BX, Wang XD, Chen HY, Kuang D Bin, et al. A CsPbBr3 Perovskite Quantum Dot/Graphene Oxide Composite for Photocatalytic CO2 Reduction. J Am Chem Soc 2017;139:5660–3. https://doi.org/10.1021/jacs.7b00489.
[696] Mu Q, Zhu W, Li X, Zhang C, Su Y, Lian Y, et al. Electrostatic charge transfer for boosting the photocatalytic CO2 reduction on metal centers of 2D MOF/rGO heterostructure. Appl Catal B Environ 2020;262. https://doi.org/10.1016/j.apcatb.2019.118144.
[697] Bafaqeer A, Tahir M, Amin NAS. Synergistic effects of 2D/2D ZnV2O6/RGO nanosheets heterojunction for stable and high performance photo-induced CO2 reduction to solar fuels. Chem Eng J 2018;334:2142–53. https://doi.org/10.1016/j.cej.2017.11.111.
[698] Liu Z, Wang Z, Qing S, Xue N, Jia S, Zhang L, et al. Improving methane selectivity of photo-induced CO2 reduction on carbon dots through modification of nitrogen-containing groups and graphitization. Appl Catal B Environ 2018;232:86–92. https://doi.org/10.1016/j.apcatb.2018.03.045.
[699] Wang Y, Wang S, Lou XW. Dispersed Nickel Cobalt Oxyphosphide Nanoparticles Confined in Multichannel Hollow Carbon Fibers for Photocatalytic CO2 Reduction. Angew Chemie - Int Ed 2019;58:17236–40. https://doi.org/10.1002/anie.201909707.
[700] Gui MM, Chai SP, Xu BQ, Mohamed AR. Enhanced visible light responsive MWCNT/TiO2 core-shell nanocomposites as the potential photocatalyst for reduction of CO2 into methane. Sol Energy Mater Sol Cells 2014;122:183–9. https://doi.org/10.1016/j.solmat.2013.11.034.
[701] Cui X, Wang J, Liu B, Ling S, Long R, Xiong Y. Turning Au Nanoclusters Catalytically Active for Visible-Light-Driven CO 2 Reduction through Bridging Ligands. J Am Chem

Soc 2018;140:16514–20. https://doi.org/10.1021/jacs.8b06723.
[702] Su Y, Song Z, Zhu W, Mu Q, Yuan X, Lian Y, et al. Visible-Light Photocatalytic CO2 Reduction Using Metal-Organic Framework Derived Ni(OH)2 Nanocages: A Synergy from Multiple Light Reflection, Static Charge Transfer, and Oxygen Vacancies. ACS Catal 2021;11:345–54. https://doi.org/10.1021/acscatal.0c04020.
[703] Lu KQ, Li YH, Zhang F, Qi MY, Chen X, Tang ZR, et al. Rationally designed transition metal hydroxide nanosheet arrays on graphene for artificial CO2 reduction. Nat Commun 2020;11. https://doi.org/10.1038/s41467-020-18944-1.
[704] Chen W, Han B, Xie Y, Liang S, Deng H, Lin Z. Ultrathin Co-Co LDHs nanosheets assembled vertically on MXene: 3D nanoarrays for boosted visible-light-driven CO2 reduction. Chem Eng J 2020;391. https://doi.org/10.1016/j.cej.2019.123519.
[705] Zhu X, Huang S, Yu Q, She Y, Yang J, Zhou G, et al. In-situ hydroxyl modification of monolayer black phosphorus for stable photocatalytic carbon dioxide conversion. Appl Catal B Environ 2020;269. https://doi.org/10.1016/j.apcatb.2020.118760.
[706] Jiang S, Liu J, Zhao K, Cui D, Liu P, Yin H, et al. Ru(bpy)32+-sensitized {001} facets LiCoO2 nanosheets catalyzed CO2 reduction reaction with 100% carbonaceous products. Nano Res 2021. https://doi.org/10.1007/s12274-021-3599-1.
[707] Wang Y, Zhang L, Zhang X, Zhang Z, Tong Y, Li F, et al. Openmouthed B-SiC hollow-sphere with highly photocatalytic activity for reduction of CO2 with H2O. Appl Catal B Environ 2017;206:158–67. https://doi.org/10.1016/j.apcatb.2017.01.028.
[708] Li H, Sun J. Highly Selective Photocatalytic CO2Reduction to CH4by Ball-Milled Cubic Silicon Carbide Nanoparticles under Visible-Light Irradiation. ACS Appl Mater Interfaces 2021;13:5073–8. https://doi.org/10.1021/acsami.0c19945.
[709] Jin J, He T. Facile synthesis of Bi 2 S 3 nanoribbons for photocatalytic reduction of CO 2 into CH 3 OH. Appl Surf Sci 2017;394:364–70. https://doi.org/10.1016/j.apsusc.2016.10.118.
[710] Li J, Pan W, Liu Q, Chen Z, Chen Z, Feng X, et al. Interfacial Engineering of Bi19Br3S27Nanowires Promotes Metallic Photocatalytic CO2Reduction Activity under Near-Infrared Light Irradiation. J Am Chem Soc 2021;143:6551–9. https://doi.org/10.1021/jacs.1c01109.
[711] Bie C, Zhu B, Xu F, Zhang L, Yu J. In Situ Grown Monolayer N-Doped Graphene on CdS Hollow Spheres with Seamless Contact for Photocatalytic CO2 Reduction. Adv Mater 2019;31. https://doi.org/10.1002/adma.201902868.
[712] Jin J, Yu J, Guo D, Cui C, Ho W. A Hierarchical Z-Scheme CdS-WO3 Photocatalyst with Enhanced CO2 Reduction Activity. Small 2015;11:5262–71. https://doi.org/10.1002/smll.201500926.
[713] Guo Q, Liang F, Li XB, Gao YJ, Huang MY, Wang Y, et al. Efficient and Selective CO2 Reduction Integrated with Organic Synthesis by Solar Energy. Chem 2019;5:2605–16. https://doi.org/10.1016/j.chempr.2019.06.019.
[714] Zhou M, Wang S, Yang P, Huang C, Wang X. Boron Carbon Nitride Semiconductors Decorated with CdS Nanoparticles for Photocatalytic Reduction of CO2. ACS Catal 2018;8:4928–36. https://doi.org/10.1021/acscatal.8b00104.
[715] Li P, Zhou Y, Li H, Xu Q, Meng X, Wang X, et al. All-solid-state Z-scheme system arrays of Fe2V4O13/RGO/CdS for visible light-driving photocatalytic CO2 reduction into renewable hydrocarbon fuel. Chem Commun 2015;51:800–3. https://doi.org/10.1039/c4cc08744e.
[716] Wang S, Wang X. Photocatalytic CO2 reduction by CdS promoted with a zeolitic imidazolate framework. Appl Catal B Environ 2015;162:494–500. https://doi.org/10.1016/j.apcatb.2014.07.026.
[717] Tian F, Zhang H, Liu S, Wu T, Yu J, Wang D, et al. Visible-light-driven CO2 reduction to ethylene on CdS: Enabled by structural relaxation-induced intermediate dimerization and enhanced by ZIF-8 coating. Appl Catal B Environ 2021;285. https://doi.org/10.1016/j.apcatb.2020.119834.
[718] Kuehnel MF, Orchard KL, Dalle KE, Reisner E. Selective Photocatalytic CO2 Reduction in Water through Anchoring of a Molecular Ni Catalyst on CdS Nanocrystals.

J Am Chem Soc 2017;139:7217–23. https://doi.org/10.1021/jacs.7b00369.
[719] Meier AJ, Garg A, Sutter B, Kuhn JN, Bhethanabotla VR. MoS 2 Nanoflowers as a Gateway for Solar-Driven CO 2 Photoreduction. ACS Sustain Chem Eng 2019;7:265–75. https://doi.org/10.1021/acssuschemeng.8b03168.
[720] Wang Y, Zhang Z, Zhang L, Luo Z, Shen J, Lin H, et al. Visible-Light Driven Overall Conversion of CO2 and H2O to CH4 and O2 on 3D-SiC@2D-MoS2 Heterostructure. J Am Chem Soc 2018;140:14595–8. https://doi.org/10.1021/jacs.8b09344.
[721] Wang X, He J, Mao L, Cai X, Sun C, Zhu M. CsPbBr3 perovskite nanocrystals anchoring on monolayer MoS2 nanosheets for efficient photocatalytic CO2 reduction. Chem Eng J 2021;416. https://doi.org/10.1016/j.cej.2020.128077.
[722] Pang H, Meng X, Li P, Chang K, Zhou W, Wang X, et al. Cation Vacancy-Initiated CO2 Photoreduction over ZnS for Efficient Formate Production. ACS Energy Lett 2019;4:1387–93. https://doi.org/10.1021/acsenergylett.9b00711.
[723] Meng X, Yu Q, Liu G, Shi L, Zhao G, Liu H, et al. Efficient photocatalytic CO2 reduction in all-inorganic aqueous environment: Cooperation between reaction medium and Cd(II) modified colloidal ZnS. Nano Energy 2017;34:524–32. https://doi.org/10.1016/j.nanoen.2017.03.021.
[724] Ehsan MF, Ashiq MN, He T. Hollow and mesoporous ZnTe microspheres: Synthesis and visible-light photocatalytic reduction of carbon dioxide into methane. RSC Adv 2015;5:6186–94. https://doi.org/10.1039/c4ra13593h.
[725] Ehsan MF, He T. In situ synthesis of ZnO/ZnTe common cation heterostructure and its visible-light photocatalytic reduction of CO2 into CH4. Appl Catal B Environ 2015;166–167:345–52. https://doi.org/10.1016/j.apcatb.2014.11.058.
[726] Li D, Hussain S, Wang Y, Huang C, Li P, Wang M, et al. ZnSe/CdSe Z-scheme composites with Se vacancy for efficient photocatalytic CO2 reduction. Appl Catal B Environ 2021;286. https://doi.org/10.1016/j.apcatb.2021.119887.
[727] Jiang W, Yin X, Xin F, Bi Y, Liu Y, Li X. Preparation of CdIn 2 S 4 microspheres and application for photocatalytic reduction of carbon dioxide. Appl Surf Sci 2014;288:138–42. https://doi.org/10.1016/j.apsusc.2013.09.165.
[728] Zhang Z, Cao Y, Zhang F, Li W, Li Y, Yu H, et al. Tungsten oxide quantum dots deposited onto ultrathin CdIn2S4 nanosheets for efficient S-scheme photocatalytic CO2 reduction via cascade charge transfer. Chem Eng J 2022;428:131218. https://doi.org/10.1016/j.cej.2021.131218.
[729] He Y, Rao H, Song K, Li J, Yu Y, Lou Y, et al. 3D Hierarchical ZnIn2S4 Nanosheets with Rich Zn Vacancies Boosting Photocatalytic CO2 Reduction. Adv Funct Mater 2019;29. https://doi.org/10.1002/adfm.201905153.
[730] Jiao X, Chen Z, Li X, Sun Y, Gao S, Yan W, et al. Defect-Mediated Electron-Hole Separation in One-Unit-Cell ZnIn2S4 Layers for Boosted Solar-Driven CO2 Reduction. J Am Chem Soc 2017;139:7586–94. https://doi.org/10.1021/jacs.7b02290.
[731] Wang S, Guan BY, Lu Y, Lou XW. Formation of Hierarchical In2S3-CdIn2S4 Heterostructured Nanotubes for Efficient and Stable Visible Light CO2 Reduction. J Am Chem Soc 2017;139:17305–8. https://doi.org/10.1021/jacs.7b10733.
[732] Gao W, Li S, He H, Li X, Cheng Z, Yang Y, et al. Vacancy-defect modulated pathway of photoreduction of CO2 on single atomically thin AgInP2S6 sheets into olefiant gas. Nat Commun 2021;12. https://doi.org/10.1038/s41467-021-25068-7.
[733] Chen L-J, Liu T-T, Liu S-M, Cai S, Zou X-X, Jiang J-W, et al. S vacant CuIn5S8 confined in a few-layer MoSe2 with interlayer-expanded hollow heterostructures boost photocatalytic CO2 reduction. Rare Met 2021. https://doi.org/10.1007/s12598-021-01809-x.
[734] Wang Y, Wang S, Zhang SL, Lou XW. Formation of Hierarchical FeCoS2–CoS2 Double-Shelled Nanotubes with Enhanced Performance for Photocatalytic Reduction of CO2. Angew Chemie - Int Ed 2020;59:11918–22. https://doi.org/10.1002/anie.202004609.
[735] Bai S, Wang Z, Tan L, Waterhouse GIN, Zhao Y, Song YF. 600 nm Irradiation-Induced Efficient Photocatalytic CO2 Reduction by Ultrathin Layered Double Hydroxide

Nanosheets. Ind Eng Chem Res 2020;59:5848–57. https://doi.org/10.1021/acs.iecr.0c00522.
[736] Xu YF, Wang XD, Liao JF, Chen BX, Chen HY, Kuang D Bin. Amorphous-TiO2-Encapsulated CsPbBr3 Nanocrystal Composite Photocatalyst with Enhanced Charge Separation and CO2 Fixation. Adv Mater Interfaces 2018;5. https://doi.org/10.1002/admi.201801015.
[737] Cheng XM, Dao XY, Wang SQ, Zhao J, Sun WY. Enhanced Photocatalytic CO2 Reduction Activity over NH2-MIL-125(Ti) by Facet Regulation. ACS Catal 2021;11:650–8. https://doi.org/10.1021/acscatal.0c04426.
[738] Jiang Y, Yu Y, Zhang X, Weinert M, Song X, Ai J, et al. N-Heterocyclic Carbene-Stabilized Ultrasmall Gold Nanoclusters in a Metal-Organic Framework for Photocatalytic CO2 Reduction. Angew Chemie - Int Ed 2021;60:17388–93. https://doi.org/10.1002/anie.202105420.
[739] Wu LY, Mu YF, Guo XX, Zhang W, Zhang ZM, Zhang M, et al. Encapsulating Perovskite Quantum Dots in Iron-Based Metal–Organic Frameworks (MOFs) for Efficient Photocatalytic CO2 Reduction. Angew Chemie - Int Ed 2019;58:9491–5. https://doi.org/10.1002/anie.201904537.
[740] Xi Y, Zhang X, Shen Y, Dong W, Fan Z, Wang K, et al. Aspect ratio dependent photocatalytic enhancement of CsPbBr3 in CO2 reduction with two-dimensional metal organic framework as a cocatalyst. Appl Catal B Environ 2021;297. https://doi.org/10.1016/j.apcatb.2021.120411.
[741] Kong ZC, Liao JF, Dong YJ, Xu YF, Chen HY, Kuang D Bin, et al. Core@shell cspbbr3@zeolitic imidazolate framework nanocomposite for efficient photocatalytic co2 reduction. ACS Energy Lett 2018;3:2656–62. https://doi.org/10.1021/acsenergylett.8b01658.
[742] Kong ZC, Zhang HH, Liao JF, Dong YJ, Jiang Y, Chen HY, et al. Immobilizing Re(CO)3Br(dcbpy) Complex on CsPbBr3 Nanocrystal for Boosted Charge Separation and Photocatalytic CO2 Reduction. Sol RRL 2020;4. https://doi.org/10.1002/solr.201900365.
[743] Liu W, Li X, Wang C, Pan H, Liu W, Wang K, et al. A Scalable General Synthetic Approach toward Ultrathin Imine-Linked Two-Dimensional Covalent Organic Framework Nanosheets for Photocatalytic CO2 Reduction. J Am Chem Soc 2019;141:17431–40. https://doi.org/10.1021/jacs.9b09502.
[744] Niu K, Xu Y, Wang H, Ye R, Xin HL, Lin F, et al. A spongy nickel-organic CO2 reduction photocatalyst for nearly 100% selective CO production. Sci Adv 2017;3:1–10. https://doi.org/10.1126/sciadv.1700921.
[745] Fu Y, Sun D, Chen Y, Huang R, Ding Z, Fu X, et al. An amine-functionalized titanium metal-organic framework photocatalyst with visible-light-induced activity for CO 2 reduction. Angew Chemie - Int Ed 2012;51:3364–7. https://doi.org/10.1002/anie.201108357.
[746] Wang D, Huang R, Liu W, Sun D, Li Z. Fe-based MOFs for photocatalytic CO2 reduction: Role of coordination unsaturated sites and dual excitation pathways. ACS Catal 2014;4:4254–60. https://doi.org/10.1021/cs501169t.
[747] Wang Y, Huang NY, Shen JQ, Liao PQ, Chen XM, Zhang JP. Hydroxide Ligands Cooperate with Catalytic Centers in Metal-Organic Frameworks for Efficient Photocatalytic CO 2 Reduction. J Am Chem Soc 2018;140:38–41. https://doi.org/10.1021/jacs.7b10107.
[748] Li, J., Huang, H., Xue W et al. Self-adaptive dual-metal-site pairs in metal-organic frameworks for selective CO2 photoreduction to CH4. Nat Catal 2021;4:719–729. https://doi.org/10.1038/s41929-021-00665-3.
[749] Shi L, Wang T, Zhang H, Chang K, Ye J. Electrostatic Self-Assembly of Nanosized Carbon Nitride Nanosheet onto a Zirconium Metal-Organic Framework for Enhanced Photocatalytic CO2 Reduction. Adv Funct Mater 2015;25:5360–7. https://doi.org/10.1002/adfm.201502253.
[750] Wang G, He CT, Huang R, Mao J, Wang D, Li Y. Photoinduction of Cu single atoms

decorated on UiO-66-NH2for enhanced photocatalytic reduction of CO2to liquid fuels. J Am Chem Soc 2020;142:19339–45. https://doi.org/10.1021/jacs.0c09599.
[751] Gong YN, Zhong W, Li Y, Qiu Y, Zheng L, Jiang J, et al. Regulating photocatalysis by spin-state manipulation of cobalt in covalent organic frameworks. J Am Chem Soc 2020;142:16723–31. https://doi.org/10.1021/jacs.0c07206.
[752] Jiang Z, Xu X, Ma Y, Cho HS, Ding D, Wang C, et al. Filling metal–organic framework mesopores with TiO2 for CO2 photoreduction. Nature 2020;586:549–54. https://doi.org/10.1038/s41586-020-2738-2.
[753] Fu Y, Zhu X, Huang L, Zhang X, Zhang F, Zhu W. Azine-based covalent organic frameworks as metal-free visible light photocatalysts for CO2 reduction with H2O. Appl Catal B Environ 2018;239:46–51. https://doi.org/10.1016/j.apcatb.2018.08.004.
[754] Han B, Ou X, Zhong Z, Liang S, Deng H, Lin Z. Rational Design of FeNi Bimetal Modified Covalent Organic Frameworks for Photoconversion of Anthropogenic CO2 into Widely Tunable Syngas. Small 2020;16. https://doi.org/10.1002/smll.202002985.
[755] Han B, Ou X, Deng Z, Song Y, Tian C, Deng H, et al. Nickel Metal–Organic Framework Monolayers for Photoreduction of Diluted CO2: Metal-Node-Dependent Activity and Selectivity. Angew Chemie - Int Ed 2018;57:16811–5. https://doi.org/10.1002/anie.201811545.
[756] Kajiwara T, Fujii M, Tsujimoto M, Kobayashi K, Higuchi M, Tanaka K, et al. Photochemical Reduction of Low Concentrations of CO2 in a Porous Coordination Polymer with a Ruthenium(II)-CO Complex. Angew Chemie - Int Ed 2016;55:2697–700. https://doi.org/10.1002/anie.201508941.
[757] Ma Y, Tang Q, Sun WY, Yao ZY, Zhu W, Li T, et al. Assembling ultrafine TiO2 nanoparticles on UiO-66 octahedrons to promote selective photocatalytic conversion of CO2 to CH4 at a low concentration. Appl Catal B Environ 2020;270. https://doi.org/10.1016/j.apcatb.2020.118856.
[758] Dong XY, Si YN, Wang QY, Wang S, Zang SQ. Integrating Single Atoms with Different Microenvironments into One Porous Organic Polymer for Efficient Photocatalytic CO2 Reduction. Adv Mater 2021. https://doi.org/10.1002/adma.202101568.
[759] Zhong W, Sa R, Li L, He Y, Li L, Bi J, et al. A Covalent Organic Framework Bearing Single Ni Sites as a Synergistic Photocatalyst for Selective Photoreduction of CO2 to CO. J Am Chem Soc 2019;141:7615–21. https://doi.org/10.1021/jacs.9b02997.
[760] Sun M, Wang C, Sun CY, Zhang M, Wang XL, Su ZM. Ultra stable multinuclear metal complexes as homogeneous catalysts for visible-light driven syngas production from pure and diluted CO2. J Catal 2020;385:70–5. https://doi.org/10.1016/j.jcat.2020.03.005.
[761] Liu DC, Wang HJ, Wang JW, Zhong DC, Jiang L, Lu TB. Highly efficient and selective visible-light driven CO2-to-CO conversion by a Co-based cryptate in H2O/CH3CN solution. Chem Commun 2018;54:11308–11. https://doi.org/10.1039/c8cc04892d.
[762] Ouyang T, Huang HH, Wang JW, Zhong DC, Lu TB. A Dinuclear Cobalt Cryptate as a Homogeneous Photocatalyst for Highly Selective and Efficient Visible-Light Driven CO2Reduction to CO in CH3CN/H2O Solution. Angew Chemie - Int Ed 2017;56:738–43. https://doi.org/10.1002/anie.201610607.
[763] Nakajima T, Tamaki Y, Ueno K, Kato E, Nishikawa T, Ohkubo K, et al. Photocatalytic Reduction of Low Concentration of CO2. J Am Chem Soc 2016;138:13818–21. https://doi.org/10.1021/jacs.6b08824.
[764] Chen Y, Ji G, Guo S, Yu B, Zhao Y, Wu Y, et al. Visible-light-driven conversion of CO2 from air to CO using an ionic liquid and a conjugated polymer. Green Chem 2017;19:5777–81. https://doi.org/10.1039/c7gc02346d.
[765] Xu H, You S, Lang Z, Sun Y, Sun C, Zhou J, et al. Highly Efficient Photoreduction of Low-Concentration CO2 to Syngas by Using a Polyoxometalates/RuII Composite. Chem - A Eur J 2020;26:2735–40. https://doi.org/10.1002/chem.201905155.
[766] Zhao X, Zhou J, Sun CY, You SQ, Wang XL, Su ZM. A ruthenium/polyoxometalate for efficient CO2 photoreduction under visible light in diluted CO2. Nanotechnology 2020;31. https://doi.org/10.1088/1361-6528/ab7d73.

[767] Tang G, Hou L, Li J, Song T, Li J, Yue P, et al. Line defects in plasmatic hollow copper ball boost excellent photocatalytic reaction with pure water under ultra-low CO2 concentration. J Colloid Interface Sci 2021;603:530–8. https://doi.org/10.1016/j.jcis.2021.06.127.
[768] Wu X, Li Y, Zhang G, Chen H, Li J, Wang K, et al. Photocatalytic CO 2 Conversion of M 0.33 WO 3 Directly from the Air with High Selectivity: Insight into Full Spectrum-Induced Reaction Mechanism. J Am Chem Soc 2019;141:5267–74. https://doi.org/10.1021/jacs.8b12928.
[769] Yi L, Zhao W, Huang Y, Wu X, Wang J, Zhang G. Tungsten bronze Cs0.33WO3 nanorods modified by molybdenum for improved photocatalytic CO2 reduction directly from air. Sci China Mater 2020. https://doi.org/10.1007/s40843-019-1263-1.
[770] Han B, Song J, Liang S, Chen W, Deng H, Ou X, et al. Hierarchical NiCo2O4 hollow nanocages for photoreduction of diluted CO2: Adsorption and active sites engineering. Appl Catal B Environ 2020;260. https://doi.org/10.1016/j.apcatb.2019.118208.
[771] Zheng YL, Ren JT, Zhou L, Yuan K, Sun XC, Yin HJ, et al. Biphasic Titania Derivatives of Titanium Metal-Organic Framework Nanoplates for High-Efficiency Photoreduction of Diluted CO2 to Methane. ChemCatChem 2021;13:2215–21. https://doi.org/10.1002/cctc.202002005.
[772] Guan Y, Xia M, Marchetti A, Wang X, Cao W, Guan H, et al. Photocatalytic reduction of CO2 from simulated flue gas with colored anatase. Catalysts 2018;8. https://doi.org/10.3390/catal8020078.
[773] Zhang X, Han F, Shi B, Farsinezhad S, Dechaine GP, Shankar K. Photocatalytic conversion of diluted CO2 into light hydrocarbons using periodically modulated multiwalled nanotube arrays. Angew Chemie - Int Ed 2012;51:12732–5. https://doi.org/10.1002/anie.201205619.
[774] Ali S, Lee J, Kim H, Hwang Y, Razzaq A, Jung JW, et al. Sustained, photocatalytic CO2 reduction to CH4 in a continuous flow reactor by earth-abundant materials: Reduced titania-Cu2O Z-scheme heterostructures. Appl Catal B Environ 2020;279. https://doi.org/10.1016/j.apcatb.2020.119344.
[775] Kang Q, Wang T, Li P, Liu L, Chang K, Li M, et al. Photocatalytic reduction of carbon dioxide by hydrous hydrazine over Au-Cu alloy nanoparticles supported on SrTiO3/TiO2 coaxial nanotube arrays. Angew Chemie - Int Ed 2015;54:841–5. https://doi.org/10.1002/anie.201409183.
[776] Chen W, Liu X, Han B, Liang S, Deng H, Lin Z. Boosted photoreduction of diluted CO2 through oxygen vacancy engineering in NiO nanoplatelets. Nano Res 2021;14:730–7. https://doi.org/10.1007/s12274-020-3105-1.
[777] Liang S, Han B, Ou X, Ye X, Chen W, Deng H, et al. Lattice-strained nickel hydroxide nanosheets for the boosted diluted CO 2 photoreduction . Environ Sci Nano 2021;8:2360–71. https://doi.org/10.1039/d1en00268f.
[778] He Y, Wang Y, Zhang L, Teng B, Fan M. High-efficiency conversion of CO2 to fuel over ZnO/g-C3N4 photocatalyst. Appl Catal B Environ 2015;168–169:1–8. https://doi.org/10.1016/j.apcatb.2014.12.017.
[779] Zhang F, Li YH, Qi MY, Tang ZR, Xu YJ. Boosting the activity and stability of Ag-Cu2O/ZnO nanorods for photocatalytic CO2 reduction. Appl Catal B Environ 2020;268. https://doi.org/10.1016/j.apcatb.2019.118380.
[780] Wang F, Hou T, Zhao X, Yao W, Fang R, Shen K, et al. Ordered Macroporous Carbonous Frameworks Implanted with CdS Quantum Dots for Efficient Photocatalytic CO 2 Reduction . Adv Mater 2021:2102690. https://doi.org/10.1002/adma.202102690.
[781] Cho KM, Kim KH, Park K, Kim C, Kim S, Al-Saggaf A, et al. Amine-functionalized graphene/CdS composite for photocatalytic reduction of CO2. ACS Catal 2017;7:7064–9. https://doi.org/10.1021/acscatal.7b01908.
[782] You S, Guo S, Zhao X, Sun M, Sun C, Su Z, et al. All-inorganic perovskite/graphitic carbon nitride composites for CO2 photoreduction into C1 compounds under low concentrations of CO2. Dalt Trans 2019;48:14115–21. https://doi.org/10.1039/c9dt02468a.

[783] Zhang G, Yang X, He C, Zhang P, Mi H. Constructing a tunable defect structure in TiO2 for photocatalytic nitrogen fixation. J Mater Chem A 2020;8:334–41. https://doi.org/10.1039/c9ta10471b.
[784] Zhao Y, Zhao Y, Shi R, Wang B, Waterhouse GIN, Wu LZ, et al. Tuning Oxygen Vacancies in Ultrathin TiO 2 Nanosheets to Boost Photocatalytic Nitrogen Fixation up to 700 nm. Adv Mater 2019;31. https://doi.org/10.1002/adma.201806482.
[785] Guan R, Wang D, Zhang Y, Liu C, Xu W, Wang J, et al. Enhanced photocatalytic N2 fixation via defective and fluoride modified TiO2 surface. Appl Catal B Environ 2021;282. https://doi.org/10.1016/j.apcatb.2020.119580.
[786] Han Q, Wu C, Jiao H, Xu R, Wang Y, Xie J, et al. Rational Design of High-Concentration Ti3+ in Porous Carbon-Doped TiO2 Nanosheets for Efficient Photocatalytic Ammonia Synthesis. Adv Mater 2021;33. https://doi.org/10.1002/adma.202008180.
[787] Xue X, Chen H, Xiong Y, Chen R, Jiang M, Fu G, et al. Near-Infrared-Responsive Photo-Driven Nitrogen Fixation Enabled by Oxygen Vacancies and Sulfur Doping in Black TiO2-xSy Nanoplatelets. ACS Appl Mater Interfaces 2021;13:4975–83. https://doi.org/10.1021/acsami.0c17947.
[788] Yang J, Bai H, Guo Y, Zhang H, Jiang R, Yang B, et al. Photodriven Disproportionation of Nitrogen and Its Change to Reductive Nitrogen Photofixation. Angew Chemie - Int Ed 2021;60:927–36. https://doi.org/10.1002/anie.202010192.
[789] Wu S, Chen Z, Yue W, Mine S, Toyao T, Matsuoka M, et al. Single-Atom High-Valent Fe(IV) for Promoted Photocatalytic Nitrogen Hydrogenation on Porous TiO2-SiO2. ACS Catal 2021;11:4362–71. https://doi.org/10.1021/acscatal.1c00072.
[790] Bo Y, Wang H, Lin Y, Yang T, Ye R, Li Y, et al. Altering Hydrogenation Pathways in Photocatalytic Nitrogen Fixation by Tuning Local Electronic Structure of Oxygen Vacancy with Dopant. Angew Chemie - Int Ed 2021;60:16085–92. https://doi.org/10.1002/anie.202104001.
[791] Rong X, Chen H, Rong J, Zhang X, Wei J, Liu S, et al. An all-solid-state Z-scheme TiO2/ZnFe2O4 photocatalytic system for the N2 photofixation enhancement. Chem Eng J 2019;371:286–93. https://doi.org/10.1016/j.cej.2019.04.052.
[792] Liu Q, Ai L, Jiang J. MXene-derived TiO2@C/g-C3N4 heterojunctions for highly efficient nitrogen photofixation. J Mater Chem A 2018;6:4102–10. https://doi.org/10.1039/c7ta09350k.
[793] Ying Z, Chen S, Peng T, Li R, Zhang J. Fabrication of an Fe-Doped SrTiO 3 Photocatalyst with Enhanced Dinitrogen Photofixation Performance. Eur J Inorg Chem 2019;2019:2182–92. https://doi.org/10.1002/ejic.201900098.
[794] Zhao Z, Wang D, Gao R, Wen G, Feng M, Song G, et al. Magnetic-Field-Stimulated Efficient Photocatalytic N2 Fixation over Defective BaTiO3 Perovskites. Angew Chemie - Int Ed 2021;60:11910–8. https://doi.org/10.1002/anie.202100726.
[795] Janet CM, Navaladian S, Viswanathan B, Varadarajan TK, Viswanath RP. Heterogeneous wet chemical synthesis of superlattice-type hierarchical ZnO architectures for concurrent H2 production and N2 reduction. J Phys Chem C 2010;114:2622–32. https://doi.org/10.1021/jp908683x.
[796] Zhao W, Xi H, Zhang M, Li Y, Chen J, Zhang J, et al. Enhanced quantum yield of nitrogen fixation for hydrogen storage with in situ-formed carbonaceous radicals. Chem Commun 2015;51:4785–8. https://doi.org/10.1039/c5cc00589b.
[797] Devthade V, Gupta A, Umare SS. Graphitic carbon nitride-γ-gallium oxide (GCN-γ - Ga2O3) nanohybrid photocatalyst for dinitrogen fixation and pollutant decomposition. ACS Appl Nano Mater 2018;1:5581–8. https://doi.org/10.1021/acsanm.8b01145.
[798] Zhao Z, Choi C, Hong S, Shen H, Yan C, Masa J, et al. Surface-engineered oxidized two-dimensional Sb for efficient visible light-driven N2 fixation. Nano Energy 2020;78. https://doi.org/10.1016/j.nanoen.2020.105368.
[799] Sun S, An Q, Wang W, Zhang L, Liu J, Goddard WA. Efficient photocatalytic reduction of dinitrogen to ammonia on bismuth monoxide quantum dots. J Mater Chem A 2017;5:201–9. https://doi.org/10.1039/C6TA09275F.

[800] Ying Z, Chen S, Zhang S, Peng T, Li R. Efficiently enhanced N2 photofixation performance of sea-urchin-like W18O49 microspheres with Mn-doping. Appl Catal B Environ 2019;254:351–9. https://doi.org/10.1016/j.apcatb.2019.05.005.
[801] Zhang N, Jalil A, Wu D, Chen S, Liu Y, Gao C, et al. Refining Defect States in W18O49 by Mo Doping: A Strategy for Tuning N2 Activation towards Solar-Driven Nitrogen Fixation. J Am Chem Soc 2018;140:9434–43. https://doi.org/10.1021/jacs.8b02076.
[802] Qiu P, Huang C, Dong G, Chen F, Zhao F, Yu Y, et al. Plasmonic gold nanocrystals simulated efficient photocatalytic nitrogen fixation over Mo doped W18O49nanowires. J Mater Chem A 2021;9:14459–65. https://doi.org/10.1039/d1ta03339e.
[803] Hou T, Xiao Y, Cui P, Huang Y, Tan X, Zheng X, et al. Operando Oxygen Vacancies for Enhanced Activity and Stability toward Nitrogen Photofixation. Adv Energy Mater 2019;9. https://doi.org/10.1002/aenm.201902319.
[804] Zhang Y, Hou T, Xu Q, Wang Q, Bai Y, Yang S, et al. Dual-Metal Sites Boosting Polarization of Nitrogen Molecules for Efficient Nitrogen Photofixation. Adv Sci 2021;8. https://doi.org/10.1002/advs.202100302.
[805] Li X, Wang W, Jiang D, Sun S, Zhang L, Sun X. Efficient Solar-Driven Nitrogen Fixation over Carbon–Tungstic-Acid Hybrids. Chem - A Eur J 2016;22:13819–22. https://doi.org/10.1002/chem.201603277.
[806] Wang L, Li M, Zhang Q, Li F, Xu L. Constructing electron transfer pathways and active centers over W18O49nanowires by doping Fe3+and incorporating g-C3N5for enhanced photocatalytic nitrogen fixation. Inorg Chem Front 2021;8:3566–75. https://doi.org/10.1039/d1qi00503k.
[807] Wang T, Feng C, Liu J, Wang D, Hu H, Hu J, et al. Bi2WO6 hollow microspheres with high specific surface area and oxygen vacancies for efficient photocatalysis N2 fixation. Chem Eng J 2021;414. https://doi.org/10.1016/j.cej.2021.128827.
[808] Xiao C, Hu H, Zhang X, MacFarlane DR. Nanostructured Gold/Bismutite Hybrid Heterocatalysts for Plasmon-Enhanced Photosynthesis of Ammonia. ACS Sustain Chem Eng 2017;5:10858–63. https://doi.org/10.1021/acssuschemeng.7b02788.
[809] Li H, Shang J, Ai Z, Zhang L. Efficient visible light nitrogen fixation with BiOBr nanosheets of oxygen vacancies on the exposed {001} Facets. J Am Chem Soc 2015;137:6393–9. https://doi.org/10.1021/jacs.5b03105.
[810] Li P, Zhou Z, Wang Q, Guo M, Chen S, Low J, et al. Visible-Light-Driven Nitrogen Fixation Catalyzed by Bi5O7Br Nanostructures: Enhanced Performance by Oxygen Vacancies. J Am Chem Soc 2020;142:12430–9. https://doi.org/10.1021/jacs.0c05097.
[811] Huang Y, Zhu Y, Chen S, Xie X, Wu Z, Zhang N. Schottky Junctions with Bi Cocatalyst for Taming Aqueous Phase N2 Reduction toward Enhanced Solar Ammonia Production. Adv Sci 2021;8. https://doi.org/10.1002/advs.202003626.
[812] Liu Y, Hu Z, Yu JC. Fe enhanced visible-light-driven nitrogen fixation on biobr nanosheets. Chem Mater 2020;32:1488–94. https://doi.org/10.1021/acs.chemmater.9b04448.
[813] Shen Z, Li F, Lu J, Wang Z, Li R, Zhang X, et al. Enhanced N2 photofixation activity of flower-like BiOCl by in situ Fe(III) doped as an activation center. J Colloid Interface Sci 2021;584:174–81. https://doi.org/10.1016/j.jcis.2020.09.111.
[814] Zhang N, Li L, Shao Q, Zhu T, Huang X, Xiao X. Fe-Doped BiOCl Nanosheets with Light-Switchable Oxygen Vacancies for Photocatalytic Nitrogen Fixation. ACS Appl Energy Mater 2019;2:8394–8. https://doi.org/10.1021/acsaem.9b01961.
[815] Xiao C, Wang H, Zhang L, Sun S, Wang W. Enhanced Photocatalytic Nitrogen Fixation on MoO2/BiOCl Composite. ChemCatChem 2019;11:6467–72. https://doi.org/10.1002/cctc.201901635.
[816] Guo L, Han X, Zhang K, Zhang Y, Zhao Q, Wang D, et al. In-situ construction of 2D/2D znin2s4/BiOCl heterostructure with enhanced photocatalytic activity for N2 fixation and phenol degradation. Catalysts 2019;9. https://doi.org/10.3390/catal9090729.
[817] Bai Y, Ye L, Chen T, Wang L, Shi X, Zhang X, et al. Facet-Dependent Photocatalytic N2 Fixation of Bismuth-Rich Bi5O7I Nanosheets. ACS Appl Mater Interfaces 2016;8:27661–8. https://doi.org/10.1021/acsami.6b08129.

[818] Lan M, Zheng N, Dong X, Hua C, Ma H, Zhang X. Bismuth-rich bismuth oxyiodide microspheres with abundant oxygen vacancies as an efficient photocatalyst for nitrogen fixation. Dalt Trans 2020;49:9123–9. https://doi.org/10.1039/d0dt01332c.
[819] Rong X, Mao Y, Xu J, Zhang X, Zhang L, Zhou X, et al. Bi2Te3 sheet contributing to the formation of flower-like BiOCl composite and its N2 photofixation ability enhancement. Catal Commun 2018;116:16–9. https://doi.org/10.1016/j.catcom.2018.07.018.
[820] Xue X, Chen R, Yan C, Hu Y, Zhang W, Yang S, et al. Efficient photocatalytic nitrogen fixation under ambient conditions enabled by the heterojunctions of n-type Bi2MoO6 and oxygen-vacancy-rich p-type BiOBr. Nanoscale 2019;11:10439–45. https://doi.org/10.1039/c9nr02279a.
[821] Zhang S, Zhao Y, Shi R, Zhou C, Waterhouse GIN, Wang Z, et al. Sub-3 nm Ultrafine Cu2O for Visible Light Driven Nitrogen Fixation. Angew Chemie - Int Ed 2021;60:2554–60. https://doi.org/10.1002/anie.202013594.
[822] Ojha N, Bajpai A, Kumar S. Enriched oxygen vacancies of Cu2O/SnS2/SnO2 heterostructure for enhanced photocatalytic reduction of CO2 by water and nitrogen fixation. J Colloid Interface Sci 2021;585:764–77. https://doi.org/10.1016/j.jcis.2020.10.056.
[823] Su Q, Wang W, Zhang Z, Duan J. Enhanced photocatalytic performance of Cu2O/MoS2/ZnO composites on Cu mesh substrate for nitrogen reduction. Nanotechnology 2021;32. https://doi.org/10.1088/1361-6528/abf378.
[824] Xing P, Wu S, Chen Y, Chen P, Hu X, Lin H, et al. New Application and Excellent Performance of Ag/KNbO3 Nanocomposite in Photocatalytic NH3 Synthesis. ACS Sustain Chem Eng 2019;7:12408–18. https://doi.org/10.1021/acssuschemeng.9b01938.
[825] Zhang W, Xing P, Zhang J, Chen L, Yang J, Hu X, et al. Facile preparation of novel nickel sulfide modified KNbO3 heterojunction composite and its enhanced performance in photocatalytic nitrogen fixation. J Colloid Interface Sci 2021;590:548–60. https://doi.org/10.1016/j.jcis.2021.01.086.
[826] Chen L, Dai X, Li X, Wang J, Chen H, Hu X, et al. A novel Bi2S3/KTa0.75Nb0.25O3nanocomposite with high efficiency for photocatalytic and piezocatalytic N2fixation. J Mater Chem A 2021;9:13344–54. https://doi.org/10.1039/d1ta02270a.
[827] Han Q, Bai X, Chen J, Feng S, Gao W, Tu W, et al. Hollow InVO 4 Nanocuboid Assemblies toward Promoting Photocatalytic N 2 Conversion Performance . Adv Mater 2021:2006780. https://doi.org/10.1002/adma.202006780.
[828] Dong G, Ho W, Wang C. Selective photocatalytic N2 fixation dependent on g-C3N4 induced by nitrogen vacancies. J Mater Chem A 2015;3:23435–41. https://doi.org/10.1039/c5ta06540b.
[829] Wang W, Zhou H, Liu Y, Zhang S, Zhang Y, Wang G, et al. Formation of B□N□C Coordination to Stabilize the Exposed Active Nitrogen Atoms in g-C3N4 for Dramatically Enhanced Photocatalytic Ammonia Synthesis Performance. Small 2020;16. https://doi.org/10.1002/smll.201906880.
[830] Shiraishi Y, Shiota S, Kofuji Y, Hashimoto M, Chishiro K, Hirakawa H, et al. Nitrogen Fixation with Water on Carbon-Nitride-Based Metal-Free Photocatalysts with 0.1% Solar-to-Ammonia Energy Conversion Efficiency. ACS Appl Energy Mater 2018;1:4169–77. https://doi.org/10.1021/acsaem.8b00829.
[831] Wang W, Zhang H, Zhang S, Liu Y, Wang G, Sun C, et al. Potassium-Ion-Assisted Regeneration of Active Cyano Groups in Carbon Nitride Nanoribbons: Visible-Light-Driven Photocatalytic Nitrogen Reduction. Angew Chemie - Int Ed 2019;58:16644–50. https://doi.org/10.1002/anie.201908640.
[832] Hu S, Chen X, Li Q, Li F, Fan Z, Wang H, et al. Fe3+ doping promoted N2 photofixation ability of honeycombed graphitic carbon nitride: The experimental and density functional theory simulation analysis. Appl Catal B Environ 2017;201:58–69. https://doi.org/10.1016/j.apcatb.2016.08.002.
[833] Li J, Li Q, Chen Y, Lv S, Liao X, Yao Y. Size effects of Ag nanoparticle for N2

photofixation over Ag/g-C3N4: Built-in electric fields determine photocatalytic performance. Colloids Surfaces A Physicochem Eng Asp 2021;626:127053. https://doi.org/10.1016/j.colsurfa.2021.127053.
[834] Diarmand-Khalilabad H, Habibi-Yangjeh A, Seifzadeh D, Asadzadeh-Khaneghah S, Vesali-Kermani E. g-C3N4 nanosheets decorated with carbon dots and CdS nanoparticles: Novel nanocomposites with excellent nitrogen photofixation ability under simulated solar irradiation. Ceram Int 2019;45:2542–55. https://doi.org/10.1016/j.ceramint.2018.10.185.
[835] Mou H, Wang J, Yu D, Zhang D, Chen W, Wang Y, et al. Fabricating Amorphous g-C3N4/ZrO2 Photocatalysts by One-Step Pyrolysis for Solar-Driven Ambient Ammonia Synthesis. ACS Appl Mater Interfaces 2019;11:44360–5. https://doi.org/10.1021/acsami.9b16432.
[836] Hu S, Li Y, Li F, Fan Z, Ma H, Li W, et al. Construction of g-C3N4/Zn0.11Sn0.12Cd0.88S1.12 Hybrid Heterojunction Catalyst with Outstanding Nitrogen Photofixation Performance Induced by Sulfur Vacancies. ACS Sustain Chem Eng 2016;4:2269–78. https://doi.org/10.1021/acssuschemeng.5b01742.
[837] Li H, Liu Y, Liu Y, Wang L, Tang R, Deng P, et al. Efficient Visible Light Driven Ammonia Synthesis on Sandwich Structured C3N4/MoS2/Mn3O4 catalyst. Appl Catal B Environ 2021;281. https://doi.org/10.1016/j.apcatb.2020.119476.
[838] Jiang H, Zang C, Zhang Y, Wang W, Yang C, Sun B, et al. 2D MXene-derived Nb2O5/C/Nb2C/g-C3N4heterojunctions for efficient nitrogen photofixation. Catal Sci Technol 2020;10:5964–72. https://doi.org/10.1039/d0cy00656d.
[839] Fang Y, Xue Y, Hui L, Yu H, Li Y. Graphdiyne@Janus Magnetite for Photocatalytic Nitrogen Fixation. Angew Chemie - Int Ed 2021;60:3170–4. https://doi.org/10.1002/anie.202012357.
[840] Li XH, Chen WL, Tan HQ, Li FR, Li JP, Li YG, et al. Reduced State of the Graphene Oxide@Polyoxometalate Nanocatalyst Achieving High-Efficiency Nitrogen Fixation under Light Driving Conditions. ACS Appl Mater Interfaces 2019;11:37927–38. https://doi.org/10.1021/acsami.9b12328.
[841] Wang SX, Maimaiti H, Xu B, Awati A, Zhou G Bin, Cui Y dan. Synthesis and visible-light photocatalytic N2/H2O to ammonia of ZnS nanoparticles supported by petroleum pitch-based graphene oxide. Appl Surf Sci 2019;493:514–24. https://doi.org/10.1016/j.apsusc.2019.06.287.
[842] Han H, Yang Y, Liu J, Zheng X, Wang X, Meng S, et al. Effect of Zn vacancies in Zn3In2S6 nanosheets on boosting photocatalytic N2 fixation. ACS Appl Energy Mater 2020;3:11275–84. https://doi.org/10.1021/acsaem.0c02202.
[843] Sun S, Li X, Wang W, Zhang L, Sun X. Photocatalytic robust solar energy reduction of dinitrogen to ammonia on ultrathin MoS2. Appl Catal B Environ 2017;200:323–9. https://doi.org/10.1016/j.apcatb.2016.07.025.
[844] Liu B, Qin J, Yang H, Hu X, Zhao W, Zhang Z. MoS2 nano-flowers stacked by ultrathin sheets coupling with oxygen self-doped porous biochar for efficient photocatalytic N2 fixation. ChemCatChem 2020;12:5221–8. https://doi.org/10.1002/cctc.202000992.
[845] Ye L, Han C, Ma Z, Leng Y, Li J, Ji X, et al. Ni2P loading on Cd0.5Zn0.5S solid solution for exceptional photocatalytic nitrogen fixation under visible light. Chem Eng J 2017;307:311–8. https://doi.org/10.1016/j.cej.2016.08.102.
[846] Zhao Y, Zheng L, Shi R, Zhang S, Bian X, Wu F, et al. Alkali Etching of Layered Double Hydroxide Nanosheets for Enhanced Photocatalytic N2 Reduction to NH3. Adv Energy Mater 2020;10. https://doi.org/10.1002/aenm.202002199.
[847] Zhang S, Zhao Y, Shi R, Zhou C, Waterhouse GIN, Wu LZ, et al. Efficient Photocatalytic Nitrogen Fixation over Cuδ+-Modified Defective ZnAl-Layered Double Hydroxide Nanosheets. Adv Energy Mater 2020;10. https://doi.org/10.1002/aenm.201901973.
[848] Zhao Y, Zhao Y, Waterhouse GIN, Zheng L, Cao X, Teng F, et al. Layered-Double-Hydroxide Nanosheets as Efficient Visible-Light-Driven Photocatalysts for Dinitrogen Fixation. Adv Mater 2017;29. https://doi.org/10.1002/adma.201703828.

[849] Liu X, Li Y, Zhang J, Lu J. Ultrathin Ni/V-layered double hydroxide nanosheets for efficient visible-light-driven photocatalytic nitrogen reduction to ammonia. Nano Res 2021. https://doi.org/10.1007/s12274-021-3641-3.
[850] Huang H, Wang XS, Philo D, Ichihara F, Song H, Li Y, et al. Toward visible-light-assisted photocatalytic nitrogen fixation: A titanium metal organic framework with functionalized ligands. Appl Catal B Environ 2020;267. https://doi.org/10.1016/j.apcatb.2020.118686.
[851] Ojha N, Kumar S. Tri-phase photocatalysis for CO2 reduction and N2 fixation with efficient electron transfer on a hydrophilic surface of transition-metal-doped MIL-88A (Fe). Appl Catal B Environ 2021;292. https://doi.org/10.1016/j.apcatb.2021.120166.
[852] Shang S, Xiong W, Yang C, Johannessen B, Liu R, Hsu HY, et al. Atomically Dispersed Iron Metal Site in a Porphyrin-Based Metal-Organic Framework for Photocatalytic Nitrogen Fixation. ACS Nano 2021;15:9670–8. https://doi.org/10.1021/acsnano.0c10947.
[853] Zhao Z, Ren H, Yang D, Han Y, Shi J, An K, et al. Boosting Nitrogen Activation via Bimetallic Organic Frameworks for Photocatalytic Ammonia Synthesis. ACS Catal 2021;11:9986–95. https://doi.org/10.1021/acscatal.1c02465.
[854] Li J, Liu P, Tang Y, Huang H, Cui H, Mei D, et al. Single-Atom Pt-N3 Sites on the Stable Covalent Triazine Framework Nanosheets for Photocatalytic N2 Fixation. ACS Catal 2020;10:2431–42. https://doi.org/10.1021/acscatal.9b04925.
[855] Bian S, Wen M, Wang J, Yang N, Chu PK, Yu XF. Edge-Rich Black Phosphorus for Photocatalytic Nitrogen Fixation. J Phys Chem Lett 2020;11:1052–8. https://doi.org/10.1021/acs.jpclett.9b03507.

Vitae

Yanjie Wang

Yanjie Wang received her PhD in physical chemistry from National Center for Nanoscience and Technology, China, in 2018. After that She joined National Center for Nanoscience and Technology. Her current research focuses on the rational design of nanomaterials and their application in sustainable energy.

Juliana Arriel Torres

Meital Shviro

Marcelo Carmo
Dr. Sciences (Sao Paulo University – USP, Brazil, 2007), BSc. Chemistry (USP, 2000). Posdoc at Yale University (2009-2011) and Forschungszentrum Jülich (2011-2013). From 2014 he is Researcher of Forschungszentrum Jülich (Helmholtz Association – Germany), as Group Leader (2014-2015) and from 2015 as Head of Department (Electrochemistry Electrolysis). From 2019 to now he serves as Co-Head of Institute IEK-14
His research interests are the development of novel electrocatalysts for PEM fuel cells / electrolysis and the technology demonstration of large-scale photoelectrochemical system for solar fuel production. He has published 73 papers (Web of Science) with 4,000 citations, H index 26.

Tao He
Dr. Chemistry (Chinese Academy of Sciences – CAS, China, 2002), BSc. Chemistry (Dalian University of Technology, China, 1993). Posdoc at Rice University (2005-2009) and Weizmann Institute of Science (2002-2005). Since 2009 he is Professor at the National Center for Nanoscience and Technology (NCNST, China) and from 2015 Professor at the University of Chinese Academy of Sciences, China. Prof. He has research interests on R&D of novel photoelectric functional nanomaterials and related devices that can efficiently utilize light energy at a relatively low cost, mainly including artificial photosynthesis (conversion of CO_2 into C1 & C2 compounds over nanocatalysts) and new-concept optoelectronic devices for IR and THz detection. He has published about 144 papers in peer-reviewed journals, including 7 review articles, with more than 4,000 citations and H-Index 35 (Web of Science), 16 applied patents and 6 of them granted.

Caue Ribeiro
Dr. Physical Chemistry (Sao Carlos Federal University – UFSCar, Brazil, 2005), Materials Engineer (UFSCar, 1999). Since 2007 he is Senior Researcher at Brazilian Agriculture Research Corporation (Embrapa, Brazil) and professor in the Chemistry Graduation Program of Sao Carlos Federal University (UFSCar, Brazil). He has received the Chinese Academy of Sciences (CAS) President's International Fellowship Initiative (PIFI) as Visiting Researcher, and the Alexander von Humboldt Fellowship for Experienced Scientists (Germany) being hosted as Visiting Scientist at Forschungszentrum Jülich (2018 to 2020). His research interests are the development of photocatalysts for water

decontamination and energy conversion (CO_2 photoreduction and CH_4 controlled photooxidation); and controlled release of fertilizers by nanocomposite design. He has published 197 papers (Web of Science) with more than 5,300 citations in Web of Science and H-Index 41. He has also published 4 book chapters, 1 textbook in Materials Science, edited 1 book in Nanotechnology and requested 6 patents.

Figure captions

Figure 1. World population with and without synthetic nitrogen fertilizers: Estimates of the global population reliant on synthetic nitrogenous fertilizers, produced via the Haber-Bosch process for food production. Best estimates project that just over half of the global population could be sustained without reactive nitrogen fertilizer derived from the Haber-Bosch. Plotted using the dataset in *Our World in Data*, compiled from [193–195]. Reprint under the terms of the Creative Common Attribution 4.0 International License.

Figure 2. An overview of emissions and dynamic processes in agriculture that can be benefited by photocatalytic materials. Pollutants as N_2O, NO_2 and CH_4 can be abated or converted to other chemicals, and CO_2 can be reutilized. Inputs (fertilizers and chemicals) are also a source of contamination, which can be addressed by photocatalytic materials as well. Reprinted from Ref. [18], page 1.6, permission according to IPCC Copyright Guide (https://www.ipcc.ch/copyright/).

Figure 3. Scheme of redox reactions that can performed at the surface of irradiated semiconductors. At right, the redox potentials of different reactions of interest, according to [185], corrected to pH 7 and 300 K through Nernst Equation.

Figure 4. Illustration of the photosensitization process with dyes (direct molecule-semiconductor electron transference): a) Molecular structures of dyes (NT35, MS4, MS5, and XY1b) and copper complex ([Cu(I)(tmby)2][TFSI] and [Cu(II)(tmby)2][TFSI]2, tmby = 4,4′,6,6′-tetramethyl-2,2′-bipyridine; TFSI = bis(trifluoromethylsulfonyl)imide). b) UV–Vis absorption spectra of NT35, MS4, MS5, and XY1b adsorbed on 2.2 μm thick transparent TiO_2 films, showing the absorption in lower energies than semiconductor's

bandgap. c) Energy levels diagram of TiO_2, dyes, and [Cu(I)tmby)2][TFSI], indicating that dyes' LUMO levels (NT35, MS4, MS5 and XY1b) superpose the TiO_2 conduction band, allowing the direct electron transference. Reprint under the terms of the Creative Common Attribution 4.0 International License, [35].

Figure 5. Overview of possible reactions driven by photocatalysts, considering the oxidative (h^+) and reductive (e^-) contributions of *excitons.*

Figure 6. Pesticide utilization (in Million tons) in world and divided by continent, from 1990 to 2017. The growing tendency is seen in all the main crop producers, suggesting the increasing in contamination of water bodies by lixiviation. Plotted with database collected by *Our World in Data* [196], based in *Food and Agriculture Organization (FAO)* data [1]. Reprint under the terms of the Creative Common Attribution 4.0 International License.

Figure 7. TEM images and the related high-resolution TEM selected regions of: (A,B) TiO_2 P25, and of the same P25 powder after thermal activation in vacuum at: (D,E) 773 K and (G,H) 1,023 K; (C,F,I) fast-Fourier-transform (FFT) images of the selected nanocrystals in (A,D,G), as obtained from [111] or [-111] zone axis directions. Reprint under the terms of the Creative Common Attribution 4.0 International License, [43].

Figure 8. A general scheme of semiconductors' heterojunctions. Z-Scheme (left) comprises those systems where two semiconductors are in contact, and the interface allows electrons and holes to migrate to different materials, electrons to the upper conduction band and holes to the down valence band; Heterostructures (right) are those where the

Fermi levels of both materials are aligned at interface, promoting a contrary potential that pumps electrons to the down conduction band and holes to the upper valence band. At right, a hypothetical comparison with electrochemical pairs indicating that each charge carrier will be involved in a specific reaction (e.g., holes in O_2 evolution and electrons in CH_4 oxidation).

Figure 9. Effects of embryonic atrazine exposure on adult female zebrafish: a representative image of an adult female from the control group (a) compared to an adult female with a swollen abdomen in the 30 ppb developmentally exposed group (b). There was a ~5% incidence rate observed in this treatment group (~24–37 females assessed in each treatment of the four replicates). No significant difference in overall body weight was seen between the control and 30 ppb treatment group (c), but a significant increase in ovary weight was observed (d) (4 replicates with 10 female fish assessed per treatment replicate). Moreover, in comparison to the normal adult female zebrafish (e) an increase in atretic ovarian follicles (black arrow) was observed in those fish that presented with abdominal swelling (f) determined to be from an inability to release eggs (4 replicates with 10 female fish assessed per treatment replicate). Error bars are expressed as ± SD. (*$p < 0.05$). Reprinted under the terms of the Creative Common Attribution 4.0 International License, [59].

Figure 10. Example of components of pesticide commercial formulation. WG: Water Dispersible Granule (pesticide and adjuvants in dry form), SC: Suspension Concentrate, EC: Emulsifiable Concentrate, OD: Oil Dispersion. Reprinted under the terms of the NSW Department of Industry, [197].

Figure 11. Study effect of agriculture drainage irrigation water over propyzamide and paracetamol solutions (10 mg/L) photocatalytic decay compared with photolytic and photocatalytic decays using dionized water solutions (a); Reactor support cross section, the air inlet is shown on the right side and of purified water outlet is shown on the left side, as well as seal rings on upper and bottom parts (b) and (c) Photograph of the experimental setup of the purification system. Reprinted with permission, [63].

Figure 12. Seeds and their contaminants treated with Ag@TiO_2 and TiO_2-Cu^{2+}. (a) Treatment of *A. thaliana* seeds with 10 mg/mL of nanostructured materials prior to cultivation in vitro; (b) fungal contaminants seeds exposed to 10 mg/mL of nanostructured materials; each treatment was performed in triplicate. Reprinted under the terms of the Creative Common Attribution 4.0 International License, [74].

Figure 13. Effect of four different levels of ZnO-NPs alone and combined with biochar on Chlorophyll *a* (a), Chlorophyll *b* (b), photosynthesis rate (c), Stomatal conductance (d) and transpiration rate (e) in maize leaf under Cd stress. Bars showed the standard deviation for four replicates. Different letters on the bars demonstrate the significant differences between treatments at $p \leq 0.05$. In figures, ns = non-significant; and *** = significant at 0.001 level.; BC = biochar. Reprinted with permission, [77].

Figure 14. Nano-TiO_2 spray effect (a) and (b) Decontamination efficient of NOx under different time section. Reprinted with permission, [101].

Figure 15. A scheme of N cycle in soils boosted by photocatalytic materials. Black arrows represent the classical, well-known mechanisms: (A) gases (NH_3, NO, N_2O, and N_2)

are released to the atmosphere by nitrification or denitrification and are also produced by industrial and biological N_2 fixation, (B) gains as organic N from crops and animal residues, (C) transformations among N forms ($N_{organic}$, NH^+_4, NO_2^{2-} , NO_3^- or N gases), and (D) losses from water and wind erosion, fires and leaching. Red arrows complete this complex N cycle introducing the photochemical reactions affecting organic matter (especially soluble organic matter, SON), NO gas and nitrates. Reprinted with permission, [105].

Figure 16. Phytotoxicity effects of ZnO nanoparticles. TEM images showing the presence of nanoparticles covered by cytoplasm in the endodermal and vascular cells of the ryegrass root under the treatment of ZnO nanoparticles: A) part of a vascular cell enlarged from the upper rectangle area of B; B) part of a cross section of a ryegrass root; C) part of an endodermal cell enlarged from the lower rectangle area of B; the insert of panel C is magnified from the upper rectangle area of C. *nu:* nucleus; *ne:* nuclear envelop; *np:* nanoparticles covered by cytoplasm; *vs:* vascular cylinder with highly vacuolated metaxylem cells; *ed:* endodermis; *ct:* cortex; *cw:* cell wall. D) Ryegrass biomass reduction and E) root/shoot Zn contents under the treatments of ZnO nanoparticles or Zn^{2+}. Reprinted with permission, [108].

Figure 17. A general scheme of methane production through biodigestion. Reprinted under the terms of the Creative Common Attribution 4.0 International License, [114].

Figure 18. Photocatalytic H_2 production from waste H_2S over all tested samples under visible light irradiation ($\lambda > 420$ nm). Reprinted with permission, [143].

Figure 19. Mechanism for the oxidative degradation of lignin under TiO_2/UV catalyst system. Reprinted with permission, [156].

Figure 20. Conversion of biomass resources to methanol: Catalyst screening. Reaction conditions: 10 mg of glycerol, 10 mg of catalyst, 0.8 mL of MeCN, 0.2 mL of water, 365 nm LED (18 W, 55mWcm^{-2}) irradiation for 12 h. Reprinted under the terms of the Creative Common Attribution 4.0 International License, [166].

Figure 21. Example of monolithic Ag-pCN/TiO_2 structure used for H_2 production using glycerol as sacrificial agent: FESEM images of (a) pCN; (b) TiO_2; (c) Ag/TiO_2, (d) pCN/TiO_2; (e) Ag pCN/TiO_2; (f) uncoated monolith channels; (g) Ag-pCN/TiO_2 catalyst over the monolith channels surface and (h) nanoparticles of composite over the channel surface. Reprinted with permission, [169].

Figure 22. Schematic of the proposed mechanism of electrocatalytic nitrogen reduction reaction process, which is inspired by the proposed mechanism occurring in nitrogenase. Reprinted with permission, [188].

Figure 1

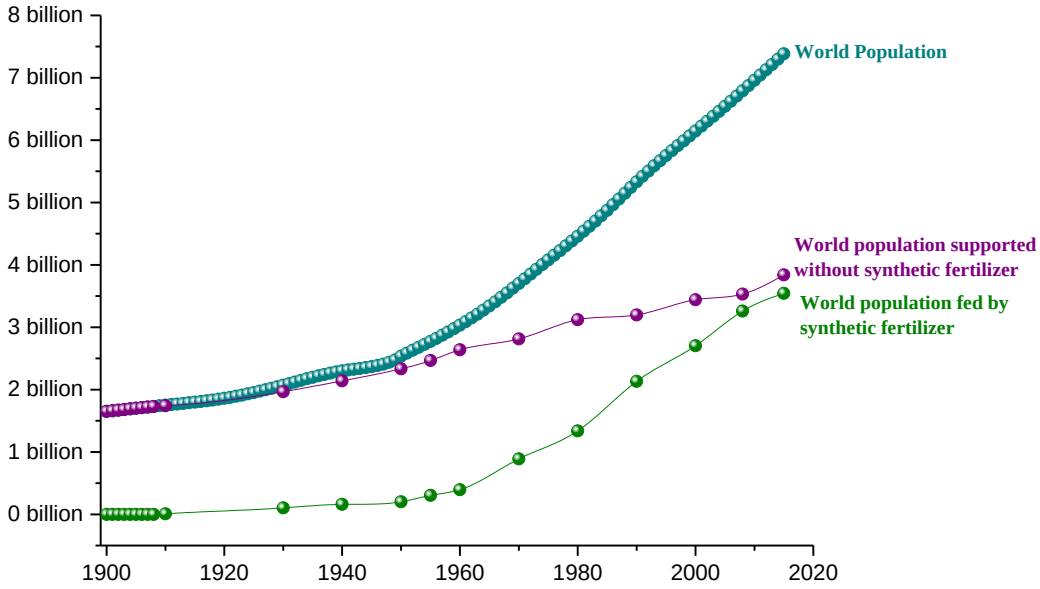
8 billion
7 billion
6 billion
5 billion
4 billion
3 billion
2 billion
1 billion
0 billion
1900
1920
1940
1960
1980
2000
2020
World Population
World population supported without synthetic fertilizer
World population fed by synthetic fertilizer

Figure 2

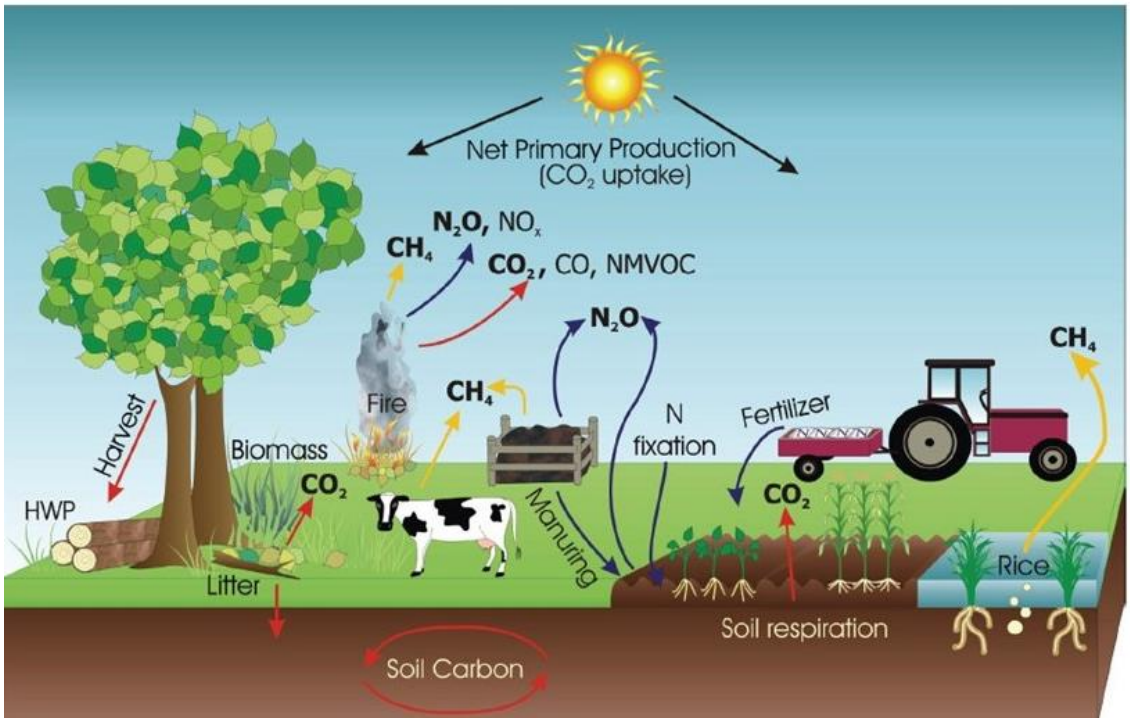
Net Primary Production
(CO_2 uptake)
N_2O, NO_x
CH_4
CO_2, CO, NMVOC
N_2O
CH_4
CH_4
Fire
Harvest
Biomass
CO_2
HWP
Litter
Manuring
N
fixation
Fertilizer
CO_2
Rice
Soil respiration
Soil Carbon

Figure 3

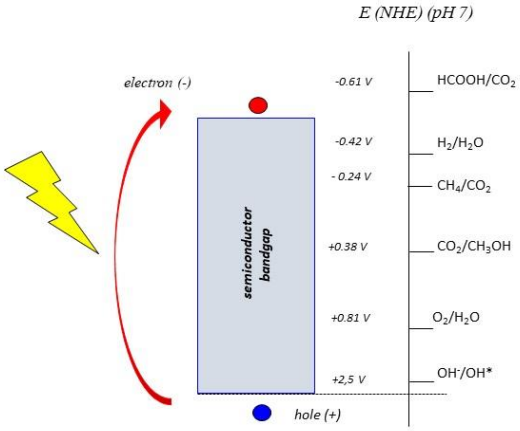

Reaction		E° (V vs. NHE, pH 7)
$3/2N_2 + H^+ + e^- \rightarrow HN_3$	(1)	-3.75
$N_2 + 2H_2O + 4H^+ + 2e^- \rightarrow 2NH_3OH^+$	(3)	-2.24
$CO_2 + 2e^- \rightarrow {}^{\bullet}CO_2^-$	(4)	-1.90
$N_2 + 5H^+ + 4e^- \rightarrow N_2H_5^+$	(7)	-0.63
$CO_2 + 2H^+ + 2e^- \rightarrow HCOOH$	(8)	-0.61
$CO_2 + 2H^+ + 2e^- \rightarrow CO + H_2O$	(9)	-0.53
$CO_2 + 4H^+ + 4e^- \rightarrow HCHO + H_2O$	(10)	-0.48
$O_2 + H^+ + e^- \rightarrow HO_2^{\bullet}$	(11)	-0.46
$2H^+ + 2e^- \rightarrow H_2$	(12)	-0.42
$CO_2 + 6H^+ + 6e^- \rightarrow CH_3OH + H_2O$	(13)	-0.38
$CO_2 + 8H^+ + 8e^- \rightarrow CH_4 + 2H_2O$	(14)	-0.24
$S + 2H^+ + 2e^- \rightarrow H_2S$	(16)	-0.24
$N_2 + 8H^+ + 6e^- \rightarrow 2NH_4^+$	(15)	-0.14
$NO_3^- + 2H^+ + e^- \rightarrow 1/2N_2O_4 + H_2O$	(17)	+0.38
$NO_3^- + 3H^+ + 2e^- \rightarrow HNO_2 + H_2O$	(18)	+0.53
$NO_3^- + 4H^+ + 3e^- \rightarrow NO + 2H_2O$	(19)	+0.54
$2H_2O + 4h^+ \rightarrow O_2 + 4H^+$	(20)	+0.81
$HO_2^{\bullet} + H^+ + e^- \rightarrow H_2O_2$	(5)	+1.03
$NO^+ + e^- \rightarrow NO$	(21)	+1.05
$2NO + 2H^+ + 2e^- \rightarrow N_2O + H_2O$	(22)	+1.17
$N_2O + 2H^+ + 2e^- \rightarrow N_2 + H_2O$	(23)	+1.35
$OH^{\bullet} + H^+ + e^- \rightarrow H_2O$	(2)	+2.15

Figure 4

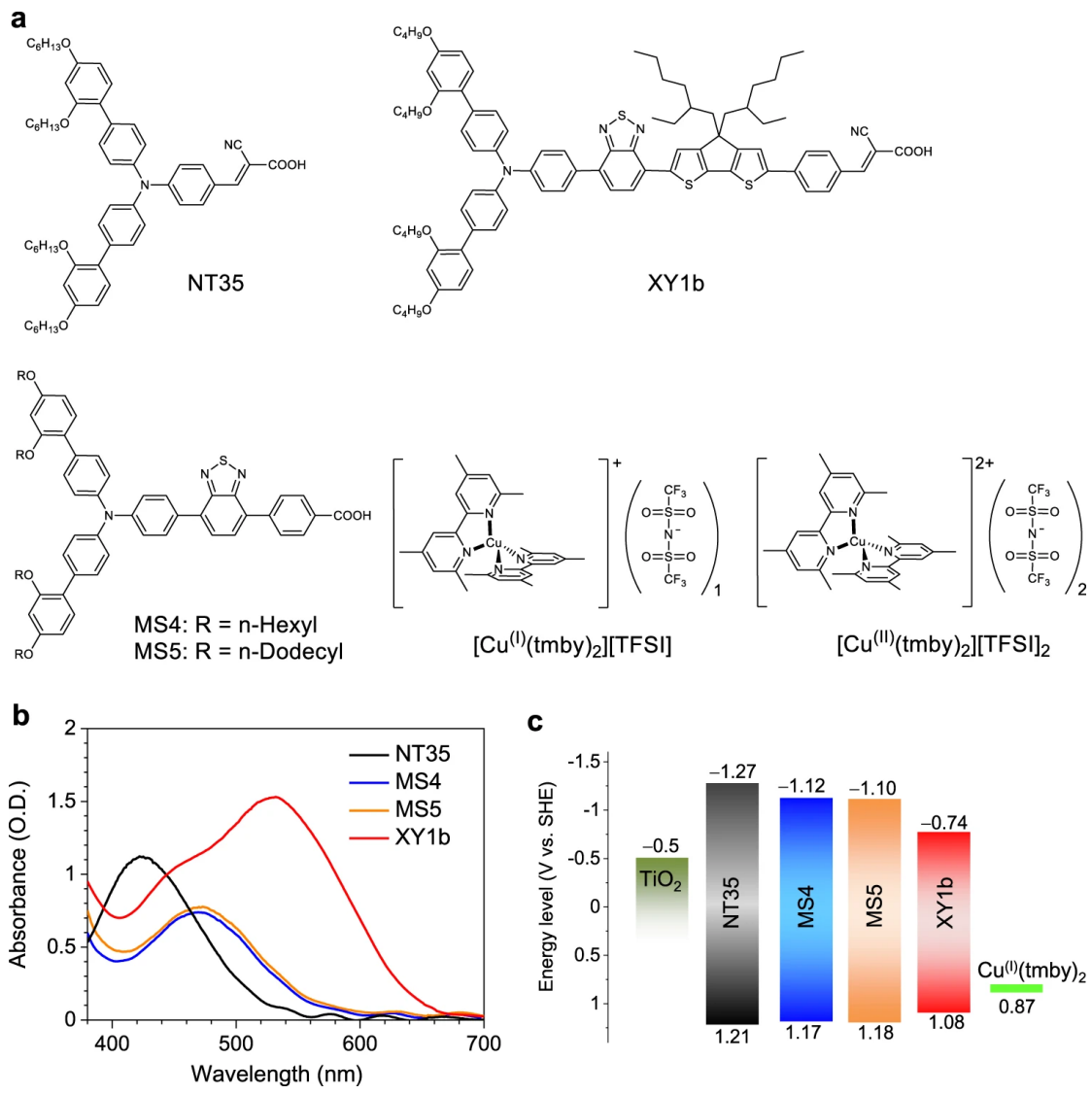
a
NT35
XY1b
MS4: R = n-Hexyl
MS5: R = n-Dodecyl
[Cu(I)(tmby)2][TFSI]
[Cu(II)(tmby)2][TFSI]2
b
Absorbance (O.D.)
Wavelength (nm)
NT35
MS4
MS5
XY1b
c
Energy level (V vs. SHE)
TiO2
−0.5
−1.27
−1.12
−1.10
−0.74
1.21
1.17
1.18
1.08
Cu(I)(tmby)2
0.87

Figure 5

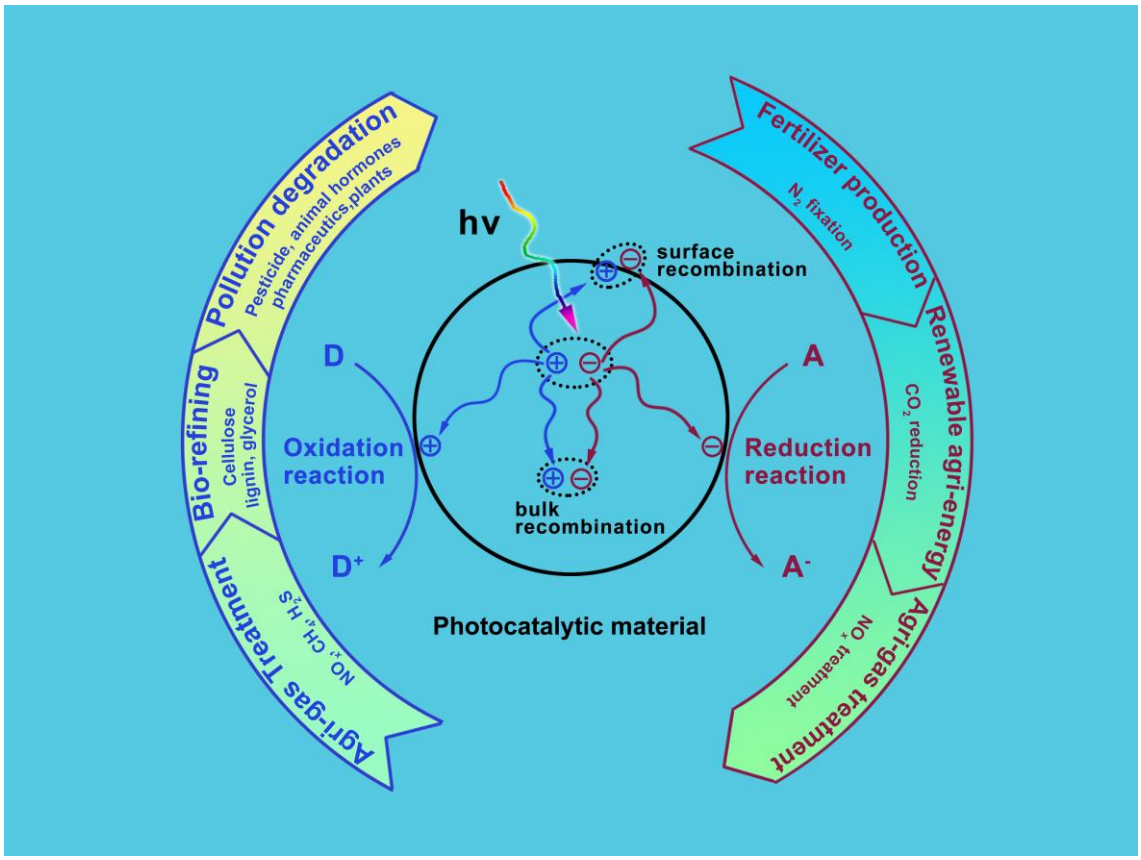
Pollution degradation
Pesticide, animal hormones
pharmaceutics,plants
Bio-refining
Cellulose
lignin, glycerol
Agri-gas Treatment
NO, CH4, H2S
Fertilizer production
N2 fixation
Renewable agri-energy
CO2 reduction
Agri-gas treatment
NO treatment
hv
surface
recombination
D
A
Oxidation
reaction
Reduction
reaction
bulk
recombination
D+
A-
Photocatalytic material

Figure 6

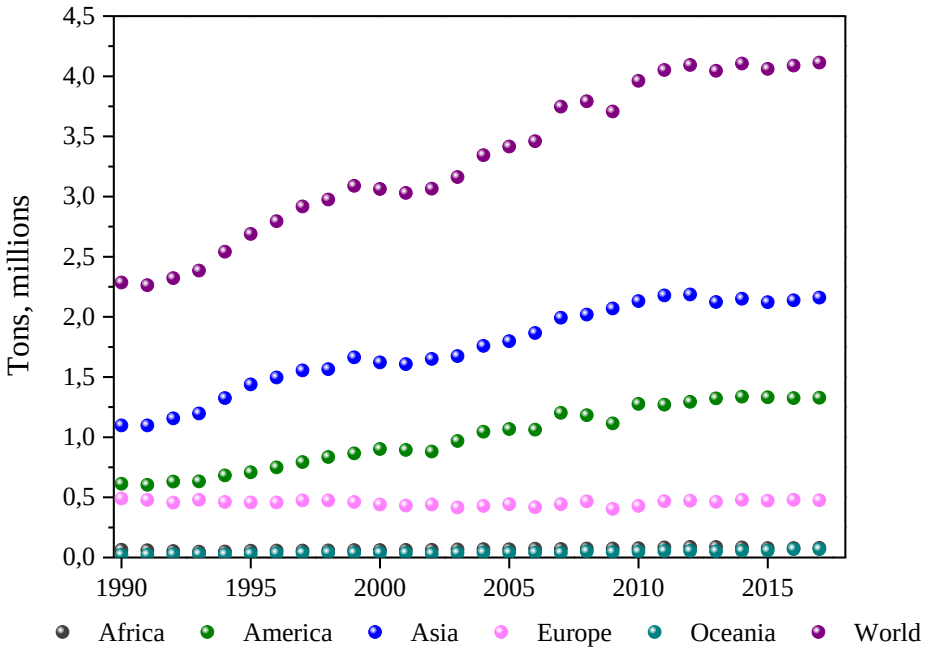
Tons, millions
4,5
4,0
3,5
3,0
2,5
2,0
1,5
1,0
0,5
0,0
1990
1995
2000
2005
2010
2015
Africa
America
Asia
Europe
Oceania
World

Figure 7

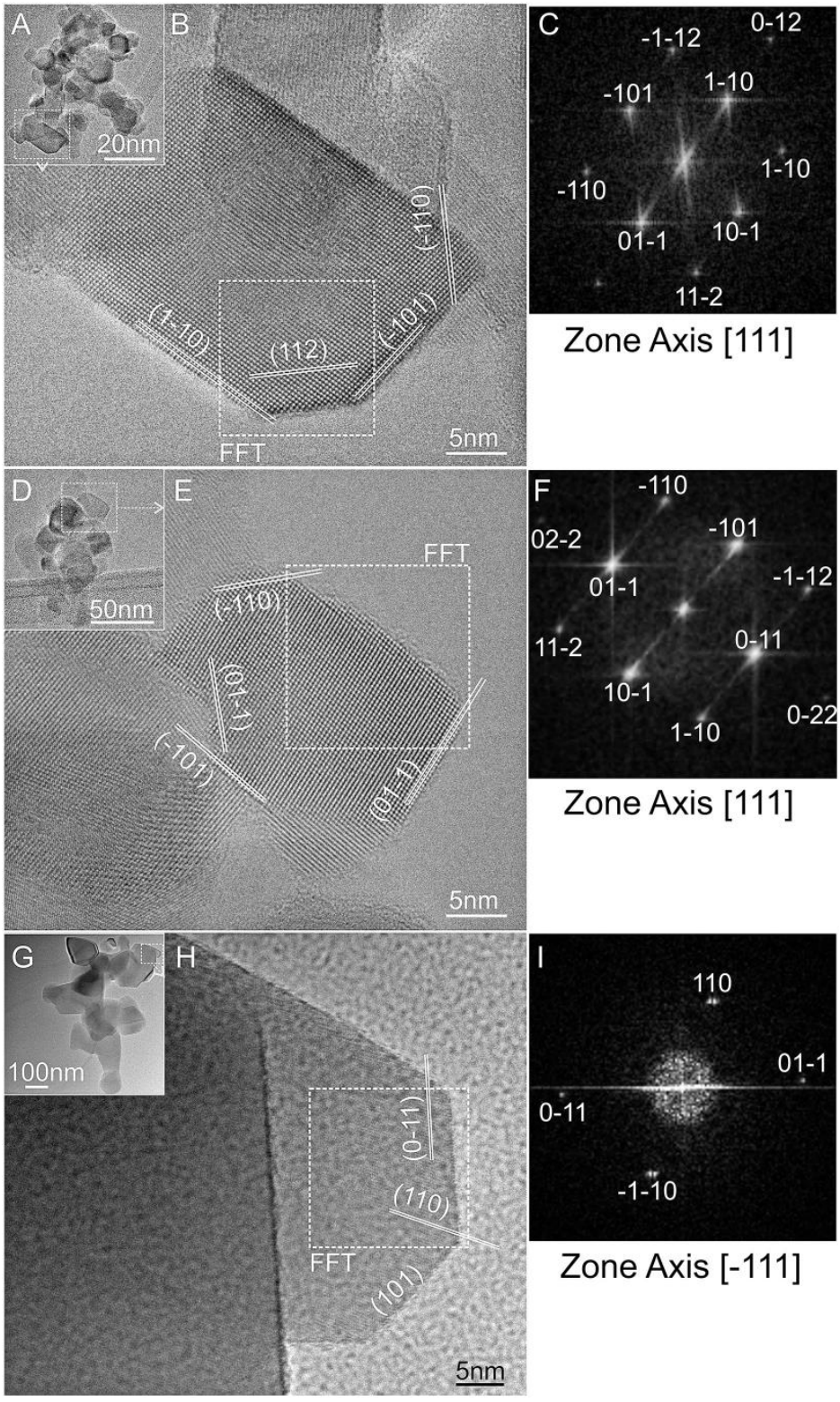
A
B
20nm
(-110)
(1-10)
(112)
(-101)
FFT
5nm
C
-1-12
0-12
-101
1-10
1-10
-110
01-1
10-1
11-2
Zone Axis [111]
D
E
50nm
FFT
(-110)
(01-1)
(-101)
(01-1)
5nm
F
-110
02-2
-101
01-1
-1-12
11-2
0-11
10-1
0-22
1-10
Zone Axis [111]
G
H
100nm
(0-11)
(110)
FFT
(101)
5nm
I
110
01-1
0-11
-1-10
Zone Axis [-111]

Figure 8

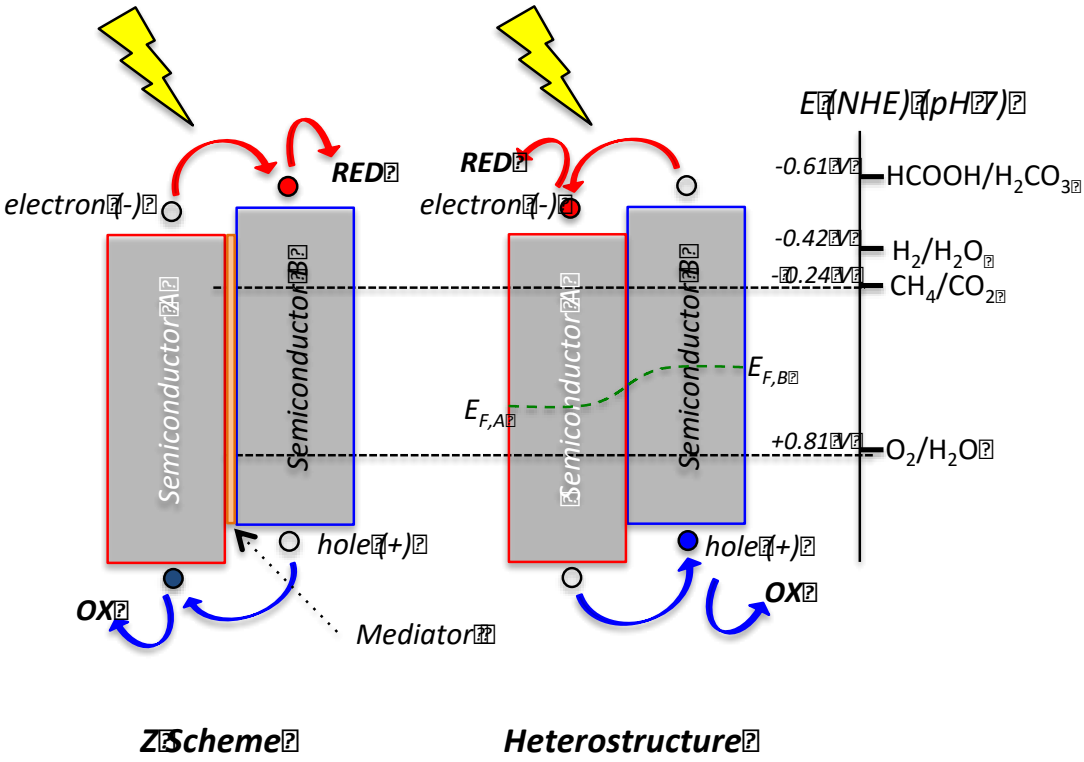
E (NHE) (pH 7)
-0.61 V
HCOOH/H2CO3
-0.42 V
H2/H2O
-0.24 V
CH4/CO2
+0.81 V
O2/H2O
RED
electron (-)
Semiconductor A
Semiconductor B
hole (+)
OX
Mediator
EF,A
EF,B
Z-Scheme
Heterostructure

Figure 9

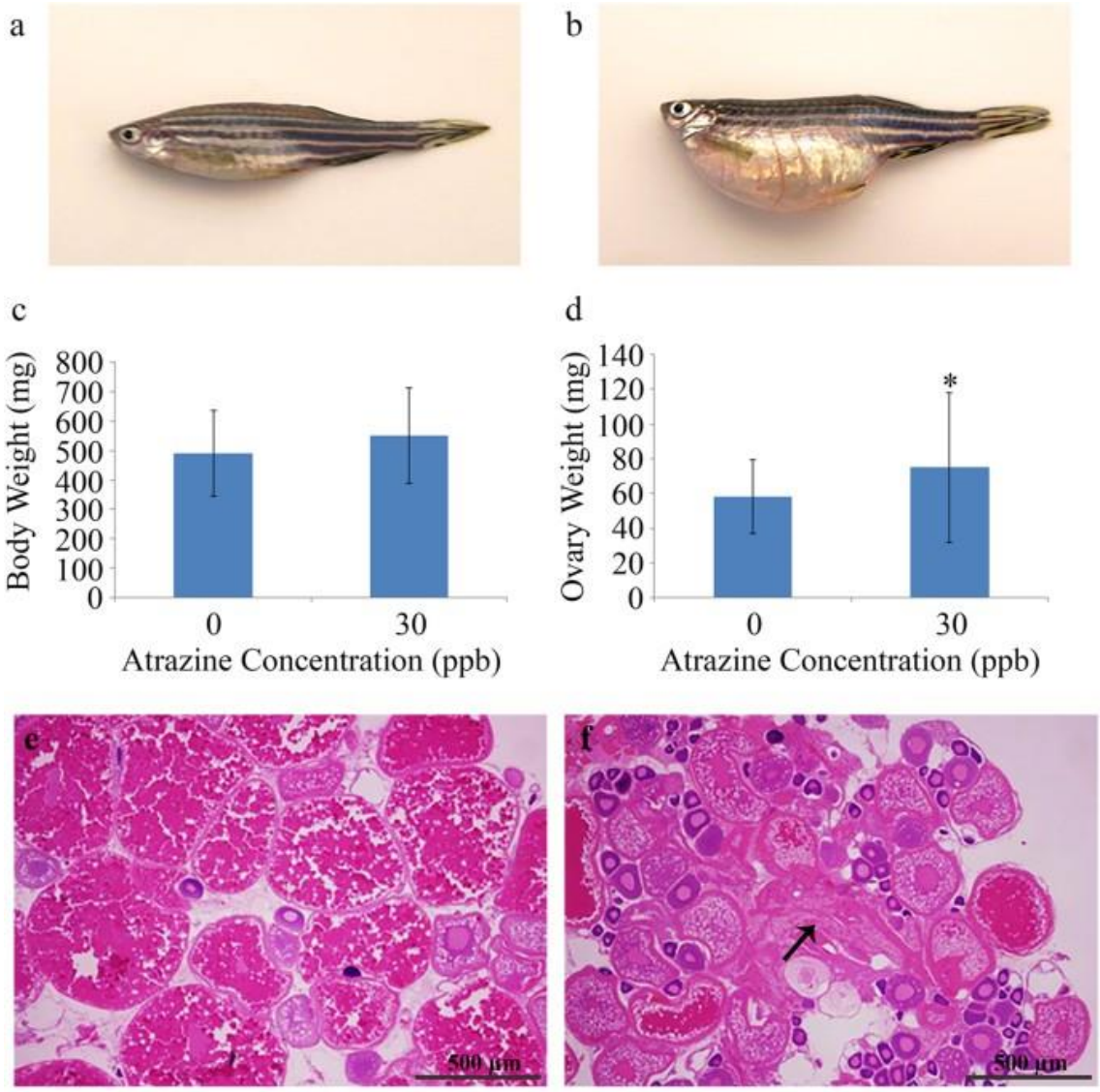
a
b
c
Body Weight (mg)
800
700
600
500
400
300
200
100
0
0
30
Atrazine Concentration (ppb)
d
Ovary Weight (mg)
140
120
100
80
60
40
20
0
*
0
30
Atrazine Concentration (ppb)
e
500 μm
f
500 μm

Figure 10

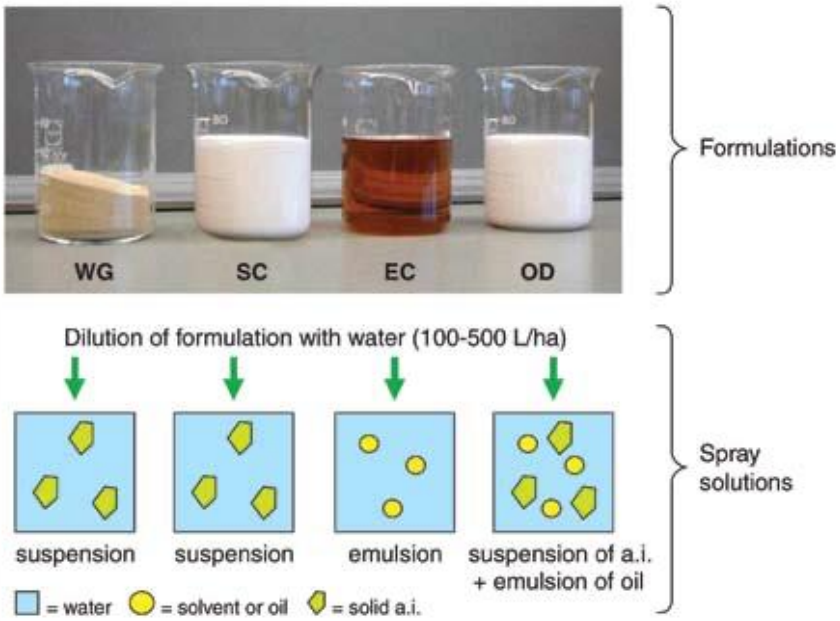
WG
SC
EC
OD
Formulations
Dilution of formulation with water (100-500 L/ha)
suspension
suspension
emulsion
suspension of a.i.
+ emulsion of oil
Spray
solutions
= water
= solvent or oil
= solid a.i.

Figure 11

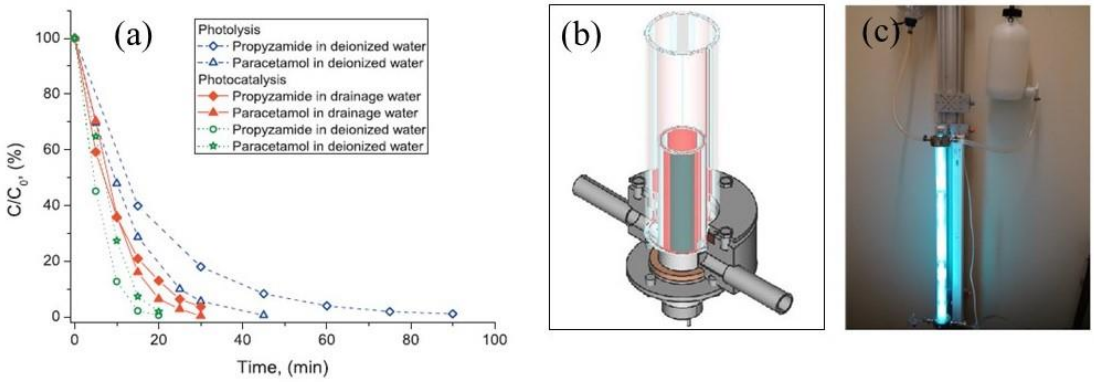
(a)
Photolysis
Propyzamide in deionized water
Paracetamol in deionized water
Photocatalysis
Propyzamide in drainage water
Paracetamol in drainage water
Propyzamide in deionized water
Paracetamol in deionized water
C/C0, (%)
Time, (min)
0
20
40
60
80
100
(b)
(c)

Figure 12

Treatment	Hypochlorite Tween 20	$Ag@TiO_2$	TiO_2-Cu^{2+}	H_2O
Disinfection (% ± SD)	100 ± 0	72 ± 12	36 ± 8	41 ± 11
A. thaliana seeds in MS				

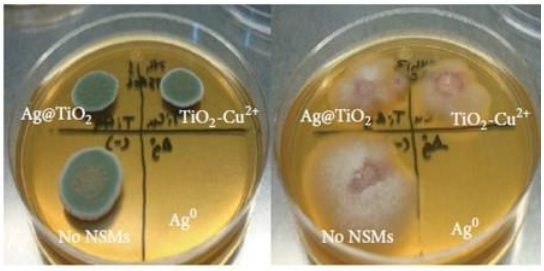

Figure 13

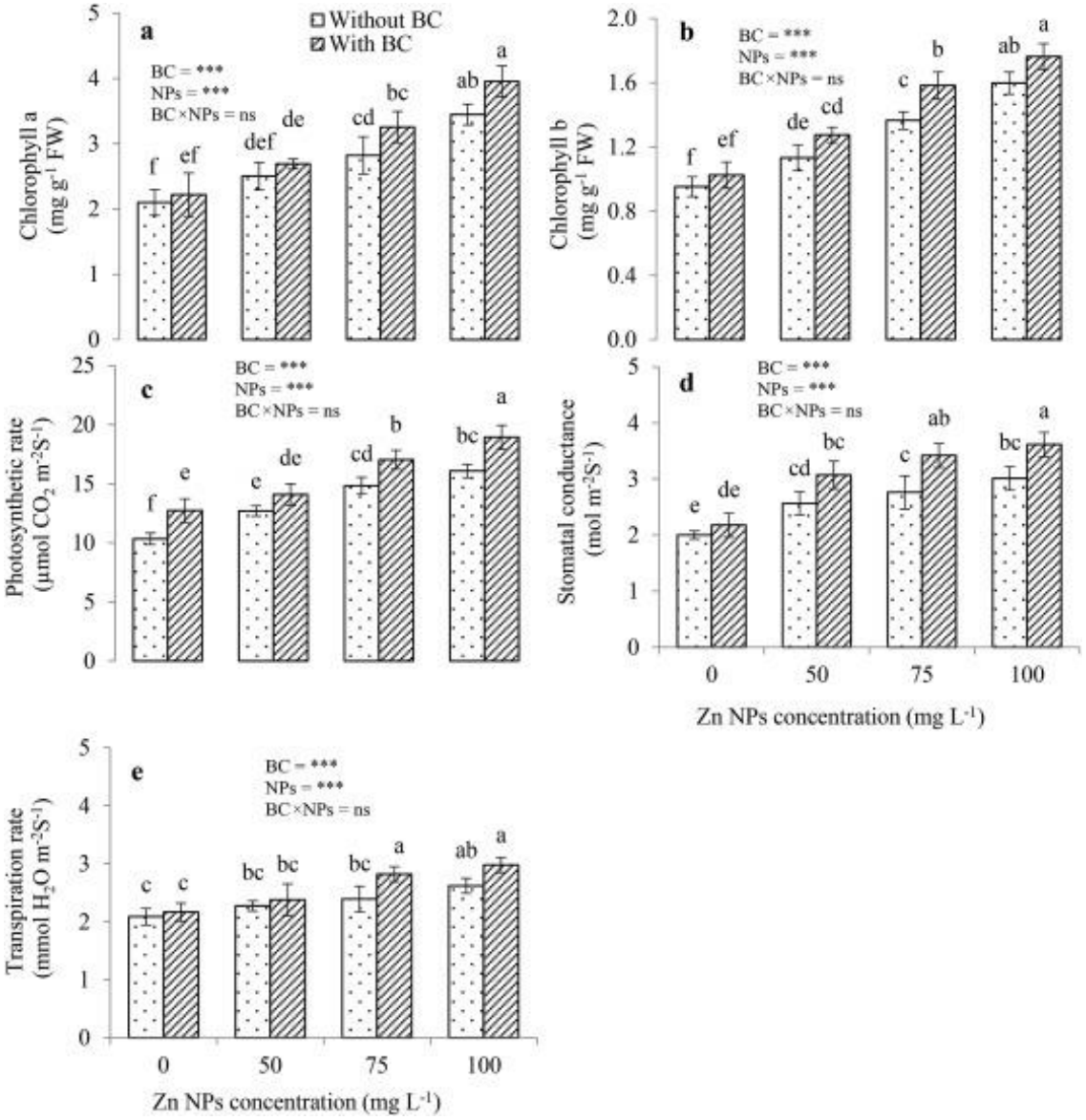
a
Without BC
With BC
BC = ***
NPs = ***
BC×NPs = ns
Chlorophyll a (mg g-1 FW)
b
Chlorophyll b (mg g-1 FW)
c
Photosynthetic rate (µmol CO2 m-2S-1)
d
Stomatal conductance (mol m-2S-1)
e
Transpiration rate (mmol H2O m-2S-1)
0
50
75
100
Zn NPs concentration (mg L-1)

Figure 14

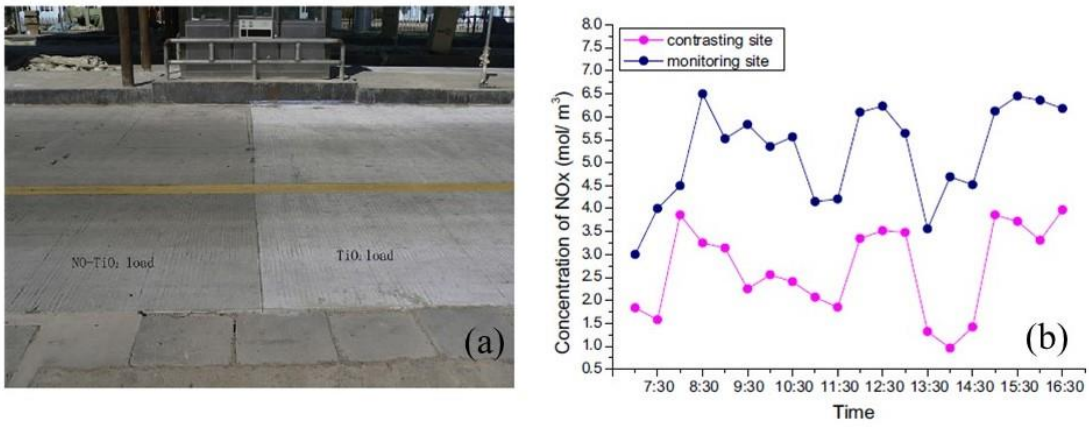
NO-TiO2 load
TiO2 load
(a)
contrasting site
monitoring site
Concentration of NOx (mol/ m3)
8.0
7.5
7.0
6.5
6.0
5.5
5.0
4.5
4.0
3.5
3.0
2.5
2.0
1.5
1.0
0.5
7:30
8:30
9:30
10:30
11:30
12:30
13:30
14:30
15:30
16:30
Time
(b)

Figure 15

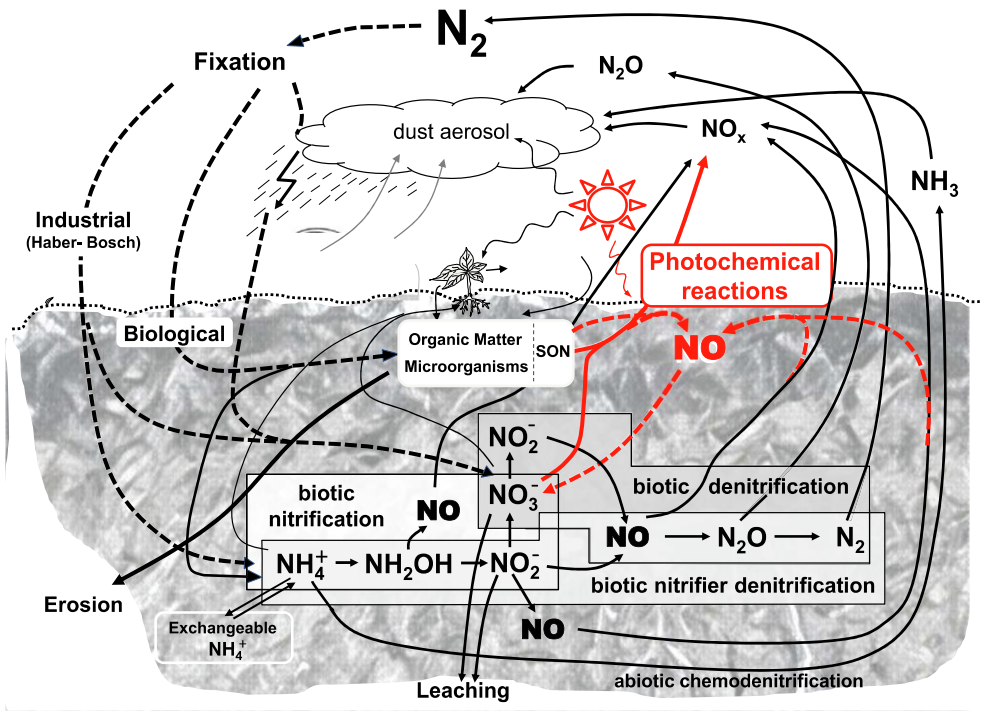
N2
Fixation
N2O
dust aerosol
NOx
NH3
Industrial
(Haber- Bosch)
Photochemical
reactions
Biological
Organic Matter
Microorganisms
SON
NO
NO2-
NO3-
biotic
nitrification
NO
biotic denitrification
NO → N2O → N2
NH4+ → NH2OH → NO2-
biotic nitrifier denitrification
Erosion
Exchangeable
NH4+
NO
Leaching
abiotic chemodenitrification

Figure 16

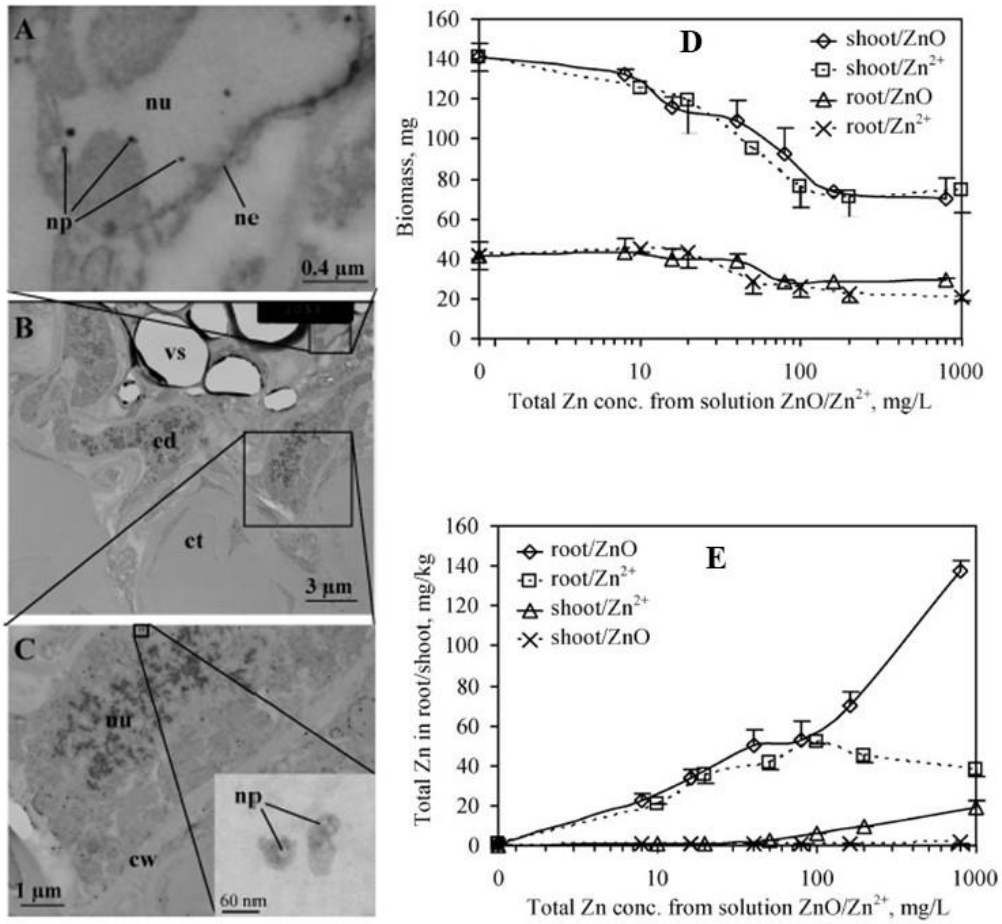
A
nu
np
ne
0.4 µm
B
vs
ed
ct
3 µm
C
nu
np
cw
1 µm
60 nm
D
shoot/ZnO
shoot/Zn2+
root/ZnO
root/Zn2+
Biomass, mg
Total Zn conc. from solution ZnO/Zn2+, mg/L
E
root/ZnO
root/Zn2+
shoot/Zn2+
shoot/ZnO
Total Zn in root/shoot, mg/kg
Total Zn conc. from solution ZnO/Zn2+, mg/L

Figure 17

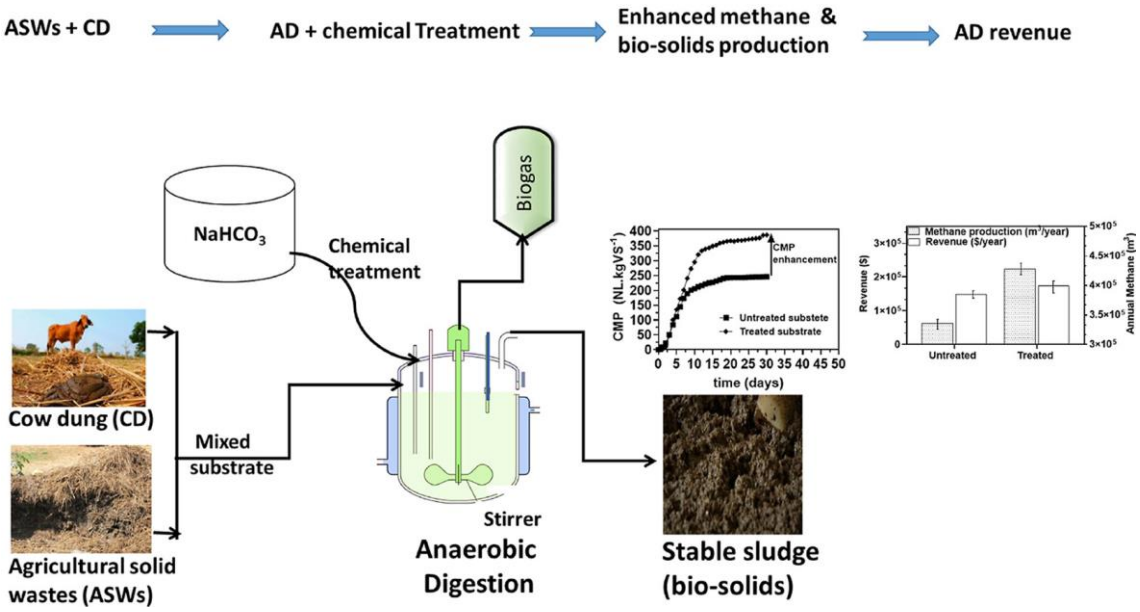
ASWs + CD
AD + chemical Treatment
Enhanced methane & bio-solids production
AD revenue
NaHCO3
Chemical treatment
Biogas
Cow dung (CD)
Agricultural solid wastes (ASWs)
Mixed substrate
Stirrer
Anaerobic Digestion
Stable sludge (bio-solids)
CMP (NL.kgVS-1)
CMP enhancement
Untreated substete
Treated substrate
time (days)
Methane production (m3/year)
Revenue ($/year)
Revenue ($)
Annual Methane (m3)
Untreated
Treated

Figure 18

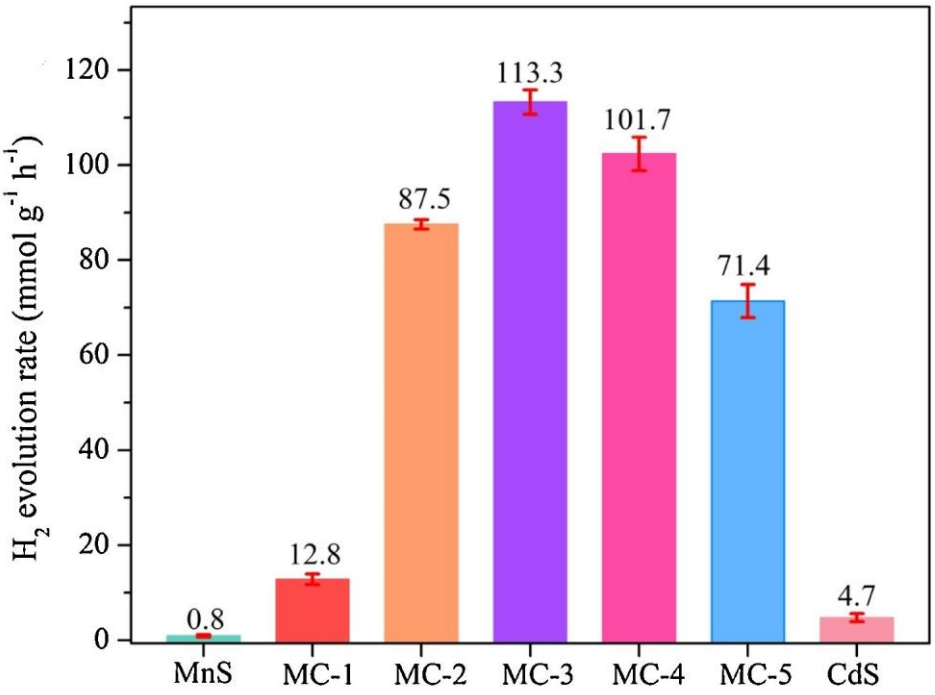
120
100
80
60
40
20
0
H2 evolution rate (mmol g-1 h-1)
0.8
12.8
87.5
113.3
101.7
71.4
4.7
MnS
MC-1
MC-2
MC-3
MC-4
MC-5
CdS

Figure 19

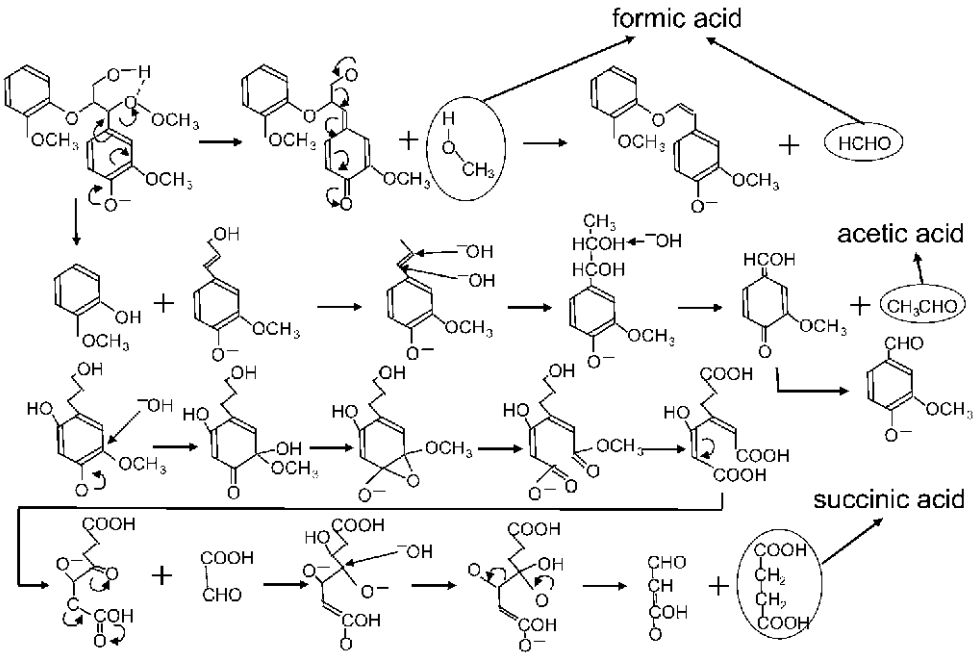

Figure 20

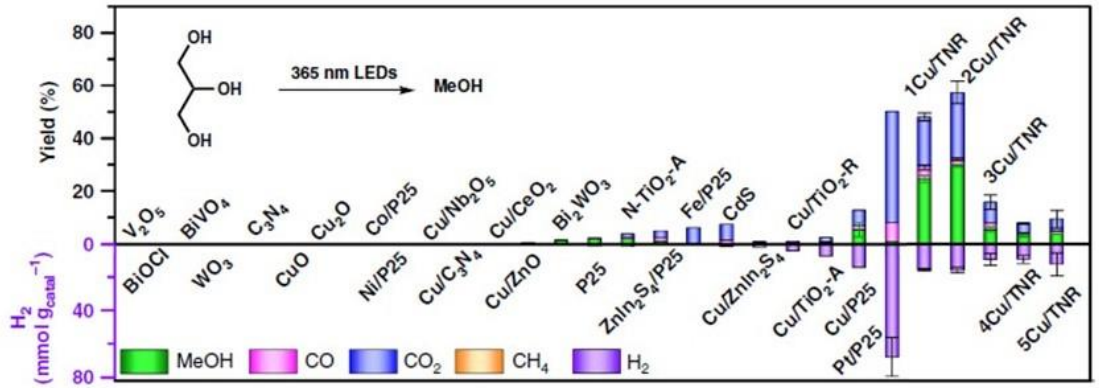
Yield (%)
80
60
40
20
0
OH
OH
OH
365 nm LEDs
MeOH
1Cu/TNR
2Cu/TNR
3Cu/TNR
4Cu/TNR
5Cu/TNR
V_2O_5
$BiVO_4$
C_3N_4
Cu_2O
Co/P25
Cu/Nb_2O_5
Cu/CeO_2
Bi_2WO_3
N-TiO_2-A
Fe/P25
CdS
Cu/TiO_2-R
BiOCl
WO_3
CuO
Ni/P25
Cu/C_3N_4
Cu/ZnO
P25
$ZnIn_2S_4$/P25
$Cu/ZnIn_2S_4$
Cu/TiO_2-A
Cu/P25
Pt/P25
H_2 (mmol g_{catal}^{-1})
40
80
MeOH
CO
CO_2
CH_4
H_2

Figure 21

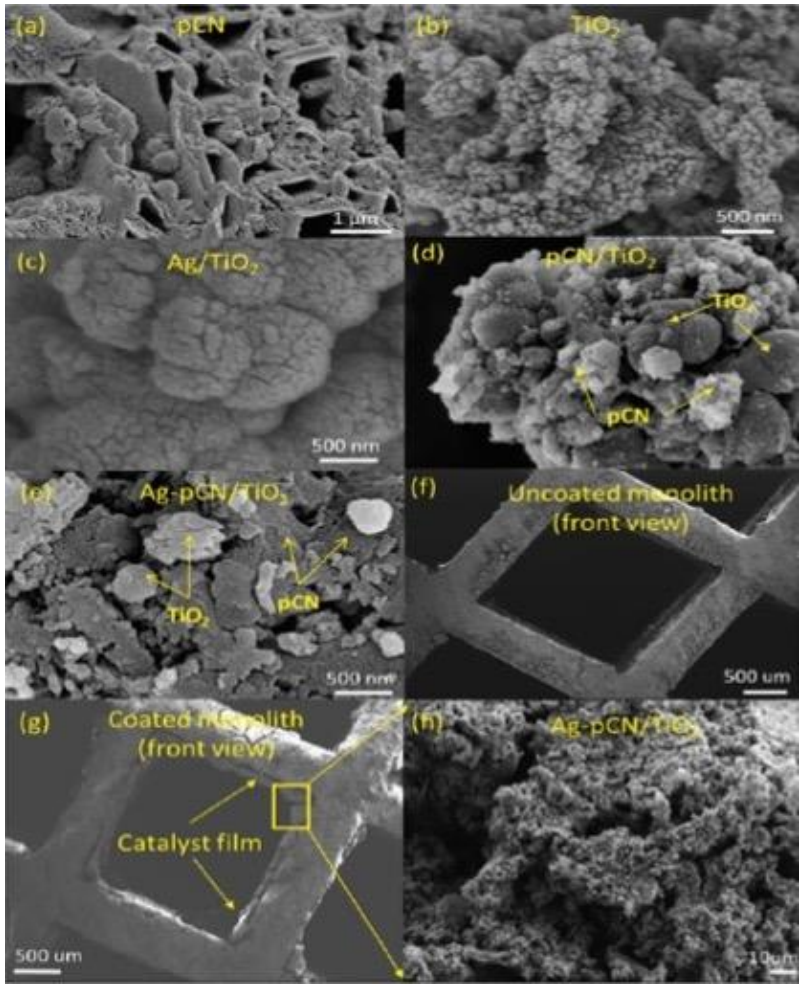
(a)
pCN
1 μm
(b)
TiO2
500 nm
(c)
Ag/TiO2
500 nm
(d)
pCN/TiO2
TiO2
pCN
(e)
Ag-pCN/TiO2
TiO2
pCN
500 nm
(f)
Uncoated monolith
(front view)
500 um
(g)
Coated monolith
(front view)
Catalyst film
500 um
(h)
Ag-pCN/TiO2
10 um

Figure 22

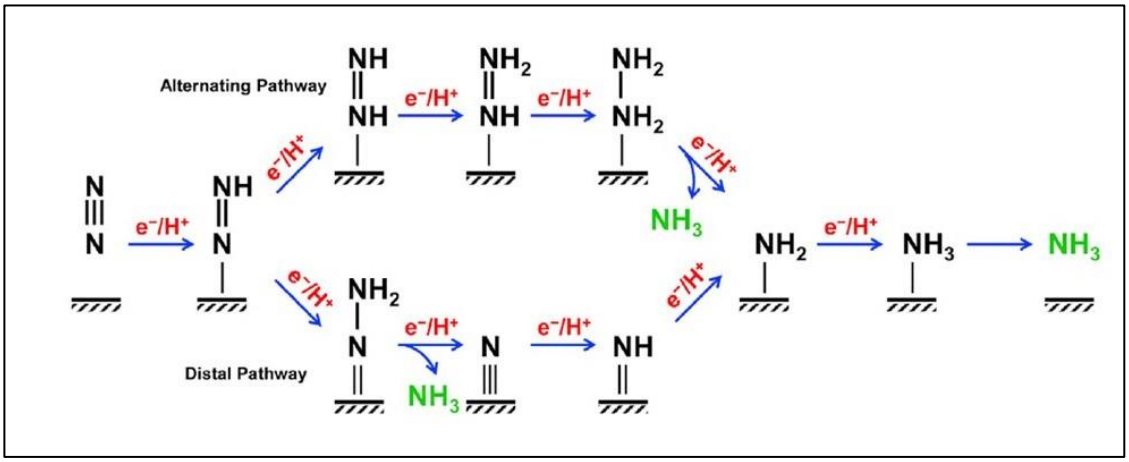

Table 1. Pesticide degradation: an overview of the last five years (2017-2021) for TiO_2 and ZnO-based materials, for experiments with simulated effluents, e.g., contaminant in deionized or distilled water.

Material	Synthesis method	Particle size	Shape	Supported/ unsupported	Degraded pesticide	Batch size	Solution concentration	Reaction time	Irradiation type	Efficiency	Ref.
TiO_2	Commercial	—	—	—	Ametryn	1 L	10 mg L^{-1}	60 min	Solar simulator	100%	[198]
TiO_2	Sol-gel method	—	Asymmetrical formations	—	Tembotrione Fluroxypyr	20 mL	0.05 mM	75 min	UV	~95% ~97%	[199]
ZnO										42% 79%	
MgO										39% 6%	
TiO_2	Sol-gel	14.2 nm anatase 30 nm brookite	—	—	Tordon 2,4-D	50 mL	10 and 20 mg L^{-1}	40 min	UV-C	100%	[200]
TiO_2 P25	Commercial	94.7 nm	—	—	Chlorpyrifos	10 mL	375 µg L^{-1}	24 h	UV	80%	[201]
TiO_2	Electro-chemical anodization	—	Nanotube array	—	4-chloro-2-methylphenoxyacetic acid	60 mL	1 mg L^{-1}	120 min	UV-LED	94.3%	[202]
Self-floating amphiphilic macro-mesoporous black TiO_2 foams	Freeze-drying method combined with cast molding technology and subsequent high-temperature surface hydrogenation	—	Macro-mesopores structure	—	Atrazine Thiobencarb	40 mL	1 mgL^{-1}	5 h	Solar simulator	~62% ~70%	[203]
Aeroxide®-TiO_2-P25	Commercial	—	—	—	Glyphosate Myclobutanil Roundu Systhane	250 mL	25 mg L^{-1} 20 mg L^{-1} 25 mg L^{-1} 35 mg L^{-1}	30 min 150 min 100 min 240 min	UV-A	100%	[204]
TiO_2	Commercial	—	—	Pilkington Active™ glass	2,4-dichlorophenoxy acetic acid	0.5 L	10 mg L^{-1}	90 min	UV-A	67%	[205]
TiO_2 P25 TiO_2 P25/multi-walled carbon TiO_2	Commercial Hydration-dehydration Sol-gel	—	—	—	Metolachlor	—	20 ppm	5 min 10 min 60 min	UV-vis	100%	[206]
Imprinted TiO_2	Chemical precipitation	0.9–1.4 µm	Spherical	—	2,4-dichlorophenoxyacetic acid	4 mL	$5x10^{-5}$ M	240 min	UV	~75%	[207]
Molecularly imprinted TiO_2	Sol-gel	—	Rough morphology with heterogeneous shaped particles	—	2,4-dichlorophenoxyacetic acid Imidacloprid	4 mL	$5x10^{-5}$ M	3 h	UV	~47% ~35%	[208]

(Table 1 – continuation)

Material	Synthesis method	Particle size	Shape	Supported/ unsupported	Degraded pesticide	Batch size	Solution concentration	Reaction time	Irradiation type	Efficiency	Ref.
Imprinted TiO_2	Hydrothermal (HTS) and liquid-phase deposition (LPD)	100 nm S-TiO_2 (LPD) and diameter and the length of the nanorods of 80 nm and 1µm S-TiO_2 (HTS)	Stacked zero-dimensional nanoparticles S-TiO_2 (LPD) and one-dimensional, vertically aligned nanorods S-TiO_2 (HTS)	TiO_2 nanorods	2-(2,4-dichlorophenoxy) propionic acid	100 mL	50 mg L^{-1}	6 h	UV-vis	90.9%	[209]
TiO_2 P25/O_2 TiO_2 P25/N_2 UV/VUV/N_2 UV/VUV/O_2 UV/O_2 UV/N_2	Commercial	—	—	—	Imidacloprid	—	1.0×10^{-4} mol dm^{-3}	20 min 60 min 10 min 50 min 50 min	UV UV UV/VUV UV/VUV UV UV	100% ~ 88% 100% 100% 100%	[210]
Fe_2O_3/TiO_2 monoliths	Nanocasting method followed by wet impregnation	—	Pomegranate-like structure	—	Fipronil	50 mL	600 mg L^{-1}	120 min	UV-vis	88.71%	[45]
Fe_3O_4-TiO_2/graphene	Hydrothermal	9 +/- 0.2 nm	TiO_2 and Fe_3O_4 spherical shaped scattered on the surface of rGO sheets	rGO	Atrazine	30 mL	15 mg L^{-1}	45 min	Sunlight	100%	[46]
r-GO/TiO_2	Ultrasonically assisted route	—	Partial layered	rGO	Clopyralid	250 mL	20 mg L^{-1}	60 min	UV-A	100%	[52]
TiO_2/GO	Surface molecular imprinting technology	—	Uniform and nonporous surface	Silylated graphene oxide	2,4-Dichlorophenoxyacetic acid	25 mL	5 mg L^{-1}	35 min	Visible	100%	[211]
CuO/TiO_2/polyaniline	In-situ polymerization	—	Polyaniline in tubular shape around the CuO/TiO_2	—	Chlorpyrifos	100 mL	5 mg L^{-1}	90 min	UV-vis	95%	[212]
CdO-TiO_2	Sol-gel	10 nm	—	TiO_2	Imazapyr	—	0.08 mM	180 min	Visible	100%	[47]
$LaFeO_3$@TiO_2	Sol-gel	—	Core-shell porous	—	Myclobutanil	100 mL	20 mg L^{-1}	240 min	Solar simulator	100%	[48]
WO_3-TiO_2-SBA-15	In situ anchoring	—	—	SBA-15 molecular sieve	2,4-Dichlorophenoxyacetic acid	100 mL	$1x10^{-4}$ mol L^{-1}	270 min	UV	76%	[213]
Au-TiO_2	Hydrothermal	—	Homogeneous nanobelt	TiO_2 nanobelt	2,4-dichlorophenoxyacetic acid	250 mL	0.53 mM	120 min	UV-A	99.2%	[49]
FeOx/TiO_2	Surface impregnation	—	—	TiO_2	2,4,6-trichlorophenol 2,4-dichlorophenoxyacetic acid	200 mL	50 ppm	240 min 180 min	UV-vis	100% 98%	[214]

(Table 1 – continuation)

Material	Synthesis method	Particle size	Shape	Supported/ unsupported	Degraded pesticide	Batch size	Solution concentration	Reaction time	Irradiation type	Efficiency	Ref.
Au/TiO_2/RaMeβ-CD Au/TiO_2/HPβ-CD Au/TiO_2/α-CD Au/TiO_2/γ-CD Au/TiO_2/β-CD	Sol-gel and impregnation	Au 40 nm Au 55 nm Au 30 nm Au 20 nm Au 15 nm	Gold nanoparticles with intimate contact with the mesoporous	TiO_2	Phenoxyacetic acid	—	0.15 g L^{-1}	7 h	Visible	87% 77% 76% 75% 62%	[215]
Sr/TiO_2-porous ceramic filter media	Liquid-phase method	—	Rough and porous surface	Porous ceramic filter media	Acephate	50 mL	50 mg L^{-1}	120 min	UV	85.28%	[216]
TiO_2 Aerosil P25 TiO_2 Aerosil P25 NiFe_700_SBA-15 CoFe_700_SBA-15	Commercial (TiO_2) and impregnation	10 nm and 20 nm (metallic oxides)	Nanowires of metallic oxides less than 10 nm diameter and 20 nm, in silica grains	SBA-15 silica mesoporous grains	Carbendazim	100 mL	20.00 ± 0.04 ppm	320 min	UV Visible Visible Visible	86% 12.5% 25% 55%	[217]
Carbon nanodots/TiO_2	Impregnation	Carbon nanodots 2-3 nm	Carbon nanodots	TiO_2	2,4-dichlorophenol	100 mL	0.025 mM	60 min	Visible	100%	[53]
FeNTiO_2/H_2O_2	Sol-gel and impregnation	—	—	—	Carbofuran	100 mL	0.015 mM	24 min	Visible	76%	[218]
Fe_2O_3/mesoporous black TiO_2	Wet-impregnation and surface hydrogenation	~700 nm	Mesoporous hollow spheres	—	Metribuzin	100 mL	10 mg L^{-1}	60 min	Visible	99%	[219]
N-doped TiO_2	Sol-gel	—	—	—	4-chlorophenoxyacetic acid	100 mL	0.008 mM	4 h	Visible	95%	[54]
N-doped TiO_2	Sol-gel	—	—	—	Monuron	100 mL	0.005 mM	25 min	Visible	100%	[55]
ZnO films	Spray pyrolysis	1.5 µm	Nanoflower	Glass substrates	Temephos	12 mL	10 mg L^{-1}	24 h	Solar simulator	55%	[220]
ZnO	Commercial	50–70 nm	—	—	Nitenpyrum	30 mL	10 ppm	30 min	Sunlight	100%	[221]
Magnetic particles composed of a silica undercoat beneath a ZnO coating	Sol-gel	—	Cluster of aggregates of ZnO deposited on the magnetic particles	Magnetic particles core (Fe_3O_4)	Pyraclostrobin Trifloxystrobin Myclobutanil Boscalid Penconazole Difenoconazole	500 mL	0.5 mg L^{-1}	240 min	Sunlight	100%	[222]
ZnO TiO_2 P25	Commercial	—	—	—	Bentazon	500 mL	20 mg L^{-1}	90 min	UV-A	97% 81%	[223]
ZnO/GO	Precipitation	—	Zinc oxide platelets attached to a graphene oxide	Graphene oxide	Simazine	4 mL	25 ppm	1 h	Visible	94%	[224]
ZnO/CuO	Sono-co-precipitation	32 nm	Spherical	—	Methyl parathion	50 mL	20 mg L^{-1}	60 min	Sunlight	100%	[225]
ZnO-Bi_2O_3	Hydrothermal	—	Nanosheet	—	Lambda-Cyhalothrin	500 mL	50 mg L^{-1}	120 min	Visible	85.7%	[226]
Cu-ZnO	Hydrothermal	—	—	ZnO	Monocrotophos	500 mL	—	180 min	Visible	90 %	[227]
rGO/Fe_3O_4/ZnO	Thermal co-precipitation	—	Layer-by-layer assembled structure	rGO	Metalaxyl	—	30 ppm	120 min	Visible	92.11%	[228]
La: ZnO/polyacrylonitrile	Hydrothermal	1.15 µm	Hexagonal rod-like morphology	Polyacrylonitrile fibers (PAN)	Methyl paraoxon	—	10 ppm	150 min	UV	100%	[229]

(Table 1 – continuation)

Material	Synthesis method	Particle size	Shape	Supported/ unsupported	Degraded pesticide	Batch size	Solution concentration	Reaction time	Irradiation type	Efficiency	Ref.
Pd@ZnONSt Ag@ZnONSt ZnO NP ZnO NSt TiO_2 NP	Microwave-hydrother-mal	Ag NP ~20 ± 2 nm Pd NP ~5–6 nm	Ag NP spherical shape and distributed ran-domly on the ZnO ma-trix and tiny particles of Pd	Zinc oxide nanostars (ZnONSt)	Trifluralin	100 mL	0.001 mg L^{-1}	90 min 90 min 160 min 90 min 160 min	Visible	~83% ~80% ~74% ~76% ~72%	[230]
ZnO@SiO_2@Fe_3O_4	Hydrothermal	40 nm ZnO 26 nm SiO_2@Fe_3O_4	Spherical	SiO_2@Fe_3O_4	Diazinon	300 mL	10, 20 and 30 mg L^{-1}	60 min	UV-vis	100%	[231]
Bi-TiO_2/graphene composites	Hydrothermal	—	Nanotubes of Bi-doped TiO_2 anchored on the surface of graphene	TiO_2	Dinoseb	180 mL	10 mg L^{-1}	180 min	Visible	72%	[232]
Bi-TiO_2	Bismuth ionic layer adsorption reaction method over TiO_2 beads	Bismuth containing clusters of 1–5 nm	Spherical	Glass beads	Pentachlorophenol	5 mL	20 ppm	4 min	Visible	~88%	[233]

Table 2. Pesticide degradation: an overview of the last five years (2017-2021) for prospective catalysts, for experiments with simulated effluents, e.g., contaminant in deionized or distilled water.

Material	Synthesis method	Particle size	Shape	Supported/ unsupported	Degraded pesticide	Batch size	Solution concentration	Reaction time	Irradiation type	Efficiency	Ref.
$CdS/BiOBr/Bi_2O_2CO_3$	Hydrothermal	—	—	BiOBr	Atrazine	100 mL	10 ppm	30 min	Visible	>95%	[234]
$CuS\text{-}Bi_2O_2CO_3$	Hydrothermal	—	CuS nanorods and $Bi_2O_2CO_3$ nanoplates	$Bi_2O_2CO_3$	Chlorpyrifos	100 mL	10 ppm	3 h	Visible	>95%	[235]
$CuS/BiFeO_3$	Hydrothermal	—	Uniformly distributed CuS nanorods and $BiFeO_3$ sheets	$BiFeO_3$	Alachlor	100 mL	5 ppm	60 min	Visible	>95%	[236]
$CuS/Bi_4Ti_3O_{12}$	Hydrothermal	—	Ultrathin CuS nanosheets and $Bi_4Ti_3O_{12}$ nanoflakes	$Bi_4Ti_3O_{12}$	2-methyl-4-chlorophenoxyacetic acid	100 mL	10 ppm	3 h	Visible	>95%	[237]
$BiOBr/Fe_3O_4$	Solvothermal	—	Spherical Fe_3O_4 nanoparticles and BiOBr microspheres	BiOBr	Glyphosate	20 mL	100 mg L^{-1}	60 min	Visible	97%	[238]
$BiMoVO_4$ photoanode	Spin coating on the FTO	—	Rounded nanoparticles embedded into the FTO structure	FTO	Simazine	50 mL	0.025 mM	1 min	Solar simulator	100%	[239]

(Table 2 – continuation)

Material	Synthesis method	Particle size	Shape	Supported/ unsupported	Degraded pesticide	Batch size	Solution concentration	Reaction time	Irradiation type	Efficiency	Ref.
g-C_3N_4/$Bi_2O_2CO_3$/$CoFe_2O_4$	Hydrothermal synthesis	—	g-C_3N_4 thin rough sheets, $Bi_2O_2CO_3$ flower shaped, $CuFe_2O_4$ cubical crystals and biochar (porous matrix)	Biochar	Paraquat	100 mL	20 ppm	90 min 120 min	Visible Sunlight	99.3% 92.1%	[240]
Carbon quantum dots/$Bi_{20}TiO_{32}$	Impregnation	Nanowire 20 nm and nanodots 3-5 nm	Nanowire and nanodots	$Bi_{20}TiO_{32}$	Isoproturon	50 mL	20 mg L^{-1}	48 h	Visible	98.1%	[241]
Ag/BiOBr-carboxymethyl cotton fabric	Anchoring metallic silver nanoparticle-decorated bismuth oxybromide nanosheet arrays on carboxymethyl cotton fabric	BiOBr nanosheets ~1 mm and Ag nanoparticles 10-20 nm in diameter	Ag nanoparticles onto the surface of BiOBr nanosheets anchored to the cotton	Carboxymethyl cotton fabric	Isoproturon	50 mL	20 mg L^{-1}	150 min	Visible	98%	[242]
$K_4Nb_6O_{17}$/alpha-Fe_2O_3/Fe_3N/g-C_3N_4	Thermal pyrolysis	~100 nm	Nanoflake	—	Acetamiprid	60 mL	50 ppm	180 min	Visible	76%	[243]
PB-g-C_3N_4	Thermal copolymerization	—	Nanosheets with small holes	—	Atrazine	100 mL	2 mg L^{-1}	120 min	Visible	94%	[244]
P-doped g-C_3N_4 coupled with fullerene (C-60/PCN/H_2O_2)	Sonochemical	—	Irregular anchoring of C60 nanoparticles over PCN nanosheets	—	Imidacloprid	—	1x10^{-4} mol L^{-1}	6 h	Visible	95%	[245]
CdS/RGO/g-C_3N_4	Hydrothermal	2 to 10 nm	Nanospheres	—	Atrazine	100 mL	10 mg L^{-1}	5 h	Solar simulator	90.5%	[246]
C_3N_4/Fe_3O_4/Ag	Hydrothermal	—	—	—	Diazinon	—	5 mg L^{-1}	60 min	UV	100%	[247]
α-Cyclodextrins/MoS_2/g-C_3N_4 β-CD/MoS_2/g-C_3N_4 γ-CD/MoS_2/g-C_3N_4	MoS_2/g-C_3N_4 impregnation on CDs	—	—	g-C_3N_4	Glyphosate	50 mL	9 g L^{-1}	170 min	Solar simulator	~49% ~66% ~80%	[248]
GO/g-C_3N_4/Ag membrane	Filtration-assisted assembly method	—	GO sheets interlocked with g-C_3N_4 sheets and stacked into lamellar structure	GO/g-C_3N_4 nanosheets	Paraoxon	—	10^{-5} M	150 min	Visible	92.8%	[249]
Graphene nanoplatelets/ZrV_2O_7	Hydrothermal	40 to 80 nm	Agglomeration of particles (cohesion of GNPs and ZrV_2O_7 particles)	Glass plates	Chlorpyrifos	200 mL	50 mg L^{-1}	90 min	UV-vis	96.8%	[250]
Ag_3PO_4/GO	Electrostatically spraying	Ag_3PO_4 nanoparticles 10 to 20 nm	Aerogel microspheres	GO	Atrazine	20 mL	—	120 min	Visible	100%	[251]

(Table 2 – continuation)

Material	Synthesis method	Particle size	Shape	Supported/ unsupported	Degraded pesticide	Batch size	Solution concentration	Reaction time	Irradiation type	Efficiency	Ref.
In, S co-doped TiO_2@rGO	Ultrasonic-assisted solvothermal	—	Lumps shape and tended to aggregate into bigger-sized particles	rGO	Atrazine	25 mL	20 mg L^{-1}	20 min	Visible	100%	[252]
$Zn_xCu_{1-x}Fe_2O_4$	Sol-gel combustion	27 nm	Agglomerated nanoparticles	—	Atrazine	20 mL	4.4 µM	30 min	UV-vis	95%	[253]
g-C_3N_4/Ag_3PO_4/AgI	In-situ ion exchange method	—	Crinkly sheets	—	Nitenpyram	50 mL	5 ppm	4 min	Visible	94.2%	[254]
Ag_3PO_4/polydopamine/Al_2O_3	Homogeneous precipitation	—	Small balls	Porous Al_2O_3	Ammonium glyphosate Acephate	—	100 ppm	20 min 5 min	Sunlight	>75 %	[255]
P/C_3N_4	Hydrothermal	—	—	g-C_3N_4	Dinotefuran	100 mL	2 mg L^{-1}	5 h	Visible	40.59%	[256]
SO_4-Ag_3PO_4	Precipitation	20 to 60 nm	Irregular	—	Thiacloprid Nitenpyram Imidacloprid Clothianidin Acetamiprid Thiamethoxam Dinotefuran	50 mL	5 mg L^{-1}	5 min 5 min 60 min 60 min 60 min 60 min 60 min	Visible	88.64% 73.66% 99.66% 90.78% 44.67% 39.94% 14.64%	[257]
Nb_2O_5:$CoFe_2O_4$ Nb_2O_5:$MgFe_2O_4$	Coprecipitation	20 and 50 nm	—	—	Atrazine	80 mL	10 mg L^{-1}	60 min	UV	88%	[258]
Fe_3O_4@WO_3/SBA-15	Co-precipitation, solvothermal and hydrothermal	WO_3 35.8 nm and Fe_3O_4 13.3 nm	Core-shell	SBA-15 molecular sieve	Dichlorophenoxyacetic acid	100 mL	1x10^{-6} mol L^{-1}	240 min	UV	90.73%	[259]
CeO_2 –Ce_2S_3	Coprecipitation	20-200 nm	3D granule-like geometric	Zeolitic channels	Acetamiprid	50 mL	50 ppm	3 h	UV	82%	[260]
WO_3 photoanode	Electrochemical anodization	—	Tiny nanorods or nanosheets	Electrodes,	Fenamiphos	14 mL	20 mg L^{-1}	120 min	UV-vis	100%	[261]
WO_3	Electrochemical anodization	—	Nanosheets or nanorods	Tungsten bar	Chlorfenvinphos Bromacil	14 mL	20 ppm	360 min	UV-vis	91.4% 84.3%	[262]
Ag_2S/Fe_3O_4@Ag_3PO_4	Solvothermal deposition followed by an in-situ anion-exchange reaction	—	Core-shell	—	Imidacloprid	60 mL	2 mg L^{-1}	60 min	Visible	100%	[263]
WO_3	Electrochemical anodization	2.1 ± 0.3 µm	Nanosheets/nanorods	—	Atrazine	14 mL	20 mg L^{-1}	180 min	UV	100%	[264]

(Table 2 – continuation)

Material	Synthesis method	Particle size	Shape	Supported/ unsupported	Degraded pesticide	Batch size	Solution concentration	Reaction time	Irradiation type	Efficiency	Ref.
Oxidized carbon nitride (OCN)	Rapid acid-assisted method	—	Porous surface	—	Acetochlor Pretilachlor Butachlor Florasulam Clodinafop-propargyl Diuron Nicosulfuron Pyrazosulfuron-ethyl Halosulfuron-methyl Rimsulfuron	100 mL	2 mg L^{-1}	180 min	Visible	~ 40% ~ 50% ~ 40% ~ 100% ~ 60% ~ 92% ~ 98% ~ 99% ~ 100% ~ 98%	[265]
ZrO_2@HKUST-1	Sol-gel	—	HKUST-1 octahedral shape with rough surface	HKUST-1	Cyhalothrin	30 mL	10 mg L^{-1}	6 h	Visible	99.6%	[266]
Metal−organic framework	Wet chemical method	90 nm	Uniform spherical	—	Nitenpyram Thifluzamide Isoproturon Atrazine	200 µL	10 µg mL^{-1}	20 min	Visible	95% 82.3% 67.4% 76.2%	[267]
WO_3	Sedimentation Magnetron sputtering Combination of both methods	2- 10 nm	Small nanocrystals Sputtered films are homogeneous and smooth surface	FTO	Monuron	20 mL	5x 10^{-5} mol dm^{-3}	4 h	Solar simulator	20% 20% 40%	[268]
Boron-doped diamond anode	Commercial	—	—	—	Diuron Atrazine (Synthetic stormwater)	80 mL	60 µg L^{-1}	2 h	Solar simulator	96% 90%	[269]

Table 3. Pesticide degradation using photocatalytic materials: an overview of the last five years (2017-2021) of experiments with real effluents.

Material	Synthesis method	Particle size	Shape	Degraded pesticide	Batch size	Solution concentration	Reaction time	Irradiation	Efficiency	Effluent	Ref.
TiO_2 thin-films*	Chemical vapor deposition	100 nm	Surface with a roughness	Azoxystrobin Iprodione Propizamid Isoproturon Fenarimol	320 mL	5 mg L^{-1}	20 min	UV-C	100%	Drainage water: 100%/25 min	[63]
BiOBr/ UiO-66	In-situ growth	—	BiOBr flakes interspersed with UiO-66 particles	Atrazine	50 mL	5 mg L^{-1}	240 min	Visible	88% pure water 0% river water	River water	[270]
$SnIn_4S_8$	Hydrothermal	1-2 µm	Network-like microspheres	Ethiofencarb	100 mL	10 mg L^{-1}	24 h	Visible	98% deionized water ~82% river water ~97% lake water	Lake and river samples	[271]
CNTs/MOF-808**	Impregnation	—	MOF-808 ovoidal between CNTs	Diazinon	200 mL	50 mg L^{-1}	60 min 2 h	Visible	99.7% diazinon 92.9% wastewater	Agrochemical wastewater	[272]
TiO_2 P25	Commercial	Anatase ~ 25 nm and rutile ~ 40 nm	—	Diuron Monuron	—	1.7×10^{-4} M	60 min	UV	90% 98%	River and thermal water (negligible results)	[273]

*Supported in quartz tube
**Supported in scarified glass plates

Table 4. Summary of photocatalytic materials used for the degradation of effluents with animal hormones and pharmaceutics contaminations.

Material	Synthesis method	Characterization	Degraded molecule	Batch size	Solution concentration	Reaction time	Efficiency	Irradiation	Ref.
TiO_2 P25	Commercial	—	Sulfamethoxazole Trimethoprim	1 L	100 mg L^{-1}	370 min	91% 100%	Solar simulator	[274]
TiO_2 P25*	—	—	Spiramycin	—	15 mg L^{-1}	168 h 168 h 0.25 h	100%	Solar simulator	[275]
TiO_2 P25	Commercial	21 nm	Sulfanilamide	100 mL	0.1 mmol L^{-1}	90 min	~10% ~96% ~80% ~96% ~96% ~88% ~90%	UV-A	[276]
TiO_2-exfoliated graphite	Sol–gel and microwave methods	Supported in graphite sheets	Sulfamethoxazole	75 mL	25 mg L^{-1}	6 h	100%	UV-vis	[277]
TiO_2 P25	Commercial	—	Ampicillin Doxycycline Tylosin Sulfathiazole	100 mL	50 mg L^{-1}	110 min 90 min 75 min 90 min	100%	UV-A	[278]
TiO_2	Commercial	—	Ivermectin	1 L	500 µg L^{-1}	600 s	98%	UV	[279]
TiO_2 P25 ** $FeCl_3$ $TiO_2/FeCl_3$	Commercial	—	Sulfadiazine Sulfamethoxazole Sulfathiazole (mixture)	100 mL	0.1 mmol L^{-1}	60 min	~82% ~92% ~98%	UV	[280]
TiO_2 P25	Commercial	—	Thimerosal	150 mL	40 mg L^{-1}	20 min	100%	UV-A	[281]
$H_2TCPP@TiO_2$	Non-covalent functionalization of TiO_2 with porphyrin	Suported in TiO_2 surface	Oxolinic acid (OXA) Oxytetracycline (OTC)	50 mL	30 µM	40 min	62% OXA 59% OTC	Solar simulator	[282]
$CuTCPP@TiO_2$							68% OXA 62% OTC		
$ZnTCPP@TiO_2$							52% OXA 54% OTC		
TiO_2 P25	Commercial	—					92% OXA 65% OCT		
TiO_2 TiO_2/H_2O_2	Commercial	—	Flumequine	1 L	500 µg L^{-1}	60 min	99% 98%	UV	[283]
$FeNi_3@SiO_2@ZnO$	Co-precipitation, sol-gel, impregantion	31-62 nm, highly agglomerated particles	Tamoxifen	250 mL	20 mg L^{-1}	60 min	100%	Solar simulator	[284]
$Bi/BiOBr/Bi_2WO_6$	Hydrothermal	Diameter of about 3 µm, spheres	Norfloxacin	50 mL	20 mg L^{-1}	180 min	96.1%	Visible	[285]

(Table 4 – continuation)

Material	Synthesis method	Characterization	Degraded molecule	Batch size	Solution concentration	Reaction time	Efficiency	Irradiation	Ref.
BiOBr	Hydrothermal	1-3 μm, irregular flake morphology with smooth edges	Ciprofloxacin	40 mL	5 mg L^{-1}	140 min	100%	Visible	[286]
Bi_2MoO_6	Hydrothermal route followed by calcination	30-100 nm, granulated	Sulfamethazine	200 mL	0.0180 mM	150 min	~90%	Solar simulator	[287]
g-C_3N_4/BiOI/ exfoliated graphite	Ultrasonication method	BiOI 0.60 μm to 1.25 μm, flower-like microspheres, irregular g-C_3N_4 sheets, and EG sheets	Sulfamethoxazole	100 mL	30 mg L^{-1}	180 min	88%	Solar simulator	[288]
$Nd_2Mo_3O_9$	Sol-gel	50-80 nm, flowerlike structures with smooth surfaces	Nitrofurantoin	100 mL	10 mg L^{-1}	45 min	> 99%	Visible	[289]
GO/nanohydroxy apatite	Chemical modification of graphene oxide (GO) by triethyl-tetramine	Sheet of GO	Aureomycine hydro-chloride	250 mL	2 mg L^{-1}	42 min	97%	Solar simulator	[290]
Co_3O_4/WO_3	Coprecipitation and impregnation	Spherical particles of Co_3O_4 deposited on top of WO_3 spongy-like 3D platelets	Diclofenac sodium salt	50 mL	15 ppm	180 min	90.8 %	Visible	[291]
Ag_3PO_4/AgBr	Precipitation	10–100 μm, Microspheres	Ciprofloxacin	50 mL	20 mg L^{-1}	120 min	96.36%	Visible	[292]
$SnO_2/SnIn_4S_8$	In situ precipitation and hydro-thermal	SnO_2 with a thickness of about 100 nm and $SnIn_4S_8$ with a thickness of ~20 nm, Spherical shell	Plaquindox	40 mL	10 mg L^{-1}	25 min	100%	Visible	[293]

* Sterilised water, river water, and sterilised water
** Municipal wastewater, a mechanical–biological wastewater treatment plant (effluent), a household septic tank and from a municipal landfills

Table 5. Animal hormones and pharmaceutics degradation by other methods (photolysis with no catalyst).

Irradiation type	Degraded hormones/ pharmaceutics	Batch size	Solution concentration	Reaction time	Efficiency	Real effluent	Ref.
UV	Tetracycline	70 mL	2 mg L^{-1}	43 h	81%	No	[294]
Solar simulator	Sulfamethazine: **1**-High performance liquid chromatography water **2**-Wastewater effluent treatment plant	20 mL	40 mg L^{-1}	**1**-45 h **2**-30 h	100%	Urban wastewater	[295]
Solar simulator	Difloxacin (DIF): **1**-Millipore water **2**-**R**iver water Sarafloxacin (SARA): **1**-Millipore water **2**-River water	50 mL	10 μg mL^{-1}	5 h	DIF: **1**-98% **2**-100% SARA: **1**-63% **2**-99%	No	[296]
UV Solar simulator	Ciprofloxacin	750 mL	20 mg L^{-1}	128 min	>98% 61%	No	[297]
Solar light	Marbofloxacin (MAR) Enrofloxacin (ENR)	1 g soil 500 mL river water	0.5 mg kg^{-1} 50 μg L^{-1}	**Soil:** MAR 150 h ENR 200 h **Water:** MAR 115 min ENR 90 min	**Soil:** MAR ~25% ENR ~30% **Water:** MAR 100% ENR 100%	Agricultural soil samples and river water	[298]
Solar light	Sulfamethazine	500 mL	20 mg L^{-1}	120 min	>70%	No	[299]
Solar simulator	Tetracycline	—	100 μM	69 min	100%	Tap water	[300]
Natural and simulated sunlight	Zeranol β-Zearalanol Zearalanone Melengestrol Melengestrol acetate 17 α-trenbolone Trendione Trenbolone acetate 17 β-trenbolone	20 mL	5 mM	60 min	0% 0% 0% ~45% ~60% ~70% ~75% ~85% ~90%	No	[301]
Solar simulator	Sulfathiazole	—	10 μM	0.9 h	90%	No	[302]
Solar simulator	Sulfamethoxazole	20 mL	100 μg L^{-1}	3 h 17 h 17 h	100% ~85% ~90%	Ultrapure water Estuarine water Riverine water	[303]
Natural solar light	Ciprofloxacin Danofloxacin Levofloxacin Moxifloxacin Enrofloxacin Marbofloxacin	100 mL	5 μg L^{-1}	300 min 480 min 600 min 600 min 480 min 480 min	~90% ~85% ~55% ~62% ~85% ~80%	River water	[304]
UV	Sulfadiazine	500 mL	11 mg L^{-1}	60 min	99%	No	[305]

(Table 5 – continuation)

Irradiation type	Degraded hormones/ pharmaceutics	Batch size	Solution concentration	Reaction time	Efficiency	Real effluent	Ref.
UV	Doxycycline	—	500 μg L^{-1}	4 min	90% 95% 85%	Ultrapure water Fountain water Tap water	[306]
Solar simulator	Febantel	40 mL	0.1 mg L^{-1}	500 min	10%	No	[307]
UV-C	Diclofenac	—	10 mg L^{-1}	10 min	90%	No	[308]
UV-C	Cephalexin	200 mL	512 mg L^{-1}	20 min	81%	No	[309]
UV	Albendazole Fenbendazole Thiabendazole	1 L	25 μg L^{-1}	5 min 15 min 30 min	99% 99% 80%	Drinking water, surface water, and reuse water	[310]
Natural sunlight	Oxyclozanide	4 mL	20 μg mL^{-1}	30 min	~99%	No	[311]
Solar simulator	Sulfadimethoxine	50 mL	4000 μg L^{-1}	4 h	64%	No	[312]
UV activated persulfate	Oxytetracycline	10 mL	10 μM	—	85%	Natural water	[313]
Microalgae *Chlorella sp*, combined with Fe^{2+} and UV light	Ciprofloxacin 17β-estradiol	0.2 L	50 mg L^{-1}	120 min	>99% 75%	No	[314]

Table 6. Summary of materials for NO_x photo-decomposition.

Material	Characterization shape&Size	Synthesis method	Products/ N_2 selectivity	NO_x conversion/ removal (max.)	Feed gas (composition, stream rate)	Batch size (reactor, volume, catalysts amount)	Irradiation	Reaction time	Test condition	Ref.
TiO_2	Thin film Thickness 100 nm	Ionized cluster beam	N_2, O_2, N_2O	—	NO	Batch reactor, —	UV: λ> 270 nm	4 h	T: 2 °C	[315]
Ag-TiO_2	—	Sol-gel	—	N_2O: 77%	990 ppm N_2O/He mixture, 110 kPa	Batch reactor; 756 mL; 0.135 g	UV: 254 nm	24 h	T: ambient temperature	[89]
Ag-TiO_2	Ag highly dispersed on TiO_2	Photodeposition	—	N_2O: ~100%	N_2O: 0.14 kPa, MeOH: 0.63 kPa, H_2O: 1.4 kPa	Batch reactor; 1.83 L; 1.0 g	UV: 1.8 mW cm^{-2}	3 h	—	[316]
Ag-TiO_2	Thin film	Sol-gel	N_2, O_2	N_2O: 45%	0.1 mol% N_2O / He mixture	Batch reactor; 450 mL	UV: 254 nm	24 h	T: ambient temperature	[317]
Ag/TiO_2	—	solvothermal	N_2; 70%	NO: 100%	10% NO/Ar	batch reactor; 275 mL; 0.5 g	UV-vis: 3728.6 μW cm^{-2}	3 h	T: 50 °C	[318]
Cr-ion-implanted TiO_2	Thin film, thickness 300 nm	Ionized cluster beam	N_2, O_2, N_2O	—	NO: 12.3 mol	Batch reactor; 30 mL; film size: 10 mm×10 mm×1 mm	Visible light: λ > 450 nm	4 h	T: 2 °C	[319]
Fe-doped TiO_2	Thin mesoporous film	Sol-gel	N_2, O_2, NO_3^-	—	NO/He gas (~1 ppm); 1 L min^{-1}	Flow reactor: 40 cm × 10 cm × 5 cm; film: 10 cm × 5 cm	UV: 1.76 mW cm^{-2}	~160 min	—	[320]
$BiMO_x$ ($BiVO_4$, Bi_2MoO_6, Bi_2WO_6)	$BiVO_4$ and Bi_2MoO_6: nanosize flake (20−30 nm of thickness, 150 nm of length) Bi_2WO_6: microflake (thickness of 20 nm)	Hydrothermal	—	N_2O: $BiVO_4$: 27.1%, Bi_2MoO_6: 17.4%, Bi_2WO_6: 12.8%	N_2O: 680 ppm, O_2: 3 vol %, Ar: balance	Batch reactor; 0.20 g	UVA: λ = 365 nm	12 h	T: 25 °C	[321]
$BiVO_4$	Structure assembled by nanoparticles with thickness of 0.2–2 μm	Hydrothermal	—	N_2O: 26.7%	O_2: 3 vol%, N_2O: 0.68 vol%, Ar balance	Batch reactor; 0.2 g	UVA: λ=365 nm	12 h	T: 25 °C	[322]
ZnS stabilized by cetyltrimethylammonium bromide	—	Precipitation	—	N_2O: 79%	100 ppm N_2O in N_2, or 100 ppm N_2O, 6.5 mol% O_2 in N_2	Batch reactor; 450 mL; 0.1 g	UVA: λ= 254 nm	24 h	—	[323]
g-C_3N_4/WO_3	—	Calcination	—	N_2O: ~15%	998 ppm N_2O in H_2	Batch reactor; 0.045 g	UVA: λ= 365 nm	20 h	—	[324]
TiO_2/g-C_3N_4	—	Calcination	—	N_2O: ~65%	N_2O/He mixture (1020 ppm)	Batch reactor; 180 mL; 0.1 g	UVA: λ= 365 nm	14 h	—	[325]
$(Zn_{1+x}Ge)N_2O_x$	—	Calcination	—	NO: ~51%	1 ppm NO in air and N_2; 200 mL min^{-1}	Flow reactor	λ > 290 nm	—	—	[326]

(Table 6 – continuation)

Material	Characterization shape&Size	Synthesis method	Products/ N_2 selectivity	NO_x conversion/ removal (max.)	Feed gas (composition, stream rate)	Batch size (reactor, volume, catalysts amount)	Irradiation	Reaction time	Test condition	Ref.
GaON	10−20 nm	Hydrothermal	—	NO_x: ~40%	1 ppm NO in air	Flow reactor	λ>290 nm λ>400 nm	—	T: room temperature	[327]
TiO_2/g-C_3N_4	Spherical TiO_2 nanoparticles dispersed over g-C_3N_4 sheets	Pressurized hot water processing	—	N_2O: 70.6%	N_2O/He mixture (998 ppm), pressure: 1.6 bar	Batch reactor; 0.1 g	UVA: λ=365 nm	20 h	—	[328]
Ni-doped protonated layered titanate/TiO_2	—	Solid-state reaction	—	NO: ~65%	1ppm NO in air	Flow reactor	λ>290 nm	—	T: room temperature	[329]
V Oxide/ZSM-5	—	Solid-state reaction	N_2, O_2, N_2O	—	NO: 1.82×10^{-4} mol g-cat^{-1} with and without propane: 1.97×10^{-4} mol g-cat^{-1}	Batch reactor	UV: >280 nm	4 h	T: 22 °C	[330]
Vanadium silicalite Ag^+/ZSM-5	—	Hydrothermal ion-exchange	VS-2: N_2, N_2O, O_2 Ag^+/ZSM-5: N_2, N_2O, NO_2	—	10 Torr of NO, O_2, H_2O (20%)	Batch reactor	λ>280 nm λ>250 nm	~3 h	T: 22 °C	[331]
($Zn_{1+x}Ge$).(N_2O_x)	Nanotube	Hydrothermal	—	NO_x: 40%	1 ppm NO in N_2 and air; 200 mL min^{-1}	Flow reactor	λ>290 nm λ>400 nm λ>510 nm	—	RH: 23 % T: room temperature	[332]
FTiO_2/(N,C)-TiO_2	Aggregated structure of primary nanoparticles, 7.3-13 nm	Solvothermal physical mixing	—	NO_x: >40%	1 ppm NO in N_2 and air; 200 mL min^{-1}	Flow reactor; volume of sample powder: 20 mm×16 mm×0.5 mm	λ=627, 530, 445, 390 nm	—	T: room temperature	[333]
Ag_3PO_4/g-C_3N_4	Ag_3PO_4: cubic particles; g-C_3N_4: mesoporous sheet structure	In-situ hydrothermal	—	NO_x: 41.76%	1 ppm NO in N_2 and air; 200 mL min^{-1}	Flow reactor; 373 mL; volume of sample powder: 20 mm×16 mm×0.5 mm	λ>290 nm λ>400 nm	—	—	[334]
Fe/TiO_2	—	Sol-gel	N_2, O_2; 100%	NO_x: 4.5%	~1000 ppb NO in air, pure N_2, or pure He; 1 L min^{-1}	Flow reactor	UV: ~2 mW cm^{-2}	—	—	[335]

[a] T−temperature, all the temperatures converted to Celsius for comparison
[b] RH−relative humidity

Table 7. Summary of materials for NO_x photo-oxidation.

Material	Characterization shape&Size	Synthesis method	Products	NO conversion/ removal (max.)	Feed gas (composition, stream rate)	Batch size (reactor[a] volume, catalysts amount)	Irradiation	Reaction time	Test condition	Ref.
CdTe/P25	CdTe (3.5−4.0 nm) QDs dispersed on P25 support	CdTe: colloidal synthesis CdTe/P25: drop-casting	NO_2	NO: 43% (vis) 42% (UVA)	0.75 standard liters per minute (SLM) N_2, 0.250 SLM O_2, 0.010 SLM NO	200 mg	Visible light UVA	—	RH[b]: 50 ± 3%; T[c]: 23± 2 °C	[336]
Ag/TiO_2	Ag particles loaded on TiO_2 particles 0.050 ± 0.001 mg	Impregnation	NO_3^-	NO_x: 90% (1 h) ~100% (6 h)	500 ppb NO_x, (by diluting 0.625% of NO_2 and 0.125% of NO with air)	Batch reactor: 20 L	Visible light: λ=400 nm−700 nm	6 h	RH: 50%	[337]
g-C_3N_4/Ti^{3+} self-doped TiO_2	Film grain-like TiO_2 nanoparticles and feather-shaped pCN nanosheets	Spray-coating	NO_3^-, NO_2^-	NO: 25.8%	NO: 400 ppb; 1.2 L min^{-1}	340 mm × 50 mm × 50 mm	λ＞420 nm	30 min	RH: 50%; T: ambient temperature	[338]
TiO_2/graphene	Layered graphene sheets intermix with the TiO_2 nanoparticles	Solvothermal	NO_2	NO_x: 42.86% (UV) 22.75% (vis)	1 ppm NO in model air; 3 L min^{-1}	—	UV-A: ~10W m^{-2}; visible light: ~7000 lux	30 min	RH: 50%	[109]
Pt-doped TiO_2	9.2–11.1 nm	Sol–gel	NO_2, NO_3^-	NO conversion: 25.9% (vis); NO_x removal: 93.7 μmol g^{-1} (vis)	39–41 ppm NO in N_2 and wet air stream; 200 mL min^{-1}	4.5 mL; 50 mg	UV, visible: λ＞420 nm	60 min	RH: 70% T: room temperature	[339]
Sn doped blue TiO_2	Nanoparticles	Li/EDA reduction method	NO_2, HNO_2, HNO_3	NO_x: 72%	NO: ~400 ppb NO_2: ~30 ppb	0.05 g	Solar light	60 min	RH: 50%	[340]
Titanate nanotubes	Nanotubular or curled sheet structure	Hydrothermal	NO_2 oxidation: HNO_2, HNO_3 NO oxidation: NO_2, HNO_2, HNO_3	NO_2 oxidation 100% (1st hour) 74% (4th hour) NO oxidation 85%-100%	(1) 9.75 ± 0.25 ppmv NO in N_2 and humidified air, (2) 9.75 ± 0.25 ppmv NO_2 in N_2 and humidified air NO_2; 400 cm^3 min^{-1}	0.11 ± 0.01 g	UV-A: highest intensity at 365 nm, 1.25 mW cm^{-2}	4 h	RH: 55 ± 5% T: 25 ± 2°C	[341]
Fe- and Cu-doped blue TiO_2	Core-shell nanoparticle of amorphous and anatase phase	Li/EDA reduction method	NO_3^-, NO_2	NO: 70% NO_x: 68.78%	NO: ~300 ppb, NO_2: ~35 ppb; 100 sccm	240 cm^3; 0.05 g	200–1200 nm, 100 mW cm^{-2}	60 min	RH: 50% T: 22–25° C	[342]
Au/CeO_2–TiO_2	Au nanoparticles and CeO_2 species well dispersed in the TiO_2 framework	Microwave-assisted solution approach	-	NO: 85%	500 ppb NO in air; 4.0 L·min^{-1}	18 L; 0.20 g	Simulated sunlight, UV: λ=365 nm	60 min	RH: 83% T: ambient temperature	[343]
N-doped and N,S-codoped TiO_2	Dense spherical nanoparticles	Chemical treatment with various modifiers	NO_2	NO: ~45% (UV), ~12% (vis)	1 ppm NO in air; 3 L min^{-1}	—	UVB: λ=288 nm, 10 W m^{-2}, visible light: 2200 lux	90 min	RH: 50%	[344]

(Table 7 – continuation)

Material	Characterization shape&Size	Synthesis method	Products	NO conversion/ removal (max.)	Feed gas (composition, stream rate)	Batch size (reactor[a] volume, catalysts amount)	Irradiation	Reaction time	Test condition	Ref.
Amorphous carbon nitride with N_3C-site vacancies	Loose porous structure	Calcination	NO_2, NO_3^-	NO_x: 57.1%	ppb level of NO in air; 1.0 L min^{-1}	4.5 L; 0.1 g	Visible light: λ≥420 nm, 12.6 mW cm^{-2}	10 min	RH: 30% ~ 80% T: normal temperature	[345]
g-C_3N_4 with N vacancy	Porous microtubes	In situ soft-chemical method	NO_3^-, NO_2^-, NO_2	NO: 32.8%	400 ppb NO in N_2 and air	4.5 L; 0.1 g	Visible light, 25.28 mW cm^{-2}	30 min		[346]
Bi_3NbO_7	Single-crystal nanoplates superstructure	Hydrothermal	—	NO: 42.3%	~400 ppb NO in N_2 and air; 4 L min^{-1}	4.5 L; 0.1 g	Visible light: λ>420 nm	40 min	RH: 70%; T: ambient temperature	[347]
Bi@Bi_2O_3	Uniform mesoporous nanospheres	HCl–ethanol chemical etching	NO_3^-, NO_2^-, NO_2	NO: 41%	400 ppb NO diluted by pure air 3 L min^{-1}	30 cm × 15 cm × 10 cm, 0.1 g	Visible light: λ>420 nm, 28.50 mW cm^{-2}	30 min	T: ambient temperature	[348]
$Bi_2O_2CO_3$/$Bi_4O_5Br_2$	Ultrathin nanosheets 0.108g	One-step hydrothermal synthesis	NO_2, NO_3^-, NO_2^-	NO_x: 53.2%	430 ppb NO in air	4.5 L	Simulated solar light	30 min	RH: 30±5%	[349]
BiOCl/$CuBi_2O_4$	3D hierarchical microspheres	solvothermal	NO_2, NO_3^-	NO: 40%	550 ppb NO in air	1.45 L; 20 mg	Visible light: λ>420 nm	600 min	—	[350]
Bi/$Bi_2O_{2-x}CO_3$	Nanosheet	Hydrothermal	NO_3^-, NO_2^-, NO_2, H_2O_2	NO_x: 50.5%	400 ppb NO in air	4.5 L; 0.2 g	Visible light: λ≥420 nm	30 min	RH: 30±5%	[351]
gC_3N_4@ Ag/$BiVO_4$ (040)	"Sandwich" composite	Reflux method	NO_3^-	NO: 83%	400 ppm NO and 7% O_2/N_2 balance (100 mL min^{-1}) and 30% H_2O_2 solution (0.02 mL min^{-1})	Tubular quartz reactor: d = 1 cm, h = 15 cm; 0.2 g	Visible light: λ>420 nm	150 min	T: room temperature	[352]
LaFeO_3-SrTiO_3	LaFeO_3 spheresewere (0.1–1μm) coated with small SrTiO_3 nanoparticles (~30 nm)	Solvothermal	NO_3^-, NO_2^-, NO_2	2. 46.7%	400 ppb NO mixed with air of 3 L min^{-1}	10 cm×30 cm×15 cm (height×lenth×width); 0.1 g	Visible light: λ≥420 nm, 28.93 mW cm^{-2}	30 min	RH: 30 ± 5% T: ambient conditions	[353]
N-doped $(BiO)_2CO_3$ / graphene oxide	3D flower-like hierarchical microspheres	One-pot hydrothermal	Fully inhibited NO_2	NO: 50.4%	400 ppb NO in N_2 and air	10×30×15cm (height×lenth×width); 0.2 g	Simulated solar light	60 min	—	[354]
Zn-Al layered double hydroxides	Hexagonal sheet-like morphology	Coprecipitation	NO_2, NO_3^-	NO: 55%	150 and 600 ppb NO in air; 0.30 L min^{-1}	500 mg	UV: 25 W cm^{-2} visible light: 580 W cm^{-2}	60 min	RH: 50 ± 5%	[355]
α-Fe_2O_3/g-C_3N_4	α-Fe_2O_3 nanoplates dispersed among g-C_3N_4 nanosheets	Impregnation-hydrothermal	NO_2, NO_3^-	2. 60.8%	600 ppb NO, in N_2 and air; 1.2 L min^{-1}	2.26 L; 100 mg	Visible light: λ>420 nm	60 min	RH: 50%	[356]
SnO_2/graphene quantum dots	Tiny particles (~2.4 nm)	Hydrolysis hydrothermal	NO_2 NO_3^-	NO: 57% (vis) 75 (full spectrum)	600 ppb NO; flow rate: NO 12.0 mL min^{-1}, dry air 2.0 L min^{-1}	4.5 L; 0.1 g	Full spectrum and visible light (λ≥420 nm)	30 min	T: ambient temperature	[357]
BiOX (X = Cl, Br, I)	Single-Crystal Nanoplates	Precipitation	NO_2, HNO_3	NO: 21.3%	600 ppb NO in N_2 and air; 2.4 L min^{-1}	4.5 L; 0.1 g	Visible light: λ>420 nm	40 min	RH: 50% T: ambient temperature	[358]

(Table 7 – continuation)

Material	Characterization shape&Size	Synthesis method	Products	NO conversion/ removal (max.)	Feed gas (composition, stream rate)	Batch size (reactor[a] volume, catalysts amount)	Irradiation	Reaction time	Test condition	Ref.
Au-TiO_2/SiO_2	TiO_2 and Au integrated in silica matrix	Sol-gel	NO_2 NO_3^- NO_2^-	NO: 73%	3 ppm NO in air 1000 cm^3 min^{-1}	6 g	UV-vis	8 min	Absolute humidity: 25 ± 2 g m^{-3}	[359]
Carbon quantum dots modified FeOOH	CQDs scattered on the spicule FeOOH surface	Hydrothermal	NO_3^- NO_2	NO: 22%	400 ppb NO in air; 3 L min^{-1}	4.5 L; 0.1 g	Visible light: λ>420 nm, 28.29 mW cm^{-2}	30 min	—	[360]
O/Ba co-functionalized amorphous carbon nitride	—	Co-pyrolysis	NO_2 NO_3^-	NO: ~55%	500 ppb NO	30 cm×15 cm×10 cm; 0.20 g	Visible-light: 0.16 mW cm^{-2}	30 min	—	[361]
Fe_3O_4/C_3N_4	Fe_3O_4 nanoparticle located on sheet-like mesoporous -C_3N_4	Sonication	NO_3^- NO_2	NO: 40%	1 ppm of NO with N_2 and O_2; 1.010 SLM ± 0.05 SLM	200 mg	Visible light: 400–700 nm	60 min	RH: 50 ± 3% T: 23 ± 2 °C,	[362]
Ni−Co bimetal oxide/g-C_3N_4	Hollow NiCoOx loaded on the surface of g-C_3N_4 nanosheets	Low-temperature annealing	NO_3^- NO_2	NO: 59.1%	600 ppb NO in N_2 and air; 1.2 L min^{-1}.	2.26 L; 100 mg	Visible light 35 mW cm^{-2}	30 min	T: ambient temperature	[363]
g-C_3N_4/Au/ $ZnIn_2S_4$	Ultrathin $ZnIn_2S4$ nanosheets covered g-C_3N_4/Au with a sheet-on-sheet hierarchical structure	Low-temperature hydrothermal	NO_3^- NO_2	NO: 59.7%	600 ppb NO in N_2 and air; 1.2 L min^{-1}	2.26 L; 100 mg	Visible light	30 min	RH: 50% T: ambient temperature	[364]
g-C_3N_4	Nanosheets with porous structure	Thermal condensation	NO_3^- NO_2^- NO_2	NO: 65.0%, NO_2: 33.8	600 ppb NO in N_2 and air, or 400 ppb NO_2 in N_2 and air; 1.0 L min^{-1}	4.5 L; 0.2 g	Visible light: λ> 420 nm, 0.16 mW cm^{-2}	30 min	T: ambient temperature	[365]
$AgVO_3$-g-C_3N_4-graphene aerogel	Porous network framework	Boiling water bath	NO_3^- NO_2	NO: 65%	600 ppb NO in N_2 and air; 1.2 L min^{-1}	2.26 L; 0.1 g	Visible light	30 min	T: room temperature	[366]
g-C_3N_4/α-$Ni(OH)_2$	Hierarchical morphology with α-$Ni(OH)_2$ microspheres wrapped by g-C_3N_4	Hydrothermal	NO_3^-	NO: 51.3%	600 ppb NO in air; air: 2 L min^{-1}, NO: 11 mL min^{-1}	0.1 g	Visible light: λ > 420 nm, 35.88 mW cm^{-2}	30 min	—	[367]
g-C_3N_4 Modified with Perylene Imides	Platelet-like g-C_3N_4 modified with PTCDI on surface	Condensation reaction	NO_3^- NO_2	NO: 47%	600 ppb NO in air; 1 L min^{-1}	0.785 L; 50 mg	Visible light: λ > 420 nm	60 min	T: ambient temperature	[368]
S-doped g-C_3N_4 with C vacancies	Regular sheet morphology with small holes in structure	Molten salt copyrolysis	NO_2 NO_3^-	NO: 93%	200 ppm NO	100 mg	Visible light: λ > 420 nm	180 min	T: room temperature	[369]
BiOI	Hollow microspheres	Solvothermal	NO_3^- NO_2	NO: 60%	600 ppb of NO in N_2 and air; 1 L min^{-1}	4.5 L; 0.15 g	Visible light: λ= 448 nm	30 min	T: ambient temperature	[370]
BiOCl	Nanosheet	Hydrothermal	NO_3^- NO_2	NO: 60%	500 ppb NO in air; 1 L min^{-1}	30 cm×15 cm×10 cm; 0.2 g	Simulated solar light	30 min	—	[371]
BiOBr-g-C_3N_4	Nanoflowers	Solvothermal	NO_3^- NO_2	NO: 63%	600 ppb NO in N_2 and air; 1.2 L min^{-1}	2.26 L; 0.1 g	Visible light	30 min	T: room temperature	[372]
Au/g-C_3N_4	Monodisperse Au nanoparticles on lamellar g-C_3N_4 surface	In-situ wetchemical reduction	NO_3^- NO_2	NO: 41.0%	500.0 ppb NO in air; 2.4 L min^{-1}	4.5 L	Visible light: λ≥420.0 nm, 0.16 mW cm^{-2}	30 min	—	[373]

[a] The type of reactor is flow reactor unless otherwise stated. [b] T−temperature [c] RH−relative humidity

Table 8. Summary of materials for photo-selective catalytic reduction (photo-SCR) of NO_x.

Material	Characterization shape&Size	Synthesis method	Products/ N_2 selectivity	NO_x conversion /removal (max.)	Feed gas (composition, stream rate)	Reducing agent	Batch size (volume, catalyts amount)	Irradiation	Test condition	Ref.
Cu^{2+}-loaded TiO_2	Film, 1.5 μm thick	Spin coating	NO, HNO_3	NO_2: 10%	NO_2–N_2 mixture, NO_2 1 ppm; ~20 mL min^{-1}	—	Cat: 5×10 cm	UV, 1 mW cm^{-2}	RH[a]: 50% T[b]: 25 °C	[374]
Commercial TiO_2 (Cristal Global PC500)	Particles	—	N_2, N_2O, NO_3^-	NO_x: 97%	NO: 3000 ppm, O_2: 5%, H_2O: 3%	Carbon	—	UV, 1.1 mW cm^{-2}	T: 150 °C	[375]
Degussa P25	Particles in 28.2 nm for anatase and 62.7 nm for rutile	Calcination	N_2, N_2O; 65%	NO conversion rate: 280 μmol h^{-1} g_{cat}^{-1}	NO: 455 ppm, CO: 1818 ppm	CO	~1 mg	UV	—	[376]
Mo-doped TiO_2 nanotubes	Tubular structure with open ends	Hydrothermal	NO	NO_x: 77%	NO_2: 9.75 ± 0.25 ppmv; 400 cm^3 min^{-1}	—	0.11 ± 0.01 g	UV-A: 365 nm, 1.25 mW cm^{-2}	RH: 55 ± 5% T: 25 ± 2 °C	[377]
MoO_3/SiO_2 (2.5 wt% of Mo)	—	Impregnation	N_2, CO_2; 100%	NO: 100%	1.8 Torr NO 1.8 Torr CO	CO	880 cm^3; 1 g	UV	T: room temperature	[378]
TiO_2	Nanosheet	Hydrothermal	N_2, NO_2	NO_x: ~65%	NO: 400 ppmv, C_4H_{10}: 2000 ppmv, H_2O: 4 v%, O_2: 4 v%, N_2 balance; 25.0 ± 2% mL min^{-1}, GHSV 10000 h^{-1}	C_4H_{10}	0.03 g	UV: 320–500 nm	T: 120 °C	[379]
Ru(2,2'-bipyridyl-4,4'-dicarboxylic acid)$_2$(NCS)$_2$ complex/TiO_2	—	Impregnation	N_2; >99%	NO: >99%	NO: 1000 ppm, NH_3: 1000 ppm, O_2: 2%, He balance; 100–500 mL min^{-1}	NH_3	12 mm×10 mm×1.0 mm; 110 mg	Visible light: >400 nm		[380]
$CeVO_4$/phosphoric acid modified natural attapulgite	Nano fibber structure	Microwave hydrothermal	N_2, N_2O, NO_2; 99%	NO: 92% (full spectrum), 60% (NIR)	NH_3: 0.1 %, NO: 0.1 %, O_2: 3 %, N_2 balance; 150 mL min^{-1}	NH_3	3 mL	(1) Full spectrum: 290−1100 nm (2) NIR: λ≥750 nm, 50 mW cm^{-2}	T: 150 °C	[381]
Si-doped TiO_2	Nanoparticles, 8.2 nm	Hydrothermal	—	NO: ＞60%	NO: 400ppm, NH_3: 400ppm, O_2: 3%, N_2 balance; 2000 mL min^{-1}	NH_3	200 mL; 0.5 g±10%	UV: 300−400 nm	T: 50 °C	[382]
CeO_2-$CeVO_4$/palygorskite	$CeVO_4$ nanoparticles, 20-50 nm	Microwave hydrothermal	N_2; 99%	NO: 95% (simulated solar light), 63% (NIR)	NO: 1000 ppm, NH_3: 1000 ppm, O_2: 3%, N_2 balance	NH_3	3 mL	(1) simulated solar light (2) NIR: λ>760 nm	T: ~25–250 °C	[383]

(Table 8 – continuation)

Material	Characterization shape&Size	Synthesis method	Products/ N_2 selectivity	NO_x conversion /removal (max.)	Feed gas (composition, stream rate)	Reducing agent	Batch size (volume, catalyts amount)	Irradiation	Test condition	Ref.
$LaFe_{1-x}Ni_xO_3$ /palygorskite	Particles, 8 nm	Sol–gel	N_2; 98%	NO_x: 92%	NO: 1000 ppm, NH_3: 1000 ppm, O_2: 3 vol. %, N_2 balance; 1 L min^{-1}, GHSV 40,000 h^{-1}	NH_3	—	Visible light: λ ＞420 nm	T: 150–250 °C	[384]
Nitrogen-doped carbon quantum dots - modified $PrFeO_3$/palygorskite (Pal)	Nanoparticles of $PrFeO_3$ and N-CQDs dispersed on the surface of Pal	Sol−gel/impregnation	N_2; 100%	NO: 93%	NH_3: 1000 ppm, NO: 1000 ppm, O_2: 3 vol %, N_2 balance; GHSV 50000 h^{-1}	NH_3	—	Visible light, 50 mW cm^{-2}	T: 30–300 °C	[385]
Pr-doped CeO_2/ attapulgite(ATP)	CeO_2/Pr^{3+} nanoparticles (5 nm) coated on ATP fibrous structure (d. 20-30 nm)	Co-precipitation	N_2, N_2O; 95%	NO_x: 90%	NH_3: 1000 ppm, NO: 1000 ppm, O_2: 3 vol%, N_2 balance; 150 mL min^{-1}, GHSV 50000 h^{-1}	NH_3	—	Visible light: λ > 420 nm	T: 50–300 °C	[386]
$LaCoO_3$/ATP/rGO	Nanoparticles of $LaCoO_3$ scattered on ATP, rGO as 2D sheet structure	Sol-gel	N_2; 100%	NO_x: 95%	NH_3: 1000 ppm, NO: 1000 ppm, O_2: 3 vol%, N_2 balance; 150 mL min^{-1}, GHSV 50000 h^{-1}	NH_3	—	Simulated solar-light irradiation	T: 20–300 °C	[387]
$Pr_{1-x}Ce_xFeO_3$/ palygorskite (Pal)	Perovskite nanoparticles (10 nm) on the surface of Pal	In-situ sol-gel	N_2; 99%	NO: 92%	NH_3: 1000 ppm, NO: 1000 ppm, O_2 : 3 vol%, N_2 balance; 150 mL min^{-1}, GHSV 50000 h^{-1}	NH_3	—	Visible light: λ > 420 nm, 50 mW cm^{-2}	T: 60–300 °C	[388]
$Fe_2O_3/SmFeO_3$/ palygorskite (Pal)	Nanoparticles of $SmFeO_3$ and Fe_2O_3 uniformly dispersed on the surface of Pal rods	sol-gel	N_2; 100%	NO_x: 95%	NH_3: 1000 ppm, NO: 1000 ppm, O_2: 3%, N_2 balance; 2 L min^{-1}, GHSV 40,000 h^{-1}	NH_3	—	Simulated sun-light	T: 30–200 °C	[389]
Porphyrin-derivative-modified TiO_2	—	Impregnation	N_2; 100%	NO: 79%	NO: 1000 ppm, NH_3: 1000 ppm, O_2: 2–10%, He balance; GHSV 50000 h^{-1}	NH_3	12mm×10mm×1 mm(height×width ×depth); 100 mg	Visible light: λ > 400 nm	-	[390]
WO_3/TiO_2	—	Impregnation	N_2, N_2O; 99%	NO: 96%	NH_3: 1000 ppm, NO: 1000 ppm, O_2: 2%, Ar balance; GHSV 32000 h^{-1}	NH_3	—	Xe lamp	T: room temperature	[391]

(Table 8 – continuation)

Material	Characterization shape&Size	Synthesis method	Products/ N_2 selectivity	NO_x conversion /removal (max.)	Feed gas (composition, stream rate)	Reducing agent	Batch size (volume, catalyts amount)	Irradiation	Test condition	Ref.
TiO_2	—	Hydrated	N_2; 100%	NO: 84%	NO: 1000 ppm, NH_3: 1000 ppm, O_2: 2%, He balance; GHSV 100000 h^{-1}	NH_3	12 mm×10 mm×1 mm; 110 mg	UV 360 mW cm^{-1}	T: 160 °C	[392]
TiO_2	—	Hydrated	N_2, N_2O; 96%	NO: 83%	NO: 1000 ppm, NH_3: 1000 ppm, O_2: 10%; GHSV 4000 h^{-1}	NH_3	50mm×15 mm×1 mm; 0.66 g	Simulated sun-light by Xe lamp	T: 50 °C	[393]
$LaFe_{1-x}Mn_xO_3$/ attapulgite (ATP)	Nanoparticles of $LaFe_{1-x}Mn_xO_3$ are dispersed on the surface of ATP uniformly	Sol-gel	N_2; 100%	NO_x: 85%	NH_3: 1000 ppm, NO: 1000 ppm, O_2: 3 vol% N_2: balance 150 mL min^{-1}, GHSV 50000 h^{-1}	NH_3	—	Visible light: $\lambda > 420$ nm	T: 20–200 °C	[394]
Pd/TiO_2	—	Incipient wetness impregnation	N_2	NO_x: 93.7%	NO: 400 ppm, C_3H_8: 5000 ppm, O_2: 5%, N_2: balance 5 mL min^{-1}	C_3H_8	0.5 g	320–500 nm 120–620 mW cm^{-2}	T: room temperature	[395]

[a] T−temperature, all the temperatures are converted to Celsius for comparison
[b] RH−relative humidity

Table 9. Application of photocatalysts for NO_x abatement in pilot site/field tests.

Photocatalytic material	NO_x conversion(max)	Treated gas composition	Test sample/setup/location	Test condition	Irradiation	Duration	Ref.
TiO_2	Mineral silicate paint: NO: 74% NO_2: 27% styrene acrylic paint: NO: 91% NO_2: 71%	Pure NO or NO_2, 220 ppb	Sample: (1) mineral silicate paint with 10% TiO_2, (2) water-based styrene acrylic paint with 10% TiO_2. Setup: Each sample set consisted of four 1 m^2 glass panels (total surface area 4 m^2), reaction in a stainless steel (30 m^{-3}) walk-in type environmental chamber	RH[a]: 50% T[b]: 30 °C	UV	6 h	[396]
TiO_2/γ-Al_2O_3	NO_x: 43.5%	NO 400 ppmv, C_4H_{10} 2000 ppmv, O_2 4 v%; H_2O 4 v%, N_2 balance; flow rate: 25 mL min^{-1}, GHSV: 10000 h^{-1}	Lab-scale photoreactor (0.15 mL)	T: 120 °C	λ=320–500 nm, 200 mW cm^{-2},	—	[397]
	NO_x: 68–75%	exhaust flue gas from the coal burning in a domestic furnace and industrial-used reductants mixture (55% of C_3H_8 and 45% of C_4H_{10}) flow rate: 2300 mL min^{-1}, GHSV: 80 h^{-1}	Pilot-scale photoreactor (1750 mL)	T: 120 °C	UV	110 min	
TiO_2	NO_x (1) 13% during the experimental period, (2) 18.9% (November 5), (3) 11.1% (November 6, fog and cloud cover), (4) 21.2% (November 7, relative sunlight)	Air	Setup: TiO_2 on the retaining wall of the expressway (1) test section (150 m × 1.9 m) (2) comparison section (200 m × 1.9 m) Location: Gyeongbu expressway, Korea	RH: 35−99% T: 6−15 °C wind speed: 1−3 m s^{-1}	Sunlight	7 days	[398]
TiO_2	No improvement on air quality (NO_x) was demonstrated. Possible reason: short contact time between air and TiO_2, and unfavourable meteorological conditions in Netherlands.	Air	Setup and Two locations (1) Four panels with TiO_2 coatings fitted to a noise barrier at Terschuur, Netherlands. (2) A porous noise barrier with TiO_2 coating at Putten, Netherlands.	—	—	—	[399]
TiO_2	NO_x: 36.7–82.0%	Artificial source	Sample: TiO_2-containing mix mortar on the surface of panels. Setup: Three canyon streets at a scale of 1:5 (2 m×5.2 m×18.2 m, width×height×length), including two canyon streets as reference. Location: Guerville, France.	Low wind speed	High solar intensities	9th July - 3rd September, 2004	[99]
TiO_2	NO_x: 12.35%-24.1%	Vehicle emission	Setup: TiO_2 coating on concrete road surface Location: road at the Zhonghe Toll Station, China	Wind speed ＜0.8 m s^{-1}	Sunlight	3 months, summer and winter, during the daytime (06:00-18:00)	[101]

(Table 9 – continuation)

Photocatalytic material	NO_x conversion(max)	Treated gas composition	Test sample/setup/location	Test condition	Irradiation	Duration	Ref.
TiO_2	NO: 22%,	Air	Setup: 200m×2 sidewalk pavers, 100 m with TiO_2 for test and 100 m without TiO_2 as reference. Location: Copenhagen central street, Denmark	RH: 25−80% T: 13−25 °C	Sunlight 0-1500 kJ m^{-2} day^{-1}	One year, April 2012 –August 2013	[400]
TiO_2	NO_x: 19% (whole day) 28% (only afternoon) 45% (ideal weather conditions)	Air	Setup: modified street: 5 m×150 m (width×length) covered with photocatalytic blocks reference street: ~ 5 m×100 m (width×length) covered with normal blocks Location: Hengelo, Netherlands	RH: 37.7−86.7 T: 2.0−27.9 °C wind speed: 0.6−2.69 m s^{-1}	44.02-744.70 W m^{-2} 3% of UVA	＞one year, January 2008 - July 2011	[401]
Photocatalytically active mortar	NO_x: ＜2% (160 m)	Air	Setup: 3 field campaigns two campaigns: photocatalytically active mortar on the side walls and ceiling of tunnel (length 70 m and 160 m), pre-campaign: test on untreated tunnel. Location: Leopold II tunnel, Brussels	RH: 70%−90% wind speed: 3 m s^{-1}	UV 315-420 nm 0.6, 1.6 W m^{-1}	June 2011-January 2013	[402]
TiO_2	NO: 19% NO_2: 20%	Car exhaust	Setup: white acrylic TiO_2-containing paint on 322 m^2 ceiling surface of the car park Location: 917 m^3 artificially closed parking area	—	UV 1 W cm^{-2}	5 h	[403]
Photocatalytic cement-based paint	NO_x: ~20% (absolute) ＞50% (real)	Air	Setup: tunnel vault (9000 m^2) treated with photocatalytic cement-based paint, tunnel dimension: 347.70 m×17 m×8.5 m (length×width×height) Location: “Umberto I” tunnel, Rome, Italy	RH: 40−70% T:23−25°C (daytime) wind speed: 0.10−1.70 m s^{-1}	UV-vis	6 weeks	[404]
Photocatalytically active mortar	NO_x removal ≤2 % possibly due to the transport limitations of the pollutants	Air	Setup: dimension of artificial street canyon: 5×5×53 m (width×height×length) one canyon coated with a photocatalytically active mortar on the walls and ground surfaces; the other canyon untreated. Location: Petosino, Italy	Wind speed: <1 m s^{-1}	UVA: ~20−40 W cm^{-2}	11th April –7th May 2013	[405]
Commercial photocatalytic products	NO_x removal 0.2-6.5% (17 months)	450 ± 50 ppbv of NO in air flow rate: 3 L min^{-1}	Setup: 9 samples: Slurries on asphalts (2), emulsions on asphalts (3), concrete tiles (4) tested using a designed PHOTONSITE device Location: Madrid, Spain	RH: 25%.	UV: 365 nm, 10 W cm^{-2}	17 months	[406]
Commercial photocatalytic products (TiO_2 as photoactive material)	NO removal: 0-75% NO_2 removal -15%-40%	Air	Setup: 10 samples including different types of commercial photocatalysts (slurries, emulsions and tiles) tested on two pilot scale demonstration platforms Location: Madrid and Arganda del Rey, Spain	RH: 10%−95% T: 0−40 °C wind speed: 0.5 m s^{-1}	Sunlight 400-1000 W cm^{-2}	~ one year	[407]
C-TiO_2	Concentration of NO_x decreased due to the reduction of NO No oxidaiton of NO_2	Vehicle emission	Setup: asphalt road (30 m×3 m, length×width), half coated with C-TiO_2, the other half as control area. Location: Sheung Shui District, New Territories, Hong Kong	—	Sunlight	60 min	[408]

(Table 9 – continuation)

Photocatalytic material	NO_x conversion(max)	Treated gas composition	Test sample/setup/location	Test condition	Irradiation	Duration	Ref.
TiO_2	N_2O: UVA: 14% UVC: 25%	Odorous gas emissions from swine manure	Panels coated with TiO_2 in a mobile laboratory (7.2×2.4×2.4 m)	T: 19−22 °C	UV-A (367 nm), UV-C (185 + 254 nm)	9.5 s	[409]
TiO_2	No	Air	Setup: test on a main street (300 m×36 m, length×width), surround buildings ~ 16 m height), the road and the dedian strip covered with photocatalytic coating (60 m×16 m, length×width). Location: the municipality of Alcobendas, Spain	—	—	41 days 12th September - 22nd October 2015	[410]
TiO_2	NO_x : ~18-79%	NO: 50, 100, 200, 500, 1000, 1500, 2000 ppb flow rate: 1, 2, 3, 4, 5 L min^{-1}	Sample: series photocatalytic cement mortar with TiO_2, Setup: standard reactor (ISO 22197–1: 2007)	RH: 16.67%, 33.34%, 50.01%, 66.68%, 83.35%	Solar simulator	—	[411]
TiO_2	NO_x: 12 % (Copenhagen airport)	Air	Setup: In Roskilde, existing asphalt treated with TiO_2 containing liquid (5000 m^2) In Copenhagen, photocatalytic concrete tiles installed (250 m^2) Location: Parking lots at Roskilde and Copenhagen airport, Denmark	—	Sunlight	2 years	[412]

[a] T−temperature
[b] RH−relative humidity

Table 10. Summary of literature about CH_4 controlled oxidation by different catalysts.

Material	Synthesis method	Particle size	Characterization remarks	Reaction setup	Phase (reaction medium)	CH_4 concentration /rate (flux)	Irradiation	Reaction time	Efficiency/ conversion/ reaction rate	Products			Ref.
TiO_2 Au/TiO_2 $PdOx/TiO_2$ PtO/TiO_2 Cu_2O/TiO_2 $FeOx/TiO_2$	Impreganation	TiO_2 ~20 nm and Fe ~2nm	Very small clusters of iron on TiO_2	10 mL/ Batch reactor	Liquid-gas	70 µ mol	UV-vis	3 h	10.9% ~7.5% ~9.0% ~7.5% ~10.5% ~15%	**CH_3OH:** ~300 µmol g^{-1} ~160 µmol g^{-1} 0 0 ~20 µmol g^{-1} ~1050 µmol g^{-1}			[123]
WO_3 TiO_2 NiO	—	—	—	60 mL/ Batch reactor	Liquid-gas	—	UV-vis	90 min	29% 21% 20%	**CH_3OH:** 140 µmol 145 µmol 80 µmol			[413]
Pt-doped TiO_2–SiO_2 (HGTS) Pt/HGTS Pt/P25 Pt/TiO_2–SiO_2	Evaporation induced self-assembly and photodeposition	Pt ~4.4 nm	Hexagonally arranged macropores	45 cm^3	Solid-gas	44.6 µmol (99.99%)	UV-vis	32 h 4 h 4 h 4 h	~28% ~6.24% 1.064% 3.92%	**C_2H_6:** 4.0 µmol 1.265 µmol 0.216 µmol 0.798 µmol	**H_2:** 7.0 µmol 1.682 µmol 0.281 µmol 1.037 µmol		[414]
Pt/TiO_2	Photodeposition	5 nm	Supported in TiO_2 P25	80 mL/ Batch reactor	Liquid-gas	99.99%	UV	6 h	~1.7%	**CO_2:** 35 µmol	**C_2H_6:** 25 µmol	**H_2:** 175 µmol	[415]
Pt/TiO_2	Photodeposition on TiO_2	—	Supported in TiO_2	95.4 mL/ Flow reactor	Solid-gas	100 µmol	UV-vis	20 h	—	**CO_2:** 0.15 µmol min^{-1} **H_2:** 0.7 µmol min^{-1}	**C_2H_6:** 0.014 µmol min^{-1}	**CO:** 0.003 µmol min^{-1}	[416]
Rh/TiO_2	Impregnation	Rh ~2.5 nm	Supported in TiO_2	—	Solid-gas	CH_4 (10%)/Ar	Visible	1 h	—	**CO_2:** 75 µmol g^{-1} min^{-1}	**H_2:** 110 µmol g^{-1} min^{-1}		[417]
SiO_2-Al_2O_3-TiO_2 SiO_2-TiO_2 SiO_2-Al_2O_3	Sol-gel	—	—	68 mL/ Batch reactor	Solid-gas	200 µmol	Visible	6 h	—	**H_2:** 2.69 µmol 0.11 µmol 0.05 µmol			[418]
$Pt/NaTaO_3$:La Pt/TiO_2 $NaTaO_3$:La $NiO/NaTaO_3$:La	Photodeposition and solid-phase reaction	—	—	1 mm^3/ Flow reactor	Solid-gas	50%	UV-vis	10 h	—	**CO_2:** 0.39 µmol min^{-1} 0.18 µmol min^{-1} 0 0	**H_2:** 1.5 µmol min^{-1} 0.76 µmol min^{-1} 0.21 µmol min^{-1} 0.18 µmol min^{-1}		[419]
$H_3PW_{12}O_{40}$ (HPW)/TiO_2 V-HPW/TiO_2 Fe-HPW/TiO_2 Ga-HPW/TiO_2 Ce-HPW/TiO_2 Co-HPW/TiO_2 Cu-HPW/TiO_2 Ag-HPW/TiO_2 Pd-HPW/TiO_2 Zn-HPW/TiO_2	Impregnation	Zn-HPW/TiO_2: TiO_2 30-40 nm	Core-shell/ Supported in TiO_2 P25	~250 mL/ Flow reactor	Solid-gas	—	UV-vis	6 h	—	**CO_2:** ~55 µmol g^{-1} h^{-1} ~40 µmol g^{-1} h^{-1} ~35 µmol g^{-1} h^{-1} ~85 µmol g^{-1} h^{-1} ~25 µmol g^{-1} h^{-1} ~35 µmol g^{-1} h^{-1} ~25 µmol g^{-1} h^{-1} ~220 µmol g^{-1} h^{-1} ~375 µmol g^{-1} h^{-1} ~85 µmol g^{-1} h^{-1}	**CO:** ~20 µmol g^{-1} h^{-1} ~20 µmol g^{-1} h^{-1} ~25 µmol g^{-1} h^{-1} ~30 µmol g^{-1} h^{-1} ~30 µmol g^{-1} h^{-1} ~45 µmol g^{-1} h^{-1} ~50 µmol g^{-1} h^{-1} ~225 µmol g^{-1} h^{-1} 0 ~425 µmol g^{-1} h^{-1}		
Pd/TiO_2	Photodeposition	2.8 nm	Supported in TiO_2 P25	80 mL/ Batch reactor	Liquid-gas	—	UV	6 h	1%	**CO_2:** 10 µmol	**C_2H_6:** 25 µmol	**H_2:** 60 µmol	[420]

(Table 10 – continuation)

Material	Synthesis method	Particle size	Characterization remarks	Reaction setup	Phase (reaction medium)	CH_4 concentration /rate (flux)	Irradiation	Reaction time	Efficiency/ conversion/ reaction rate	Products		Ref.
Pb–HPW/TiO_2 Ru-HPW/TiO_2 Pt-HPW/TiO_2 Ag-HPW/TiO_2 Cu-HPW/TiO_2 Zn-HPW/TiO_2 Bi-HPW/TiO_2 Ga-HPW/TiO_2 Ag_2O/TiO_2 TiO_2	Impregnation	TiO_2: 30-40 nm and Ag: 1.9 nm	Irregular morphology of TiO_2/ Supported in HPW/TiO_2	~250 mL/ Flow reactor	Solid-gas	—	UV-vis	7 h	—	**CO_2:** 40 μmol g^{-1} 70 μmol g^{-1} 65 μmol g^{-1} 30 μmol g^{-1} 32 μmol g^{-1} 42 μmol g^{-1} 35 μmol g^{-1} 21 μmol g^{-1} 59 μmol g^{-1} 78 μmol g^{-1}	**C_2H_6:** 38 μmol g^{-1} 45 μmol g^{-1} 68 μmol g^{-1} 143 μmol g^{-1} 20 μmol g^{-1} 3 μmol g^{-1} 12 μmol g^{-1} 13 μmol g^{-1} 43 μmol g^{-1} 0	[421]
SiO_2-Al_2O_3-TiO_2 SiO_2-TiO_2 SiO_2-Al_2O_3 Al_2O_3-TiO_2	Sol-gel	—	Supported in sílica and alumina	68 mL/ Batch reactor	Solid-gas	99.95%	UV-vis	6 h	—	**C_2H_6:** 2.07% (μmol) 0.09% (μmol) 0.10% (μmol) 0.43% (μmol)	**H_2:** 3.54 μmol 0.11 μmol 0.05 μmol 1.1 μmol	[422]
Pt/blackTiO_2	Impregnation	—	Supported in SiO_2	Flow reactor	Solid-gas	—	Visible	2 h	—	**CO_2:** 45 mmol h^{-1} g^{-1}	**H_2:** 185 mmol h^{-1} g^{-1}	[423]
TiO_2/g-C_3N_4/Ti_3C_2 g-C_3N_4 TiO_2 Ti_3C_2 TiO_2/Ti_3C_2 g-C_3N_4/Ti_3C_2	Ultrasonication and delamination	—	Ti_3C_2 sheets/Supported in Ti_3C_2	106 mL/ Batch reactor	Solid-gas	99.99%	UV-vis	4 h	—	**H_2:** 83.2 μmol g^{-1} 2 μmol g^{-1} 7.5 μmol g^{-1} 8 μmol g^{-1} 19 μmol g^{-1} 43 μmol g^{-1}	**CO:** 48.38 μmol g^{-1} 10 μmol g^{-1} 8 μmol g^{-1} 7 μmol g^{-1} 25 μmol g^{-1} 27 μmol g^{-1}	[424]
La/TiO_2	Impregnation	—	La: spherical/ Supported in TiO_2	Flow reactor	Solid-gas	22.83%	UV	146.15 min	—	**H_2:** 2.42 μmol min^{-1}		[425]
TiO_2 P25 Fe_2O_3 NiO CuO WO_3	Commercial	—	—	22 mL/ Batch reactor	Liquid-gas	99.99%	UV-vis	1 h	0.39% 0.15% 0.27% 0.43% 0.89%	**CH_3OH:** 471 μmol g^{-1} h^{-1} 71 μmol g^{-1} h^{-1} 52 μmol g^{-1} h^{-1} 151 μmol g^{-1} h^{-1} 350 μmol g^{-1} h^{-1}		[426]
Au/TiO_2 TiO_2 P25 Ag/TiO_2 Pd/TiO_2 Pt/TiO_2 Rh/TiO_2 Ru/TiO_2 Ir/TiO_2	Photodeposition	TiO_2: 25 nm and Au: 20 nm	Supported in TiO_2	Flow reactor	Solid-gas	10%	Solar simulator	~5 h	—	**C_2H_6:** 81.7 μmol g^{-1} h^{-1} 1.55 μmol g^{-1} h^{-1} 37.92 μmol g^{-1} h^{-1} 14.42 μmol g^{-1} h^{-1} 4.05 μmol g^{-1} h^{-1} 0.77 μmol g^{-1} h^{-1} 18.34 μmol g^{-1} h^{-1} 7.51 μmol g^{-1} h^{-1}		[427]
Y_2O_3:Er^{3+}-TiO_2-graphene Y_2O_3:Er^{3+}-TiO_2 TiO_2	Sol-gel	—	Platelet-shaped particles	Batch reactor	Solid-gas	—	Vis-NIR	150 min	45.1% 36.8% 6.1%		—	[428]
CuPt/TiO_2 Pt/TiO_2 Cu/TiO_2	Photodeposition and wet impregnation	3.5-6 nm	Supported in TiO_2 (PC-50)	50 mL/ Flow reactor	Solid-gas	10%	UV-vis	2 h	—	**CO_2:** 11.5 μmol h^{-1} 8.5 μmol h^{-1} 7.5 μmol h^{-1}	**C_2H_6:** 6.8 μmol h^{-1} 1.07 μmol h^{-1} 1.9 μmol h^{-1}	[429]
La/TiO_2	Sol-gel and dip-coating	8-15 nm	TiO_2: spherical	150 mL/ Flow reactor	Solid-gas	CO_2:CH_4 ratio 1.0	UV	1 h	—	**C_2H_6:** 810 μmol g^{-1}	**H_2:** 142 μmol g^{-1} **CO:** 511 μmol g^{-1}	[430]

(Table 10 – continuation)

Material	Synthesis method	Particle size	Characterization remarks	Reaction setup	Phase (reaction medium)	CH_4 concentration /rate (flux)	Irradiation	Reaction time	Efficiency/ conversion/ reaction rate	Products			Ref.
TiO_2 P25 (film)	Sol-gel	30 nm	Supported in glass fiber	Batch reactor	Solid-gas	4.96%	Solar simulator	280 min	70.8%	—			[119]
TiO_2 Pt/TiO_2 Pd/TiO_2 Au/TiO_2 $Au\text{-}CoO_x/TiO_2$ $Ag\text{-}CoO_x/TiO_2$ $Pd\text{-}CoO_x/TiO_2$ $Pt\text{-}CoO_x/TiO_2$	$NaBH_4$ chemical reduction and impregnation	Au: 4-8 nm CoO_x: 1-2 nm	Supported in TiO_2 P25	100 mL/ Batch reactor	Liquid-gas	—	UV-vis	2 h	—	**CH_3OH:** 0 50 µmol 43 µmol 29.2 µmol 50.8 µmol 60 µmol 44 µmol 48 µmol	**CO_2:** 18 µmol 98 µmol 65 µmol 39 µmol 2 µmol 8 µmol 6 µmol 23 µmol	**HCHO:** 40 µmol 12 µmol 44 µmol 45 µmol l0 µmol 15 µmol 12.5 µmol 15 µmol	[431]
Ag–ZnO ZnO (as-fabricated) ZnO (commercial) TiO_2 P25	Precipitation and impregnation	ZnO ~20nm and Ag ~2nm	Irregular	450 mL/ Batch reactor	Solid-gas	100 ppm	Solar simulator	25 min 150 min 150 min 150 min	100% 100% 35% 5%		—		[432]
Ag-ZnO	ZnO thermal decomposition and photode-positing of Ag	ZnO 30 nm	ZnO porous microflowers	400 mL/ Flow reactor	Solid-gas	250 ppm	UV-vis	120 min	98%		—		[433]
MoO_3/ ZnO ZnO	Impregnation	—	—	Batch reactor	Solid-gas	7.5 mmol h^{-1}	UV	2 h	—	**CH_3OH:** 0.1 µmol h^{-1} 0. 4 µmol h^{-1}	**CO_2:** 1 µmol h^{-1} 27 µmol h^{-1}	**HCHO:** 4.8 µmol h^{-1} 3.1 µmol h^{-1}	[434]
Ag/ZnO CuO/ZnO ZnO CuO P25	Precipitation and photodepositio n	ZnO: 20 nm	ZnO: irregular masses/Supported in ZnO	450 mL/ Batch reactor	Solid-gas	~200 ppm	UV-vis	15 min	95% 80% 20% 0 0		—		[435]
Au/ZnO NSs Au NPs ZnO NSs	Photodepositio n	NSs 3.0 nm and Au 5-86 nm	Porous nanosheets (NSs)/Supported in ZnO NSs	40 mL/ Batch reactor	Solid-gas	22.3 µmol	UV-vis	4 h	0.08%	**C_2H_6:** 45 µmol g^{-1} 0 0	**H_2:** 40 µmol g^{-1} 0 0		[436]
Au/ZnO	$NaBH_4$ reduction	Au: 7 nm	Au: spherical nano-particles/Supported in ZnO	10 mL/ Batch reactor	Liquid-gas	99.99%	Visible	2 h	—	**CH_3OH:** 1371 µmol g^{-1}	**CO_2:** 12.3 µmol g^{-1}		[437]
ZnO/$LaSrCoO_3$ ZnO/SiO_2/$LaSrCo O_3$	Colloidal deposition	ZnO: 150 nm and LSCO: 0.5-20 nm	Nanorods/ Supported in ZnO	Flow reactor	Solid-gas	500 ppm	Solar simulator	15 min	14.8% 3.64%		—		[438]
ZnO $Zn_5(OH)_8Cl_2{\cdot}H_2O$	Hydrolysis of imidazolium trichlorozincat e ionic liquids	—	Large particles with irregular shape and size	57 mL/ Batch reactor	Solid-gas	—	UV-vis	3 h	—	**CO_2:** 13.2 µmol g^{-1} h^{-1} 12.6 µmol g^{-1} h^{-1}	**H_2:** 0 1.5 µmol g^{-1} h^{-1}	**CO:** 1.5 µmol g^{-1} h^{-1} 2.0 µmol g^{-1} h^{-1}	[439]
ZnO	Hydrothermal	300 and 600 nmm	Nanosheets and nanowires	450 mL/ Batch reactor	Solid-gas	200 ppm	UV-vis	120 min	Nanorods: 10% Nanosheets: 80%		—		[440]
Bi_2WO_6 $BiVO_4$ Bi_2WO_6/TiO_2 P25	Hydrothermal	1-2 µm	Bi_2WO_6: Nanoplates $BiVO_4$: large irregular polyhedron	300 mL/ Flow reactor	Liquid-gas	CH_4 in He (20%)	UV-vis	120 min	1.4 %	**CH_3OH:** ~15 µmol g^{-1} h^{-1} 21 µmol g^{-1} h^{-1} 10 µmol g^{-1} h^{-1}	**CO_2:** 35 µmol g^{-1} h^{-1} 18 µmol g^{-1} h^{-1} 125 µmol g^{-1} h^{-1}		[441]

(Table 10 – continuation)

Material	Synthesis method	Particle size	Characterization remarks	Reaction setup	Phase (reaction medium)	CH_4 concentration /rate (flux)	Irradiation	Reaction time	Efficiency/ conversion/ reaction rate	Products			Ref.
V_2O_5/zeolite $BiVO_4/V_2O_5$/zeolite Zeolite	Impregnation	—	Agglomerated small particles of zeolite/Supported in zeolite	Flow reactor	Liquid-gas	CH_4/He (20%)	UV	90 min	—	**CH_3OH:** 12.5 μmol g^{-1} h^{-1} 11 μmol g^{-1} h^{-1} 10 μmol g^{-1} h^{-1}	**CO_2:** 300 μmol g^{-1} h^{-1} 100 μmol g^{-1} h^{-1} 300 μmol g^{-1} h^{-1}	**C_2H_6:** 3.0 μmol g^{-1} h^{-1} 3.0 μmol g^{-1} h^{-1} 13 μmol g^{-1} h^{-1}	[127]
$BiVO_4$ Bi_2WO_6	Hydrothermal	—	—	300 mL/ Flow reactor	Liquid-gas	CH_4 in He (20%)	UV-vis	90 min	—	**CH_3OH:** 6 μmol h^{-1} 5 μmol h^{-1}	**CO_2:** 7.5 μmol h^{-1} 11.5 μmol h^{-1}	**C_2H_6:** 0.75 μmol h^{-1} 0.75 μmol h^{-1}	[442]
$BiVO_4$	Hydrothermal	—	Bipyramidal and platelet	20 mL/ Flow reactor	Liquid-gas	10%	Visible	60 min	—	**CH_3OH:** 110 μmol g^{-1} h^{-1}	**CO_2:** 45 μmol g^{-1} h^{-1}		[443]
Cu/polymeric carbon nitride (PCN) PCN	Thermal condensation and calcination	—	Layered structure of PCN with Cu incorporation	25 mL/ Batch reactor	Liquid-gas	10 mL min^{-1}	UV-vis	2 h	—	**CH_3OH:** 24.5 μmol g^{-1} h^{-1} 19.5 μmol g^{-1} h^{-1}	**C_2H_6O:** 106 μmol g^{-1} h^{-1} 5.5 μmol g^{-1} h^{-1}		[444]
Ag-La/pCNNT	Template-free sonicated assisted one-pot hydrothermal	—	pCN compact sheets-like structure/Supported in pCNNT	210 mL/ Flow reactor	Solid-gas	99.99%	UV	2 h	—	**CH_3OH:** 600 μmol g^{-1}	**H_2:** 200 μmol g^{-1}	**CO:** 1400 μmol g^{-1}	[445]
g-C_3N_4	Polymerization of urea	—	Mesoporous	25 mL/ Batch reactor	Liquid-gas	99.99%	Solar simulator	2 h	—	**CH_3OH:** 4.25 μmol			[446]
g-C_3N_4@$Cs_{0.33}WO_3$	Ultrasonic-assisted	—	g-C_3N_4: cloud-like particles and $Cs_{0.33}WO_3$: rod-like/Supported in $Cs_{0.33}WO_3$	Batch reactor	Solid-gas	1000 ppm	UV-vis	4 h	—	**CH_3OH:** 9.0 μmol g^{-1}	**CO_2:** 12.5 μmol g^{-1}	**CO:** 2.0 μmol g^{-1}	[447]
2D/2D g-C_3N_4/Ti_3C_2	Ultrasonic approach	—	Ti_3C_2: nanosheets and g-C_3N_4: wrinkled sheets	106 mL/ Batch reactor	Solid-gas	99.99%	Visible	4 h	—	**H_2:** 51.24 μmol g^{-1} h^{-1}	**CO:** 73.31 μmol g^{-1} h^{-1}		[448]
g-C_3N_4	Solid-state chemical reduction	—	Fluffy and the surface rough and uneven	20 mL/ Batch reactor	Liquid-gas	99.99%	UV-vis	3 h	—	**C_2H_6O:** 281.6 μmol g^{-1} h^{-1}			[449]
WO_3/La	—	—	—	~750 ml/ Flow reactor	Liquid-gas	5 ml/min	Visible	~3.6 h	~10%	**CH_3OH:** 43 g^{-1} h^{-1}			[450]
La/WO_3	—	—	—	~750 ml/ Flow reactor	Liquid-gas	5 ml/min	Visible	~2 h	~10%	**CH_3OH:** 43 g^{-1} h^{-1}			[451]
WO_3/Fe^{3+} WO_3/Cu^{2+} WO_3/Ag^{+} WO_3	Replicating technique		Well-ordered structure with irregularly-shaped pores	300 mL/ Flow reactor	Liquid-gas	4.5 mL min^{-1}	UV-vis	2 h	—	**CH_3OH:** 55.5 μmol h^{-1} g^{-1} 45 μmol h^{-1} g^{-1} 17 μmol h^{-1} g^{-1} 27 μmol h^{-1} g^{-1}	**C_2H_6:** 2.8 μmol h^{-1} g^{-1} 0.75 μmol h^{-1} g^{-1} 0.25 μmol h^{-1} g^{-1} 2.85 μmol h^{-1} g^{-1}	**CO_2:** 87 μmol h^{-1} g^{-1} 71 μmol h^{-1} g^{-1} 121 μmol h^{-1} g^{-1} 25 μmol h^{-1} g^{-1}	[452]
Pt/$NaTaO_3$:La	Solid-state reaction	—	—	Flow reactor	Solid-gas	1020 μmol min^{-1}	UV-vis	—	0.6 %	**H_2:** 4.5 μmol min^{-1}			[453]
WO_3	Calcination	—	—	Batch reactor	Liquid-gas	—	Visible	—	—	**CH_3OH:** 32.36 mg dm^{-3}			[454]
Ag_2O@WO_3 WO_3	Wet impregnation	20–40 nm	Quasi-spherical/Supported in WO_3	70 mL/ Batch reactor	Liquid-gas	—	UV	90 min	—	**CH_3OH:** 225 % 120%	**H_2:** 4.25 mmol 1.5 mmol		[455]
WO_3 WO_3/La	Replicating technique	WO_3 225 nm and WO_3/La 125 nm	Irregular shapes	500 mL/ Flow reactor	Solid-gas	4.5 mL min^{-1}	UV-vis	2 h	—	**CH_3OH:** 5 μmol h^{-1} 9.2 μmol h^{-1}	**CO_2:** 14.5 μmol h^{-1} 9.8 μmol h^{-1}	**C_2H_6:** 1.5 μmol h^{-1} 1.0 μmol h^{-1}	[126]

(Table 10 – continuation)

Material	Synthesis method	Particle size	Characterization remarks	Reaction setup	Phase (reaction medium)	CH_4 concentration /rate (flux)	Irradiation	Reaction time	Efficiency/ conversion/ reaction rate	Products			Ref.
Pt-Ga_2O_3	Impreganation and calcination	Ga_2O_3 30 nm	—	Flow reactor	Solid-gas	1020 μmol min^{-1}	UV-vis	5 h	—	**H_2:** 0.58 μmol min^{-1}			[456]
Ga-ETS-10 Al-ETS-10 Zn-ETS-10 Fe-ETS-10 Cu-ETS-10	Ion exchange of zeolites (ETS-10)	—	—	20 mL/ Batch reactor	Solid-gas	200 μmol	UV	5 h	14.90% 8.412% 3.424% 5.992% 0.006%	**C_2H_6:** 10.89 μmol 7.164 μmol 3.417 μmol 5.285 μmol 0.006 μmol			[457]
Zeolites	Commercial	—	Porous	116 or 260 mL	Solid-gas	3 or 3.7 mmol	UV	5 min	—	**CH_3OH:** 56.5%	**H_2:** 100%		[458]
Rh-$K_2Ti_6O_{13}$ Pt-$K_2Ti_6O_{13}$ Ru-$K_2Ti_6O_{13}$	Solid-state reaction and photodeposition	0.1 to 2 μm	—	Flow reactor	Solid-gas	50%	UV-vis	6 h	—	**H_2:** 1.5 μmol min^{-1} 0.75 μmol min^{-1} 0.18 μmol min^{-1}			[459]
V_2O_5/zeolite $BiVO_4$/V_2O_5/zeolite Zeolite	Impregnation	—	Agglomerated small particles of zeolite/Supported in zeolite	Flow reactor	Liquid-gas	CH_4/He (20%)	UV	90 min	—	**CH_3OH:** 12.5 μmol g^{-1} h^{-1} 11 μmol g^{-1} h^{-1} 10 μmol g^{-1} h^{-1}	**CO_2:** 300 μmol g^{-1} h^{-1} 100 μmol g^{-1} h^{-1} 300 μmol g^{-1} h^{-1}	**C_2H_6:** 3.0 μmol g^{-1} h^{-1} 3.0 μmol g^{-1} h^{-1} 13 μmol g^{-1} h^{-1}	[127]
H-form MOR (zeolite) HMFI	—	—	—	82 cm^3/ Batch reactor	Solid-gas	200 μmol	UV-vis	3 h	—	**C_2H_6:** 0.021% ~0.03%			[460]
Silica: MCM-41 FSM-16	Sol-gel	—	Amorphous silica (MCM-41) and mesoporous silica (FSM-16)	30 mL/ Batch reactor	Solid-gas	200 μmol	UV	3 h	—	**H_2:** 4.44 x 10^{-2} μmol 5.78 x 10^{-2} μmol			[461]
SiO_2 ZrO_2/SiO_2	Sol-gel and impregnation	—	Supported in SiO_2	82 mL/ Batch reactor	Solid-gas	99.95%	UV-vis	3 h	—	**C_2H_6:** 0.021% 0.109%			[462]
WO_3/La	—	—	Larger crystallites with smoother edges	~750 mL/ Batch and flow reactor	Liquid-gas	5 ml/min	UV-vis	6 h	~4%	—			[122]
WO_3 WO_3/F WO_3/H_2O_2	WO_3 fluorination	—	—	300 mL/ Batch reactor	Liquid-gas	4.5 mL min^{-1}	UV-vis	2 h	—	**CH_3OH:** 5 μmol h^{-1} 2.4 μmol h^{-1} 2.0 μmol h^{-1}	**CO_2:** 14.5 μmol h^{-1} 8.2 μmol h^{-1} 8.3 μmol h^{-1}	**C_2H_6:** 1.5 μmol h^{-1} 1.0 μmol h^{-1} 1.8 μmol h^{-1}	[463]
V-MCM-41 (acid) V-MCM-41 (imp)	Direct synthesis acidic solution and impregnation	—	—	Flow reactor	Solid-gas	16 μmol	UV	3 h	6% 7.1%	**CH_3OH:** 87.6% 88.4%	**CO_2:** 4.2% 9.1%		[464]
SiO_2 Ce/SiO_2 Al_2O_3 Ce/Al_2O_3 CeO_2 Ce/SiO_2	Silica: sol-gel Alumina: commercial Others: impregantion	—	Supported in silica and alumina	30 mL/ Batch reactor	Solid-gas	200 μmol	UV	3 h	—	**C_2H_6:** 0.10 x 10^{-2} μmol 12 x 10^{-2} μmol 6.81 x 10^{-2} μmol 14.9 x 10^{-2} μmol 0.24 x 10^{-2} μmol 7.81 x 10^{-2} μmol	**H_2:** 0 0 12.9 x 10^{-2} μmol 0 0 18.5 x 10^{-2} μmol		[465]
VOx/SBA-15	Impregnation	—	Supported in SBA-15	Batch reactor	Solid-gas	25 mmol h-1	UV	2-5 h	810 μmol g^{-1} h^{-1}	**HCHO:** 773 μmol g^{-1} h^{-1}			[466]

(Table 10 – continuation)

Material	Synthesis method	Particle size	Characterization remarks	Reaction setup	Phase (reaction medium)	CH_4 concentration /rate (flux)	Irradiation	Reaction time	Efficiency/ conversion/ reaction rate	Products		Ref.
V-MCM-41 (acid) V-MCM-41 (imp)	Under acidic solution and impregnation	—	—	30 mL/ Flow reactor	Solid-gas	16 µmol	UV	3 h	7.1% 7.1%	**CH_3OH:** 0 88.4%	**CO_2:** 98.7% 9.1%	[467]
Pt/$NaTaO_3$:La	Flux method	160-700 nm	Cubic and rectangular/Pt supported in $NaTaO_3$:La	1 mL/ Flow reactor	Solid-gas	25%	UV-vis	4 h	—	**H_2:** 1.4 µmol min^{-1}		[468]
$SrCO_3$-$SrTiO_3$ TiO_2 g-C_3N_4 CdS Cu_2O $BiVO_4$ Ag_3PO_4	Sol-gel Commercial Thermal treatment Precipitation Precipitation Polymeric method Ion-exchange	$SrCO_3$-$SrTiO_3$: ~25 nm	Irregular morphology	450 mL/ Batch reactor	Solid-gas	200 ppm	UV-vis	5 min	100% 25% 0 0 0 0 0	—		[469]
Zn^{2+}-ZSM-5^-	Solid–vapor reaction	—	—	25 mL/ Batch reactor	Solid-gas	>99.995%	UV-vis	8 h	24%	**C_2H_6:** 23.4 µmol	**H_2:** 22.5 µmol	[470]
Cu–Ru	Impregnation	—	Cu nanoparticle 'antenna' with single-Ru atomic/Supported in Cu	Flow reactor	Solid-gas	99.99%	Visible	1 h	275 µmol g^{-1} s^{-1}	—		[471]
Pt/$CaTiO_3$	Solid-state reaction and photodeposition	0.5-1 µm	Aggregated particles/Supported in $CaTiO_3$	1mm^3/ Flow reactor	Solid-gas	50%	UV-vis	240 min	—	**H_2:** 0.40 µmol min^{-1}		[472]
V_2O_5/SiO_2	Sol-gel	—	—	Batch reactor	Solid-gas	7.5 mmol h^{-1}	UV	2 h	0.60%	**CO_2:** 12 µmol	**HCHO:** 62 µmol	**CO:** 16 µmol	[473]
Ga/SiO_2 Ga_2O_3 (synthesized) Ga_2O_3 (commercial)	Precipitation and impregnation	2-5 nm	Supported in silica	30 mL/ Batch reactor	Solid-gas	200 µmol	UV-vis	3 h	0.07% 0.14% 0.17%	**C_2H_6:** 6.2 % (µmol) 13 % (µmol) 16 % (µmol)	**H_2:** 0.04 µmol 0.07 µmol 0.11 µmol		[474]
MgO/SiO_2	Sol-gel and impregnation	—	Supported in silica	30 mL/ Batch reactor	Solid-gas	200 µmol	UV-vis	3 h	2.81% (µmol)	**C_2H_6:** 2.72% (µmol)			[475]
AlO_4/silica	Sol-gel	—	Supported in silica	82 mL/ Batch reactor	Solid-gas	200 µmol	UV	6 h	—	**C_2H_6:** 0.11%			[476]
$LaFeO_3$ (perovskite-type) $NiTiO_3$ $AgNbO_3$	Citric acid method	53 nm 38 nm 361 nm	—	0.23 mL/ Flow reactor	Solid-gas	99.99%	UV-vis	—	—	**CH_4:** 2.5% 0.9% 0.75%	**CO_2:** 1.6% 0.7% 0.25%		[477]
Ce/SiO_2 SiO_2 CeO_2 Ce/Al_2O_3 Al_2O_3	Sol-gel and impregnation	—	Supported in sílica and alumina	30 mL/ Batch reactor	Solid-gas	200 µmol	UV-vis	3 h	—	**C_2H_6:** 13.6 % (µmol) 0.10 %(µmol) 0.20% (µmol) 28.4% (µmol) 6.80% (µmol)			[478]
FeOOH/m-WO_3	Impregnation	11-13 nm	Mesoporous/Supported in m-WO_3	20 mL/ Batch reactor	Liquid-gas	10 mL/min	Visible	4 h	238.6 µmol g^{-1} h^{-1}	**CH_3OH:** 211.2 µmol g^{-1} h^{-1}	**CO_2:** ~26 µmol g^{-1} h^{-1}	**C_2H_6:** ~30 µmol g^{-1} h^{-1}	[479]
SrTiO3	—	—	—	Batch reactor	Solid-gas	1%	UV	15 min	—	**H2:** 0.038 µmol min^{-1}	**CO:** 0.35 µmol min^{-1}		[480]

(Table 10 – continuation)

Material	Synthesis method	Particle size	Characterization remarks	Reaction setup	Phase (reaction medium)	CH_4 concentration /rate (flux)	Irradiation	Reaction time	Efficiency/ conversion/ reaction rate	Products			Ref.
Ni/Al_2O_3 Ni/Ga_2O_3 Ni/TiO_2	Impregnation	—	—	Flow reactor	Solid-gas	$CO_2/CH_4/Ar$ =1/1/8	Visible	1 h	26.7% (Ni/Al_2O_3)	**H_2:** 1.73 mmol h^{-1} 0.8 mmol h^{-1} 0.9 mmol h^{-1}	**CO:** 2.58 mmol h^{-1} 1.5 mmol h^{-1} 0.9 mmol h^{-1}		[481]
Rh/tantalum oxynitride Rh/Ta_3N_5 $Rh/g\text{-}C_3N_4$ $Ru/CaFe_2O_4$ $Ru/ZnFe_2O_4$ Cu_2O $g\text{-}C_3N_4$ CdS	Hydrothermal	—	Supported in tantalum oxynitride Ta_3N_5	—	Solid-gas	$Ar/CH_4/CO_2$ =98/1/1	Visible	1 h	—	**H_2:** 50.3% 33.6% 0.1% 2.4% 2.2% 0.6% 0.2% 1.2%			[482]
$Pd@Sr_2Ta_2O_7$	Solid-state reaction and photodeposition	Pd: 13-26 nm	Pd: spherical/Supported in $Sr_2Ta_2O_7$	Flow reactor	Solid-gas	1%	UV	2 h	—	**CO_2:** 20%	**H_2:** 70%	**CO:** 72%	[483]
$\beta\text{-}Ga_2O_3$ supported on activated carbon (AC)	Hydrolysis and impregnation	Ga_2O_3: 6-15 nm	AC: porous surface/Supported in activated carbon	500 mL/ Batch reactor	Solid-gas	1.56 mmol L^{-1}	UV	150 min	91.5%		—		[484]
Pt/Ga_2O_3 Ti/Ga_2O_3 Zr/Ga_2O_3	Impregnation	—	—	Flow	Solid-gas	99.99%	UV	5 min	—	**H_2:** 5.5 µmol min^{-1} 0.5 µmol min^{-1} 0.5 µmol min^{-1}			[485]
$Au/c\text{-}WO_3$	$NaBH_4$ chemical reduction	Au: 4 nm	c-WO_3: cuboid structure/Supported in c-WO_3	150 mL/ Batch reactor	Liquid-gas	—	UV-vis	24 h	—	**HCHO:** 7202 µmol g^{-1}			[486]
$Rh/Na_2Ti_6O_{13}$	Flux method and photodeposition	1-9 µm	Hexagonal rod-like microcrystals and irregular shaped particles	1 mm^3/ Flow reactor	Solid-gas	25%	UV-vis	100 min	—	**CO_2:** 0.28 µmol min^{-1}	**H_2:** 0.96 µmol min^{-1}		[487]
CeO_2	Calcination	—	—	15 mL/ Flow reactor	Liquid-gas	99.99%	Solar simulator	2 h	—	**C_2H_6O:** 11.4 µmol g^{-1} h^{-1}			[488]
Rh/MCM Pd/MCM Ru/MCM	Precipitation and calcination	3.2nm 3.5nm 30 nm	Supported in silica	Flow reactor	Solid-gas	1%	UV	2 h	—	**CO_2:** 10% 13% 24%	**H_2:** 74% 69% 50%	**CO:** 69% 60% 34%	[489]
Au/WO_3 WO_3	Photoreduction	—	Supported in WO_3	20 mL/ Batch reactor	Liquid-gas	99.99%	Visible	1 h	94%	**C_2H_6:** 76 µmol g^{-1} h^{-1} 5 µmol g^{-1} h^{-1}	**HCHO:** 5 µmol g^{-1} h^{-1} 0		[490]
Rh/Al_2O_3 Ni/Al_2O_3	Impregnation	1.6 nm 7.9 nm	Supported in Al_2O_3	Flow reactor	Solid-gas	10%	Vis-NIR	1 h	—	**H_2:** 2.4 mmol h^{-1} 2.3 mmol h^{-1}	**CO:** 6.0 mmol h^{-1} 5.3 mmol h^{-1}		[491]
$Ag^0/Ag^+\text{-}SrTiO_3$	Photodeposition	—	Supported in $SrTiO_3$	10 mL/ Batch reactor	Liquid-gas	—	UV-vis	2 h	—	**H_2:** 21.8 µmol g^{-1} h^{-1}	**CO:** 4.3 µmol g^{-1} h^{-1}		[492]
$Pt\text{-}CaTiO_3$ $Pt/CaTiO_3$:La	Flux method, a solid-state reaction method and impregnation	$CaTiO_3$: 0.4-0.6 µm	$CaTiO_3$: polyhedral particles and well-regulated cubic or rectangular crystals	1 mm^3/ Flow reactor	Solid-gas	25%	UV-vis	2 h	—	**H_2:** 12 µmol h^{-1} 19 µmol h^{-1}			[493]

T**able 11.** Summary of research done in photocatalytic freestanding nanoparticles for H_2S photodecomposition.

Material	Synthesis method	Characterization	Product photocatalytic	Reactor/reaction volume	Gas concentration	Reaction time	Efficiency/ Conversion	Irradiation	Ref.
TiO_2	Commercial (P25)	30 nm	SO_4^{2-}	405 mL	250 ppmv	30 min	99%	UV-vis	[138]
TiO_2	Commercial	—	SO_4^{2-}	20 mL	±200 ppm	120 min	~87%	UV	[494]
TiO_2 P25/SiO_2 TiO_2/MCM-41 TiO_2-Ce/MCM-41 TiO_2-Cr/MCM-41	Hydrothermal and impregnation	—	SO_2	—	30 ppmv	3 h 6 h 6 h 0.5 h	80% 33% 0% ~40%	UV	[495]
TiO_2@MIL-101 Hollow TiO_2 Bulk TiO_2	Hard-templating method	Shells with spherical protru-sions	—	1.6 L	400 ppm	60 min	90.1% 68.8% 42.2%	UV	[496]
TiO_2 P25	Commercial	—	SO_2	—	15 ppm	5.5 h	100%	UV	[497]
TiO_2 films	Sol-gel	—	SO_4^{2-}	—	15 ppm	~2 h	~80%	UV	[498]
TiO_2 films	Thermal hydrolysis and hy-drothermal	40-50 nm/ Films porous	—	—	50 ppmv	300 min	~ 90% ~50 %	UV	[499]
N_2+H_2S+TiO_2 air+H_2S+TiO_2	Sol–gel and heat treatment	24 nm	SO_4^{2-}	—	5 mg/m^3 to 36 mg/m^3	3.35 s (residence time)	0% 61%	UV-vis	[500]
Zeolite/TiO_2	Commercail	20 nm (TiO_2)	SO_2	—	1000 ppm	180 min	97%	UV	[501]
TiO_2 P25 films	Commercial	Nanoparticles with high roughness and porosity	—	841 cm^3	12 to 14 ppmv	16 h 28 h	89% 64%	UV	[502]
TiO_2	Commercial	—	—	200 mL	0.5 ppm	40-200 s	Negligible	UV	[503]
Mn-TiO_2 TiO_2 Ni-TiO_2 Cu-TiO_2 Co-TiO_2	Modified sol-gelatin	Spherical particles clustered	SO_4^{2-}	0.5 L	150 ppm	60 min	89.9% 76.5% 71.3% 73.8% 76.9%	VUV	[504]
TiO_2	Commercial	—	—	—	—	—	Not estimated	UV	[505]
TiO_2 S-doped TiO_2	—	Nanoparticles Nanofibers	—	—	—	25 min 15 min	100% ~89%	UV	[506]
TiO_2	Commercial	—	—	52 L	4743 ± 1323 mg m^{-3}	≥20 min (retention time)	99.99%	UV	[507]
Carbon nanotube/ titanate nanotube	Hydrothermal	100–200 nm (titanate nanotube)	S	—	15 ppm	1000 min	100%	UV	[508]
Ti-Cr-MCM-48	Precipitation	—	—	—	35 ppm	60 min	92%	Visible	[509]

Table 12. Summary of supported catalysts' research for photocatalytic decomposition of H_2S.

Material	Synthesis method	Characterization	Support	Product photocatalytic	Gas concentration/ Reactor/ reaction volume	Reaction time	Efficiency/ Conversion	Irradiation	Ref.
TiO_2	Impregnation	—	Poly(ethylene terephthalate) Cellulose acetate Glass rings	—	35 ppmv	14 h	~6% ~43% ~31%	UV	[510]
Ag-TiO_2	Commercial	Rough shape	Mesoporous ceramic filter		120 ppbv/ 1000L	~10 min	100%	UV	[511]
Carbon nanofibers/TiO_2 Carbon nanofbers/TiO_2/ nanowire/MIL-100 Bulk TiO_2	Step-by-step selfassembly strategy	300-400 nm (CNs) and 10-20 nm (TiO_2)/ Carbon nanofibers (CNs): smooth surface and TiO_2 nanowires	Carbon nanofibers	—	—	120min 90 min 140 min	91.2% 93.5% 60%	UV	[512]
TiO_2	Sol–gel	20 nm	Foam nickel	S0 and SO_4^{2-}	199.54–245.48 mg/m^3 /120 L	180 min	100%	UV	[513]
TiO_2 P25 TiO_2-$SiMgO_X$ $SiMgO_X$	Extrusion of powder mixtures	—	$SiMgO_X$	SO_2	15 ppm	1.5 h	100% ~90% ~5%	UV	[514]
TiO_2, silver nanoparticles and additives	Spray coating	—	Fiber cement material	—	—	15 min	72%	UV	[515]
TiO_2 Fotosan® InterBrasil® FA-101	Commercial	22 nm 37 nm	Fibrocement tiles	SO_4^{2-}	—	6 min	77.4% ± 3.5 40.9% ± 4.1	UV	[137]
TiO_2 Fotosan® (paint)	Commercial	46 nm	Fiber cement (ceramic)	SO_4^{2-}	31 ppm	115 s (residence time)	94%	UV	[136]
Shale Shale + Fe Fe/montmorillonite	Impregnation	8-10 nm (α-Fe_2O_3)	Montmorillonite	—	90%/ 2.5 and 12 cm^3 (UV and sunlight)	40 min	100%	UV	[516]

Table 13. H_2S direct photolysis (with no catalyst) literature survey.

Material	Product photocatalytic	Reactor/reaction volume	Gas concentration	Reaction time	Efficiency/Conversion	Ref.
UV	SO_2	200 L	0.95 ppm	150 min	~50%	[517]
UV/VUV	SO_4^{2-}	—	19.5 mg m^{-3} 18.9 mg m^{-3}	1-5 s (residence time)	52% (mercury lamp) 56% (iodine lamp)	[518]
UV	SO_4^{2-}	—	3.1 mg m^{-3} 29.6 mg m^{-3}	2.9 s 5.8 s (residence time)	100% 93%	[519]
UV-vis	—	—	4 to 9 mg m^{-3} 4.3 mg m^{-3}	3.35 s (residence time)	<7% (atmosphere N_2) 84% (air atmosphere)	[520]
UV	H_2 and S	50 mL	1.5% (vol) 3.6 % (vol)	6 h 8 h	100%	[521]
UV	H_2SO_4	2 L	3 mg m^{-3} 30 mg m^{-3}	6 s (residence time)	100% 90.13%	[522]
UV	H_2 and S	2 L	12 mg m^{-3}	24 s (retention time)	74%	[523]
UV	SO_2 and H_2SO_4	—	3-23 mg m^{-3}	—	~58%	[524]

Table 14. Research summary of H_2S as a sacrificial agent for H_2 evolution by photocatalytic means.

Material	Synthesis method	Particle size	Shape	Reactor/ reaction volume	Gas concentration	Reaction time	Hydrogen prodution	Irradiation	Ref.
TiO_2	Hydrothermal	40-60 nm	Nanosheets	50 mL	3 M	5 h	95.25 μmol g^{-1} h^{-1}	UV-vis	[525]
Pt/N-TiO_2/GO**	Sol-gel and photodeposition	Pt: < 15 nm	Arbitrary shapes	18.6 mL	—	8 h	32.3 μmol h^{-1} g^{-1}	UV	[526]
Cu_2S@TiO_2	Structure-directing agent and followed by hydro-thermal treatment	—	Core-shell	50 mL	—	4 h	41.6 mmol h^{-1} g^{-1} (10.3% con-version efficiency)	Solar simulator	[527]
S,N-carbon dots/ g-C_3N_4***	Hydrothermal	S,N-carbon dots: 4 nm	g-C_3N_4: thin nanosheets and S,N-carbon dots: spherical	5 mL	7.5 mmol	3 h	832 μmol g^{-1} h^{-1}	Visible	[528]
MnCdS/CdMnS*	Solvothermal	—	Nanorods	50 mL	0.15 mol	5 h	113 mmol g^{-1} h^{-1}	Visible	[143]
Zn-InP-quantum dots	Impregnation	2-4 nm	—	5 mL	0.15 M	3 h	35 μmol mg^{-1}	Visible	[529]
NiFeZnS	Hydrothermal	—	Hybrid,porous, nano/micro-spherical	50 mL	—	3 h	90 mL	UV-vis	[530]
Ca-CdS	Impregnation	12.5 nm	—	5 mL	0.24 M	5 h	56.0 mmol g^{-1} h^{-1}	Visible	[531]
MnS/In_2S_3/PdS	Photodeposition	—	Lamellar structure	50 mL	—	5 h	22.7 mmol g^{-1} h^{-1}	Visible	[532]
FeCoZnS	Hydrothermal	—	Nano/micro-spheres	50 mL	—	3 h	8391 μmol h^{-1} g^{-1}	UV-vis	[533]

* Product photocatalytic: H_2, SO_3^{2-}, SO_4^{2-} and $S_2O_3^{2-}$ ** Supported in N-TiO_2/graphene oxide *** Supported in g-C_3N_4

Table 15. Survey of cellulose bleach photocatalytic treatments.

Material	Characterization	Reaction setup	Reaction time	Results obtained	Irradiation	Real effluent	Ref.
TiO_2 P25	—	100 mL/ Batch reactor	180 min	Conversion 15%-22%	UV	Kraft bleaching effluents	[534]
TiO_2 P25	30 nm	Batch reactor	5 h	COD: 25–30%	Solar simulator	Recycled paper mill and a kraft pulp mill	[535]
TiO_2 P25	30 nm	1 L/ Batch reactor	5 h	COD: 52%	UV	Kraft bleaching effluents	[536]
TiO_2 commercial	1 µm	24 L/Batch reactor	7 h	COD: 35%	Solar simulator	Paper industry wastewaters	[537]
TiO_2 P25 TiO_2/H_2O_2	—	300 mL/Batch reactor	360 min	COD: 326 mg L^{-1} 246 mg L^{-1}	UV	Cellulose and paper industry effluents	[538]
TiO_2 P25 ZnO Merck	—	Batch reactor	1 min	COD: 53% 51%	UV	Pulp mill effluent	[539]
ZnO Merck	—	50 mL/ Batch reactor/Cellulose concentration 120 mg L^{-1}	15 min	CO_2: 95%	UV	kraft black liquor	[540]

Table 16. Lignin model compounds photooxidation using catalysts.

Material	Characterization	Reaction setup	Lignin model compound	Reaction time	Efficiency/ conversion/ reaction rate	Irradiation	Products	Ref.
TiO_2 P25*	30 nm	1 L/Batch reactor/Lignin concentration 90 mg L^{-1}	—	420 min	56%	UV	—	[541]
TiO_2*	—	25 mL/ Batch reactor	Peroxyformic acid lignins	90 min	50%	UV-vis	—	[542]
TiO_2*	—	300 mL/ Batch reactor/ Lignin concentration 0.1 vol.%	—	150 min	100%	UV	CO_2: 15 µmol (0.003 vol.% lignin)	[158]
TiO_2 P25* ZnO*	—	Batch reactor/ Lignin concentration 0.85 mM	3-methoxy-4-hydroxyphenylmethylcarbinol	40 min 120 min	100%	UV-vis	—	[543]
ZnO* TiO_2* WO_3* In_2O_3* Fe_2O_3 CdS	0.2 µm 0.1 µm 4 µm 1 µm 4 µm 1 µm	10 mL/ Batch reactor/ Lignin concentration 0.1 g L^{-1}	—	0.6 h 0.25 h 2 h 2 h 2 h 2 h	100% 100% 100% 60% 30% 30%	UV-vis	—	[544]
CdS/CdOx** $Co(BF_4)_2$**	0.6 nm supported in quantum dots	2 mL/ Lignin concentration 0.25 mg mL^{-1}	—	24 h	—	Solar simulator	H_2: 0.53 mmol g^{-1} h^{-1}	[149]
CdS NPs*** CdS QDs****	20-40 nm 4.4 nm Cubic zinc blende structure (NPs)	15 mL/ Batch reactor/ Lignin concentration 0.1 mmol	—	12 h 3 h	97% 99%	UV-vis	Phenol: 92% 93% Acetophenone: 91% 91%	[545]

*Commercial nanoparticles **Nanoparticles obtained by precipitation ***Nanoparticles obtained hydrothermally ****Nanoparticles obtained by typical hot injection method

Table 17. Survey of research about photocatalytic materials utilization for H_2 production using glycerol as sacrificial agent.

Material	Synthesis method	Characterization	Shape	Supported/ unsupported	Glycerol concentration/ rate	Reaction time	Irradiation	Products/ Conversion	Ref.
Cu/TiO_2	Sol-gel, precipitation and photodeposition	1.6 and 4.2 nm	—	TiO_2	1 M	1 h 10 h	UV-vis and Solar simulator (SS)	**CH_4:** 25 µmol g^{-1} h^{-1} (UV-vis) and 0 (SS) **CO_2:** 225 µmol g^{-1} h^{-1} (UV-vis) 90 µmol g^{-1} h^{-1} (SS) **H_2:** 1600 µmol g^{-1} h^{-1} (UV-vis) and 600 µmol g^{-1} h^{-1} (SS)	[164]
β -Fe_2O_3 ε -Fe_2O_3	Chemical vapor deposition	200 nm/ Flow reactor	Uniform surface texture, with faceted nanopyramids	HF-etched p -type Si(100)	1 M	11 h	Solar simulator	**H_2:** 19 mmol h^{-1} m^{-2} 55 mmol h^{-1} m^{-2}	[546]
NiO/TiO_2	Impregnation	TiO_2: 20 nm/ Batch reactor	NiO: doughnut- or horseshoe-like	TiO_2	2.28 mol dm^{-3}	8 h	UV-vis	**CH_4:** 19 mmol g^{-1} h^{-1} **CO_2:** 41 mmol g^{-1} h^{-1} **H_2:** 1230 µmol g^{-1} h^{-1} **CO:** 106 mmol g^{-1} h^{-1}	[165]
Au/TiO_2	Deposition–precipitation, sol-gel, hydrothermal	Au: 5-10 nm/ Batch reactor	Au: spherical	TiO_2	10 vol.% glycerol–90 vol.% water mixture	3 h	UV	**H_2:** 27.9 mmol g^{-1} h^{-1}	[547]
Pt/TiO_2	Impregnation	Flow reactor	—	—	0.37 mM	30 h	Solar simulator	**H_2:** 0.47 µmol min^{-1} **H_2O_2:** 23 µmol	[548]
Bi_2O_3-TiO_2	Impregnation-calcination	23 nm for anatase and 44 nm for rutile; Bi_2O_3: 2-3 nm/ Batch reactor	—	TiO_2	0.1 M	—	UV-vis	**H_2:** 920 µmol h^{-1} g^{-1}	[549]
Na poly(heptazine imide)	Solid state reaction of melamine	10 nm/ Batch reactor	Small flake-like particles	—	Glycerol/water 1/9 (v/v)	18 h	Visible	**H_2:** 65 µmol	[550]
$NiOx/TiO_2$	Impregnation and calcination	TiO_2: 21-27 nm and NiO: 4-6 nm/ Batch reactor	—	—	—	4 h	UV-vis	**CO_2:** 600 µmol h^{-1} g^{-1} **H_2:** 900 µmol h^{-1} g^{-1} **CO:** 100 µmol h^{-1} g^{-1}	[551]
$Cu/Ag@TiO_2$ nanotubes	Photodeposition	Ag NPs: 5 nm and Cu NPs: 9 nm/Batch reactor	Ag NPs: spherical	TiO_2 nanotubes	5 vol.%	4 h	Sunlight	**H_2:** 56.6 mmol h^{-1} g^{-1}	[552]
Au/TiO_2	Calcination and deposition–precipitation with urea	Au: 4-7 nm/ Batch reactor	TiO_2: nanorods	TiO_2	10 vol.% glycerol–90 vol.% water	3 h	UV	**H_2:** 14.4 mmol g^{-1} h^{-1}	[553]
ZnO-ZnS/ graphene	Impregnation	40 and 90 nm/ Batch reactor	Graphene: sheet	Graphene	40 vol%	3 h	UV-vis	**H_2:** 1070 µmol h^{-1} g^{-1}	[554]
Ni/TiO_2 Au/TiO_2	Complex precipitation	Ni and Au:~5–8 nm/ Batch reactor		TiO_2	10 vol%	3 h	UV	**H_2:** 26000 µmol h^{-1} g^{-1} 30300 µmol h^{-1} g^{-1}	[555]
$CuOx/TiO_2$	Equilibrium deposition filtration	Flow reactor	—	TiO_2	0.37 mM	150 min	UV-vis	**CO_2:** 0.14 µmol min^{-1} **H_2:** 0.21 µmol min^{-1}	[556]

(Table 17 – continuation)

Material	Synthesis method	Characterization	Shape	Supported/ unsupported	Glycerol concentration/rate	Reaction time	Irradiation	Products/ Conversion	Ref.
g-C_3N_4/Montmorillonite/TiO_2 TiO_2	Sol-gel assisted hydrothermal	Batch reactor	MMT: sheets with almost smooth layers, g-C_3N_4: nanosheets and TiO_2 spherical particles	—	5%	4 h	Visible	**H_2:** 4425 ppm h^{-1} g^{-1} 2085 ppm h^{-1} g^{-1}	[557]
Au loaded mesoporous silica Au-KIT-6 Au-SBA-15 Au-MCM-41 AuCu-mesoporous silica	Impregnation	Au: 2 nm/ Batch reactor	Spherical	Mesoporous SiO_2	0.05 M	5 h	Visible	32% 22% 18% 7.5% 45%	[558]
Cu/TiO_2 P25*	Photodeposition	Batch reactor	—	TiO_2	800 mM (hole scavenger)	10 min	UV-vis	**H_2:** 14 µM	[559]
Cu/TiO_2 Ag/TiO_2 Co/TiO_2 Ni/TiO_2 TiO_2	Hydrothermal and impregnation	TiO_2: 60–125 nm/ Batch reactor	TiO_2: hollow spheres	TiO_2	5% (v/v)	4 h	Solar irradiation	**H_2:** 17000 µmol g^{-1} 6000 µmol g^{-1} 2000 µmol g^{-1} 1500 µmol g^{-1} 500 µmol g^{-1}	[560]
Cu/TiO_2	Reducing with $NaBH_4$	26 nm/ Batch reactor	Roundish small particles	TiO_2	0.05 M	5 h	Solar irradiation	**H_2:** 1240 µmol L^{-1}	[561]
Pt/TiO_2	Impregnation-chemical reduction	Pt: 2-6 nm and TiO_2: 7 nm/ Flow reactor	—	TiO_2	2.7 x 10^{-3} M	3 h	UV-vis	**CH_4:** 0.9 µmol h^{-1} **CO_2:** 0.125 mmol h^{-1} **H_2:** 0.3 mmol h^{-1}	[562]
Multiwall carbon natubes@TiO_2/ montmorillonite	Sol-gel and wet impregnation	Flow reactor	Core-shell	Montmorillonite	5%	2 h	Visible	**H_2:** 1888 ppm h^{-1}	[563]
Ag_2O-TiO_2 Bi_2O_3-TiO_2 ZnO-TiO_2 TiO_2	Sol-gel	150–220 nm/ Batch reactor	Spherical	—	10 vol%	10 h	UV-vis	**H_2:** 1250 µmol g^{-1} 1000 µmol g^{-1} 750 µmol g^{-1} 100 µmol g^{-1}	[564]
Bi/BiMoO	Solvothermal	20 nm/ Batch reactor	—	—	65 mmol L^{-1}	4 h	UV-vis	**1, 3-dihydroxyacetone:** 97.6% Conversion: 42.3%	[167]
$Ni(OH)_2$/TNT	Wet impregnation	$Ni(OH)_2$: 8.4 nm/ Batch reactor	Nanotubes hollow inside	TiO_2 nanotubes	5% v/v	4 h	Solar irradiation	**H_2:** 4719 µmol h^{-1} g^{-1}	[565]
Rh/TiO_2	Impregnation	Flow reactor	—	—	20 mM	12 h	UV-vis	**CO_2:** 366 µmol **H_2:** 1405 µmol Conversion: 39%	[566]
NiO/Al_2O_3	Sol-gel	Batch reactor	—	—	—	10 h	UV	**H_2:** 770 µmol h^{-1} g^{-1}	[567]

(Table 17 – continuation)

Material	Synthesis method	Characterization	Shape	Supported/ unsupported	Glycerol concentration/rate	Reaction time	Irradiation	Products/ Conversion	Ref.
Au-WO_3/TiO_2 TiO_2 WO_3/TiO_2 Au/TiO_2	Sol-gel assisted photo-deposition	Batch reactor	WO_3/TiO_2: spherical	WO_3/TiO_2	10% v/v	4 h	Visible	**H_2:** 17200 ppm h^{-1} g^{-1} 2920 ppm h^{-1} g^{-1} 3870 ppm h^{-1} g^{-1} 7358 ppm h^{-1} g^{-1}	[568]
TiO_2	Commercial	<25 nm/ Batch reactor	—	—	0.3 M	8 h	UV	**1, 3-dihydroxyacetone:** 23.63% **Glyceraldehyde:** 68.21%	[168]
CNTs-Pd@TiO_2	Impregnation	TiO_2: 10 nm and Pd: 3-5 nm/ Flow reactor	Nanotubes	CNTs	1 M	24 h	UV-vis	**CO_2:** 0.5 mmol g^{-1} h^{-1} **H_2:** 6 mmol g^{-1} h^{-1} **CO:** 0.3 mmol g^{-1} h^{-1}	[569]
$Cu(OH)_2$-$Ni(OH)_2$/P25	Co-deposition-precipitation	TiO_2: 20-60 nm/ Batch reactor	TiO_2: spherical and hydroxide: 1-3 nm	P25	5 vol%	5 h	UV	**H_2:** 22 mmol h^{-1} g^{-1}	[570]
Ag-pCN/TiO_2	Dip-coating monolith in a sol-gel solution	9 nm/ Flow reactor	Monolith	TiO_2	5 wt%	4 h	UV	**H_2:** 10150 μmol h^{-1}	[169]
(Ag-Co)coloaded TNP	In-situ photoreduction and impregnation	13.4 nm/ Batch reactor	Core-shell	—	5 vol %	15 h	Sunlight	**H_2:** 60000 μmol g^{-1}	[571]
$TiSi_2$	Commercial	Batch reactor	—	—	10 wt%	6 h	Solar simulator	Conversion: 64%	[572]
Cu/TNR	Hydrothermal and ion-exchange reaction	Batch reactor	Nanorod	Titanium oxide nanorod (TNR)	10 mg mL^{-1}	12 h	UV	**CO_2:** 570 μmol g^{-1} h^{-1} **H_2:** 1308 μmol g^{-1} h^{-1} **CO:** 52 μmol g^{-1} h^{-1} **CH_3OH:** 788 μmol g^{-1} h^{-1}	[166]
TiO_2 P25	Commercial	21 nm/ Flow reactor	—	—	5% (v/v)	2 h	UV-vis	**H_2:** 0.95 mmol	[573]
Polymeric carbon nitrides K, Na-poly(heptazine imide)	Thermal condensation	~10±3 nm/ Batch reactor	—	—	1 wt%	4 h	UV	**H_2O_2:** 7.5 μmol 20 μmol	[574]
Au/$ZnWO_4$-ZnO	Hydrothermal and impregnation	Batch reactor	—	—	10 mmol	6 h	Visible	Conversion: 8.4%	[575]
Pd-TiO_2	Impregnation/photo-reduction	Pd~3 nm and TiO_2~ 40 nm/ Batch reactor	—	TiO_2 P25	1 M	350 min	UV-vis	**H_2:** 450 mmol	[576]
Au_xCu-CuS	e-Beam deposition and thermal dewetting	NPs: 20-30 nm/ Batch reactor	Core-shell	TiO_2	0.05 M	5 h	Solar simulator	**1, 3-dihydroxyacetone:** 63-72% Conversion: 72%	[577]
Cu-In_2O_3 NRs/TiO_2 NWs	Hydrothermal and photodeposition	Flow reactor	Nanowires and nanorods	TiO_2 NWs	10 vol%	1 h	Visible	**H_2:** 6090 ppm g^{-1} h^{-1}	[578]

(Table 17 – continuation)

Material	Synthesis method	Characterization	Shape	Supported/ unsupported	Glycerol concentration/ rate	Reaction time	Irradiation	Products/ Conversion	Ref.
Rh/$SrTiO_3$-Al RhCrOx/ $SrTiO_3$-Al	Wet impregnation and photodeposition	2.3 nm ± 0.9 nm/ Flow reactor	Aggregates of irregularly shaped	—	20 mM	5 h	UV-vis	**CO_2:** 0 2300 μmol **H_2:** 1500 μmol 3000μmol **CO:** 0 25 μmol	[579]
TiO_2	Hydrothermal	17-24 nm/ Batch reactor	Nanosphere (TNP) Nanobelt (TNB) Nanotube (TNT) Nanosheet (TNS)	—	10 vol%	5 h	UV-vis	**H_2:** TNT: 12 μmol g^{-1} h^{-1} TNP: 6 μmol g^{-1} h^{-1} TNS: 9 μmol g^{-1} h^{-1} TNB: 9 μmol g^{-1} h^{-1}	[580]
CuO+TiO_2 mixtures	Commercial	25-50 nm/ Batch reactor	—	—	0.05 M	6 h	Solar irradiation	**H_2:** 2575 μmol L^{-1}	[581]
Pt/TiO_2	Photodeposition	Batch reactor	—	—	1.09 mol L^{-1}	1 h	UV-vis	**H_2:** 45 μmol	[582]
Pt/TiO_2	Photodeposition	25 nm/ Batch reactor	—	—	0.5 % v/v	4 h	UV	**H_2:** 2110 μmol g^{-1} h^{-1}	[583]
$BiVO_4$	Solvent-assisted hydro-thermal	0.5 μm and 1.0-1.2 μm/ Batch reactor	Densely packed micro-crystals and plate-like particles	—	0.1 M	2 h	Solar simulator	**1, 3-dihydroxyacetone:** 18.5 μmol **Glyceraldehyde:** 8.5 μmol	[584]
Bi/TiO_2	Electrospinning	<100 nm/ Batch reactor	Nanofibers	—	5% v/v	3 h	UV-vis	**H_2:** 4509 μmol g^{-1} h^{-1}	[585]
WO_3/TiO_2	Seed-assisted hydrother-mal	Batch reactor	WO_3 nanoplates	Carbon fibers	0.1 M	5 h	Solar simulator	**CO_2:** 21.7 μmol **1, 3-dihydroxyacetone:** 28.2 μmol **Glyceraldehyde:** 77.7 μmol	[586]
CuO/TiO_2 Cu_2O/TiO_2	Impregnation	Batch reactor	—	TiO_2	5% v/v	10 h	Solar irradiation	**CO_2:** 6050 μmol h^{-1} 7500 μmol h^{-1} **H_2:** 16500 μmol h^{-1} 20060 μmol h^{-1}	[587]
Bi_2WO_6	Hydrothermal	3-4 μm/ Batch reactor	Flower-like	—	0.1 mmol	5 h	Visible	**1, 3-dihydroxyacetone:** 87% Conversion: 96%	[588]
Pt/TiO_2	Impregnation	Flow reactor	—	—	0.368 mM	35 min	Solar simulator	**H_2:** 0.47 μmol min^{-1}	[589]
CuO–TiO_2	Impregnation	20–60 nm/ Batch reactor	—	TiO_2 P25	0.1 M	8 h	UV	**H_2:** 2061 μmol h^{-1} g^{-1}	[590]
CuOx/TiO_2	Water-in-oil microemulsion	Cu: 2.9 nm/ Batch reactor	—	—	1 M	25 h	UV-vis	**CO_2:** 320 μmol h^{-1} g^{-1} **H_2:** 950 μmol h^{-1} g^{-1}	[591]
Pt/TiO_2	Wet impregnation	Flow reactor	—	—	~1 mol L^{-1}	30 min	Solar simulator	**H_2:** 0.58 μmol min^{-1}	[592]

(Table 17 – continuation)

Material	Synthesis method	Characterization	Shape	Supported/ unsupported	Glycerol concentration/rate	Reaction time	Irradiation	Products/ Conversion	Ref.
CuO/TiO_2	Wet impregnation	8–12 nm/ Batch reactor	Tubular shapes, hollow in nature and open-ended on both sides	TiO_2 nanotubes	5 vol.%	4 h	Solar irradiation	**H_2:** 99823 μmol h^{-1} g^{-1}	[593]
Cu_2O-TiO_2/rGO	Ultrasound assisted wet impregnation	Cu_2O-TiO_2: 13 to 21 nm/ Batch reactor	Cu_2O-TiO_2: spherical	Reduced graphene oxide (rGO)	5 vol.%	90 min	Visible	**H_2:** 110968 μmol h^{-1} g^{-1}	[594]
Co/TiO_2	Impregnation	Batch reactor	—	—	5 vol.%	10 h	Solar irradiation	**CO_2:** 3051 μmol h^{-1} g^{-1} **H_2:** 11021 μmol h^{-1} g^{-1}	[595]
ZnO/ZnS	New water bath route	100 nm/ Flow reactor	Core/shell nanorods	—	7 vol.%	—	UV	**H_2:** 2608.7 μmol h^{-1} g^{-1}	[596]
Cu_2O/TiO_2	Wet impregnation	Batch reactor	Nanorods	—	5 vol.%	4 h	Solar irradiation	**H_2:** 50339 μmol h^{-1} g^{-1}	[597]
Pd/TiO_2	Impregnation	Batch reactor	—	—	0.1 vol.%	180 min	UV-vis	**H_2:** 13 mL	[598]
Pt–Au/TiO_2	Impregnation	TiO_2: 14 nm and Pt-Au ~1 nm/ Batch reactor	TiO_2: cubic shape	TiO_2	1 M	7 h	UV	**CO_2:** 450 μmol h^{-1} g^{-1} **H_2:** 2400 μmol h^{-1} g^{-1}	[599]
Pd/TiO_2	Impregnation	Batch reactor	—	—	0.1 vol.%	170 min	UV	**H_2:** 15 mL	[600]
TiO_2	Standard air-free Schlenk-type techniques	25-45 nm/ Batch reactor	Nanorods	—	1 M	20 h	Solar simulator	**H_2:** ~25 mmol h^{-1} g^{-1}	[601]
Pt/TiO_2	Sol-gel and photodeposition	Pt: 5 nm/ Flow reactor	—	TiO_2	7.34 M	3.5 h	UV	**CO_2:** 18.90 μmol **H_2:** 1663 μmol	[602]
Rh/TiO_2	Hydrothermal and photodeposition	Flow reactor	—	—	0.02 M	2 h	UV-vis	**CO_2:** 178 μmol **H_2:** 2242 μmol	[603]

*****Photocatalytic reduction of nitrate using glycerol as sacrificial agent

Table 18. Summary of materials for photocatalytic CO_2 reduction.

Material	Characterization Shape&size	Synthesis method	Reduction product yield[a] (max.)	Apparent quantum efficiency	Sacrificial electron donor	Reaction medium	Batch size (reactor type&volume, catalyst amount)	Irradiation	Reaction time / h	Reaction type, Temp.[b]	Ref.
TiO_2	Particle size: 30 nm	—	CH_4: 200 ppm CO: 200 ppm H_2: 120 ppm	—	—	CO_2, H_2O (vapor)	Batch reactor: 300 × 74 × 3.0 mm (length × outside diameter × thickness)	UVC: λ = 253.7 nm, UVA: 365 nm	48 h	Gas phase	[604]
TiO_2	Particle size: 4.5 to 29 nm	Precipitation and sol–gel method	CH_4: ~0.40 μmol h^{-1} g^{-1} CH_3OH:~0.05 μmol h^{-1} g^{-1} CO: ~0.04 μmol h^{-1} g^{-1} H_2: ~6.25 μmol h^{-1} g^{-1}	—	—	Aqueous solution： 100 mL, NaOH (0.2 M)	Batch annular reactor: 380 cm^3; Catalyst: 100 mg	UV: λ = 254 nm, 1.72 mW cm^{-2}	24 h	Liquid phase	[605]
TiO_2	Ultrathin flakes (1.66 nm thick)	Solvothermal – sonication	HCOOH: 1.9 μmol h^{-1} g^{-}	—	—	H_2O: 140 mL	Batch reactor; Catalyst: 500 mg	300 W Hg lamp, 100 mW cm^{-2}	8 h	Liquid phase; 0 °C	[606]
TiO_2	Anatase: aggregates of nanoparticles (NPs) rutile: aggregated flower–like structures brookite: nanorod	Hydrolysis and hydrothermal	TiB(He) CH_4: ~1.9 μmol g^{-1} CO: ~17 μmol g^{-1}		—	CO_2, H_2O (vapor)	Flow reactor; Catalyst: 100 mg	λ = 200−1000 nm, ~90 mW cm^{-2}	6 h	Gas phase	[607]
Pt/blue TiO_2	Pt NPs dispersed on TiO_2 (disordered shell crystalline core)	$NaBH_4$ reducing – photodepostion	CH_4: 80.35 μmol h^{-1} g^{-1}	12.40%	—	CO_2, H_2O (vapor)	Flow reactor; Catalyst: 40 mg	Simulated solar light	6 h	Gas phase	[608]
Pt/TiO_2	Pt NPs (1.94 nm) distributed on TiO_2	In situ hydrogenation	CH_4: 115 μmol h^{-1} g^{-1} CO: 26 μmol h^{-1} g^{-1}	1.49% (λ = 250–430 nm)	—	CO_2, H_2O (vapor)	Flow reactor; Catalyst: 15 mg	Xe lamp	8 h	Gas phase	[609]
In–doped TiO_2	Mesoporous spherical particles (d ＜ 13 nm)	Sol–gel	CH_4: 244 μmol h^{-1} g^{-1} CO: 81 μmol h^{-1} g^{-1} C_2H_4: 0.06 μmol h^{-1} g^{-1} C_2H_6: 2.78 μmol h^{-1} g^{-1} C_3H_6: 0.02 μmol h^{-1} g^{-1} C_3H_8: 0.02 μmol h^{-1} g^{-1}	—	—	CO_2, H_2O (vapor)	Batch reactor: 108 cm^3; Catalyst: 250 mg	UV: λ = 365 nm, 40 mW cm^{-2}	8 h	Gas phase; 100 °C	[610]
La–modified TiO_2	Uniform particle (~10–15 nm)	Sol–gel	CH_4: 1.73 μmol h^{-1} g^{-1} CO: ~0.35 μmol h^{-1} g^{-1}	—	—	CO_2, H_2O (vapor)	Batch reactor; Catalyst: 100 mg	UV visible light	20 h	Gas phase	[611]
Cu/TiO_2	Cu/TiO_2 (20 nm) supported by mesoporous silica	One–pot sol–gel	CO: 60 μmol h^{-1} g^{-1} CH_4: 10 μmol h^{-1} g^{-1}	1.41%	—	CO_2, H_2O (vapor)	Flow reactor: 6.0 × 2.5 cm (diameter × depth)	UV visible light	—	Gas phase	[612]
Cu/TiO_2	Cu NPs on TiO_2	Ionic liquid synthesis	CH_3OH: 230.3 μmol h^{-1} g^{-1} HCOOH: 23.5 μmol h^{-1} g^{-1} C_2H_5OH: 87.1 μmol h^{-1} g^{-1}	2.5 % (CH_3OH)	—	CO_2, H_2O (vapor)	Flow reactor: 476 cm^3; catalyst: 500 mg	UV: 2.5−10 mW cm^{-2}	120 min	Gas phase	[613]

(Table 18 – continuation)

Material	Characterization Shape&size	Synthesis method	Reduction product yield[a] (max.)	Apparent quantum efficiency	Sacrificial electron donor	Reaction medium	Batch size (reactor type&volume, catalyst amount)	Irradiation	Reaction time / h	Reaction type, Temp.[b]	Ref.
Au/TiO_{2-x}	Au clusters distributed on the surface of TiO_2 (~20 nm)	Deposition – precipitation	λ =365 nm CO: 7.52 μmol h^{-1} g^{-1} CH_4: 3.57 μmol h^{-1} g^{-1} C_2H_6: 0.59 μmol h^{-1} g^{-1} λ =530 nm C_2H_6: 0.66 μmol h^{-1} g^{-1} CH_4: ~2.7 μmol h^{-1} g^{-1}	—	—	CO_2, H_2O (vapor)	Flow reactor; Catalyst: 50 mg	(1) UV: λ = 365 nm, ~49.5 mW cm^{-2}; (2) visible light: λ = 530 nm, 64.9 mW cm^{-2}	0.5h–3h	Gas phase 30 °C	[614]
Au–In/TiO_2	Au and In evenly scattered over mesoporous TiO_2 NPs	Sol–gel	CO: 8982 μmol h^{-1} g^{-1} CH_4: 82.65 μmol h^{-1} g^{-1} C_2H_4: 1.057 μmol h^{-1} g^{-1} C_2H_6: 6.975 μmol h^{-1} g^{-1} C_3H_6: 0.527 μmol h^{-1} g^{-1} C_3H_8: 0.7425 μmol h^{-1} g^{-1}	0.79% (λ = 254 nm)	—	CO_2, H_2, He	Batch reactor: 150 cm^3	UV: 150 mW cm^{-2}	8 h	Gas phase; 100 °C	[615]
$Ni/TiO_{2[Vo]}$	Ni nanocluster (17.5 ± 3.4 nm) dispersed on TiO_2	One–pot hydrothermal	Acetaldehyde: ~1.7 μmol h^{-1} g^{-1}	—	—	CO_2, H_2O (vapor)	Flow reactor; Catalyst: 100 mg	Visible light	6 h	Gas phase; 25 ± 3 °C	[616]
N doped TiO_2	Microsheets	Hydrothermal	CH_3OH: 0.355 μmol h^{-1} g^{-1} (UV–vis) 0.14 μmol h^{-1} g^{-1} (vis)	—	—	CO_2, H_2O (vapor)	Batch reactor: 200 mL; Catalyst: 100 mg	(1) UV visible light; (2) visible light: λ＞400 nm	2 h	Gas phase; room temperature	[617]
Graphene oxide(GO)/ TiO_2	—	Wet chemical impregnation	CH_4: 0.43 μmol h^{-1} g^{-1} CO: 1.13 μmol h^{-1} g^{-1} C_2H_6: 0.02 μmol h^{-1} g^{-1} C_2H_4: 0.58 μmol h^{-1} g^{-1}	—	—	CO_2, H_2O (vapor)	Flow reactor: 9 × 250 mm (inner diameter × length)	Visible light: λ ＞400 nm, 81.0 mW cm^{-2}	8 h	Gas phase; 25 ± 5 °C	[618]
Black TiO_2	Nanotube arrays	Anodic oxidation – aluminothermic reduction	CO: 185.39 μmol h^{-1} g^{-1}	—	—	H_2O: 50 mL	Batch reactor; Catalyst: 10 mg	Visible light: λ ＞420 nm	7 h	Liquid phase; 3 °C	[619]
$CuInS_2$/ TiO_2	TiO_2 nanofiber coated with $CuInS_2$ nanoplates	Hydrothermal	CH_3OH: 0.86 μmol h^{-1} g^{-1} CH_4: 2.5 μmol h^{-1} g^{-1}	—	—	CO_2, H_2O (vapor)	Batch reactor; Catalyst: 50 mg	Simulated solar light	1 h	Gas phase	[620]
MgO/TiO_2	Microspheres	Spray pyrolysis	CO: ~30 μmol h^{-1} g^{-1} CH_4: trace	—	—	CO_2, H_2O (vapor)	Flow reactor; catalyst: 30 mg	UV visible light: λ = 200–1000 nm, 420 mW cm^{-2}	5 h	Gas phase; 150 °C	[621]
MgAl–layered double oxide (LDO) /TiO_2	MgAl–LDOs with platelet shape grafted on the surface of TiO_2 cuboids (~μm)	Hydrothermal –coprecipitation	CO: 1.7 μmol h^{-1} g^{-1} (50 °C) 4.3 μmol h^{-1} g^{-1} (150 °C)	—	—	CO_2, H_2O (vapor)	Flow reactor; Catalyst: 100 mg	UV	—	Gas phase; 50 °C, 150 °C	[622]

(Table 18 – continuation)

Material	Characterization Shape&size	Synthesis method	Reduction product yield[a] (max.)	Apparent quantum efficiency	Sacrificial electron donor	Reaction medium	Batch size (reactor type&volume, catalyst amount)	Irradiation	Reaction time / h	Reaction type, Temp.[b]	Ref.
TiO_2/MnO_x /Pt	MnO_x nanoflakes and Pt NPs on TiO_2 nanosheets	Hydrothermal – photodeposition	CH_4: 34.7 μmol m^{-2} h^{-1} CH_3OH: 30.3 μmol m^{-2} h^{-1}	—	—	CO_2, H_2O (vapor)	Batch reactor: 200 mL	UV visible light	3 h	Gas phase	[623]
TiO_2/Ti_3C_2	Ti_3C_2 dispersed on the surface of TiO_2 laminar	Calcination	CH_4: 4.4 μmol h^{-1} g^{-1} CH_3OH: trace C_2H_5OH: trace	—	—	CO_2, H_2O (vapor)	Batch reactor: 200 mL; Catalyst: 50 mg	Simulated solar light	1 h	Gas phase; room temperature	[624]
$AgBr/TiO_2$	AgBr NPs (~5 nm) on TiO_2 particles	Deposition – precipitation	CH_4: 25.7 μmol h^{-1} g^{-1} CH_3OH: 15.6 μmol h^{-1} g^{-1} C_2H_5OH: 2.7 μmol h^{-1} g^{-1} CO: 6.4 μmol h^{-1} g^{-1}	—	—	Aqueous solution: 100 mL, $KHCO_3$ (0.2 M)	Batch reactor; Catalyst: 500 mg	Visible light: λ > 420 nm	5 h	Liquid phase; room temperature	[625]
Graphene/ $Ti_{0.91}O_2$	Hollow spheres	Layer–by–layer method	CO: 8.91 μmol h^{-1} g^{-1} CH_4: 1.14 μmol h^{-1} g^{-1}	—	—	CO_2, H_2O (vapor)	Batch reactor: 230 mL; Catalyst: 10 mg	UV visible light	~6 h	Gas phase	[626]
NiO–In_2O_3/TiO_2	Mesoporous structure (6–18 nm)	Sol–gel	CO: 12029 μmol h^{-1} g^{-1} CH_4: 34 μmol h^{-1} g^{-1} C_2H_4: 0.33 μmol h^{-1} g^{-1} C_2H_6: 1.95 μmol h^{-1} g^{-1} C_3H_6: 2.36 μmol h^{-1} g^{-1} C_3H_8: 1.01 μmol h^{-1} g^{-1}	—	—	CO_2, H_2, He (balance)	Batch reactor: 150 cm^3; Catalyst: 50 mg	UV: 150 mW cm^{-2}	8 h	Gas phase; 120 °C	[627]
Ag–MWCNT@ TiO_2	Core–shell structures	One–pot synthesis	CH_4: 0.91 μmol h^{-1} g^{-1} C_2H_4: 0.048 μmol h^{-1} g^{-1}	—	—	CO_2, H_2O (vapor)	Flow reactor: 10 × 20 mm(OD × length)	Visible light	7.5 h	Gas phase	[628]
$Sr_2Bi_2Nb_2TiO_{12}$	Nanosheets	Hydrothermal – glyoxal assisted reduction treatment	CO: 17.11 μmol h^{-1} g^{-1}	—	—	CO_2, H_2O (vapor)	Batch reactor; catalyst: 100 mg	Simulated solar light	4 h	Gas phase; 20 °C	[629]
Ga_2O_3	—	Calcination	CO: 105 μmol h^{-1} g^{-1} H_2: 92.1 μmol h^{-1} g^{-1}	—	—	Aqueous solution: 10 mL, $NaHCO_3$ (1 M)	Flow reactor; Catalyst: 100 mg	UV: λ<400 nm	4 h	Liquid phase	[630]
Co_3O_4	Hollow multi–shelled structures of dodecahedron	Sequential templating approach	CO: 46.3 μmol h^{-1} g^{-1}	—	—	CO_2, H_2O (vapor)	Batch reactor: 100 mL; Catalyst: 5 mg	Simulated solar light : λ<780 nm, 100 mW cm^{-2}	5 h	Gas phase	[631]
Pt/In_2O_3	Pt particles (4 nm) dispersed on In_2O_3 nanorods	Precipitation – photodeposition	CO: 1.4 μmol h^{-1} g^{-1} CH_4: 3.5 μmol h^{-1} g^{-1}	—	—	CO_2, H_2O (vapor)	Batch reactor; catalyst: 20 mg	Simulated light: 0.120 W cm^{-2}	6 h	Gas phase; 25 °C	[632]

(Table 18 – continuation)

Material	Characterization Shape&size	Synthesis method	Reduction product yield[a] (max.)	Apparent quantum efficiency	Sacrificial electron donor	Reaction medium	Batch size (reactor type&volume, catalyst amount)	Irradiation	Reaction time / h	Reaction type, Temp.[b]	Ref.
Pt/C–In_2O_3	In_2O_3 nanobelts coated by carbon layer (5 nm thick)	Hydrothermal – photodepostion	CO: 633 μmol h^{-1} g^{-1} CH_4: 139.5 μmol h^{-1} g^{-1}	—	Triethanolamine (TEOA)	200 mL of aqueous solution with TEOA(10 vol%, pH=9)	Batch reactor: 400 mL; catalyst: 200 mg	300 W Xe–lamp	4 h	Liquid phase; 25 °C	[633]
Cu_2O	Nanocubes	Copper foam oxidation – HCl treatment – ultrasonication	CO: 8.8×10^4 μmol h^{-1} g^{-1}(with dehydrated zeolite) CO: 7.0×10^4 μmol h^{-1} g^{-1}(without dehydrated zeolite) CO: 1.4×10^5 μmol h^{-1} g^{-1}(LED flow reactor, 60 h)	—	—	CO_2, H_2	Batch reactor: 11.8 mL	Xe lamp: 40 suns light intensity	1 h per run	Gas phase	[634]
Cu_2O	Nanocrystals (cubic or mix of cubic and octahedral)	Colloidal synthesis	CH_3OH: 1.2 $\times10^6$ μmol h^{-1} g^{-1}	35.8% (λ = 530–550 nm)	—	H_2O: 5 mL	Flow reactor: 20 mL; Catalyst: 10 mg	Xe lamp: 204 W	60 min	Liquid/gas phase	[635]
Cu_2O@Cu	Nanorod arrays	In situ reduction method	CH_4: 0.12 μmol cm^{-2} C_2H_4: 0.07 μmol cm^{-2}	2.40% (λ = 420–620 nm)	—	220 mL of solution, $KHCO_3$ (0.1 M)	—	Visible light: λ > 420 nm, 1.16 mW cm^{-2}	4 h	Liquid phase; room temperature	[636]
Cu_2O/TiO_2	Nanotube arrays	Electrodeposition	CH_3OH: 55.15 μM 100 mL^{-1}	—	—	H_2O: 100 mL	catalyst: 3 cm × 3 cm	λ = 355 nm, 40 mJ $pulse^{-1}$	6 h	Liquid phase	[637]
CeO_2	Network–like porous structure consisting of NPs (12−18 nm)	Sunlight–assisted combustion synthesis	CH_3OH: 0.702 μmol h^{-1} g^{-1}	0.23% (λ = 350 nm)	—	CO_2, H_2O (vapor)	Batch reactor: 135 mL; Catalyst: 50 mg	Simulated sunlight	8 h	Gas phase; room temperature	[638]
Ni single atom/ZrO_2	Porous structure	Solvothermal – calcination – etching	CO: 11.8 μmol h^{-1} g^{-1} H_2: 0.96 μmol h^{-1} g^{-1}	0.92% (λ = 365 nm) 0.36% (λ = 420 nm)	—	CO_2, H_2O (vapor)	Batch reactor: 50 cm^3; Catalyst: 10 mg	UV visible light	5 h	Gas phase	[639]
ZnO	Opaline ZnO photonic crystal film	Spin coating	CO: 79 μmol CH_4: 0.4 μmol	—	—	CO_2, H_2O (vapor)	Batch reactor: 500 mL; Catalyst: 336 mg	UV visible light: 52 mW cm^{-2}	6 h	Gas phase; 35 °C	[640]
Mn, C–codoped ZnO	Core–triple shell hollow spheres (diameter 650 nm)	One–pot coordination polymer strategy	CO: 0.21 μmol h^{-1} g^{-1}	0.03% (λ = 365 nm)	—	CO_2, H_2O (vapor)	Batch reactor; Catalyst: 50 mg	Simulated solar light	4 h	Gas phase	[641]

(Table 18 – continuation)

Material	Characterization Shape&size	Synthesis method	Reduction product yield[a] (max.)	Apparent quantum efficiency	Sacrificial electron donor	Reaction medium	Batch size (reactor type&volume, catalyst amount)	Irradiation	Reaction time / h	Reaction type, Temp.[b]	Ref.
Ru_{ps}–Ru_{cat}/Ag /GaN:ZnO	—	—	λ > 400 nm $HCOO^-$: 4.1 μmol (TON 359) H_2: 1.2 μmol (TON 102) λ = 365 nm $HCOO^-$: 2.7 μmol (TON 223) H_2: 1.0 μmol (TON 90)	1.0% (λ = 400 nm)	Na_4EDTA	Aqueous solution: 4 mL, Na_2CO_3 (20 mM), Na_4EDTA (10 mM)	Catalyst hybrid: 4 mg, Ru_{ps}–Ru_{cat}: 3 μmol g^{-1}	λ > 400 nm; λ = 365 nm	15 h	Liquid phase; 25 °C	[642]
CuO–ZnO/TiO_2	Filamentous structures on TiO_2	Co–precipitation deposition	CH_4: 7.67 μmol h^{-1} g^{-1} CO: 66.67 μmol h^{-1} g^{-1}	2.16%	—	Aqueous solution: 600 mL, NaOH (0.2 M)	Batch reactor: 1180 mL; Catalyst: 600 mg	UVC: λ = 254 nm, 18 W	24 h	Liquid phase; 25 °C	[643]
Ag–Bi_4TaO_8Br–F	Ag NPs (~5–20 nm) dispersed on the surface of Bi_4TaO_8Br–F nanoplates	Solid state reaction	CO: ~1.4 μmol h^{-1} g^{-1}	—	—	Aqueous solution: 5 mL, $KHCO_3$ (saturated)	Batch reactor; Catalyst: 50 mg	Visible light: λ ≥ 420 nm	8 h	Liquid phase	[644]
$Bi_{12}O_{17}Cl_2$	Nanotube	Hydorthermal	CO: 48.6 μmol h^{-1} g^{-1} CH_4: trace	0.14% (λ = 400 nm)	—	H_2O: 50 mL	Batch reactor: 500 mL; Catalyst: 30 mg	Solar light by Xe lamp	4 h	Liquid phase; 5 °C	[645]
BiOCl	Nanosheets	Hot injection	CH_4: 5.2 μmol h^{-1} g^{-1}	—	—	H_2O: 80 mL	Batch reactor; Catalyst: 20 mg	UV light: λ = 250–380 nm	8 h	Liquid phase; at 25 ± 2 °C	[646]
B–doped BiOCl	Nanosheets	Molten strategy	CO: 83.64 μmol h^{-1} g^{-1} H_2: ＜1.71 μmol h^{-1} g^{-1}	~1.95% (λ = 405 nm)	—	H_2O: 100 mL	Batch reactor; Catalyst: 50 mg	Visible light: λ＞400 nm, AM 1.5, 100 mW cm^{-2}	10 h	Liquid phase; 20 ± 0.2 °C	[647]
BiOBr	Sheet–like morphology (0.81 nm thick)	Hydorthermal – ultrasonication – UV light irridiation	CO: 87.4 μmol h^{-1} g^{-1}	—	—	H_2O: 100 mL	Batch reactor; Catalyst: 100 mg	Visible light: λ＞400 nm	12 h	Liquid phase; 5 °C	[648]
BiOI	Nanosheets	Hydrothermal	CH_4: 1.78 μmol h^{-1} g^{-1} CO: 5.18 μmol h^{-1} g^{-1}	—	—	CO_2, H_2O (vapor)	Batch reactor; Catalyst: 50 mg	Xe lamp	4 h	Gas phase; 20 °C	[649]
Bi_2WO_6	Atomically thin nanosheets	Hydrothermal	CO: 7.12 μmol h^{-1} g^{-1} CH_4: 0.63 μmol h^{-1} g^{-1}	—	—	CO_2, H_2O (vapor)	Catalyst: 30 mg	Simulated solar irradiation: AM 1.5	5 h	Gas phase; 25 °C	[650]

$BiVO_4$	Rod–like structures (1 μm) sheet–like structures (400 nm–1μm)	Microwave assisted hydrothermal	C_2H_5OH: 2033 (UV–vis, monoclinc)	—	—	H_2O: 100 mL	Flow reactor; catalyst: 200 mg	(1) UV visible light (2) visible light: λ≥400 nm	80 min	Liquid phase; 0 °C	[651]

(Table 18 – continuation)

Material	Characterization Shape&size	Synthesis method	Reduction product yield[a] (max.)	Apparent quantum efficiency	Sacrificial electron donor	Reaction medium	Batch size (reactor type&volume, catalyst amount)	Irradiation	Reaction time / h	Reaction type, Temp.[b]	Ref.
(001)TiO_2–g–C_3N_4/$BiVO_4$	Nanosheets	Two–step hydroxyl–induced assembly strategy	CH_4: 0.38 μmol h^{-1} g^{-1} CO: 5.18 μmol h^{-1} g^{-1}	—	—	H_2O: 5 mL	Batch reactor; Catalyst: 100 mg	Visible light: λ≥420 nm	4 h	Liquid phase	[652]
$Bi_2O_2CO_3$	Nanosheets	Hydrothermal – UV light irradiation	CO: 275 μmol h^{-1} g^{-1}(TON 20.6) H_2: trace	2.74% (λ = 420 nm)	—	CO_2, H_2O (vapor)	Catalyst: 40 mg	Visible light: λ ＞420 nm, 50 mW cm^{-2}	—	Gas phase; 25 °C	[653]
Bi_3TiNbO_9	Nanosheets	Hydrothermal – Corona poling	CO: 20.9 μmol h^{-1} g^{-1} CH_4: 0.96 μmol h^{-1} g^{-1} H_2: 0.19 μmol h^{-1} g^{-1}	0.74% (λ = 365 nm) 0.46% (λ = 420 nm) 0.35% (λ = 450 nm)	—	CO_2, H_2O (vapor)	Batch reactor; Catalyst: 50 mg	UV visible light: AM 1.5 G, 100 mW cm^{-2}	4 h	Gas phase; ~20 °C	[654]
MXene/Bi_2WO_6	Ultrathin nanosheets	Etching – ultrasonic exfoliation – in situ growth	CH_3OH: 0.44 μmol h^{-1} g^{-1} CH_4: 1.78 μmol h^{-1} g^{-1}	—	—	CO_2, H_2O (vapor)	Batch reactor: 200 mL; catalyst: 100 mg	Simulated solar irradiation	—	Gas phase	[655]
$InVO_4$	Atomically thin sheets (~1.5 nm)	Hydrothermal	CO: 18.28 μmol h^{-1} g^{-1} CH_4: 0.28 μmol h^{-1} g^{-1}	0.54% (CO, λ = 385 nm)	—	CO_2, H_2O (vapor)	Batch reactor; catalyst: 100 mg	Simulated solar irradiation	7 h	Gas phase; room temperature	[656]
rGO/$InVO_4$ /Fe_2O_3	$InVO_4$: spherical shape (~μm)	Deposition − precipitation	CH_3OH: 708.1 μmol h^{-1} g^{-1}	—	TEA	Dimethylformamide (DMF)/H_2O/triethylamine (TEA) (3:1:1)	Batch reactor; Catalyst: 100 mg	Visible light: λ ＞400 nm	24 h	Liquid phase	[657]
Nb_2O_5/CuO	CuO NPs on the surface of Nb_2O_5 rods (700 nm)	Solvothermal	CH_4: 2 μmol h^{-1} g^{-1} HCOOH: 3.1 μmol h^{-1} g^{-1} CH_3COOH: 0.3 μmol h^{-1} g^{-1}	λ = 254 nm CH_4: 0.285% HCOOH: 0.110% CH_3COOH: 0.0415	—	H_2O: 300 mL	Batch reactor: 500 mL; Catalyst: 300 mg	UVC: λ_{max} =253.7 nm, 21.49 mW cm^{-2}	24 h	Liquid phase; 25 ± 3 °C	[658]

$SrNb_2O_6$	Nanoplates	Hydrothermal	CO: 16.6 μmol h^{-1} g^{-1} CH_4: 3.3 μmol h^{-1} g^{-1} H_2: 6.5 μmol h^{-1} g^{-1}	0.065% (λ = 330 nm)		CO_2, H_2O (vapor)	Batch reactor: ~100 mL; Catalyst: 10 mg	UV visible light: λ = 300–780 nm	10 h	Gas phase; 50 °C	[659]
Ag/ $SrNb_2O_6$	Nanorods	Flux method – chemical reduction/ impregnation/ photodeposition	CO: 102.4 μmol h^{-1} g^{-1} H: 2.2 μmol h^{-1} g^{-1}	—	—	Aqueous solution: 1.0 L, $NaHCO_3$ (0.1 M)	Flow reactor; catalyst: 500 mg	UV	1 h	Liquid phase	[660]

(Table 18 – continuation)

Material	**Characterization Shape&size**	**Synthesis method**	**Reduction product yield[a] (max.)**	**Apparent quantum efficiency**	**Sacrificial electron donor**	**Reaction medium**	**Batch size (reactor type&volume, catalyst amount)**	**Irradiation**	**Reaction time / h**	**Reaction type, Temp.[b]**	**Ref.**
Ag/$ALa_4Ti_4O_{15}$ (A = Ca, Sr, and Ba)	Ag NPs (30–40 nm) on the edge of $BaLa_4Ti_4O_{15}$ plate (100 nm thick, 1 μm width)	Polymerizable complex method–chemical reduction	CO: 73.3 μmol h^{-1} g^{-1} HCOOH: 2.3 μmol h^{-1} g^{-1} H_2: 33.3 μmol h^{-1} g^{-1}	—	—–	H_2O: 360 mL	Flow reactor; Catalyst: 300 mg	400 W high–pressure mercury lamp	7 h	Liquid phase; ambient temperature	[661]
$NaNbO_3$, $NaTaO_3$	Particles $NaNbO_3$: 178 nm $NaTaO_3$: 160 nm	Solid–state reaction	$NaNbO_3$: CO: ~5 μmol h^{-1} g^{-1} CH_4: ~0.09 μmol h^{-1} g^{-1} CH_3OH: 0.2 μmol h^{-1} g^{-1} H_2: ~1.3 μmol h^{-1} g^{-1} $NaTaO_3$: CO: ~5 μmol h^{-1} g^{-1} CH_4: ~0.17 μmol h^{-1} g^{-1} CH_3OH: 0.2 μmol h^{-1} g^{-1} H_2: ~1 μmol h^{-1} g^{-1}	—	—	CO_2, H_2O (vapor)	Flow reactor: 280 mL; Catalyst: 100 mg	UV: λ_{max}= 365 nm	15 h	Gas phase; 50 °C	[662]
Ag/ $NaTaO_3$:A (A=Mg, Ca, Sr, Ba, and La)	—	Solid state reaction –photodeposition/impregnation/liquid–phase reduction	CO: 318 μmol h^{-1} H_2: ~33.3 μmol h^{-1}	—	—	H_2O: 350–370 mL, one of the following chemicals is added: H_2SO_4, NaCl, Na_2SO_4, $NaHCO_3$, $KHCO_3$, Na_2CO_3, K_2CO_3, NaOH, KOH	Flow reactor; Catalyst: 250–1000 mg	UV	~6 h	Liquid phase	[663]
Graphene/ TaON	Island–shaped graphene on TaON particles	CVD	CH_4: 1.61 μmol h^{-1} g^{-1} CO: trace	0.41% (λ = 500 nm)	—	CO_2, H_2O (vapor)	Batch reactor: 230 mL; Catalyst: 100 mg	Visible light: λ>420 nm	8 h	Gas phase; 20 °C	[664]

Ag/TaON–RuBLRu′	—	—	HCOOH: 969 nmol (TON 41) H_2: 678 nmol CO: 68 nmol	—	CH_3OH	CH_3OH: 4 mL	Catalyst: semiconductor:8 mg, complex: 24 nmol	Visible light: λ＞400 nm	15 h	Liquid phase	[665]
$Na_2V_6O_{16}·x H_2O$	Nanoribbons (~5 nm thickness, ~500 mm length)	Hydrothermal	$Na_2V_6O_{16}·xH_2O$ CH_4: 0.01 μmol h^{-1} g^{-1}(1st hour) RuO_2/Pt/$Na_2V_6O_{16}·xH_2O$ CH_4: ＞0.3 μmol h^{-1} g^{-1}(1st hour)	—	—	CO_2, H_2O (vapor)	Batch ractor: 230 mL; Catalyst: 100 mg	Visible light: λ＞420 nm	10 h	Gas phase	[666]

(Table 18 – continuation)

Material	Characterization Shape&size	Synthesis method	Reduction product yield[a] (max.)	Apparent quantum efficiency	Sacrificial electron donor	Reaction medium	Batch size (reactor type&volume, catalyst amount)	Irradiation	Reaction time / h	Reaction type, Temp.[b]	Ref.
Cu(II)–grafted $Nb_3O_8^-$	Cu(II) nanocluster (2–3 nm) on monodispersed sheet of $Nb_3O_8^-$ (＜2 nm thick)	Delamination – impregnation	CO: ~0.7 μmol h^{-1} g^{-1}(20 h)	—	—	Aqueous solution: 20 mL, $KHCO_3$ (0.5 M), pH=12 using NaOH	Catalyst: 100 mg	UV: λ = 240–300 nm	~25 h	Liquid phase	[667]
Ag/$SrTiO_3$	Ag NPs on $SrTiO_3$ with cubic and all edge–truncated morphology	Solvothermal – photodeposition	CO: 2.00 μmol h^{-1} g^{-1} CH_4: trace	—	TEOA	N,N–dimethylacetamide(DMA): 80 mL, TEOA: 20 mL	Batch reactor; Catalyst: 20 mg	Visible light: λ ＞420 nm	8 h	Liquid phase	[668]
Pt/$LaPO_4$	Pt NPs on $LaPO_4$ nanorods	Hydrothermal	CH_4: 12.4 μmol h^{-1} g^{-1} H_2: 4.6 μmol h^{-1} g^{-1}	0.15%	—	H_2O: 70 mL	Batch reactor: 200 mL; Catalyst: 50 mg	UV	5 h	Liquid phase 20 ℃	[669]
$ZnGa_2O_4$	Microsphere consists of ultrathin nanosheets	Solvothermal	CH_4: 69 ppm g^{-1} h^{-1}	0.035% (λ = 280 nm)	—	CO_2, H_2O (vapor)	Batch reactor: 230 mL; catalyst: 100 mg	300 W Xe lamp (IR cut)	12 h	Gas phase; room temperature	[670]
g–C_3N_4	Thin nanosheets	Thermal condensation of melamine – ultrasonic exfoliation	CH_4: 0.93 μmol h^{-1} g^{-1}	—	—	H_2O: 80 mL	Batch reactor; Catalyst: 5, 10, 20 mg	Visible light: λ ＞420 nm	8 h	Liquid phase; 15 ℃	[671]
Nitrogen–rich g–C_3N_4	Porous nanotubes, length: 2–3 μm, diameter: 30–60 nm	Supramolecular self–assembly strategy	CO: 103.6 μmol h^{-1} g^{-1} H_2: ~18 μmol h^{-1} g^{-1}	0.43% (λ = 400 nm)	TEOA	H_2O: 4 mL, TEOA: 2 mL, acetonitrile (MeCN): 6 mL	Batch reactor: 300 mL; Catalyst: 10 mg, $CoCl_2$: 4 μmol, bipyridine (bpy): 15 mg	Visible light	—	Liquid phase; 10 ℃	[672]
Sulfur–doped g–C_3N_4	Layered structures with irregular pore (10–40 nm)	Thermolysis	CH_3OH: 0.37 μmol h^{-1} g^{-1}	—	—	CO_2, H_2O (vapor)	Batch reactor: 200 mL; Catalyst: 100 mg (1wt% Pt cocatalyst)	UV visible light	3 h	Gas phase; ambient temperature	[673]

PO_4^{3-} modified g–C_3N_4	Mesoporous structure	Concentrated phosphoric acid post–treatment	CO: 38.5 μmol h^{-1} g^{-1} CH_4: 73 μmol h^{-1} g^{-1}	0.86% (λ = 420 nm) ~1.3% (λ = 365 nm)	—	CO_2, H_2O (vapor)	Batch reactor: 350 mL; Catalyst: 200 mg	Simulated solar light	4 h	Gas phase; 10 °C	[674]
O–Doped g–C_3N_4	Hierarchically porous structure	Thermal oxidation exfoliation and curling–condensation of bulk g–C_3N_4	CH_3OH: 0.88 μmol h^{-1} g^{-1} small amount of C_2H_5OH, HCOOH, HCHO and CH_4	—	—	CO_2, H_2O (vapor)	Batch reactor: 200 mL; catalyst: 50 mg	Visible light: λ> 420 nm	3 h	Gas phase	[675]

(Table 18 – continuation)

Material	Characterization Shape&size	Synthesis method	Reduction product yield[a] (max.)	Apparent quantum efficiency	Sacrificial electron donor	Reaction medium	Batch size (reactor type&volume, catalyst amount)	Irradiation	Reaction time / h	Reaction type, Temp.[b]	Ref.
Ni/g–CN	Ni NPs homogeneously distributed on laminar g–CN	Wet impregnation – thermal reduction	CH_4: 28 μmol h^{-1} g^{-1}	—	—	CO_2, H_2	Batch reactor: 51 mL; catalyst: 25 mg	UV visible light: 1080 W m^{-2}	24 h	Gas phase; 150 °C	[676]
Pd/g–C_3N_4	Cubic or tetrahedral Pd NPs distributed on the surface of g–C_3N_4	Electrostatic assembly	CH_3OH: 3.17 μmol h^{-1} g^{-1} CH_4: 0.4 μmol h^{-1} g^{-1}	—	—	CO_2, H_2O (vapor)	Batch reactor: 200 mL; catalyst: 50 mg	300W Xe arc lamp	1 h	Gas phase; ambient temperature	[677]
Single Co(II) sites anchoring g–C_3N_4	Sheets	Ligand replacement – pyrolysis	CO: 464.1 μmol h^{-1} g^{-1} H_2: 92.6 μmol h^{-1} g^{-1}	—	TEOA	5.0 mL of solution, MeCN/H_2O/TEOA (v/v/v = 3:1:1)	Reactor: 7.5 mL Catalyst: 2 mg, 2,2′ –bpy: 15 mg	Visible light: λ> 420 nm	10 h	Liquid phase; 25 °C	[678]
Ru single atom/ mC_3N_4	Mesoporous structure	Calcination – microwave heating	CH_3OH: 250 μmol h^{-1} g^{-1}	—	—	DMF: 7 mL, H_2O: 1 mL	Batch reactor: 15 mL; catalyst: 50 mg	Visible light: λ = 400–500 nm	6 h	Liquid phase	[679]
Co−quaterpyridine molecular complex/ g–C_3N_4	Mesoporous	Covalent grafting	CO: 8.0 μmol h^{-1} g^{-1}(TON 128) H_2: 0.4 μmol h^{-1} g^{-1}	0.25% (CO)	BIH	MeCN solution: 3 mL, BIH (0.05 M), phenol (PhOH, 0.03 M)	Batch reactor: 6 mL; catalyst: 6 mg (Coqpy: 3 μM)	Visible light: λ> 400 nm	24 h	Liquid phase; 25 °C	[680]
Pt–g–C_3N_4/ $KNbO_3$	$KNbO_3$ randomly distributed on the surface of g–C_3N_4	Ultrasonic dispersion – heat treatment	CH_4: 2.5 μmol h^{-1} g^{-1}	—	—	CO_2, H_2O (vapor)	Batch reactor; catalyst: 100 mg	Visible light: λ> 420 nm	8 h	Gas phase	[681]
MnO_2/ g–C_3N_4	Layered structure	In–situ redox reaction	CO: 9.6 μmol h^{-1} g^{-1} (1st h) 3.4 μmol h^{-1} g^{-1}(6 h)	—	—	CO_2, H_2O (vapor)	Batch reactor: 500 mL; catalyst: 50 mg	UV visible light: 230 mW cm^{-2}	6 h	Gas phase; 25 °C	[682]

g–C_3N_4/ ZnO	ZnO NPs surrounded by g–C_3N_4	One–step calcination	CH_3OH: 0.6 μmol h^{-1} g^{-1}	—	—	CO_2, H_2O (vapor)	Batch reactor: 200 mL; Catalyst: 100 mg	UV visible light	1 h	Gas phase; ambient temperature	[683]
g–C_3N_4/ CeO_2	Hollow mesospheres	Template preparation – reduction	CH_4: 0.88 μmol h^{-1} g^{-1} CH_3OH: 1.3 μmol h^{-1} g^{-1} CO: 4.2 μmol h^{-1} g^{-1}	17.1% (λ = 525 nm)	—	H_2O: 10 mL	Catalyst: 50 mg	Visible light: λ> 420 nm	4 h	Liquid phase; 25 °C	[684]
WO_3/ g–C_3N_4	WO_3 hollow microspheres coupled with g–C_3N_4 nanosheets	Hydrothermal	CO: 173 μmol h^{-1} g^{-1} CH_4: 226 μmol h^{-1} g^{-1}	λ =420 nm CO: 0.733% CH_4: 3.819%		CO_2, H_2O (vapor)	Catalyst: 150 mg	Visible light: 20 mW cm^{-2}	120 min	Gas phase	[685]

(Table 18 – continuation)

Material	Characterization Shape&size	Synthesis method	Reduction product yield[a] (max.)	Apparent quantum efficiency	Sacrificial electron donor	Reaction medium	Batch size (reactor type&volume, catalyst amount)	Irradiation	Reaction time / h	Reaction type, Temp.[b]	Ref.
α–Fe_2O_3/ g–C_3N_4	Urchinlike α–Fe_2O_3, g–C_3N_4 nanosheets	Impregnation – hydrothermal	CO: 27.2 μmol h^{-1} g^{-1}	0.499% (λ = 365 nm) 0.963% (λ = 420 nm)	—	CO_2, H_2O (vapor)	Batch reactor: 500 mL; Catalyst: 25 mg	Xe lamp: 0.21 W cm^{-2}	4 h	Gas phase; 20 °C	[686]
$CsPbBr_3$/ g–C_3N_4	$CsPbBr_3$ quantum dots (~10 nm) on porous g–C_3N_4 nanosheets	Self–assembly	CO: 148.9 μmol h^{-1} g^{-1}	—	—	MeCN or ethyl acetate (EA): 30 mL, H_2O: 100 μL	Batch reactor; Catalyst: 8 mg	Visible light: λ> 420 nm	—	Liquid phase; 20 °C	[687]
g–C_3N_4/ SnS_2	SnS_2 quantum dots (2–3 nm) loaded on the surface of g–C_3N_4	One–step hydrothermal	CH_4: 2.24 μmol h^{-1} g^{-1}(1st h) CH_3OH: 0.64 μmol h^{-1} g^{-1}(1st h)	—	—	CO_2, H_2O (vapor)	Batch reactor: 200 mL; catalyst: 50 mg	Visible light: λ≥420 nm	3 h	Gas phase	[688]
Au@ gC_3N_4/SnS	Nanospheres (100 nm) with yolk−shell structure	Template–assisted strategy	CO: 4.28 μmol h^{-1} g^{-1} CH_3OH: 1.33 μmol h^{-1} g^{-1} CH_4: 0.95 μmol h^{-1} g^{-1}	17.2% (λ = 450 nm) 15.3% (λ = 525 nm)	—	CO_2, H_2O (vapor)	Catalyst: 50 mg	Visible light: λ> 420 nm	4 h	25 °C	[689]
Ag_2CrO_4/ gC_3N_4/graphene oxide (GO)	Lamellar stacking of g–C_3N_4 and GO layer, Ag_2CrO_4 NPs on the surface of the sheets	Self–assembly	Full spectrum light CH_3OH: ~0.29 μmol h^{-1} g^{-1} CH_4: ~0.05 μmol h^{-1} g^{-1}	—	—	CO_2, H_2O (vapor)	Reactor: 200 mL; Catalyst: 100 mg	(1) visible light: λ> 420 nm; (2) full light spectrum	3 h	Gas phase	[690]
TiO_{2-x}/ g–C_3N_4	TiO_{2-x} quantum dots (~5 nm) anchored on g–C_3N_4 nanosheets	In–situ pyrolysis	CO: 77.8 μmol h^{-1} g^{-1} H_2: 16.2 μmol h^{-1} g^{-1}	—	TEOA	MeCN: 4 mL, TEOA: 1 mL	Batch reactor: 43 mL; Catalyst: 5 mg cocatalyst: bpy, 10 mM, $CoCl_2$ aq., 25 μL, 20 mM	Visible light: λ> 400 nm	5 h	Liquid phase; 25 °C	[691]

$TiO_2/C_3N_4/Ti_3C_2$	Ti_3C_2 quantum dots decorated TiO_2/C_3N_4 core–shell nanosheets	Interfacial self–assembly	CO: 4.39 μmol h^{-1} g^{-1} CH_4: 1.20 μmol h^{-1} g^{-1}	—	—	CO_2, H_2O (vapor)	Batch reactor; Catalyst: 30 mg	Xe lamp	1 h	Gas phase	[692]
AgBr/g–C_3N_4/nitrogen–doped graphene	AgBr NPs on the surface of graphene and g–C_3N_4	Oxidation – thermal polymerization – ion exchange	CH_3OH: 21.2 μmol h^{-1} g^{-1} C_2H_5OH: 51.3 μmol h^{-1} g^{-1}	3.41%	—	Aqueous solution: 20 mL, $NaHCO_3$ (0.1 M)	Catalyst: 20 mg	Visible light: λ≥420 nm, 150 mW cm^{-2}	5 h	Liquid phase; –1 °C	[693]
Functionalized graphene quantum dots	—	Solvothermal	GQD–BNPTL CH_3OH: 0.695 μmol h^{-1} g^{-1}	—	—	CO_2, H_2O (vapor)	Batch reactor; Catalyst: 100 mg	Visible light: λ> 420 nm	10 h	Gas phase	[694]

(Table 18 – continuation)

Material	Characterization Shape&size	Synthesis method	Reduction product yield[a] (max.)	Apparent quantum efficiency	Sacrificial electron donor	Reaction medium	Batch size (reactor type&volume, catalyst amount)	Irradiation	Reaction time / h	Reaction type, Temp.[b]	Ref.
$CsPbBr_3$ quantum dot/graphene oxide (GO)	Spherical $CsPbBr_3$ QDs evenly distributed on GO sheets	Antisolvent precipitation	CO: 4.9 μmol h^{-1} g^{-1} CH_4: 2.5 μmol h^{-1} g^{-1} H_2: 0.13 μmol h^{-1} g^{-1}	0.026% (λ = 400 nm)	—	EA: 10 mL	Batch reactor: 40 mL; Catalyst: 4 mg	Simulated solar light: 150 mW cm^{-2}	12 h	Liquid phase	[695]
MOF (Ni_3HITP_2)/rGO	Ni_3HITP_2 nanosheets attached to the surface rGO parallelly	Vacuum filtration	CO: 3.8×10^4 μmol h^{-1} g_{film}^{-1} H_2: μmol h^{-1} g^{-1}	—	TEOA	TEOA: 2 mL, H_2O: 2 mL, MeCN: 12 mL	Batch reactor: 250 mL; Catlayst: 1 cm in diameter, photosensitizer: $[Ru(bpy)_3]Cl_2\cdot6H_2O$, 40 mg	Visible light: λ> 420 nm	3 h	Liquid phase; 4 °C	[696]
ZnV_2O_6/rGO	ZnV_2O_6 sheets partially covered by rGO nanosheets	One–pot solvothermal	CH_3OH: 5153.97 μmol g^{-1} HCOOH: 1942.41 μmol g^{-1} CH_3COOH: 385.44 μmol g^{-1}		—	Aqueous solution: 100 mL, NaOH (0.1M)	Flow reactor; catalyst: 100 mg	Visible light	10 h	Liquid phase; room tepera-ture	[697]
Carbon dots	Spherical shape (＜3 nm)	Ultrasonic–assisted hydrothermal	GO–h–GCD CH_4: 983 μmol h^{-1} g^{-1} CO: 350 μmol h^{-1} g^{-1} H_2: 975 μmol h^{-1} g^{-1}	—	—	H_2O: 220 mL	Batch reactor	UV	5 h	Liquid phase; 20 °C	[698]
NiCoOP/carbon	NiCoOP NPs (10 nm) in multichannel hollow carbon fibers	Electrospinning –phosphidation – thermal annealing	CO: 1.66×10^5 μmol h^{-1} g^{-1} H_2: 8.6×10^4 μmol h^{-1} g^{-1}	—	TEOA	TEOA: 1.0 mL, H_2O: 2.0 mL, MeCN: 3.0 mL	Batch reactor: 80 mL; Catalyst: 0.1 mg, photosensitizer: $[Ru(bpy)_3]Cl_2\cdot6H_2O$, 10 mg	Visible light: λ≥ 400 nm	4 h	Liquid phase; 30 °C	[699]
MWCNT/TiO_2	TiO_2 NPs as a shell on MWCNT, diameter 40–60 nm	Core–shell coating	CH_4: 0.17 μmol h^{-1} g^{-1}	—	—	CO_2, H_2O (vapor)	Flow reactor: 10 × 200 mm (OD×length)	Visible light: λ> 400 nm	6 h	Gas phase	[700]

Au nanocluster –metal cation	—	Ligand grafting	Au_c–C–Co CO: 3.54 μmol h^{-1} g^{-1} H_2: 1.5 μmol h^{-1} g^{-1} CH_4: trace	—	TEOA	TEOA: 1 mL, pristine Au_c–C–M solution: 10 mL	Batch reactor: 50 mL; Catalyst: 10 mg	Visible light: λ ≥ 420 nm, 100 mW cm^{-2}	3 h	Liquid phase; room temperature	[701]
$Ni(OH)_2$	Hollow nanocages	Ion–assisted etching protocol	CO: 1.44 × 10^5 μmol·$g^{-1}_{co\text{-}cat}$·h^{-1}, H_2: 5.8 × 10^3 μmol·$g^{-1}_{co\text{-}cat}$·h^{-1}	2.50% (λ = 420 nm)	TEOA	TEOA: 0.5 mL, H_2O: 0.5 mL, MeCN: 10 mL	Batch reactor: 10 mL cocatalyst: 0.3 mg photosensitizer: $[Ru(bpy)_3]Cl_2·6H_2O$, 10 mg	λ = 420 nm	3 h	Liquid phase; 15 °C	[702]
$Ni(OH)_2$/ graphene	Hiearchical $Ni(OH)_2$ nanosheet arrays dispersed on graphene	Hydrothermal	CO: 10725 μmol h^{-1} g^{-1} H_2: 446.9 μmol h^{-1} g^{-1}	1.03% (λ = 450 nm)	TEOA	MeCN: 3 mL, H_2O: 2 mL, TEOA: 1 mL	Catalyst: 1 mg photosensitizer: $[Ru(bpy)_3]Cl_2·6H_2O$, 7.5 mg	Vsible light: λ ≥ 420 nm, 405 mW cm^{-2}	—	Liquid phase; room temperature	[703]

(Table 18 – continued)

Material	**Characterization Shape&size**	**Synthesis method**	**Reduction product yield[a] (max.)**	**Apparent quantum efficiency**	**Sacrificial electron donor**	**Reaction medium**	**Batch size (reactor type&volume, catalyst amount)**	**Irradiation**	**Reaction time / h**	**Reaction type, Temp.[b]**	**Ref.**
Co–Co layered double hydroxide (LDH) /$Ti_3C_2T_X$	3D hierarchical nanoarray architecture	In–situ MOF–derived strategy	CO: 1.25 × 10^4 μmol h^{-1} g^{-1} H_2: 7 × 10^3 μmol h^{-1} g^{-1}	0.92% (λ = 420 nm)	TEOA	MeCN: 3 mL, H_2O: 2 mL, TEOA: 1 mL	Batch reactor Catalyst: 0.5 mg, photosensitizer: $[Ru(bpy)_3]Cl_2·6H_2O$, 7.5 mg	Visible light: λ = 400–1000 nm	—	Liquid phase	[704]
Black phosphorus	Nanosheets, 0.62 nm	Exfoliation method assisted by liquid nitrogen	CO: 112.6 μmol h^{-1} g^{-1} H_2: ~11.4 μmol h^{-1} g^{-1}	0.21 % (λ = 400 nm)	TEOA	MeCN: 6 mL, H_2O: 4 mL, TEOA: 2 mL	Batch reactor; catalyst: 10 mg	Visible light: λ ＞420 nm	5 h	Liquid phase; 10 °C	[705]
$Ru(bpy)_3^{2+}$–sensitized $LiCoO_2$	Nanosheets, lateral dimensions 10−60 nm, thickness 2.7–2.9 nm	Precipitation – sonication –hydrothermal	Visible light (12 h) CO: 21.2 μmol h^{-1} g^{-1} CH_4: 4.42 μmol h^{-1} g^{-1} simulated sunlight (2 h) CO: 722 μmol h^{-1} g^{-1} CH_4: 108 μmol h^{-1} g^{-1}	—	TEOA	30 mL of solvent: MeCN, TEOA, H_2O (v/v ratio, 3:1:1)	Batch reactor: 300 mL; Catalyst: 5.0 mg, photosensitizer: $[Ru(bpy)_3]Cl_2·6H_2O$, 10 mg	(1) visible light: λ ≥ 420 nm, 245 mW cm^{-2}; (2) simulated sunlight: 310 mW cm^{-2},	12 h	Liquid phase; 15 °C	[706]
β–SiC	Hollow sphere with open mouth	Sol–gel – carbothermic reduction	β–SiC CH_4: 7.0 μmol h^{-1} g^{-1} Pt/β–SiC CH_4: 16.8 μmol h^{-1} g^{-1}	—	—	CO_2, H_2O (vapor)	Batch reactor: 40 mL; catalyst: 10 mg	Simulated solar light	4 h	Gas phase; 25 °C	[707]
3C–SiC	Nanosized 3C–SiC particles with amorphous SiO_x shell	Top–down ball–milling	CH_4: 4.9 μmol h^{-1} g^{-1} CH_3OH: 0.3 μmol h^{-1} g^{-1}	—	—	CO_2, H_2O (vapor)	Batch reactor: 200 mL; Catalyst: 50 mg	Visible light: λ ＞420 nm	5 h	Gas phase	[708]
Bi_2S_3	Nanoribbons	Solvothermal	CH_3OH: 32.02 μmol h^{-1} g^{-1}	—	—	H_2O: 80 mL	Batch reactor; Catalyst: 20 mg	Visible light: λ ≥420 nm	10 h	Liquid phase; 15 °C	[709]

$Bi_{19}Br_3S_{27}$	Nanowires	Alkali–etching strategy	NIR CH_3OH: 0.4 μmol h^{-1} g^{-1} visible light CH_4: 0.65 μmol h^{-1} g^{-1} CH_3OH: 0.6 μmol h^{-1} g^{-1} CO: 0.3 μmol h^{-1} g^{-1} full spectrum CH_4: 1.15 μmol h^{-1} g^{-1} CH_3OH: 0.89 μmol h^{-1} g^{-1} CO: 0.46 μmol h^{-1} g^{-1}	—	—	CO_2, H_2O (vapor)	Catalyst: 30 mg	(1) full spectrum; (2) visible light: λ ＞420 nm; (3) NIR light: λ ＞720 nm	4 h	Gas phase	[710]
N–doped Graphene (NG) /CdS	NG layer on the surface of CdS hollow spheres	Chemical vapor deposition	CH_4: 0.33 μmol h^{-1} g^{-1} CO: 2.59 μmol h^{-1} g^{-1}	0.9% (λ = 420 nm)	—	CO_2, H_2O (vapor)	Batch reactor: 200 mL; Catalyst: 50 mg	Visible light: λ ≥420 nm	3 h	Gas phase	[711]
CdS/WO_3	CdS NPs on WO_3 hollow spheres	Precipitation	CH_4: 1.02 μmol h^{-1} g^{-1}	0.4% (λ = 420 nm)	—	CO_2, H_2O (vapor)	Batch reactor: 200 mL; Catalyst: 100 mg	Visible light: λ ≥ 420 nm, 150 mW cm^{-2}	—	Gas phase; ambient temperature	[712]

(Table 18 – continuation)

Material	**Characterization Shape&size**	**Synthesis method**	**Reduction product yield[a] (max.)**	**Apparent quantum efficiency**	**Sacrificial electron donor**	**Reaction medium**	**Batch size (reactor type&volume, catalyst amount)**	**Irradiation**	**Reaction time / h**	**Reaction type, Temp.[b]**	**Ref.**
CdSe/CdS	CdSe QDs (~2.0 nm) covered with CdS shell	Successive ion layer adsorption and reaction	CO: 4.13×10^5 μmol h^{-1} g^{-1} H_2: trace	32.7% (λ = 450 nm)	TEA	TEA: 1.0 mL, QDs DMF solution: 5 mL	Batch reactor; catalyst: 2.9 mg	Visible light: λ = 450 nm, 130 mW cm^{-2}	1 h	Liquid phase; room temperature	[713]
Boron carbon nitride/CdS	CdS NPs on the surface of boron carbon nitride	Photodeposition	CO: 250 μmol h^{-1} g^{-1}(1st h) H_2: 56 μmol h^{-1} g^{-1}(1st h)	—	TEOA	MeCN: 4 mL, H_2O: 2 mL, TEOA: 1 mL	Batch reactor: 80 mL; Catalyst: 50 mg cocatalyst ($Co(bpy)_3^{2+}$): bpy, 20 mg, $CoCl_2$, 1 μmol	Visible light: λ ＞420 nm	150 min	Liquid phase; 40 °C	[714]
$Fe_2V_4O_{13}$/rGO/CdS	rGO sheet on the surface of $Fe_2V_4O_{13}$ nanoribbon, CdS NPs (10 nm) decorated on rGO	Hydrothermal – annealing – chemical vapor deposition	CH_4: ~2.3 μmol h^{-1} g^{-1}	—	—	CO_2, H_2O (vapor)	Batch reactor: 230 mL; Catalyst: 25 mg	Visible light: λ ＞420 nm	9 h	Gas phase	[715]
Co–ZIF–9/CdS	—	—	1 h, 40 °C CO: 56 μmol H_2: 12.2 μmol	1.93% (λ = 420 nm)	TEOA	MeCN: 3 mL, H_2O: 2 mL, bpy: 10 mg, TEOA: 1 mL	Batch reactor: 80 mL; Catalyst: CdS, 20 mg Co–ZIF–9, 1 mg	Visible light: λ ＞420 nm	1 h	Liquid phase; 10–60 °C	[716]
ZIF–8/CdS	Spherical particles (~90 nm) with ZIF–8 shell (thickness 10 nm)	Solvothermal – precipitation	C_2H_4: 0.8 μmol h^{-1} g^{-1} CO: 5.8 μmol h^{-1} g^{-1}	—	—	CO_2, H_2O (vapor)	Batch reactor; catalyst: 20 mg	Visible light: λ ＞420 nm	5 h	Gas phase; 25 °C	[717]

CdS/nickel terpyridine complexes	–	Ligand stripping	CO: 1 μmol H_2: ~0.2 μmol	0.28 ± 0.04% (λ = 400 nm)	TEOA	Aqeous solution of 0.1 M TEOA: 1.98 mL, stock solution of electrocatalyst: 20 μL, 10 mM in MeCN or MeCN/H_2O 1:1	Batch reactor	Solar light: AM 1.5G, λ > 400 nm, 100 mW cm^{-2}	4 h	Liquid phase; 25 °C	[718]
MoS_2	Nanoflower	CVD	MoS_2 CO: 0.22 μmol h^{-1} g^{-1} SZF–5 MoS_2 CO: 0.35 μmol h^{-1} g^{-1}	—	—	CO_2, H_2O (vapor)	Reactor: 73 cm^3; Catalyst: 150 mg	Visible light: λ = 400–700 nm, ~589 W m^{-2}	—	Gas phase; 25 and 100 °C	[719]
SiC@MoS_2	Nanoflower	Self assembly	CH_4: 323 μL g^{-1} h^{-1} H_2: ~47.5μL g^{-1} h^{-1}	1.75% (CH_4, λ = 400 nm)	—	CO_2, H_2O (vapor)	Batch reactor: 40 mL; Catalyst: 10 mg	Visible light: λ ≥ 420 nm	4 h	Gas phase; 25 °C	[720]

(Table 18 – continuation)

Material	**Characterization Shape&size**	**Synthesis method**	**Reduction product yield[a] (max.)**	**Apparent quantum efficiency**	**Sacrificial electron donor**	**Reaction medium**	**Batch size (reactor type&volume, catalyst amount)**	**Irradiation**	**Reaction time / h**	**Reaction type, Temp.[b]**	**Ref.**
$CsPbBr_3$/MoS_2	$CsPbBr_3$ nanocrystals (5 nm) on the surface of MoS_2 nanosheets	Sonication – self assembly	CH_4: 12.8 μmol h^{-1} g^{-1} CO: 25.0 μmol h^{-1} g^{-1}	—	—	EA: 5 mL H_2O: 20 μL	Batch reactor: 60 mL; Catalyst: 5 mg	Visible light: λ > 420 nm, 200 mW cm^{-2}	3 h	Liquid phase	[721]
ZnS	—	Acid–etching	HCOOH: ~68 μmol h^{-1} g^{-1} CO: ~0.4 μmol h^{-1} g^{-1} H_2: ~12 μmol h^{-1} g^{-1}	1.24% (λ = 300 nm)	K_2SO_3	Aqueous solution: 50 mL, 1.0 M $KHCO_3$ (1.0 M), K_2SO_3 (0.2 M)	Batch reactor; Catalyst: 100 mg	300 W Xe lamp: λ = 200–350 nm, 7.67 mW cm^{-2}	100 h	Liquid phase	[722]
Colloidal ZnS	5 nm	—	Cd^{2+} modified colloidal ZnS HCOOH: 1.1×10^4 μmol h^{-1} g^{-1} CO: 51.3 μmol h^{-1} g^{-1} H_2: 537.9 μmol h^{-1} g^{-1}	76% (HCOOH, λ = 280 nm)	K_2SO_3	aqueous solution: 100 mL, K_2SO_3 (0.1 M), $KHCO_3$ (0.5 M)	Batch reactor; Catalyst: 100 mg	UV visible light: λ = 240–600 nm	8 h	Liquid phase	[723]
ZnTe	Microsphere	Hydrothermal	CH_4: 1.05 μmol h^{-1} g^{-1}	—	—	H_2O: 80 mL	Batch reactor; Catalyst: 10 mg	Visible light: λ ≥420 nm	8 h	Liquid phase; 15 °C	[724]
ZnO/ZnTe	Flower–like 3D superstructure	One–pot hydrothermal	CH_4: 4.6 μmol h^{-1} g^{-1}	—	—	H_2O: 80 mL	Batch reactor; Catalyst: 10 mg	Visible light: λ ≥420 nm	8 h	Liquid phase; 15 °C	[725]

ZnSe/CdSe	CdSe NPs on the surface of ZnSe crystal	Hydrothermal – cation exchange	CO: 19.5 μmol h^{-1} g^{-1}	—	TEOA	H_2O: 80 mL, TEOA: 20 mL	Batch reactor; Catalyst: 30 mg	Visible light: 420 nm< λ < 780 nm	6 h	Liquid phase; 15 °C	[726]
$CdIn_2S_4$	Microsphere	Hydrothermal	$CdIn_2S_4$ (L–cysteine) dimethoxymethane: 2968 μmol h^{-1} g^{-1} methyl formate: 2857 μmol h^{-1} g^{-1} $CdIn_2S_4$ (thioacetamide) methyl formate: 3604 μmol h^{-1} g^{-1} $CdIn_2S_4$ (thiourea) methyl formate: 5258 μmol h^{-1} g^{-1}	—	CH_3OH	CH_3OH: 20 mL	Batch reactor; catalyst: 20 mg	250 W high pressure mercury lamp: 2500 μW cm^{-2}	10 h	Liquid phase	[727]
WO_3/ $CdIn_2S_4$	WO_3 quantum dots decorated on ultrathin $CdIn_2S_4$ nanosheets	Hydrothermal	CO: 8.2 μmol h^{-1} g^{-1} CH_4: 1.6 μmol h^{-1} g^{-1}	1.05% (CO, λ = 420 nm)	—	H_2O: 10 mL	Batch reactor; Catalyst: 10 mg	Visible light: λ ≥420 nm	5 h	Liquid phase	[728]

(Table 18 – continuation)

Material	Characterization Shape&size	Synthesis method	Reduction product yield[a] (max.)	Apparent quantum efficiency	Sacrificial electron donor	Reaction medium	Batch size (reactor type&volume, catalyst amount)	Irradiation	Reaction time / h	Reaction type, Temp.[b]	Ref.
$ZnIn_2S_4$	3D flower–like hierarchical structure	Solvothermal	CO: 276.7 μmol h^{-1} g^{-1}	—	TEOA	MeCN: 45 mL TEOA: 5 mL	Batch reactor; catalyst: 20 mg	Simulated sunlight	5 h	Liquid phase	[729]
$ZnIn_2S_4$	Atomic layers (one–unit–cell thick)	Hydrothermal	CO: 33.2 μmol h^{-1} g^{-1}(1st h)	0.23% (λ = 400 nm)	—	H_2O: 2 mL	Batch reactor; Catalyst: 100 mg	Simulated sunlight: 100 mW cm^{-2}	24 h	Liquid phase; 25 °C	[730]
In_2S_3/ $CdIn_2S_4$	Hierarchical nanotubes	Self templated strategy (two ion exchange reactions)	CO: 825 μmol h^{-1} g^{-1} H_2: ~312 μmol h^{-1} g^{-1}	—	TEOA	H_2O: 2 mL MeCN: 3 mL TEOA: 1 mL	Batch reactor: 80 mL; Catalyst: 4 mg cocatalyst: $CoCl_2$, 2 μmol, bpy: 15 mg	Visible light: λ ≥ 400 nm	12 h	Liquid phase; 30 °C	[731]
$AgInP_2S_6$	Sheets (~ 0.70 nm)	Ultrasonic exfoliation	1st h C_2H_4: 44.3 μmol h^{-1} g^{-1} CO: 10.9 μmol h^{-1} g^{-1} CH_4: 5.6 μmol h^{-1} g^{-1} H_2: ~7 μmol h^{-1} g^{-1}	0.51% (λ = 415 nm)	—	CO_2, H_2O (vapor)	Batch reactor: 460 mL; catalyst: 4–5 mg	UV visible light	6 h	Gas phase	[732]
$CuIn_5S_8$@ $MoSe_2$	Hollow structure	Hydrothermal – thermal treatment	CO: 3.8 μmol h^{-1} g^{-1} CH_4: 1.8 μmol h^{-1} g^{-1}	—	TEOA	MeCN: 24 mL, TEOA: 6 mL	Catalyst: 12 mg	Visible light: λ ＞420 nm	8 h	Liquid phase	[733]

$FeCoS_2$/ CoS_2	Double–shelled nanotubes	Two step cation–exchange reactions	CO: 5.6×10^4 μmol h^{-1} g^{-1} H_2: 3.5×10^4 μmol h^{-1} g^{-1}	—	TEOA	TEOA: 1 mL, H_2O: 2 mL, MeCN: 3 mL	Batch reactor: 80 mL; Catalyst: 0.5 mg photosensitizer: $[Ru(bpy)_3]Cl_2\cdot6H_2O$, 10 mg	Visible light: λ≥ 400 nm	1 h	Liquid phase; 30 °C	[734]
MAl–LDH (M = Mg^{2+}, Co^{2+}, Ni^{2+}, and Zn^{2+})	Ultrathin sheets (2−4 nm)	Titration method	u–CoAl–LDH, λ = 600 nm CO: 4.37×10^4 μmol h^{-1} g^{-1} H_2: ~3.5×10^4 μmol h^{-1} g^{-1}	0.22% (CO, λ = 600 nm)	TEOA	TEOA: 2 mL, H_2O: 2 mL, MeCN: 6 mL	Batch reactor; Catalyst: 0.05 mg photosensitizer: $[Ru(bpy)_3]Cl_2\cdot6H_2O$, 3.3 mg	Visible light: 400 ≤ λ ≤ 800 nm, 500 mW cm^{-2};	—	Liquid phase	[735]
$CsPbBr_3$/ TiO_2	$CsPbBr_3$ nanocrystals encapsulated by amorphous TiO_2	Solution processing	CO: 3.9 μmol h^{-1} g^{-1} CH_4: 6.7 μmol h^{-1} g^{-1} H_2: 1.5 μmol h^{-1} g^{-1}	—	Isopropanol	EA: 10 mL, isopropanol: 100 μL	Batch reactor: 40 mL; Catalyst: 5 mg	UV visible light: 150 mW cm^{-2}	3 h	Liquid phase	[736]
NH_2–MIL–125(Ti)	Shapes of disk, octahedron or truncated octahedrons	Solvothermal	CO: 8.25 μmol h^{-1} g^{-1} CH_4: 1.01 μmol h^{-1} g^{-1}	CO: 0.14% CH_4: 0.07%	TEOA	MeCN: 15 mL, H_2O: 1 mL, TEOA:3 mL	Catalyst: 10 mg	Visible light	5 h	Liquid phase; 4 ℃	[737]
Au@UiO–68–NHC	Au nanocrystals (1.8±0.2 nm) in UiO–68–NHC	Nucleation	CO: 57.6 μmol h^{-1} g^{-1} CH_4: 1.8 μmol h^{-1} g^{-1} H_2: 12.6 μmol h^{-1} g^{-1}	—	CH_3OH	MeCN: 90 mL, CH_3OH: 10 mL	Batch reactor; catalyst: 20 mg	300 nm ≤ λ ≤ 800 nm	5 h	Liquid phase	[738]

(Table 18 – continuation)

Material	Characterization Shape&size	Synthesis method	Reduction product yield[a] (max.)	Apparent quantum efficiency	Sacrificial electron donor	Reaction medium	Batch size (reactor type&volume, catalyst amount)	Irradiation	Reaction time / h	Reaction type, Temp.[b]	Ref.
$CH_3NH_3PbI_3$/ PCN–221(Fe_x)	$MAPbI_3$ QDs (1.8 nm) encapsulated in the pores of MOF PCN–221(Fe_x)	Sequential deposition route	CO: 6.6 μmol h^{-1} g^{-1}(80 h) CH_4: 12.9 μmol h^{-1} g^{-1}(80 h)	—	—	5 mL of EA or MeCN and small amount of H_2O (v/v, 1:0.012)	Batch reactor: 10 mL; catalyst: 4 mg	Visible light: λ ＞400 nm, 100 mW cm^{-2}	25 h, 80 h	Liquid phase	[739]
Ni based MOF/ $CsPbBr_3$	$CsPbBr_3$ nanocubes, nanorods or nanowires scattered on the surface of Ni based MOF nanosheets	Liquid exfoliation – sonication	CO: 81.0 μmol h^{-1} g^{-1}	0.05 % (λ = 420 nm)	—	EA/H_2O (5 mL, v/v, 49:1,)	Batch reacor: 100 mL; catalyst: 5 mg	Visible light: 420 < λ < 780 nm, 100 mW cm^{-2}	4 h	Liquid phase	[740]
$CsPbBr_3$@ ZIF-67	Core–shell: $CsPbBr_3$ quantum dots (8−9 nm) coated by ZIF network	In situ growth	CH_4: 3.51 μmol h^{-1} g^{-1} CO: 0.77 μmol h^{-1} g^{-1}	0.035% (λ = 386 nm) 0.012% (λ = 576 nm)	—	CO_2, H_2O (vapor)	Batch reactor: 40 mL; catalyst: 4.5 mg	UV visible light: AM 1.5G, 150 mW cm^{-2}	3 h	Gas phase	[741]

$CsPbBr_3$–$Re(CO)_3Br$(dcbpy) (dcbpy=4,4'–dicarboxy–2,2'–bpy)	NPs	Anti–solvent method	CO: 34.8 μmol h^{-1} g^{-1} H_2: 1.9 μmol h^{-1} g^{-1}	—	Isopropanol	Toluene: 9 mL, isopropanol: 1 mL	Batch reactor: 40 mL	Visible light: λ > 420 nm, 150 mW cm^{-2}	3 h	Liquid phase	[742]
Omine–based COF	Ultrathin nanosheets	Solvothermal	CO: 10162 μmol h^{-1} g^{-1}(TON 20.2) H_2: 2875 μmol h^{-1} g^{-1}	—	Ascorbic acid (AA)	Aqueous solution: 20 mL $KHCO_3$ (0.1 M), AA (352 mg, 2 mmol)	Batch reactor Catalyst: COF–367–Co, 5 mg, photosensitizer: $[Ru(bpy)_3]Cl_2$, 19 mg, 0.025 mmol	Visible light: λ ≥ 420 nm	2 h	Liquid phase; room temperature	[743]

(Table 18 – continuation)

Material	**Characterization Shape&size**	**Synthesis method**	**Reduction product yield[a] (max.)**	**Apparent quantum efficiency**	**Sacrificial electron donor**	**Reaction medium**	**Batch size (reactor type&volume, catalyst amount)**	**Irradiation**	**Reaction time / h**	**Reaction type, Temp.[b]**	**Ref.**
Ni–organic composites: Ni (TPA/TEG)	Disordered spongy network structure	Laser–induced solution reaction	Ni(TPA/TEG) CO: 15866 μmol h^{-1} g^{-1}(2 h) 7606 μmol h^{-1} g^{-1}(6 h, TON 11.5) HCOOH: 29.2 μM (6 h) CH_3COOH: 72.5 μM (6 h) Ni(TPA/TEG)–Rh CO: ~2500 μmol h^{-1} g^{-1}(6 h) HCOOH: 313.5 μM (6 h) CH_3COOH:~142 μM (6 h) Ni(TPA/TEG)–Ag CO: ~556 μmol h^{-1} g^{-1} HCOOH: ~8.3 μM (6 h) CH_3COOH: 195.6 μM (6 h)	—	TEOA	TEOA: 2 mL, MeCN: 8 mL, H_2O: 2 mL	Batch reactor; Catalyst: 3 mg, photosensitizer: $Ru(bpy)_3Cl_2·6H_2O$,2.5mmol	Visible light: λ> 420 nm	6 h	Liquid phase; 20 °C	[744]
Amine–functionalized Titanium MOF: NH_2–MIL–125(Ti)	—	Solvothermal	$HCOO^-$: 16.3 μmol h^{-1} g^{-1}	—	TEOA	MeCN: 50 mL TEOA: 10 mL	Catalyst: 50 mg	Visible light: λ = 420–800 nm	10 h	Liquid phase	[745]

Fe–based MOFs: MIL–101(Fe), MIL–53(Fe), MIL–88B(Fe)	—	Hydrothermal	NH_2–MIL–101(Fe) $HCOO^-$: 445 μmol h^{-1} g^{-1} MIL–101(Fe) $HCOO^-$: 147.5 μmol h^{-1} g^{-1}	QE for NH_2–MIL–101(Fe): 1.3×10^{-4}	TEOA	MeCN: 50 mL TEOA: 10 mL	Batch reactor; catalyst: 50 mg	Visible light: λ = 420–800 nm	8 h	Liquid phase	[746]
Cobalt–based MOFs	—	Solvothermal	MAF–X27l–OH CO: ~45 μmol (TOF: 0.059 s^{-1}) H_2: ~0.8 μmol	2% (CO, λ = 420 nm)	TEOA	MeCN: 5 mL, H_2O: 1 mL, TEOA 0.1 mol	Batch reactor: 16 mL; Catalyst: nCo^{2+}, 30 nmol, photosensitizer: $[Ru(bpy)_3]Cl_2 \cdot 6H_2O$, 2 μmol	Visible light: λ = 420 nm	10 h	Liquid phase; 25 °C	[747]

(Table 18 – continuation)

Material	Characterization Shape&size	Synthesis method	Reduction product yield[a] (max.)	Apparent quantum efficiency	Sacrificial electron donor	Reaction medium	Batch size (reactor type&volume, catalyst amount)	Irradiation	Reaction time / h	Reaction type, Temp.[b]	Ref.
MOF-808-CuNi	Single-site of Cu and Ni in MOF-808-CuNi	Solvothermal	CH_4: 158.7 μmol h^{-1} g^{-1} CO: 2.3 μmol h^{-1} g^{-1} H_2: 1.7 μmol h^{-1} g^{-1}	~2.31% (CH_4, λ = 420 nm)	TEOA	MeCN: 30 mL H_2O: 10 mL TEOA: 10 mL	Batch reactor: 250 mL Catalyst: 25 mg, photosensitizer: $[Ru(bpy)_3]Cl_2 \cdot 6H_2O$, 50 mg	Visible light: 420 nm < λ < 760 nm	10 h	Liquid phase; 25 °C	[748]
UiO–66/CN	CN nanosheets well coated on the surface of UiO–66	Electrostatic self–assembly	CO: 9.9 μmol g_{CN}^{-1} h^{-1}	—	TEOA	MeCN: 4 mL TEOA: 1 mL	Batch reactor: 330 mL	Visible light: 400 nm < λ < 800 nm	6 h	Liquid phase	[749]
Cu single atom/UiO–66–NH_2	—	Photoinduction	CH_3OH: 5.33 μmol h^{-1} g^{-1} C_2H_5OH: 4.22 μmol h^{-1} g^{-1}	—	TEOA	H_2O: 50 mL TEOA: 100 μL	Flow reactor catalyst: 100 mg	Visible light: λ ＞400 nm	10 h	Liquid phase; 25 °C	[750]
COF–367–Co^{III}	Rectangular rod–shaped morphology	—	HCOOH: 93.0±4.63 μmol h^{-1} g^{-1} CO: 5.5±0.88 μmol h^{-1} g^{-1} CH_4: 10.1±1.12 μmol h^{-1} g^{-1}	—	TEA	MeCN: 20 mL, TEA: 2 mL	Batch reactor: 160 mL; catalyst: 10 mg	Visible light	8 h	Liquid phase;	[751]

TiO_2 in MOF	—	Inclusion and gradual hydrolysis	TiO_2–in–MIL–101–Cr–NO_2 CO: 1.1×10^4 μmol h^{-1} g^{-1} CH_4: 1.1×10^4 μmol h^{-1} g^{-1}	11.3% (λ = 350 nm)	—	CO_2, H_2O (vapor)	Batch reactor	300 W Xe lamp	1 h	Gas phase; 45 °C	[752]

Table 19. Materials for photocatalytic reduction of CO_2 in low concentrations.

Material	Characterization Shape&size	Synthesis method	Reduction product yield[a] (max.)	Apparent quantum efficiency	Feed gas	Sacrificial electron donor	Reaction medium	Batch size (reactor type&volume, catalyst amount)	Irradiation	Reaction time	Reaction type, Temp.[b]	Ref.
Imine-based COF	Ultrathin nanosheets	Solvothermal	CO: 2587 μmol h^{-1} g^{-1} H_2: 1006 μmol h^{-1} g^{-1}	—	10% CO_2 in N_2 (CO_2: 0.1 atm)	AA	Aqueous solution: $KHCO_3$: 20 mL, 0.1 M, AA: 352 mg, 2 mmol	Batch reactor; Catalyst: COF–367–Co, 5 mg, photosensitizer: $[Ru(bpy)_3]Cl_2$, 19 mg, 0.025 mmol	Visible light: λ ≥ 420 nm	—	Liquid phase; room temperature	[743]
Azine-based COFs	—	—	(1) 10% CO_2 CH_3OH: 0.46 μmol h^{-1} g^{-1} (2) 1% CO_2 CH_3OH: 0.41 μmol h^{-1} g^{-1}	—	1%, 10% CO_2 in N_2 (0.4 Mpa)	—	CO_2, H_2O (vapor)	Reactor: 132 mL; Catalyst: 10 mg	Visible light: λ= 420 − 800 nm	24 h	Gas phase; 80 °C	[753]

Fe/Ni-COFs	Nanowires	Solvothermal-precipitation	(1) Fe/Ni-COFs, syngas CO/H_2 ratio can be tuned between 1:19−9:1 (2) Ni COF CO: 4530 μmol h^{-1} g^{-1} H_2: 580 μmol h^{-1} g^{-1}	—	10% CO_2 in Ar (atmos-pheric pressure)	TEOA	MeCN: 3 mL, H_2O: 2 mL, TEOA: 1 mL	Batch reactor: 60 mL; Catalyst: 2 mg, photosensitizer: $[Ru(bpy)_3]Cl_2·6H_2O$: 7.5 mg	Visible light: λ= 400 − 800 nm	—	Liquid phase; room temperat ure	[754]
Cobalt–based MOFs	—	Solvothermal	MAF–X27l–OH CO: ~36 μmol (TOF: 0.049 s^{-1}) H_2: ~0.8 μmol	1.63% (CO, λ = 420 nm)	10% CO_2 in Ar (CO_2: 0.1 atm)	TEOA	MeCN: 4 mL, H_2O: 1 mL, TEOA: 0.1 mol	Batch reactor: 16 mL; Catalyst: nCO_2^+, 30 nmol, photosensitizer: $[Ru(bpy)_3]Cl_2·6H_2O$, 2 μmol	Visible light: λ = 420 nm	10 h	Liquid phase; 25 °C	[747]
Ni MOF	Ultrathin nanosheets	Ultrasonicatio n	CO: 12500 μmol h^{-1} g^{-1} H_2: 380 μmol h^{-1} g^{-1}	1.96% (λ = 420 nm)	10% CO_2 in Ar (atmos-pheric pressure)	TEOA	MeCN: 3 mL, H_2O: 2 mL, TEOA: 1 mL	Batch reactor: 60 mL; Catalyst: 1 mg, photosensitizer: $[Ru(bpy)_3]Cl_2·6H_2O$, 7.5 mg	Visible light: λ= 400 − 800 nm	2 h	Liquid phase; ambient temperat ure	[755]
Zr-bpdc/ RuCO	Highly porous	Post-synthetic exchange method	10% CO_2 TON (CO): 4.4 μmol h^{-1} g^{-1} TON (HCOOH): 33.8 μmol h^{-1} g^{-1} TON (H_2): 12.9 μmol h^{-1} g^{-1}	—	5%, 10%, 20% CO_2 in Ar	TEOA	MeCN: 14 mL, TEOA: 1 mL, 7.5 mmol	Reactor: 100 mL; Catalyst: 4.5 μmol, photosensitizer: $[Ru(bpy)_3](PF_6)_2$, 39 mg, 45 μmol	λ = 385 – 740 nm, 67 mW cm^{-2}	6 h	Liquid phase; room temperat ure	[756]
TiO_2/UiO-66	TiO_2 clusters distributed on the surface of UiO-66 octa-hedrons	Solvothermal-assembly	CH_4: ＞17 μmol h^{-1} g^{-1}(＞ 2% CO_2 pressure)	—	0%~100 % CO_2 in Ar		CO_2, H_2O (vapor)	Batch reactor: 500 mL; catalyst: 50 mg	Full spectrum light	5 h	Gas phase	[757]

(Table 19 – continuation)

Material	Characterization Shape&size	Synthesis method	Reduction product yield[a] (max.)	Apparent quantum efficiency	Feed gas	Sacrificial electron donor	Reaction medium	Batch size (reactor type&volume, catalyst amount)	Irradiation	Reaction time	Reaction type, Temp.[b]	Ref.
NiPc–NiPOP	Porous structure	—	CO: 1770 μmol h^{-1} g^{-1} H_2: 500 μmol h^{-1} g^{-1}	—	10% CO_2	TEOA	MeCN: 7.2 mL, H_2O: 0.8 mL, TEOA: 2 mL	Reactor: 60 mL; Catalyst: 1 mg, photosensitizer: $[Ru(bpy)_3]Cl_2·6H_2O$, 10.0 mg	Visible light: λ= 400 − 800 nm	4 h	Liquid phase	[758]

Ni-TpBpy	Ni (~0.17 nm) atomically dispersed in TpBpy (3D network)	Solvothermal	CO: 228.8 μmol h^{-1} g^{-1} H_2: 72.2 μmol h^{-1} g^{-1}	—	10% CO_2 in Ar (CO_2: 0.1 atm)	TEOA	MeCN: 3 mL, H_2O: 1 mL TEOA: 1 mL	Batch reactor; Catalyst: 10 mg, photosensitizer: $[Ru(bpy)_3]Cl_2·6H_2O$, 6.5 mg, 0.01 mmol, 2,2′-bpy: 15 mg, 0.1 mmol	Visible light: λ ≥ 420 nm	4 h	Liquid phase; 25 °C	[759]
Pentanuclear Co(II) complex	—	—	(1) 20% CO_2 CO: 20 μmol (TON, 254; TOF, 4 h^{-1}) H_2: 42 μmol (TON, 525; TOF, 8 h^{-1}) (2) Results in 5% CO_2 are nearly the same to that in 20% CO_2.	—	5%, 20% CO_2 in Ar (1 atm)	TEOA	MeCN: 5 mL, TEOA: 1 mL	Reactor: 5 mL; Catalyst: 0.08 μmol, photosensitizer: $[Ru(bpy)_3]Cl_2$, 0.01 mmol	Visible light: λ ≥ 420 nm	70 h	Liquid phase; 20 °C	[760]
Co(II) cryptate	—	—	CO: 1.50 μmol (TON, 600; TOF 0.017 s^{-1}) H_2: 0.071μmol	—	10% CO_2 in Ar (1 atm)	TEOA	MeCN: 4 mL, H_2O: 1 mL, TEOA: 0.3 M	Batch reactor: 16 mL; Catalyst: 0.5 μM, photosensitizer: $[Ru(phen)_3](PF_6)_2$, 0.4 mM	λ = 420 nm, 100 mW cm^{-2}	10 h	Liquid phase; 25 °C	[761]
Dinuclear cobalt complex: $[CO_2\text{-}(OH)L^1](ClO_4)_3$	—	—	CO: 1.71 μmol (TON, 684; TOF 0.019 s^{-1}) H_2: 0.14 μmol	—	10% CO_2 in Ar	TEOA	MeCN: 4 mL, H_2O: 1 mL, TEOA: 0.3 M	Batch reactor: 16 mL; Catalyst: 0.5 μM, photosensitizer: $[Ru(phen)_3]$-$(PF_6)_2$, 0.4 mM	λ = 450 nm, 100 mW cm^{-2}	10 h	Liquid phase; 25 °C	[762]
Ru(II)−Re(I) dinuclear complex	—	—	10 % CO_2/Ar (5 h) TON (CO): 300 μmol h^{-1} g^{-1}	—	0.5%−100 % CO_2 in Ar	BIH	20 mL solution: DMF:TEOA (v/v, 5:1), BIH (0.1 M)	Flow reactor; catalyst: 0.05 mM	λ = 480 nm	19 h	Liquid phase	[763]
Pyrene-based conjugated polymer	Irregular morphology	Yamamoto reaction	CO: 47.37 μmol h^{-1} g^{-1} H_2: 0.81 μmol h^{-1} g^{-1}	—	Air	TEOA	ionic liquids (treated with CO_2 for 48 h): 10 g, TEOA: 1 g	Batch reactor; catalyst: 50 mg	Visible light: λ > 420 nm	10 h	Liquid phase	[764]

(Table 19 – continuation)

Material	Characterization Shape&size	Synthesis method	Reduction product yield[a] (max.)	Apparent quantum efficiency	Feed gas	Sacrificial electron donor	Reaction medium	Batch size (reactor type&volume, catalyst amount)	Irradiation	Reaction time	Reaction type, Temp.[b]	Ref.

$[Ru(bpy)_3]$/ $[CO_{20}Mo_{16}P_{24}]$	—	Hydrothermal	Syngas (CO, H_2) (1) 3% CO_2: 74700 μmol h^{-1} g^{-1} (TON, 523.1) (2) 10% CO_2: 122000 μmol h^{-1} g^{-1} (TON, 853.6) (3) 20% CO_2: 138000 μmol h^{-1} g^{-1} (TON, 964.9)	—	3%, 10%, 20% CO_2 in Ar	TEOA	MeCN, H_2O, TEOA	Catalyst: CO_2 $[CO_{20}Mo_{16}P_{24}]$, 0.1 μmol, $[Ru(bpy)_3]^{2+}$, 4 μmol	Visible light: λ > 420 nm	1 h	Liquid phase; 20 °C	[765]
$[Co(H_2O)_6]$ [Co-POM]	—	—	20% CO_2 CO: 9400 μmol h^{-1} g^{-1} H_2: 47400 μmol h^{-1} g^{-1}	—	5%, 20% CO_2	TEOA	MeCN: 4 mL, TEOA: 1 mL, H_2O: 1 mL	Batch reactor: 50 mL; Catalyst: $[Co(H_2O)_6]$[Co-POM]: 0.1 μmol, photosensitizer: $[Ru(bpy)_3]Cl_2$, 0.01 mmol	Visible light: λ > 420 nm	2.5 h	Liquid phase; 20 °C	[766]
Hollow Cu ball	Hollow structure consisting of fragments	Molten-salt strategy	0.53% atm CO_2 CO: 3.9 μmol h^{-1} g^{-1} CH_4: ~0.8 μmol h^{-1} g^{-1} H_2: trace	—	0.53%, 0.93%, 3.25% CO_2 (1 atm)	—	H_2O: 10 mL	Reactor: 100 mL; Catalyst: 10 mg	Simulated solar light	12 h	Liquid phase; room temperature	[767]
$M_{0.33}WO_3$ (M = K, Rb, Cs)	Flower-like shape	Solvothermal	$Rb_{0.33}WO_3$: (1) full spectrum CH_4: 0.02 μmol h^{-1} g^{-1} CO: 0.07 μmol h^{-1} g^{-1} CH_3OH: 3.73 μmol h^{-1} g^{-1} HCHO: 1.05 μmol h^{-1} g^{-1} (2) NIR: λ > 800 nm CH_4: 0.01 μmol h^{-1} g^{-1} CO: 0.03 μmol h^{-1} g^{-1} CH_3OH: 2.33 μmol h^{-1} g^{-1}	—	Fresh air, atmospheric pressure	—	CO_2, H_2O (vapor)	Batch reactor; catalyst: 50 mg	(1) full spectrum: 350−2500 nm, (2) λ > 800 nm	4 h	Gas phase	[768]
Mo-$Cs_{0.33}WO_3$	Nanorods	Solvothermal	(1) fresh air: CO: 3.4 μmol h^{-1} g^{-1} CH_3OH: 1 μmol h^{-1} g^{-1} (2) low CO_2: CO: 7.5 μmol h^{-1} g^{-1} CH_3OH: 3.0 μmol h^{-1} g^{-1}	—	(1) normal atmosphere: fresh air (2) low CO_2: 1000 ppm CO_2 in N_2	—	CO_2, H_2O (vapor)	Reactor: 500 mL; Catalyst: 50 mg	UV visible light: 850 mW cm^{-2}	4 h	Gas phase	[769]

(Table 19 – continuation)

Material	Characterization Shape&size	Synthesis method	Reduction product yield[a] (max.)	Apparent quantum efficiency	Feed gas	Sacrificial electron donor	Reaction medium	Batch size (reactor type&volume, catalyst amount)	Irradiation	Reaction time	Reaction type, Temp.[b]	Ref.

$NiCO_2O_4$	Hollow nanocages	Sequential templating strategy	CO: 8900 μmol h^{-1} g^{-1} H_2: 1100 μmol h^{-1} g^{-1}	1.56 (λ = 420 nm)	10% CO_2 atmos-pheric pressure	TEOA	H_2O: 2mL MeCN: 3 mL TEOA: 1 mL	Batch reactor: 60 mL; catalyst: 1 mg, photosensitizer: $[Ru(bpy)_3]Cl_2·6H_2O$, 7.5 mg	λ = 400 – 800 nm	—	Liquid phase	[770]
Biphasic TiO_2	Nanoplates	Solvothermal – calcination – hydrogen pretreatment	10% CO_2 CH_4: 51.4 μmol h^{-1} g^{-1} H_2: 5 μmol h^{-1} g^{-1} CO: 2 μmol h^{-1} g^{-1} 1% CO_2 CH_4: 45.59 μmol h^{-1} g^{-1} H_2: 7 μmol h^{-1} g^{-1} CO: 2 μmol h^{-1} g^{-1}	—	1%, 10% CO_2 in Ar	—	CO_2, H_2O (vapor)	Reactor: 250 mL; Catalyst: 10 mg	UV visible light: λ = 320–780 nm, 650 mW cm^{-2}	8 h	Gas phase; 25 °C	[771]
TiO_2	NPs	$NaBH_4$ reduction	CO: 0.83 μmol h^{-1} g^{-1}(UV-vis) CO: 0.2 μmol h^{-1} g^{-1}(vis)	—	10% CO_2 in N_2	—	CO_2, H_2O (vapor)	Flow reactor	(1) UV-visible light (2) visible light	6 h	Gas phase; 80 °C	[772]
Cu-Pt/TiO_2	Nanotube arrays	Pulse anodization – photodeposition	C_xH_y (major CH_4): 3.7 mL g^{-1} h^{-1}	—	0.998% CO_2	—	H_2O, CO_2	Reactor: 30 mL; Catalyst: 6.7 mg	Simulated sunlight, AM 1.5	—	25 °C	[773]
Reduced TiO_2/Cu_2O	NPs	Thermochemical reduction – photodeposition	CH_4	CO_2 conversion: 0.13%	1000 ppm CO_2 in He	—	CO_2, H_2O (vapor)	Flow reactor; Catalyst: 40 mg	Simulated solar light, AM 1.5	6 h	Gas phase	[774]
Au-Cu@$SrTiO_3$/TiO_2	Nanotube arrays	Anodic oxidation – hydrothermal – solvothermal	CO: 3770 μmol h^{-1} g^{-1} C_xH_y: 725.4 μmol h^{-1} g^{-1}	—	33.3% CO_2 in Ar	—	$N_2H_4·H_2O$: 10 mL	Batch reactor: 1.1 L; Catalyst: ~5 mg	UV visible light	6 h	Liquid phase	[775]
NiO	Nanoplatelets	Calcination	CO: 6280 μmol h^{-1} g^{-1} H_2: 1370 μmol h^{-1} g^{-1}	0.46% (CO, λ = 420 nm)	10% CO_2 in Ar (CO_2: 0.1 atm)	TEOA	MeCN: 3 mL, H_2O: 2 mL, TEOA: 1 mL	Batch reactor; Catalyst: 0.5 mg, photosensitizer: $[Ru(bpy)_3]Cl_2·6H_2O$: 7.5 mg	Visible light: λ > 400 nm	—	Liquid phase	[776]

(Table 19 – continuation)

Material	Characterization Shape&size	Synthesis method	Reduction product yield[a] (max.)	Apparent quantum efficiency	Feed gas	Sacrificial electron donor	Reaction medium	Batch size (reactor type&volume, catalyst amount)	Irradiation	Reaction time	Reaction type, Temp.[b]	Ref.
$Ni_2(OH)(PO_4)$	Nanotubes	Hydrothermal	(1) visible light, 0.1 atm of CO_2 in lab CO: 5500 μmol h^{-1} g^{-1} H_2: 580 μmol h^{-1} g^{-1} (2) pure CO_2, natural sunlight (08:00−17:00, December 26th, 2019, China) CO: 2980 μmol h^{-1} g^{-1} H_2: 95 μmol h^{-1} g^{-1}	—	CO_2: 0.1 atm Atmospheric pressure	TEOA	Mecn; 3 ml, H_2O: 2 ml, TEOA: 1 ml	Reactor: 60 ml; Catalyst: 1 mg, Photosensitizer: $[Ru(bpy)_3]Cl_2·6H_2O$: 7.5 mg	(1) visible light: λ= 400 − 800 nm (2) natural sunlight	3 h 9 h	Liquid phase; Room temperature	[182]
$Ni(OH)_2$	Nanosheets	Hydrothermal	(1) 0.1 atm CO_2 CO: 5900 μmol h^{-1} g^{-1} H_2: 553 μmol h^{-1} g^{-1} (2) 0.05 atm CO_2 CO: 3800 μmol h^{-1} g^{-1} H_2: 546 μmol h^{-1} g^{-1}	λ = 420 nm 0.1 atm CO_2: 0.95% 0.05 atm CO_2: 0.6%	CO_2: 0.05 atm, 0.1 atm	TEOA	Mecn; 3 ml, H_2O: 2 ml, TEOA: 1 ml	Reactor: 60 ml; Catalyst: 1 mg, Photosensitizer: $[Ru(bpy)_3]Cl_2·6H_2O$: 7.5 mg	Visible light: λ= 400 − 800 nm	3 h	Liquid phase; Room temperature	[777]
$Ni(OH)_2$/ graphene	Hiearchical $Ni(OH)_2$ nanosheet arrays dispersed on graphene	Hydrothermal	CO: 7432 μmol h^{-1} g^{-1} H_2: 646 μmol h^{-1} g^{-1}	0.95% (λ = 450 nm)	10% CO_2	TEOA	Mecn: 3 ml, H_2O: 2 ml, TEOA: 1 ml	Catalyst: 1 mg, Photosensitizer: $[Ru(bpy)_3]Cl_2·6H_2O$, 7.5 mg	Visible light: λ ≥ 420 nm, 405 mw cm^{-2}	—	Liquid phase; Room temperature	[703]
Zno/g-C_3N_4	Zn nps coupled with g-C_3N_4 (wrinkled sheets)	Impregnation	Total yield of products (CO, CH_3OH, CH_4, C_2H_5OH): (1) 10% CO_2: ~23 μmol h^{-1} g^{-1} (2) 1% CO_2: 18 μmol h^{-1} g^{-1}	—	1%, 10% CO_2 in N_2 (0.4 Mpa)	—	CO_2, H_2O (vapor)	Reactor: 132 ml; Catalyst: 10 mg	(1) UV visible light: 175 mw cm^{-2} (2) visible light: λ > 400 nm, 105 mw cm^{-2}	4 h	Gas phase; 80 °C	[778]
$AgCu_2O$/ZnO	Nanorods	Chemical reduction	CO: 2.49 μmol h^{-1} g^{-1}	—	10% CO_2 (CO_2: 0.1 atm)	—	CO_2, H_2O (vapor)	Batch reactor: 40 ml; Catalyst: 10 mg	UV visible light: λ = 320 − 780 nm, 820 mw cm^{-2}	4 h	Gas phase	[779]
Cds/N-doped carbon	Cds qds (~4.5 nm) scattered on the 3D ordered macroporous N-doped carbon	In situ transformation	CO: 1780 μmol h^{-1} g^{-1} H_2: 2540 μmol h^{-1} g^{-1}	—	10% CO_2	—	Mecn: 3 ml, H_2O: 2 ml, Benzylamine: 0.1 ml	Reactor: 50 ml; Catalyst: 10 mg, $Cocl_2$: 1 μmol, Bipyridine: 15 mg	Visible light: λ > 420 nm	—	Liquid phase; 25 °C	[780]

(Table 19 – continuation)

Material	Characterization Shape&size	Synthesis method	Reduction product yield[a] (max.)	Apparent quantum efficiency	Feed gas	Sacrificial electron donor	Reaction medium	Batch size (reactor type&volume, catalyst amount)	Irradiation	Reaction time	Reaction type, Temp.[b]	Ref.
Amine-functionalized graphene/cds	Graphene layers uniformly scattered on the surface of cds nanoparticles	Solvothermal – electrostatic reaction – coupling reaction	CH_4: 1.62 μmol h^{-1} g^{-1} CO: ~0.4 μmol h^{-1} g^{-1}	—	CO_2: 0.1 bar	—	CO_2, H_2O (vapor)	Catalyst: 50 mg	Visible light: λ > 420 nm, 100 mw cm^{-2}	4 h	Gas phase; 40 °C	[781]
$CsPbBr_3$ @g-C_3N_4	Cspbbr$_3$ (polyhedral shape) on the surface of g-C_3N_4 sheet	Mixing in toluene	CH_4: 7.1 μmol h^{-1} g^{-1} CO: 1.7 μmol h^{-1} g^{-1}	—	11% CO_2 in Ar	—	EA: 6 ml	Batch reactor: 50 ml; Catalyst: 5 mg	Visible light: λ ＞ 420 nm, AM 1.5	12 h	Liquid phase; 20 °C	[782]

Table 20. Summary of materials applied for photocatalytic nitrogen fixation.

Material	Characterization Shape&size	Synthesis method	NH_3 yield	Apparent quantum efficiency	Sacrificial electron donor	Reaction medium	Batch size (reactor type&volume, catalyst amount)	Irradiation	Reaction time	Reaction Temperature [a]	Ref.
TiO_2	Nps (20–50 nm)	Solid phase reduction	324.86 μmol h^{-1} g^{-1}	1.1% (λ = 365 nm)	CH_3OH	H_2O: 90 ml, CH_3OH: 10 ml	Batch reactor; Catalyst: 50 mg	Full spectrum	1 h	25 °C	[783]
TiO_2	Untrathin nanosheets	Hydrothermal	78.9 μmol h^{-1} g^{-1} (UV vis) 1.54 (λ = 600 nm) 0.72 (λ = 700 nm)	0.74% (λ = 380 nm) 0.23% (λ = 420 nm) 0.08% (λ = 600 nm) 0.05% (λ = 700 nm)	—	H_2O: 20 ml	Flow reactor; Catalyst: 20 mg	UV visible light	1 h	25 °C	[784]
F-TiO_2	Nps with disordered surface layer	Reduction−hydrothermal	206 μmol h^{-1} g^{-1}	0.38 % (λ = 420 nm)	—	H_2O: 500 ml	Catalyst: 500 mg	Full spectrum	5 h	2 °C	[785]
C-TiO_x/Ru	Nanosheets	Bottom−up approach	109.3 μmol h^{-1} g^{-1}	1.1 % (λ = 400 nm)	CH_3OH	H_2O: 10 ml, 10% CH_3OH	Reactor: 175 ml; Catalyst: 10 mg	Visible light: λ > 395 nm	2 h	25 °C	[786]
$TiO_{2-x}S_y$	Nanoplatelets	Ion exchange	114.1 μmol h^{-1} g^{-1} (full spectrum) 86.2 (vis – NIR) 14.1 (NIR)	—	—	H_2O: 60 ml	Reactor: 250 ml; Catalyst: 20 mg	(1) full spectrum, (2) visible light – NIR: λ > 420 nm (3) NIR: λ = 800−1100 nm	2 h	25 °C	[787]
Ru/TiO_2	TiO_2 nanosheets (40 nm) decorated with single atom Ru	Hydrothermal–thermal treatment– precipitation– thermal treatment	56.3 μg h^{-1} g_{cat}^{-1}	—	C_2H_5OH	H_2O: 100 ml, 20% C_2H_5OH	Flow reactor; Catalyst: 40 mg	Fulll spectrum	4 h	25 °C	[191]
Fe-TiO_2/Au	Microsphere	Electrospinning − annealing	~ 200 μmol L^{-1}	0.39% (λ = 600 nm)	—	H_2O: 15 ml	Catalyst: 5 mg	Visible light	4 h	Room temperature	[788]
Fe-TiO_2-SiO_2	Fe single atom Porous structure	Evaporation−induced self-assembly	32 μmol h^{-1} g^{-1}	—	—	H_2O: 100 ml	Flow reactor; Catalyst: 50 mg	Xe lamp	2 h	—	[789]
Fe-TiO_2	—	Heat treatment	11.6 μmol h^{-1} g^{-1}	—	—	H_2O	Batch reactor: 38 ml; Catalyst: 0.2 g	λ = 390−420 nm	3 h	40 °C	[187]
Fe-TiO_2	Nanofibers	Electrospinning	64.2 μmol h^{-1} g^{-1}	1% (λ = 380 nm)	—	H_2O: 15 ml	Flow reactor; Catalyst: 5 mg	Full spectrum: 200 mw cm^{-2}	3 h	Room temperature	[790]
TiO_2/$ZnFe_2O_4$	$ZnFe_2O_4$ nps on TiO_2 microspheres	Solvothermal − calcination	1.48 μmol L^{-1} min^{-1}	—	CH_3OH	Aqueous solution: 100 ml, CH_3OH	Flow reactor	Visible light	10 h	25 °C	[791]

(Table 20 – continuation)

Material	Characterization Shape&size	Synthesis method	NH_3 yield	Apparent quantum efficiency	Sacrificial electron donor	Reaction medium	Batch size (reactor type&volume, catalyst amount)	Irradiation	Reaction time	Reaction Temperature[a]	Ref.
TiO_2@ C/g-C_3N_4	TiO_2 nanocrystals wrapped by C_3N_4 nanosheet on carbon nanosheet	Thermal treatment	250.6 μmol h^{-1} g^{-1}	0.14 % (λ = 420 nm)	CH_3OH	H_2O: 80 ml CH_3OH: 20 ml	Reactor: 500 ml; Catalyst: 50 mg	Visible light: λ > 420 nm	2 h	—	[792]
$Fe_xSr_{1-x}TiO_3$	Quasi sphere-like nanoparticles	Hydrothermal−calcination	30.1 μmol h^{-1} g^{-1}	—	—	H_2O: 150 ml	Catalyst: 15 mg	Xe lamp	2 h	Room temperature	[793]
$BaTiO_3$	Nps with disordered surface	Sol−gel hydrothermal− $nabh_4$ thermal reduction	1.35 mg L^{-1} h^{-1} 1.93 mg L^{-1} h^{-1} (under magnetic field)	—	—	H_2O: 500 ml	Catalyst: 50 mg	Xe lamp: 100 W cm^{-2}	4 h	23 °C	[794]
Pt-ZnO	Hexagonal plates	Wet etching−impregnation	860 μmol h^{-1} g^{-1}	—	Na_2SO_3	H_2O: 25 ml Na_2SO_3 solution: 10 ml, 500 ppm	Catalyst: 100 mg	Hg lamp	1 h	—	[795]
B-Ga_2O_3	Nanorods	Hydrothermal	Reaction rate: 0.851 μmol L^{-1} s^{-1} TOF: 8.51 μmol g^{-1} s^{-1}	Quantum yield: 36%	*T*-butanol	Solution: 100 ml, *T*-butanol: 0.02 M	Catalyst: 100 mg	λ = 254 nm	3 h	25 °C	[796]
g-C_3N_4/ γ-Ga_2O_3	γ -Ga_2O_3 flower embedded on the surface of g-C_3N_4 layer	Hydrothermal	355.5 μmol h^{-1} g^{-1}	—	C_2H_5OH	Aqueous solution: 50 ml, 20% C_2H_5OH	Batch reactor; Catalyst: 100 mg	Visible light: 346 W cm^{-2}	1 h	Room temperature	[797]
Sb	Nanosheets	Exfoliation	388.5 μg_{nh3} h^{-1} g_{cat}^{-1}	—	CH_3OH	Aqueous solution: 5 ml, 20% CH_3OH	Batch reactor; Catalyst: 1 mg	Visible light: λ ≥ 420 nm	1 h	25 °C	[798]
BiO	Spherical-like morphology (2–5 nm)	Hydrothermal	1226 μmol h^{-1} g^{-1}	—	—	H_2O: 200 ml	Batch reactor: 600 ml; Catalyst: 50 mg	Simulated solar light	24 h	25 °C	[799]
Mn-$W_{18}O_{49}$	Microspheres	Solvothermal	97.9 μmol h^{-1} g^{-1}	0.14% (λ = 350 nm) 0.023% (λ = 435 nm)	Na_2SO_3	Aqueous solution: 150 ml, Na_2SO_3: 1 mm	Catalyst: 15 mg	Full spectrum: λ = 320–780 nm	2 h	Room temperature	[800]
Mo-$W_{18}O_{49}$	Nanowires	Solvothermal	195.5 μmol h^{-1} g^{-1} (full spectrum, Na_2SO_3)	0.33% (λ = 400 nm, in pure H_2O)	Na_2SO_3	(1) H_2O: 10 ml, (2) aqueous solution: 10 ml, Na_2SO_3: 1 mm	Catalyst: 10 mg	(1) full spectrum (2) visible NIR light: λ > 400 nm 200 mw cm^{-2}	2 h	Room temperature	[801]

(Table 20 – continuation)

Material	Characterization Shape&size	Synthesis method	NH_3 yield	Apparent quantum efficiency	Sacrificial electron donor	Reaction medium	Batch size (reactor type&volume, catalyst amount)	Irradiation	Reaction time	Reaction Temperature[a]	Ref.
Mo-$W_{18}O_{49}$	Nanowires	Hydrothermal− photodeposition	399.24 μmol h^{-1} g^{-1}	0.611% (λ = 540 nm)	CH_3OH	H_2O: 80 ml, CH_3OH: 20 ml	Catalyst: 20 mg	Full spectrum	2 h	—	[802]
WO_3	Nanoporous structure	Etching− calcination	230 μmol h^{-1} g^{-1}	0.13% (λ = 420 nm)	—	H_2O: 20 ml	Reactor: 100 ml; Catalyst: 10 mg	Full spectrum: λ = 320−780 nm, 250 mw cm^{-2}	0.5 h	25 °C	[803]
Mn-WO_3	Aggregated nanocrystalline	Etching− thermal treatment	425 μmol h^{-1} g^{-1}	0.18% (λ = 450 nm)	—	H_2O: 20 ml	Reactor: 100 ml; Catalyst: 10 mg	Full spectrum: 250 mw cm^{-2}	0.5 h	25 °C	[804]
C-$WO_3 \cdot H_2O$	Carbon coating on the surface of $WO_3 \cdot H_2O$ microspheres	Microwave-assisted method− post-microwave treatment	205.73 μmol h^{-1} g^{-1}	—	—	H_2O	Catalyst: 50 mg	Xe lamp: 500 mw cm^{-2}	1 h	25 °C	[805]
Fe-$W_{18}O_{49}$/ g-C_3N_5	Fe-$W_{18}O_{49}$ nanowires attached to porous g-C_3N_5	Solvothermal	131.6 μmol h^{-1} g^{-1}	—	Na_2SO_3	Aqueous solution: 100 ml, Na_2SO_3	Reactor: 500 ml; Catalyst: 50 mg	Simulated sunlight: AM 1.5	—	20 °C	[806]
Bi_2WO_6	Hollow microspheres	Solvothermal	(1) 106.4 μmol h^{-1} g^{-1} (simulated sunlight) (2) 57.1 (vis)	0.18% (λ = 350 nm) 0.11% (λ = 380 nm) 0.07% (λ = 400 nm) 0.04% (λ = 420 nm)	—	H_2O: 150 ml	Catalyst: 150 mg	(1)simulated sunlight (2) visible light: λ > 420 nm 400 mw cm^{-2}	2 h	Room temperature	[807]
Au/(bio)$_{2.}$ CO_3	Nanodisks	Hydrothermal− chemical bath deposition	38.2 μmol h^{-1} g^{-1}	—	—	H_2O: 20 ml	Flow reactor; Catalyst: 20 mg	Xe lamp	1 h	Ambient temperature	[808]
Biobr	Nanosheets	Solvothermal	(1) 104.2 μmol h^{-1} g^{-1} (vis) (2) 223.3 (UV vis)	0.23% (λ = 420 nm)	—	H_2O: 100 ml	Flow reactor; Catalyst: 50 mg	Visible light: λ > 420 nm	1 h	25 °C	[809]
Bi_5O_7Br	Nanotubular or plate-like structures	Thermal treatment	12.72 mm g^{-1} h^{-1}	—	—	H_2O: 100 ml	Catalyst: 25 mg	Visible light: λ > 400 nm	0.5 h	—	[810]
Bi/BiOBr	Bi nps (4 nm) are loaded on BiOBr plates	Hydrolysis − solvothermal	222.6 μg $g_{cat.}^{-1}$	0.23% (λ = 420 nm)	Na_2SO_3	Solution: 50 ml, H_2SO_4: 0.025 M, Na_2SO_3: 0.025 M	Flow reactor; Catalyst: 25 mg	Visible light: $\lambda \geq 420$ nm	10 min	—	[811]
Fe-BiOBr	Microsphere consisting of nanosheets	Solvothermal	382.68 μmol h^{-1} g^{-1}	—	—	H_2O: 100 ml	Flow reactor; Catalyst: 50 mg	Visible light: λ > 420 nm	1 h	25 °C	[812]
Fe-BiOCl	Hierarchical microspheres	Solvothermal	30 μmol L^{-1} h^{-1}	—	—	H_2O: 100 ml	Catalyst: 50 mg	λ = 200–800 nm	—	Ambient temperature	[813]

(Table 20 – continuation)

Material	Characterization Shape&size	Synthesis method	NH_3 yield	Apparent quantum efficiency	Sacrificial electron donor	Reaction medium	Batch size (reactor type&volume, catalyst amount)	Irradiation	Reaction time	Reaction Temperature[a]	Ref.
Fe-BiOCl	Nanosheets	Hydrothermal	1022 μmol h^{-1} g^{-1} (TOF 0.863 h^{-1})	1.8% (λ = 420 nm)	—	H_2O: 20 ml	Catalyst: 10 mg	Xe lamp	1 h	Room temperature	[814]
MoO_2/BiOCl	MoO_2 nanosheets on the surface of biocl nanoplates	Hydrothermal − electrostatic adsorption	35 μmol h^{-1} g^{-1}	—	—	H_2O: 200 ml	Catalyst: 50 mg	Xe lamp: 500 mw cm^{-2}	1 h	—	[815]
$ZnIn_2S_4$/ BiOCl	Nanosheets	Solvothermal	14.6 μmol h^{-1} g^{-1}	—	—	H_2O: 200 ml	Reactor: 500 ml; Catalyst: 200 mg	Visible light: λ ≥ 420 nm	1.5 h	Ambient temperature	[816]
Bi_5O_7I	Nanosheets	Hydrolysis or calcination.	111.5 μmol L^{-1} h^{-1} (TOF, 21.02 h^{-1})	5.1% (λ = 365 nm)	CH_3OH	Aqueous solution: 100 ml, 20% CH_3OH	Batch reactor; Catalyst: 50 mg	λ = 280 – 800 nm, 2.36 W cm^{-2}	100 min	20 °C	[817]
Hydrogenated Bi_5O_7I	Microspheres	Calcination−hydrogen reduction	162.48 μmol h^{-1} g^{-1}	—	—	H_2O: 100 ml	Flow reactor; Catalyst: 20 mg	Visible light	3 h	15 °C	[818]
Bi_2Te_3/BiOCl	Microflowers	Hydrothermal−hydrolysis	315.9 μmol L^{-1} h^{-1}	—	CH_3OH	Aqueous solution: 500 ml, CH_3OH: 0.02 M	Catalyst: 20 mg	UV	6 h	Ambient temperature	[819]
Bi_2MoO_6/ BiOBr	Bi_2MoO_6 nanorods covered with with biobr nanosheets	Solution-phase reflux−solvothermal	~90.7 μmol h^{-1} g^{-1} (full spectrum) 81 (vis)	—	—	H_2O: 60 ml	Flow reactor: 250 ml; Catalyst: 30 mg	(1) full spectrum, (2) visible light: λ > 420 nm	1 h	25 °C	[820]
Cu_2O	Platelets (< 3 nm)	In situ topotactic reduction	30.31 μmol h^{-1} g^{-1} (4100 μmol g_{cu2o}^{-1} h^{-1})	0.14% (λ = 400 nm) 0.11% (λ = 450 nm)	—	H_2O: 30 ml	Flow reactor; Catalyst: 5 mg	Visible light: λ = 400-800 nm, 0.9 W cm^{-2}	1 h	20 °C	[821]
Cu_2O/SnS_2/ SnO_2	Hierarchical accordion-like layered nanosheets	Solvothermal	66.35 μmol h^{-1} g^{-1} (without C_2H_5OH) 372.05 (with C_2H_5OH)	—	C_2H_5OH	(1) H_2O: 50 ml (2) aqueous solution: 50 ml, 20% C_2H_5OH	Batch reactor; Catalyst: 100 mg	Xe lamp	12 h	Room temperature	[822]
Cu_2O/MoS_2/ Zno	Truncated octahedral Cu_2O, mos_2 nanoflowers, ZnO nanospheres	Hydrothermal−electrodeposition	54.11 μmol cm^{-2} h^{-1}	—	—	H_2O: 10 ml	Flow reactor	Visible light: λ > 420 nm	—	—	[823]

(Table 20 – continuation)

Material	Characterization Shape&size	Synthesis method	NH_3 yield	Apparent quantum efficiency	Sacrificial electron donor	Reaction medium	Batch size (reactor type&volume, catalyst amount)	Irradiation	Reaction time	Reaction Temperature[a]	Ref.
$Ag/KNbO_3$	Nanorods	Hydrothermal−photodeposition	(1) 385 μmol L−1 g^{-1} h^{-1} (simulated sunlight), (2) 95.3 μmol L^{-1} g^{-1} h^{-1} (vis)	—	C_2H_5OH	5% C_2H_5OH	Catalyst: 100 mg	(1) simulated sunlight, (2) visible light	5 h	—	[824]
$NiS/KNbO_3$	NiS nps on the surface of $KNbO_3$ nanorods	Two−step hydrothermal	155.6μmol L^{-1} g_{cat}^{-1} h^{-1}	—	C_2H_5OH	H_2O: 95 ml, CH_3OH: 5 ml	Flow reactor; Catalyst: 50 mg	Simulated sunlight	5 h	25 °C	[825]
$Bi_2S_3/KTa_{0.75}Nb_{0.25}O_3$	Bi_2S_3 nps on the surface of $KTa_{0.75}Nb_{0.25}O_3$ nanocubes	Two−step hydrothermal	561.6 μmol L^{-1} g^{-1} h^{-1}	0.008% (λ = 360 nm)	CH_3OH	H_2O: 95 ml, CH_3OH: 5 ml	Flow reactor; Catalyst: 50 mg	Simulated sunlight: λ = 300−1000 nm, 54 mw cm^{-2}	5 h	—	[826]
$InVO_4$	Hollow nanocuboid assembly	Hydrothermal	101.02 μmol h^{-1} g^{-1}	0.50% (λ = 385 nm)	—	H_2O: 150 ml	Catalyst: 20 mg	Full spectrum	2 h	Room temperature	[827]
g-C_3N_4	—	Calcination	1.24 mmol h^{-1} g^{-1}	—	CH_3OH	Aqueous solution: 50 ml, 20% CH_3OH	Batch reactor: 100 ml; Catalyst: 50 mg	Visible light: λ > 420 nm	15 h	Ambient temperature	[828]
B-g-C_3N_4	Porous structure	Thermal treatment	313.9 μmol h^{-1} g^{-1}	0.64% (λ = 420 nm)	Na_2SO_3	Aqueous solution: 40 ml, Na_2SO_3: 1 mm	Catalyst: 20 mg	Visible light: λ > 420 nm, 0.5 W cm^{-2}	2 h	—	[829]
P-carbon nitride	Sheet-like structure	Calcination	~9.2 μmol	Solar-to-chemical conversion (SCC) efficiency: 0.1%	—	H_2O: 100 ml	Flow reactor; Catalyst: 200 mg	Visible light: λ > 420 nm	24 h	30°C	[830]
g-C_3N_4 (modified with cyano groups and intercalated K^+)	Nanoribbons	Calcination	3420 μmol h^{-1} g^{-1}	—	Ethylene glycol (EG)	EG: 40 ml	Catalyst: 10 mg	Visible light: λ > 400 nm, 1 W cm^{-2}	—	Ambient temperature	[831]
Fe-g-C_3N_4	Honeycombed structure	HNO_3 protonation−impregnation	5.4 mg L^{-1} h^{-1} g_{cat}^{-1}	—	C_2H_5OH	Solution: 500 ml, C_2H_5OH: 0.789 g L^{-1}	Flow reactor; Catalyst: 200 mg	Visible light: λ = 400−800 nm	4 h	30°C	[832]
Ag/g-C_3N_4	Ag clusters on the surface of C_3N_4	Ultra-low temperature reduced deposit	1.95 mmol L^{-1} h^{-1} g_{cat}^{-1}	—	Alcohols	Solution: 200 ml, 5% alcohols	Catalyst: 100 mg	Visible light: λ > 400 nm	4 h	—	[833]

g-C_3N_4/C/cds	Carbon dots and cds nps deposited over g-C_3N_4 sheets	Microwave–assisted method	1060 μmol L^{-1} g^{-1} h^{-1}	—	C_2H_5OH	H_2O: 50 ml, C_2H_5OH: 50 μl, 0.789 g L^{-1}	Catalyst: 50 mg	Xe lamp: 100 mw cm^{-2}	3 h	25°C	[834]

(Table 20 – continuation)

Material	Characterization Shape&size	Synthesis method	NH_3 yield	Apparent quantum efficiency	Sacrificial electron donor	Reaction medium	Batch size (reactor type&volume, catalyst amount)	Irradiation	Reaction time	Reaction Temperature[a]	Ref.
g-C_3N_4/ZrO_2	ZrO_2 NPs dispersed in g-C_3N_4 nanosheets.	One-step pyrolysis	1446 μmol L^{-1} h^{-1}	2.14% (λ = 400 nm)	CH_3OH	Aqueous solution: 100 mL, 10% CH_3OH	Catalyst: 100 mg	UV visible light: 100 mW cm^{-2}	9 h	25°C	[835]
g-C_3N_4/$Zn_{0.11}Sn_{0.12}Cd_{0.88}S_{1.12}$	ZnSnCdS NPs on the surface of sheet-like g-C_3N_4	Hydrothermal	7.543 mg L^{-1} h^{-1} g_{cat}^{-1}	—	C_2H_5OH	Solution: 500 mL, C_2H_5OH: 0.789 g L^{-1}	Flow reactor; catalyst: 200 mg	Visible light: λ = 400–800 nm	4 h	—	[836]
C_3N_4/MoS_2/Mn_3O_4	C_3N_4 nanosheets covers MoS_2 layers, Mn_3O_4 NPs loaded on MoS_2/C_3N_4	Chemical lithium intercalation method– pyrolysis– sol gel loading	185 μmol h^{-1} g^{-1}	1.2% (λ = 420 nm)	Na_2SO_3	H_2O: 25 mL, Na_2SO_3	Batch reactor; catalyst: 5 mg	Visible light: λ > 420 nm	10 h	—	[837]
Nb_2O_5/C/Nb_2C/g-C_3N_4	Structure with stacked layers	Calcination	927 μmol h^{-1} g^{-1}	—	CH_3OH	Squeous solution: 50 mL, 20% CH_3OH	Reactor: 500 mL; catalyst: 50 mg	Visible light: λ > 420 nm, 0.5 W cm^{-2}	2 h	—	[838]
Graphdiyne@Fe_3O_4	Fe_3O_4 nanorods/cubes on the surface of graphdiyne	Co-precipitation or microwave hydrothermal	1762.35 μmol h^{-1} g^{-1} ±153.71	—	—	Aqueous solution: 30 mL, Na_2SO_4: 0.1M	Reactor: 100 mL	Visible light: λ ≥ 400 nm	8 h	—	[839]
rGO/polyoxometalate	rGO loaded with polyoxometalate NPs (~2 nm)	Reducing by L-ascorbic acid	rGO@ $H_5[PMo_{10}V_2O_{40}]$ 130.3 μmol L^{-1} h^{-1}	—	—	H_2O: 100 mL	Catalyst: 150 mg	Simulated sunlight	1 h	Room temperature	[840]
ZnS/GO	ZnS spherical NPs coated with GO	Hummers method– hydrothermal	151.8 μmol L^{-1} g^{-1} h^{-1}	—	—	H_2O: 100 mL	Reactor: 250 mL; catalyst: 50 mg	Visible light	6 h	—	[841]
$Zn_3In_2S_6$	Nanosheet-assembled spheres	Solvothermal	355.2 mg L^{-1} g_{cat}^{-1}	—	CH_3OH	CH_3OH: 50 mL	Reactor: 100 mL; catalyst: 30 mg	Visible light: λ = 420–800 nm	4 h	—	[842]
MoS_2	Lamellar morphology	Hydrothermal– ultrasonic treatment	325 μmol h^{-1} g^{-1}	—	—	H_2O: 200 mL	Batch reactor; catalyst: 150 mg	Visible light: λ > 400 nm	10 h	25 °C	[843]
MoS_2/oxygen self-doped porous biochar	Nanoflowers	Pyrolysis– hydrothermal	37.9 μmol h^{-1} g^{-1}	—	—	H_2O: 100 mL	Catalyst: 20 mg	Visible light: λ > 400 nm	5 h	—	[844]

(Table 20 – continuation)

Material	Characterization Shape&size	Synthesis method	NH_3 yield	Apparent quantum efficiency	Sacrificial electron donor	Reaction medium	Batch size (reactor type&volume, catalyst amount)	Irradiation	Reaction time	Reaction Temperature[a]	Ref.
Ni_2P/ $Cd_{0.5}Zn_{0.5}S$	Ni_2P loaded on $Cd_{0.5}Zn_{0.5}S$ NPs (~20 nm)	Hydrothermal− solvothermal	101.5 μmol L^{-1}	4.32% (λ = 420 nm)	—	H_2O: 50 mL	Batch reactor; catalyst: 20 mg	Visible light: λ > 400 nm	1 h	20 °C	[845]
ZnCr-LDH	Nanosheets	Coprecipitation − alkali etching	33.19 μmol h^{-1} g^{-1}	0.95% (λ = 380 nm) 0.34% (λ = 420 nm) 0.11% (λ = 550 nm)	—	H_2O: 150 mL	Flow reactor; catalyst: 30 mg	UV visible light: λ = 200−800 nm, 5 W cm^{-2}	3 h	25 °C	[846]
$Cu^{\delta+}$-ZnAl-LDH	Nanosheets	Coprecipitation	110 μmol h^{-1} g^{-1}	1.77% (λ = 265 nm) 0.56% (λ = 365 nm)	—	H_2O: 100 mL	Catalyst: 5 mg	UV visible light: λ = 200−800 nm, 5.1 W cm^{-2}	1 h	25 °C	[847]
CuCr-LDH	Nanosheets	Coprecipitation	3696 μmol g^{-1} L^{-1} (UV vis) 2858 μmol g^{-1} L^{-1} (vis)	~0.44% (λ = 380 nm) 0.1% (λ = 500 nm)	—	H_2O: 20 mL	Catalyst: 50 mg	(1) UV visible light: λ = 200−800 nm, (2) visible light: λ ≥ 400 nm	1 h	25 °C	[848]
Ni/V-LDH	Nanosheets	Aqueous miscible organic solvent method	176 μmol h^{-1} g^{-1}	—	—	H_2O: 20 mL	Catalyst: 50 mg	Xe lamp	1 h	25 °C	[849]
NH_2-MIL-125 (Ti)	Mooncake-shaped crystallites	Solvothermal	12.3 μmol h^{-1} g^{-1}	0.26% (λ = 400 nm)	—	H_2O: 100 mL	Catalyst: 25 mg	Visible light: λ = 400–800 nm	15 h	—	[850]
Zn-MIL-88A	Hexagonal rod-like structure	Hydrothermal	300 μmol h^{-1} g^{-1}	—	—	H_2O: 60 mL	Batch reactor: 85 mL; catalyst: 50 mg	Xe lamp	14 h	Room temperature	[851]
Al-PMOF(Fe)	Nanoplate-like structure (15−25 nm thick)	Hydrothermal	127 μg h^{-1} g^{-1}_{cat}	—	CH_3OH	H_2O: 24 mL, CH_3OH: 6 mL	Catalyst: 10 mg	Visible light: λ > 400 nm, 100 mW cm^{-2}	5 h	25 °C	[852]
MOF(Sr)- Fe	Prism morphology	Solvothermal	780 μmol h^{-1} g^{-1}	—	K_2SO_3	H_2O: 100 mL K_2SO_3: 16 mg	Catalyst: 10 mg	Xe lamp: 0.15 mW cm^{-2}	3 h	—	[853]
Pt-SACs/covalent triazine framework (CTF)	Nanosheets	Depostion− reduction	171 μmol h^{-1} g^{-1}	1.4% (λ = 420 nm)	—	H_2O: 100 mL	Reactor: 250 mL; catalyst: 50 mg	Visible light: λ = 420−780 nm	5 h	Ambient temperature	[854]
Black phosphorus	Nanoflakes	Chemical etching exfoliation	2370 μmol h^{-1} g^{-1}	—	Na_2S/ Na_2SO_3	Aqueous solution, Na_2S/Na_2SO_3, 0.05 M	Catalyst: ~0.5 mg	Visible light: λ = 420 nm	—	—	[855]